

**UNIVERSIDADE FEDERAL DE SANTA CATARINA
PROGRAMA DE PÓS-GRADUAÇÃO EM ENGENHARIA MECÂNICA**

**DESENVOLVIMENTO E ESTUDO DINÂMICO DE RADIADOR ESPACIAL
INTEGRADO A TUBOS DE CALOR DE CONDUTÂNCIA VARIÁVEL**

**TESE SUBMETIDA À UNIVERSIDADE FEDERAL DE SANTA CATARINA
PARA A OBTENÇÃO DO GRAU DE DOUTOR EM ENGENHARIA MECÂNICA**

ANDREAS EDOM

FLORIANÓPOLIS, NOVEMBRO DE 1999

**DESENVOLVIMENTO E ESTUDO DINÂMICO DE RADIADOR ESPACIAL
INTEGRADO A TUBOS DE CALOR DE CONDUTÂNCIA VARIÁVEL**

ANDREAS EDOM

ESTA TESE FOI JULGADA ADEQUADA PARA A OBTENÇÃO DO TÍTULO DE

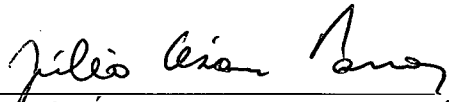
DOUTOR EM ENGENHARIA

SPECIALIDADE ENGENHARIA MECÂNICA, ÁREA DE CONCENTRAÇÃO
CIÊNCIAS TÉRMICAS

E APROVADA EM SUA FORMA FINAL
PELO PROGRAMA DE PÓS-GRADUAÇÃO EM ENGENHARIA MECÂNICA

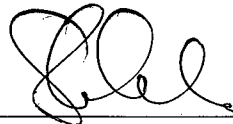


Prof. SERGIO COLLE, Dr.Sc.
Orientador



Prof. JÚLIO C. PASSOS, Dr.
Coordinador do Curso

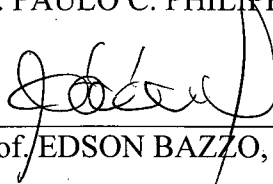
BANCA EXAMINADORA:



Prof. SERGIO COLLE, Dr.Sc.
Presidente



Prof. PAULO C. PHILIPPI, Dr.Eng.



Prof. EDSON BAZZO, Dr.Eng.



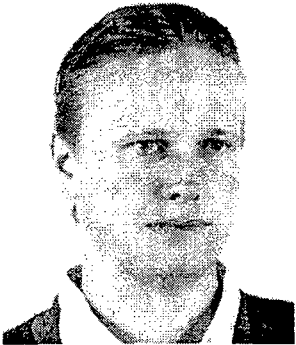
Prof. VALERI V. VLASSOV, Dr.
Relator Externo
Instituto de Pesquisas Espaciais (INPE)



Prof. GENRIKH A. DREYTSER, Dr.
Membro Externo

Instituto Aeronáutico de Moscou (MAI), Rússia

ABOUT THE AUTHOR



Andreas Edom, was born in Düsseldorf (Germany) on the 11th of May 1964. In the same city he visited the high school until 1983 specializing on foreign languages. After the conclusion of the basic course of Economics at the Technical University of Braunschweig in 1986 he moved to the University of Stuttgart to study Aerospace Engineering. After 2 years he went to Indonesia spending a practical training semester at the National Aircraft Industries IPTN in Bandung, Westjava. Back to Stuttgart he continued Aerospace Engineering with an emphasis on the areas of Thermodynamics and Space Technology. At the same time he joined the scientific team at the Institute of Space Systems (IRS) of the same university to work as a research assistant in the development of low power arcjets during almost three years. At the end of 1993 he graduated obtaining the Diplom-Ingenieur degree. The diploma thesis involved the development of a high temperature heat pipe interface to be integrated into a German-Japanese solar-dynamic power supply unit. This work he performed at the German Aerospace Center (DLR), where he also took care of the preparation of a cyclic test with a heat pipe / latent energy storage system for nearly one year. In September 1994 he followed the invitation of Prof. Sergio Colle to join the Satellite Thermal Control Group (NTSC) at the Solar Energy Laboratory (Labsolar) in Florianópolis, Brazil, and to start the doctoral course at the Federal University of Santa Catarina.

*To my grandmother
Nina Zinkevitch*

ACKNOWLEDGEMENTS

This thesis would not have been possible and its content not so comprehensive without the help of several persons and institutions from Brazil and Germany, to whom I like to express my sincere thanks. These are in the sequence of their appearance:

Prof. Manfred Groll from the Institute of Nuclear Research and Energy Systems (IKE) in Stuttgart, Germany, who recommended me to go to Labsolar in order to proceed my studies on heat pipes and contributed with various useful advices to the project of the experimental setup. Labsolar owes most of its infrastructure to his moving power in the German-Brazilian cooperation supported by the German Ministry for Research and Technology (BMFT).

My supervisor **Prof. Sergio Colle** who initiated this work and was always convinced of its valuable contribution to the science and technology of satellite thermal control. It was his help of getting installed in Brazil and the unrelenting and often really unbureaucratic undertakings to put up the funds and boundary conditions that facilitated the progress of my project and studies.

The Brazilian National Council of Scientific and Technological Development (CNPQ) for granting me, as the first doctor candidate from Germany, a four years' sponsorship for my studies and providing the funds to acquire necessary material.

Prof. Edson Bazzo, who often assisted sincerely and patiently in official and private matters, and with whom I passed hours of fruitful discussion about theoretical aspects of gas-loaded heat pipes.

Telesmagnó N. Teles and **Ivanete Mourão**, two very special persons from Brazil, for their precious encouragement and assistance in word and deed.

Prof. Antônio Fábio C. da Silva for his spontaneous disposition to clean together with me the simulation program from numerical problems that prevented it from converging.

Prof. Walter L. Weingaertner for his effort that he made producing a special tool to achieve the desired shape of the heat pipe prototype and personally machining the pipe afterwards.

Dr. Reinhard Schlitt from OHB-System in Bremen, Germany, who provided me with crucial literature and further facilitated the publication and thus recognition of the numerical results, even though the admission deadline has passed by far.

Sergio Dalmás, doctoral candidate at Labsolar and long-time inmate, who gave some helpful mathematical hints, beside plenty kind favors inside and outside of university concerns.

Egon Sigismund, welding engineer at the Research Center Jülich, Germany, for the donation of friction-welded aluminum-stainless-steel sample rods necessary for the fabrication of special heat pipe parts, as well as electron beam welding and leak testing of delicate joints.

Thomas Brenner, fine mechanics technician at the Laue Langevin Institute in Grenoble, France, for his impressive skill to machine long and tiny tubes out of a friction-welded sample rod.

The Brazilian Space Agency (**AEB**) that financed experimental equipment through the UNIESPAÇO project (program for the stimulation of national space activities at universities).

The National Institute of Space Research (**INPE**) that invited me to conduct the experimental phase of my work during a stay of 4 months and provided all the necessary infrastructure to accomplish the tests, and especially the team at INPE, where everybody of the subsequently mentioned and shown persons fulfilled a substantial part of the work that made a successful conclusion of the tests possible. These are (from left to right): **Rose M. do Prado Demori** (helium leak testing), **Benedito A. das Neves** (machining of all large radiator parts), **Dr. Valeri V. Vlassov** (technical adviser and main responsible for my stay at INPE), **Alice H. N. Ueda** (heat pipe cleaning), **Luis E. Barbosa** (joining, bonding and insulation), **Geraldo O. Mendes** (TIG welding), **José G. de Godoi** (mechanical project and mounting), **Oswaldo D. da Silva** (in charge of vacuum and thermal test facilities), **Pedro A. Cândido** (preparation of data acquisition and supply lines) and **Antônio C. Marques** (painting of radiating surfaces).



INPE staff assisting the experimental project phase

Gabriel I. M. Tapia and **Paulo Couto**, doctoral candidates at Labsolar, for their kind attention and the assistance in getting some of the figures so expressive.

And my special thanks are finally directed to **Prof. Adrianus A. M. Delil**, a worldwide known specialist (not only) on gas-loaded heat pipes from the National Aerospace Laboratory (NLR) in the Netherlands, who took my doctor defense as the occasion to come all the way over to Brazil to participate in the public and closed session, to review my thesis and to appreciate my work.

"God does not only play with dice,
He sometimes throws them where they can't be seen"

Stephen Hawking (English physicist)

TABLE OF CONTENTS

ABSTRACT	x		
RESUMO	xi		
RESÜMEE	xii		
LIST OF FIGURES	xiii		
LIST OF TABLES	xvi		
NOMENCLATURE	xvii		
1. INTRODUCTION	1		
1.1 Some fundamentals of telecommunication satellites			1
1.2 Scope of the research project			2
2. PRINCIPLES AND TYPES OF VARIABLE CONDUCTANCE HEAT PIPES	6		
2.1 General overview			6
2.2 Gas-Loaded Heat Pipes: Temperature control by noncondensable gas			7
3. GLHP RADIATORS: STATE OF THE ART IN SATELLITE TECHNOLOGY	16		
4. BIBLIOGRAPHICAL REVIEW OF GLHP MODELS	22		
4.1 Chronological survey			23
4.2 Classical steady-state flat front model			31
4.3 Transient lumped capacity model including start-up			32
4.4 Antoniuk's vapor space model			36
4.5 Transient lumped capacity model with axial heat conduction			37
4.6 Verification of the applicability of GHP model assumptions			41
5. MODELING OF THE GLHP RADIATOR SYSTEM	46		
5.1 Discretization of the radiator			46
5.2 Simple steady-state analyses of various radiator configurations			50
5.3 Transient radiator analyses based on Antoniuk's vapor space model			57

5.4	Transient vapor space model considering start-up and feed tube mass flow	64
5.5	Main features of the simulation program	67
5.6	Parametric study of a simulated transient failure behavior	72
6.	GLHP DESIGN PROJECT	78
6.1	Selection of the working fluid	78
6.2	Selection of heat pipe dimensions and wick	83
6.3	Selection of the noncondensable gas	90
6.4	Selection of the gas reservoir volume	92
7.	EXPERIMENTS AND VALIDATION ANALYSES	97
7.1	Finding a hypothetical flat front position from experimental data	98
7.2	Correlation of the internal condenser heat transfer coefficient	103
7.3	Technological aspects of GLHP manufacturing and filling	105
7.4	Experimental radiator setup for thermal vacuum tests	110
7.5	Radiator test results and comparison with simulation	115
7.6	Experimental single GLHP setup for tests with convective cooling	128
7.7	Single GLHP test results and comparison with simulation	131
7.8	Start-up characteristics in test and simulation	137
8.	FINAL REMARKS	139
	REFERENCES	142
APPENDICES		
A1.	IMPLICIT LINE-BY-LINE DISCRETIZATION METHOD APPLIED TO THE RADIATING SHEET	147
A2.	ALGORITHM TO ESTIMATE THE TEMPERATURE PROFILE OF THE COOLING AIR STREAM	152
A3.	RADIATOR TEST DATA PLOTS (RUNS A - F)	155
A4.	SINGLE GLHP TEST DATA PLOTS (RUNS 0 - 3)	188

ABSTRACT

The high heat dissipation density of modern high power amplifiers and other electronic equipment in communication satellites demands for an efficient cooling device to remove the heat from the hot zones of the base-plate and to dump it to space. Moreover the temperature at the base-plate must be maintained within a narrow range regardless of alteration in heat dissipation. A light, compact and reliable concept is a radiator that is based on gas-loaded variable conductance heat pipes as heat transfer controlling elements. The control of the operating temperature is feasible by connecting a gas reservoir to the cold end of the heat pipe in order to accommodate a noncondensable gas buffer. As the waste heat is generated on a small area and the radiator surface tends to be small because of weight and efficiency reasons, homogeneous heat withdrawal requires closely spaced parallel heat pipes leading to a highly coupled system.

A numerical and experimental investigation of such a heat pipe radiator has been conducted in order to get an insight into the dynamic behavior of the system that is strongly dependent on interactions between the heat pipes and reactions of the respective reservoirs. A configuration was chosen that couples three heat pipes to a base-plate on the heat entry side and to two faces of radiation on the heat exit side. According to the design goals of a heat transport capability up to 60 W and a 12 degree temperature control range, axially grooved 14 mm outer diameter aluminum heat pipes were selected and connected to 150 cm³ sized, cold, non-wicked stainless steel reservoirs by long and narrow feed tubes. The working fluid is acetone and the noncondensable gas is argon.

In the numerical model the complex metallic structure of the system (excluding the reservoirs) was represented by differently shaped one- and two-dimensional conjugated sub-domains using a finite control volume conduction model. For the vapor space a flat front type model has been developed that specifically considers start-up and the mass flow between heat pipe and reservoir. The vapor space model was then validated, and the assumption of a flat vapor/gas front was checked for cases near and at overload conditions. Firstly three single heat pipe tests with a compressed air cooled prototype were conducted at ambient temperature. In another six tests the radiator was cooled by radiation in a vacuum chamber at -50 °C, with varying gas masses and heat loads. The radiator was also tested in a configuration where the radiating sheets were cut in segments transverse to the pipes. Special attention was paid to study the effect of a possible loss of one outside radiator heat pipe. The failure was simulated by an abrupt opening of the gas valve at the respective heat pipe. The dynamic responses of the radiator were recorded and investigated and showed that, in all cases and for the time of observation, the system did not behave critically to the heat pipe failure.

Using a method that transforms the measured axial wall temperature profile into a hypothetical flat front at a computed position, the real diffuse front behavior could be contrasted with numerical results. Measurements of temperatures inside the vapor space facilitated the estimation of internal heat transfer coefficients and led to the formulation of a correlation that better incorporated in the model the influence of these coefficients in the simulation. The numerical results showed a good agreement with all features that were observed in the experiments, from start-up until operation under overload.

RESUMO

A grande densidade de calor dissipado por amplificadores modernos de alta potência e outros equipamentos eletrônicos em satélites de telecomunicação exige um sistema de resfriamento eficaz que seja capaz de remover o calor das regiões quentes na placa base e rejeita-lo ao espaço. Além disso a temperatura da placa base deve ser mantida dentro de uma faixa estreita independente de alterações de calor dissipado. Uma concepção leve, compacta e confiável consiste de um radiador baseado em tubos de calor de condutância variável, carregados com gás não condensável, para controle da transferência de calor. O controle da temperatura de operação é realizado conectando-se um reservatório de gás ao lado frio do tubo de calor, com objetivo de acomodar um tampão de gás não condensável. Como o calor parasita é gerado em uma área pequena e a superfície de radiação deve ser pequena por razões de peso e eficiência, uma remoção homogênea do calor exige um arranjo paralelo dos tubos de calor, colocados próximos uns aos outros, resultando em um sistema altamente acoplado.

Uma investigação numérica e experimental deste tipo de radiador foi feita para conhecer o comportamento dinâmico deste sistema, que é muito dependente das iterações entre os tubos e das reações dos respectivos reservatórios. Uma configuração foi escolhida, na qual três tubos de calor são acoplados a uma placa base no lugar da entrada do calor e a duas faces de radiação no lugar da saída do calor. Conforme o projeto, dimensionado para transportar calor de até 60 W de capacidade e controlar a temperatura dentro de um faixa de 12 graus centígrados, tubos de alumínio axialmente ranhurados com 14 mm de diâmetro externo foram escolhidos e conectados aos reservatórios de gás frios, sem estrutura capilar, de aço inoxidável com 150 cm³ de volume, através de tubos de conexão delgados e longos. O fluido de trabalho é acetona, e o gás não condensável é argônio.

Na modelagem numérica, a complexa estrutura metálica do sistema (sem os reservatórios) foi representada por sub-domínios conjugados, uni- e bidimensionais, de várias formas, utilizando a técnica de volumes de controle finitos. Para o espaço de vapor, um modelo do tipo frente plana foi desenvolvido, considerando-se especialmente a partida de operação e o fluxo de massa entre tubo e reservatório. O modelo do espaço de vapor foi então validado, e a hipótese de uma frente plana entre vapor e gás foi examinada, para casos correspondentes às condições próximas de sobre-carga. Inicialmente, três testes foram conduzidos na temperatura ambiente com um único tubo resfriado com ar comprimido. Em mais seis testes o radiador foi resfriado por radiação em câmara de vácuo a -50 °C, aplicando diferentes massas de gás e diferentes potências térmicas e testando uma configuração onde as placas radiantes foram cortadas em segmentos transversais aos tubos. Atenção especial foi dedicada ao estudo do efeito de uma eventual falha de um tubo exterior. A falha foi simulada por uma abertura abrupta da válvula de gás do respectivo tubo. As respostas dinâmicas do sistema foram observadas e analisadas, mostrando que em todos os casos e para o tempo de observação o radiador não revelou um comportamento crítico à falha.

Utilizando-se uma técnica que transforma o perfil axial da temperatura de parede medida em uma hipotética frente plana em posição calculada, o comportamento da frente difusa real pôde ser confrontado com os resultados numéricos. Medições de temperaturas dentro do espaço de vapor facilitaram a estimação de coeficientes internos de transferência de calor e levaram à formulação de uma correlação que melhor incorporou no modelo a influência desses coeficientes na simulação. Os resultados numéricos mostraram boa concordância com os fenômenos observados nos experimentos, desde a partida de operação até a operação de sobre-carga.

RESÜMEE

Die hohe Dichte abzuführender Wärme beim Betrieb von modernen Hochleistungsverstärkern und anderem elektronischen Gerät in Nachrichtensatelliten erfordert ein wirksames Kühlsystem, das die Wärme von heißen Bereichen der Grundplatte abführt und an den Weltraum abgibt. Zudem muß die Temperatur der Grundplatte innerhalb enger Toleranzen gehalten werden, unabhängig von Schwankungen des Wärmestroms. Eine leichtes, kompaktes und zuverlässiges Konzept ist ein Radiator, in dem die Wärmeübertragung durch gasgefüllte Wärmerohre mit variabler Wärmeleitfähigkeit geregelt wird. Die Kontrolle der Betriebstemperatur ist möglich, wenn an das kalte Ende des Wärmerohres ein Reservoir angefügt wird, um dort ein Puffer nicht-kondensierbaren Gases unterzubringen. Da die Abwärme auf engem Raume erzeugt wird und die Radiatorfläche aus Gewichts- und Wirkungsgradgründen klein gehalten werden sollte, wird für eine gleichmäßige Wärmeabfuhr eine dichte parallele Anordnung der Wärmerohre erforderlich und somit ein stark gekoppeltes System.

Ein solcher Wärmerohr-Radiator wurde numerisch und experimentell untersucht, um einen Einblick in das dynamische Systemverhalten zu erhalten, das stark abhängig ist von Wechselwirkungen zwischen den Wärmerohren und von den Reaktionen der entsprechenden Reservoirs. Eine Anordnung wurde gewählt, bei der drei Wärmerohre auf der Wärmeeingangsseite an eine Grundplatte und auf der Wärmeausgangsseite an zwei Abstrahlflächen gekoppelt sind. Nach Zugrundelegen der Entwurfsvorgaben mit einer Wärmetransportkapazität von bis zu 60 W und einem Temperaturkontrollbereich von 12 Grad wurden Axialrillen-Aluminiumrohre mit 14 mm Aussendurchmesser ausgewählt, die über lange und schmale Gasverbindungsrohre mit ungeheizten, 150 cm³ großen Edelstahlreservoirs ohne Kapillarstruktur verbunden sind. Die Betriebsflüssigkeit ist Azeton, und das nicht-kondensierbare Gas ist Argon.

Bei der numerischen Modellbildung wurde die vielfältige Metallstruktur des Systems (ohne Reservoirs) durch verschieden geformte verknüpfte ein- und zweidimensionale Teilbereiche dargestellt, unter Verwendung eines Wärmeleitungsmodells aus finiten Kontrollvolumina. Für den Dampfraum wurde ein Modell basierend auf einer flachen Front entwickelt, das im besonderen den Betriebsanlauf und den Massenstrom zwischen Wärmerohr und Reservoir berücksichtigt. Das Dampfraummodell wurde daraufhin für geeignet befunden, und die Annahme einer flachen Dampf/Gasfront für Fälle nahe dem und bei Überlastbetrieb überprüft. Anfänglich wurden drei Tests bei Umgebungstemperatur mit einem einzelnen mit Druckluft gekühlten Wärmerohr-Prototyp durchgeführt. In weitere sechs Tests wurde der Radiator in einer Vakuumkammer bei -50 °C strahlungsgekühlt. Verschiedene Gasfüllungen und Wärmelasten wurde getestet, sowie eine Konfiguration mit quer zu den Rohren segmentierten Abstrahlflächen. Besonderer Wert wurde darauf gelegt zu untersuchen, welchen Effekt der Verlust eines äußeren Wärmerohres zur Folge hat. Das Versagen wurde durch ein plötzliches Öffnen des Gasventils am betroffenen Wärmerohr verursacht. Die dynamische Reaktion des Systems wurde aufgezeichnet und untersucht, und zeigte, daß in allen Fällen und für die Zeit der Beobachtung der Radiator unkritisch auf das Wärmerohrversagen reagiert.

Unter Anwendung einer Methode, die den gemessenen axialen Wandtemperaturverlauf in eine hypothetische flache Front an errechneter Position umsetzt, konnte das Verhalten der in Wirklichkeit diffusen Front den numerischen Ergebnissen gegenübergestellt werden. Temperaturmessungen im Dampfraum ermöglichten die Schätzung von internen Wärmeübertragungskoeffizienten und führten zur Formulierung einer Korrelation, die den Einfluß der Koeffizienten in der Simulation besser berücksichtigt. Vom Anlauf bis hin zum Überlastbetrieb stimmten die numerischen Ergebnisse gut mit experimentell beobachteten Merkmalen überein.

LIST OF FIGURES

Fig. 2.1	Schematic of a gas-loaded heat pipe	8
Fig. 2.2	GLHP with a cold wicked reservoir	10
Fig. 2.3	GLHP with a separate cold non-wicked reservoir	11
Fig. 2.4	Actively controlled GLHP	13
Fig. 3.1	Radiator configuration with one GLHP on the astronomical satellite OAO	16
Fig. 3.2	Configuration of the AHPE experiment with a hot reservoir GLHP on the astronomical satellite OAO-C	17
Fig. 3.3	GLHP radiator of the lunar magnetometer LSM	17
Fig. 3.4	Multiple GLHP radiator of the communication satellite CTS	18
Fig. 3.5	Base-plate with GLHP radiators of the communication satellite MAROTS	19
Fig. 3.6	Thermal control module of the communication satellite ETS 5	20
Fig. 4.1	Solutions for the quasi steady-state condenser temperature profile with $L_{ca}=0.3m$, $L_c=0.5m$, $T_{ca}=50^\circ C$, $T_{ci}=30^\circ C$ for radiative and convective cooling	40
Fig. 5.1	Cut-out of a 30×50cm radiator showing the nodal network in heat pipes, fins and radiating sheet	47
Fig. 5.2	Main dimensions of the GLHP radiator as used in the steady-state partial model	51
Fig. 5.3	Effect of node density on calculated radiator heat output	53
Fig. 5.4	Wall temperature profiles of two GLHP neighbors in the broad radiator	54
Fig. 5.5	Sheet temperature fields of normal and slitted broad radiator	54
Fig. 5.6	Wall temperature profiles of two GLHP neighbors in the medium radiator	55
Fig. 5.7	Sheet temperature fields of normal and slitted medium radiator	55
Fig. 5.8	Wall temperature profiles of two GLHP neighbors in the narrow radiator	56
Fig. 5.9	Sheet temperature fields of normal and slitted narrow radiator	56

Fig. 5.10	Relevant GLHP dimensions for the vapor space model	58
Fig. 5.11	Numerical consideration of exact flat front position through weighting factor U	60
Fig. 5.12	Broad radiator simulation results for active lengths and operating temperatures	62
Fig. 5.13	Medium radiator simulation results for active lengths and operating temperatures	62
Fig. 5.14	Narrow radiator simulation results for active lengths and operating temperatures	63
Fig. 5.15	Heat-out to heat-in ratio for the 3 simulated radiator sizes	63
Fig. 5.16	Gas-blocked part of a GLHP with feed tube	64
Fig. 5.17	View of the complete GLHP radiator and its function	67
Fig. 5.18	Comparison of original and extended vapor space models at 34.5 W heat input	68
Fig. 5.19	Simulation program flowchart	70
Fig. 5.20	Front behavior, standard case	75
Fig. 5.21	Front behavior, variation: lower heat input	75
Fig. 5.22	Front behavior, variation: slitted radiator	75
Fig. 5.23	Front behavior, variation: higher gas inventory	75
Fig. 5.24	Front behavior, variation: methanol as working fluid	76
Fig. 5.25	Front behavior, variation: large feed tube diameter	76
Fig. 5.26	Active zone temperature behavior for all variations	76
Fig. 6.1	Vapor saturation pressure for 3 common heat pipe fluids	81
Fig. 6.2	Sink to evaporator temperature vapor pressure ratio for 3 common heat pipe fluids	81
Fig. 6.3	Dimensions of the selected heat pipe profile	84
Fig. 6.4	Partial schematic of a GLHP with a partially gas-blocked condenser	93
Fig. 6.5	Temperature control capability diagrams for two reservoir sizes related to sink temperature and desired evaporator temperature level and range	96
Fig. 7.1	Steady-state wall temperature and gas concentration profiles of the radiator GLHP's and flat front positions according to energy balance and gas balance approaches	102

Fig. 7.2	Steady-state wall temperature and gas concentration profiles of the single GLHP and respective hypothetical flat front positions according to the gas balance approach	103
Fig. 7.3	Radiator heat pipes after machining and connecting to the gas reservoirs	106
Fig. 7.4	Fixation of vapor space thermocouples inside the heat pipe container	107
Fig. 7.5	Sensor arrangement at each radiator GLHP	110
Fig. 7.6	Layout of temperature and pressure sensor channels and power supply lines for the radiator tests	112
Fig. 7.7	Close-up view at the mounting of the lever responsible for the simulated failure of HP1	113
Fig. 7.8	Fully assembled radiator test frame before insertion into the vacuum chamber	114
Fig. 7.9	Cooldown behavior of HP1 during failure: experiment and numerical counterpart	116
Fig. 7.10	Comparison of experimental and regression values for the condenser film coefficient	118
Fig. 7.11	Test performance Run A	120
Fig. 7.12	Operating point hysteresis between the start of all heat pipes and the restart of the outside heat pipes after temporary switch-off of their heat loads	121
Fig. 7.13	Test performance Run B	122
Fig. 7.14	Condenser end temperature responses of HP2 and HP3 to the failure of HP1	122
Fig. 7.15	Test performance Run C	123
Fig. 7.16	Test performance Run D	124
Fig. 7.17	Test performance Run E	125
Fig. 7.18	Test performance Run F (slitted radiator)	126
Fig. 7.19	Comparison of experimental and numerical wall temperature profiles of the radiator heat pipes	127
Fig. 7.20	Assembly of temperature and heat flux sensors, heater and cooling devices for the single GLHP experiment	129

Fig. 7.21	Front view of the experimental setup for single GLHP tests	131
Fig. 7.22	Test performance Run 1	134
Fig. 7.23	Test performance Run 3	135
Fig. 7.24	Experimental and numerical wall temperature profiles for two transient and two steady-state situations during single GLHP test run 3	136
Fig. 7.25	Start-up behavior of a radiator GLHP	138
Fig. 7.26	Start-up behavior of the single GLHP	138

LIST OF TABLES

Table 1	Overview of GLHP models with respect to their features and assumptions	30
Table 2	Gas control sensitivity factors at 30 °C for common heat pipe fluids	45
Table 3	Input data and parameters as used in the steady-state analysis	52
Table 4	Diffusion coefficients for some vapor/gas combinations at an operating temperature of 50 °C	91
Table 5	Reservoir size determination for 3 selected situations with acetone operated GLHP's	95
Table 6	Summary of radiator design details	114
Table 7	Radiator test run scheme featuring gas inventories and heat load cycles	115

NOMENCLATURE

<p>a heat pipe spacing [m]</p> <p>A area [m²]</p> <p>B width of contact area [m]</p> <p>c molar density [kmol/m³]</p> <p>c specific heat [J/kg·K]</p> <p>C heat capacity [J/K]</p> <p>d depth [m]</p> <p>D diameter [m]</p> <p>Đ mass diffusivity [m²/s]</p> <p>e fin thickness [m]</p> <p>f weighting factor</p> <p>g gravitational acceleration [m/s²]</p> <p>h heat transfer coefficient [W/m²K]</p> <p>h_{lv} latent heat of evaporation [J/kg]</p> <p>i counting variable, x-direction</p> <p>j counting variable, y-direction</p> <p>k thermal conductivity [W/mK]</p> <p>K permeability [m²]</p> <p>L length [m]</p> <p>m mass [kg]</p> <p>M molecular weight [kg/kmol]</p> <p>N mole number [kmol]</p> <p>p pressure [Pa]</p> <p>P perimeter [m]</p> <p>q heat flux per unit length [W/m]</p> <p>Q heat flux [W]</p> <p>r radius [m]</p> <p>R specific gas constant [J/kg·K]</p> <p>℞ universal gas constant [J/kmol·K]</p>	<p>s sheet thickness [m]</p> <p>t time [s]</p> <p>T temperature [K]</p> <p>v molar velocity [m/s]</p> <p>V volume [m³]</p> <p>w width [m]</p> <p>x transversal coordinate [m]</p> <p>y axial coordinate [m]</p> <p>z heat pipe axis [m]</p> <p>χ molar fraction</p> <p>δ molecular diameter [Å]</p> <p>ε emissivity</p> <p>η efficiency</p> <p>φ porosity</p> <p>κ ratio of specific heats</p> <p>μ dynamic viscosity [Pa·s]</p> <p>ν kinematic viscosity [m²/s]</p> <p>ρ density [kg/m³]</p> <p>σ Boltzmann's constant [W/m²K⁴]</p> <p>σ surface tension [N/m]</p> <p>τ time constant [s]</p>
	<p>Subscripts</p> <p>0 initial value</p> <p>∞ ambient, sink</p> <p>a active</p> <p>ad adiabatic</p>

b	contact
c	condenser
ca	active condenser
ci	inactive condenser
e	evaporator
e	east
ef	effective
ext	external
f	fin
f	feed tube
ff	flat front
g	noncondensable gas
h	hydraulic
h	homogeneous
HP	heat pipe
i	interface between vapor and liquid
int	internal
j	counting index
l	liquid
n	north
p	heat pipe wall
r	gas reservoir
r	radial
R	radiating sheet
s	solid
s	south
sat	saturation
so	source
ss	steady-state
t	total
v	vapor
w	wick
w	west

z axial

Superscripts

($\dot{\quad}$)	time derivative
($\bar{\quad}$)	referring to the mixture
*	reference value
0	anterior value
m	heat pipe number

1.1 Some fundamentals of telecommunication satellites

The use of radiators with integrated heat pipes is a common practice in modern satellite technology to cool high power electronic equipment located inside the satellite body. The function of a telecommunication satellite is that of an amplifying relay, that is, to receive electromagnetic signals in a large range of frequencies (television, broadcast, telephone, radar), to amplify them uniformly and to send them back in form of a narrow beam to a specified area on earth over a distance of at least 35800 kilometers. This is the height of a geostationary orbit which the satellite needs to remain motionless with respect to a reference point on earth.

To achieve a good quality of transmission the very low intensity signals that reach the satellite receiver have to undergo a series of treatments. They pass through a noise filter, are pre-amplified and separated into distinct channels by a demultiplexer. Then every channel passes through a high power transmitter. The signals from all the terminals of the transmitter are unified by a remultiplexer and finally emitted to earth by a single antenna.

Two types of transmitters are generally used [1]:

- Traveling Wave Tube Amplifiers (TWTA) and
- Solid State Power Amplifiers (SSPA).

The first type is distinguished by long operational history and a high output power of up to 400 watts for high radio frequencies. Recently SSPA have gained more importance in satellite missions due to their better linearity in the range of transmission and their lower weight.

TWTA, as well as SSPA in multiple stages, can produce an amplification gain of up to 60 dB (which is one million times the signal input). With respect to the energy supply they have an efficiency of approximately 30 %, which gives a good idea of the amount of energy dissipated in form of heat that the thermal control system of the satellite has to cope with.

The amplifiers are mounted on base-plates (structures of the satellite body) by means of rectangular adapter plates. They are made of a special highly conductive aluminum alloy to distribute the heat flux uniformly, as it enters the base-plate. The hot area of contact on the plate is called the “footprint”. If thermal control is based on heat pipes, on the opposite side of the

footprints the heat pipe evaporators are in immediate contact with the base-plate. The heat flux density within these hot areas is usually about 1 W/cm^2 [2].

In conventional passive thermal control the amplifiers are mounted on large and thick high-conductivity plates with large heat capacity, called thermal doublers. These elements are part of the carrying satellite structure, and one surface is used as a solid radiator. In this case the dissipated heat is spread quickly through the doubler material and directly radiated to space from the outer surface which is covered by a layer of Optical Solar Reflectors (OSR). However, with the expansion of telecommunication media power consumption and conversion requirements inside the satellite have correspondingly increased and sometimes exceed 10 kW of electric power. Reasonable capacitive coolers, such as thermal doublers, were no longer able to cope with such a big amount of generated heat. Either the footprint temperatures exceeded tolerated values, or the satellite became too massive. Additional mass always means additional fuel for orbit maneuvers and position keeping, and as the satellite is a one-way product, its lifetime is actually dependent on a fuel stock that cannot be recharged. Heat pipes therefore represent the alternative to meet the demands of profitability, reliability, a sufficient degree of redundancy and proven flight experience [3].

As previously mentioned, the heat removing evaporators of heat pipes can be positioned exactly where hot zones appear on the base-plate. Due to evaporation of a working fluid that is enclosed in the heat pipe container incoming sensible heat is converted into latent heat which is released in colder regions of the satellite or even transported out of the satellite body to external radiators. The working fluid evaporates from a capillary structure (the wick) that covers the entire interior surface of the heat pipe. As the vapor stream is formed in the evaporator, it gains density, then passes a zone that is isolated against the environment (adiabatic zone) and is gradually trapped along the cold condenser releasing its latent heat. The resulting condensate is carried back to the evaporator by the capillary forces of the wick.

Besides the mass reduction that heat pipes offer to the thermal control system, they also serve as reinforcing elements, thus contributing to the static design of the satellite body.

1.2 Scope of the research project

The development of an advanced system to cool electronic components in satellites was motivated by a raising interest in Brazil to gain technological experience and more independence when realizing national space related tasks that can only be met by appropriate satellites. Having

at disposal a very favorable launching point only 2 degrees latitude south of the equator and, in view of the great challenge to provide an efficient communication and monitoring network in such a vast country, the Brazilian government is becoming aware of the necessity to create a national space technology pool, in order to avoid the need for imported ready satellite solutions including their corresponding technical assistance services.

As a consequence of this interest, zones of activity were created in the laboratories of the National Institute of Space Research (INPE) and in various universities, to encourage the development of components of different subsystems that belong to a telecommunication satellite. The role of Labsolar at the Federal University of Santa Catarina in this alliance is the technological study of applicable and reliable thermal control subsystems.

The appropriate equipment to control the temperature of a compact bunch of powerful yet delicate transmitters is a radiator with integrated gas-loaded variable conductance heat pipes. This special type of heat pipe that is to be investigated in the present project automatically adjusts its thermal conductance to the amount of waste heat originated from the transmitters. The radiator should be a cantilever construction standing out of the satellite body to take advantage of two radiating surfaces exposed to space.

As the object of theoretical and experimental investigation a radiator was chosen that is made entirely of aluminum. It incorporates three geometrically equal acetone driven heat pipes with argon gas filling separated by equal spacing. Three heat pipes were considered to be sufficient

- to meet the need of redundancy for spaceborne vehicles
- to equally distribute the heat charge on base plate and radiating surfaces and
- in case of a heat pipe failure to facilitate the shunting of excessive heat load to two still operative heat pipes.

The radiator can be seen as a system that responds dynamically to thermal excitations at three entry locations, the evaporators of the heat pipes. On the exit side it is coupled, in a non-linear way, to the environment conditions by two radiating plates. In between there are three energy tracks made up by transfer elements (heat conducting wall and working fluid vapor) and dampers (thermal inertia and gas buffer).

Like every dynamic system the present one should also be investigated with respect to critical operational situations such as overcharge, asymmetric operation modes and partial failure occurrences. A heat pipe can suddenly fail for instance, when any part of the shell is damaged by

a meteorite impact. Due to working fluid leakage the heat pipe loses its extraordinary conductivity and merely continues working as a common solid heat conductor. The capability of self-regulation and instability phenomena must be detected and registered to condition the system for a future successful practical application.

The objective of the thesis can be seen in the provision of appropriate theoretical tools and experimental test devices to obtain a profound insight into the system's transient performance and to give some evidence of service reliability of coupled gas-loaded variable conductance heat pipes. However, it is not intended to take a closer look at heat transfer phenomena inside a single heat pipe, nor to optimize a radiator in terms of weight and size. Literature that deals with these tasks can be found in abundance.

Although radiators with more than one of these heat pipes have been employed for more than 20 years (chapter 3), as yet a transient analysis cannot be found in the literature. Models dealing with gas-loaded heat pipes are numerous [4-18]. They differ with respect to boundary conditions, temperature ranges, simplifying assumptions and degree of complexity. Chapter 4 gives a compilation of these models and mentions their main features.

A steady-state system analysis of a heat pipe radiator similar to the current one has been made by Peterson and Tien [19]. Their model is rather simplified. It is restricted to three heat pipe condenser shells which are coupled to one radiating sheet. The effects of interacting heat pipes under prescribed conditions are shown by spatial temperature distributions on the radiating sheet. This work serves as a starting point for the numerical analyses in chapter 5. In this way some radiator configurations and the design of the solid thermal network itself are checked. Later the network is extended to the whole system, the transient terms are introduced, and then a special vapor space model is derived to represent the heat pipe core dynamics. An extensive parameter analysis employs this complete model to give some information about transient failure operation modes.

As activities with variable conductance heat pipes are quite recent at Labsolar, it was thought to manufacture a heat pipe prototype in order to check both function and feasibility under simple laboratory conditions. The design calculations that led to the real gas-loaded heat pipes used in the experiments are presented in chapter 6. It is shown there that the gas-loaded heat pipe, as opposed to the conventional heat pipe, requires special attention with respect to some specific criteria. Chapter 7 deals with all aspects of the experimental work: manufacturing, filling, instrumentation and testing. The heat pipe radiator was run in a vacuum chamber with liquid nitrogen cooled shrouds, while the prototype was tested at ambient temperature cooled by a

guided air stream. Two of the test runs with the prototype are included in this thesis. They contribute to the validation of the vapor space model, as uncertainties in thermal masses and resistances are avoided, and the numerical treatment gets reasonably close to the actual heat transferring element. As the model is capable of handling start-up performance, some interesting aspects of theory and practice on this are presented in section 7.8.

2.1 General overview

Among heat transfer devices heat pipes distinguish themselves by the capability of transporting thermal energy over distances of several meters, displaying only a small temperature drop between the entrance of the heat flux (at the evaporator) and its withdrawal (at the condenser). This is due to their inherent high conductance which can exceed the conductance of a copper bar with the same cross section by a factor of more than 90 [20].

Being so conductive, light and slim, and thus having a good power-to-weight ratio, these thermal control components are welcome especially in narrow and enclosed spaces, where large amounts of heat are generated, as is the case of satellites. In order to maximize the radiative heat transfer, according to Boltzmann's law, the superfluous heat dissipated within the satellite body has to be dumped to space by means of radiating panels at a temperature only slightly lower than the temperature at which the heat flux is generated.

As electronic equipment has continuously become more sophisticated and smaller, the size of payload required by a certain mission has been reduced, providing space for additional devices within a given satellite structure. However, the miniaturization of electronic components was accompanied by an increased sensitivity to environmental influences such as mechanical, electromagnetic and thermal oscillations, and thermal shocks. Desired long lifetimes can only be achieved when operating at a specified temperature with only slight fluctuations. It was found that operation at a temperature 10 °C higher than the recommended led to a loss of functional reliability of 50 % [21]. This situation requires elements that can cool these components to nearly always the same temperature, regardless of variation in heat dissipation.

In a conventional fixed conductance heat pipe there is a pronounced dependence of the operating temperature on external conditions. When the incoming heat flux or the ambient temperature changes, the temperature of the heat transporting agent (the vapor) adjusts itself to the new conditions according to energy conservation, as do the temperatures of the evaporator and heat source.

From the necessity to maintain the footprint temperature almost constant over a wide range of heat input and heat sink conditions, the idea arose to induce the heat pipe to adjust its thermal conductance instead of its temperature. Three basic techniques were found to control a heat pipe in this way:

- a) Control of vapor flow: If a throttling valve is put into the vapor space at the transition from evaporator to adiabatic zone, the vapor stream through the pipe can be controlled. A change of heat input at the evaporator causes a pressure variation in a control fluid inside a bellow. The resulting movement of the bellow opens or closes the valve.
- b) Control of liquid flow: Working fluid in its liquid phase can be withdrawn from the active section of the pipe by a trap, or the condenser can be gradually flooded by excess liquid. In the first case the liquid is being captured in a chamber that has good thermal contact but no capillary connection to the evaporator. In the second case a bellow, similar to case a), is driven by the changing pressure of a control fluid and thus modifies the amount of liquid in the condenser. In the flooded section of the condenser condensation heat transfer is blocked.
- c) Control by means of a noncondensable gas buffer: A partial blockage of the condenser can also be realized by the addition of an inert gas to the vapor space of the heat pipe. With the gas filling a certain part at the end of the condenser the vapor cannot advance to this part, which means that condensation cannot take place there. Thus heat transfer is restricted to the condenser section which is not reached by the gas, the so-called active condenser.

Because of low reliability, mechanical complexity, weight and size, the first two techniques did not go further than the phase of prototype testing in laboratory. In common practice the temperature control of a heat pipe is realized by an inert gas which adjusts the heat transfer area in the condenser and thus the thermal resistance of the whole pipe according to technique c).

2.2 Gas-Loaded Heat Pipes: Temperature control by noncondensable gas

In the non-operating mode both gaseous components (vapor and noncondensable gas) are equally distributed throughout the heat pipe. During start-up the rising temperature and the subsequent evaporation of working fluid in the evaporator lead to pressure waves that push the gas, together with vapor, towards the colder end of the pipe, the condenser. The vapor condenses here and is pumped back through the wick by capillary forces, whereas the gas is repelled to the condenser

end by the momentum of the continuous stream of just evaporated vapor molecules. The fluids begin to separate and form a diffuse front between them. This front acts as a penetration barrier: It stops the axial velocity of the vapor stream, and the gas filled condenser section is effectively blocked against heat transfer to the environment.

Fig. 2.1 presents a schematic of a gas-loaded heat pipe together with the profiles of axial temperature and partial and total pressures. A certain amount of vapor is always present amidst the gas in the inactive region of the GLHP, in the non-operating mode as well as later due to gradual diffusion, when operating. The vapor pressure here corresponds to the saturation pressure at the temperatures of the inactive condenser and (if wicked) of the reservoir. They are equal to the ambient temperature, if there is no heat transfer to the environment in that region.

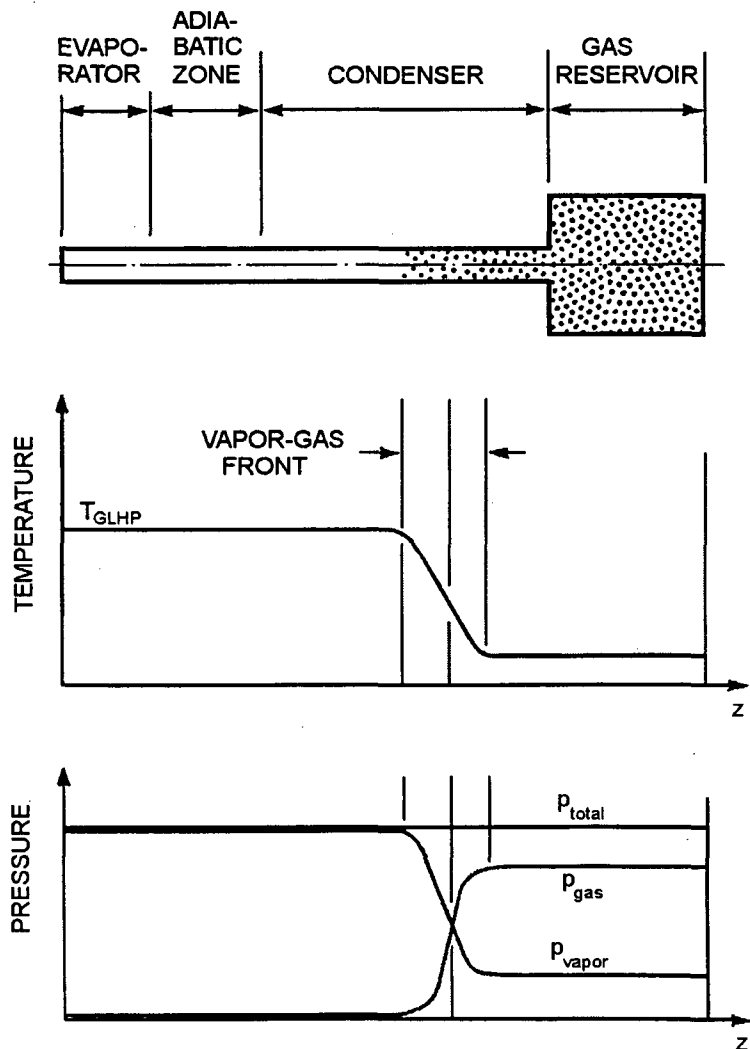


Fig. 2.1 - Schematic of a gas-loaded heat pipe

Since the present work deals with heat pipes in the so-called moderate temperature range and the vapor velocity is relatively small, compressibility effects do not alter the pressure neither in the axial nor in the radial direction. The total pressure is assumed to be constant along the GLHP and to coincide with the vapor saturation pressure at the interface between liquid and vapor in the evaporator.

When the heat input increases, more vapor is generated, absorbing the additional heat in latent form. The subsequent rise of vapor pressure in the active part of the GLHP results in a retreat of the gas buffer in the direction of the reservoir. Thus more thermally active volume (or length) in the condenser is taken up by the vapor-liquid cycle. This causes the thermal conductance to increase, which in turn minimizes the variation of the heat pipe temperature.

Since the vapor pressure has an exponential dependence on temperature, a small rise of temperature results in a large rise of pressure and consequently a substantial displacement of the gas buffer. If the reservoir volume is much larger than the heat pipe vapor space, the gas buffer acts like a smooth damper, so that the gas, as well as the whole pipe, will not feel a significant pressure increase. For this reason the gas buffer changes the total pressure very slightly, and affects even less the operating temperature, despite of large variations in heat load of typically one order of magnitude [22]. A large ratio of V_r to V_c therefore is an important requirement for good controllability of a GLHP.

This fact implies that it would be useless to take a conventional fixed conductance heat pipe and just add a certain quantity of gas to the already existent working fluid. The volume that must be provided for the gas in this case would make the heat pipe extremely long and heavy. GLHP's for real applications therefore have a special receptacle for the noncondensable gas, which is the reservoir, where the gas buffer can retreat completely, letting the whole length of the condenser to be active in case of maximum heat load.

Fig. 2.2 shows a GLHP with a reservoir that is formed by a flaring funnel-shaped extension of the end of the condenser. The wick covers the whole inner surface of the reservoir and follows the changing cross section homogeneously and with good contact to the wall to ensure an undisturbed liquid return flow. The figure also shows the temperature profile along the GLHP for three cases with constant (!) ambient temperature: the pipe is submitted to maximum (Q_{\max}), medium (Q) and minimum (Q_{\min}) heat loads respectively. For maximum heat load the whole length of the condenser becomes active, that is, available for heat transfer to the environment. For

minimum heat load the condenser is filled up by gas and essentially blocked against heat transfer. Just a small heat flux reaches the condenser by conduction from the adiabatic zone. A dashed line indicates the vapor/gas front referring to a medium heat load and a partially opened condenser.

As can be noted, this type of GLHP presents a good evaporator temperature controllability for the whole applicable heat range, provided that the ambient temperature is kept constant. In the contrary case the GLHP completely loses its controllability, when the liquid that exists in the reservoir causes a strong vapor pressure generation accompanied by a strong gas buffer expansion.

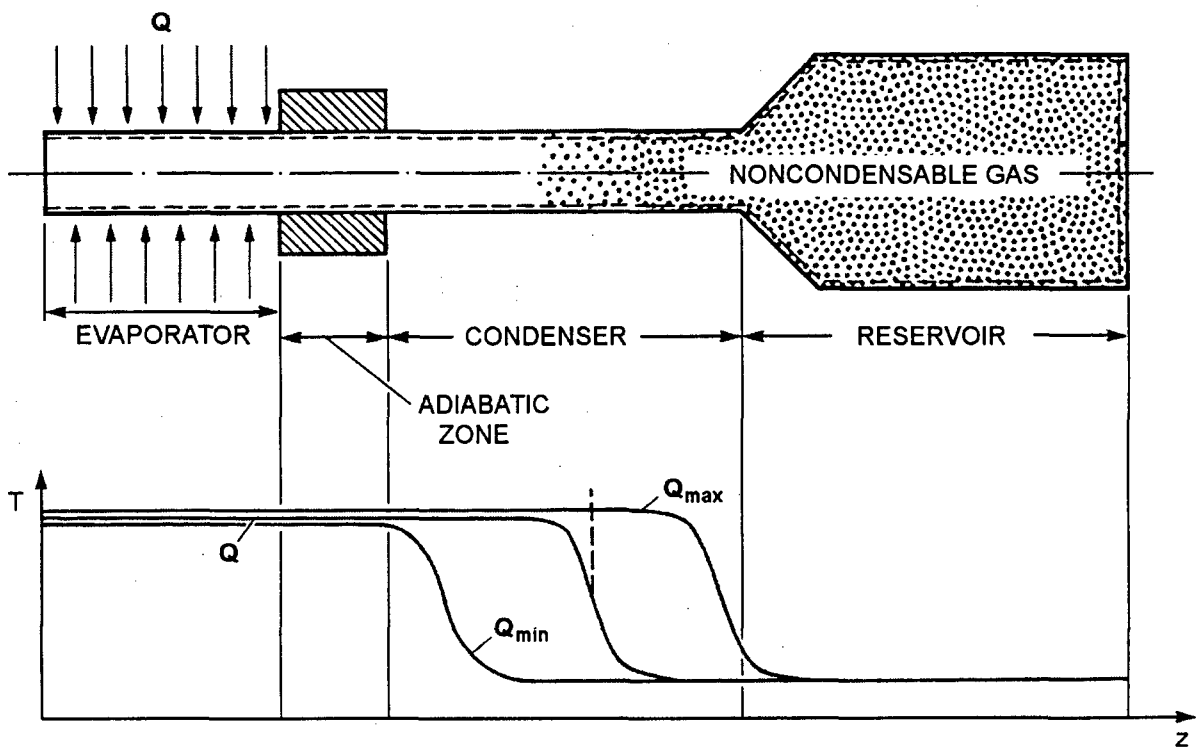


Fig. 2.2 - GLHP with a cold wicked reservoir

The vapor pressure in the reservoir is assumed to be equal to the saturation pressure of the working fluid at ambient temperature in this section. The advantage that the sensitivity of the vapor pressure to the temperature offered, allowing the active length to vary widely, now has a detrimental effect on the performance of the GLHP. An ambient temperature increase will put up the operating temperature, as the expansion of the gas will shut off the condenser and diminish the thermal conductance of the heat pipe. Temperature changes in the reservoir are negligible, if the temperature is much lower there than the temperature in the active part of the heat pipe. In this case the exponential dependence of the pressure on the temperature is not noticeable.

Consequently the applicability of a GLHP with a wicked reservoir fairly depends on outer thermal conditions of a space mission.

The gas buffer reacts in a linear way to environmental changes, if there is no liquid in the reservoir. This type of GLHP has a non-wicked reservoir. The gas-vapor mixture that forms the buffer ideally follows the ambient temperature variation according to the perfect gas law. Fig. 2.3 shows this kind of GLHP with a distinctly separated non-wicked reservoir. Providing a thin and long connection (feed tube) with a small wall thickness, it is possible to thermally decouple the reservoir from the conditions at the condenser end.

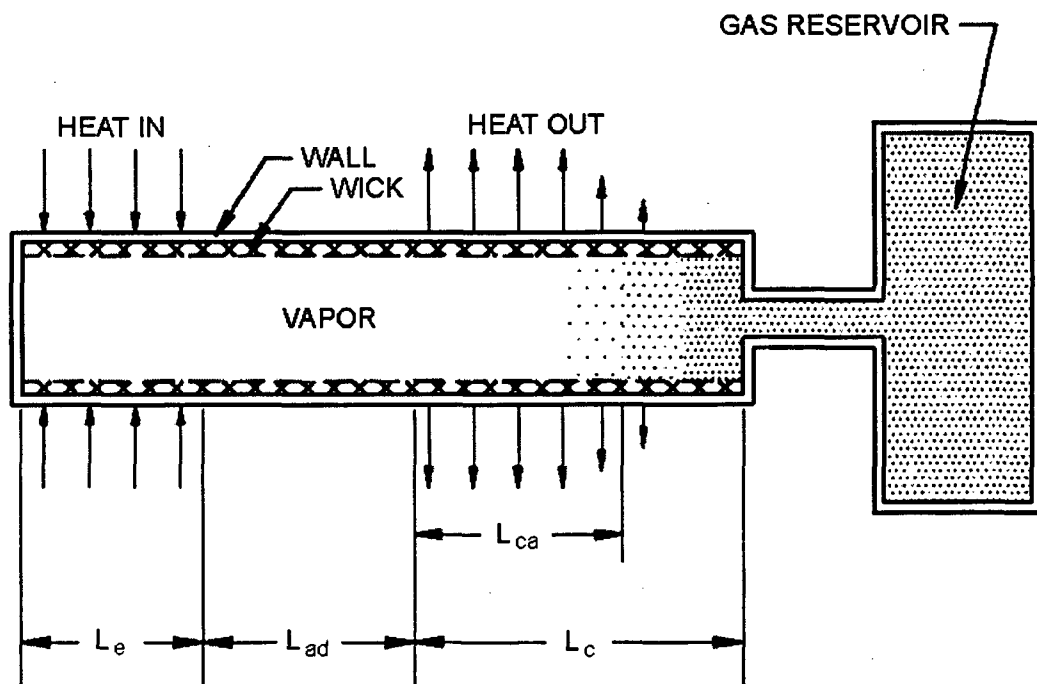


Fig. 2.3 - GLHP with a separate cold non-wicked reservoir

A disadvantage is the fact that vapor can diffuse into the reservoir, and there is no mechanism to bring it back to the evaporation-condensation cycle, except for possibly some back-diffusion. But depending on the cross section and length of the connecting tube, characteristic diffusion times on the way to the reservoir can take weeks up to several months [23]. This means that the partial vapor pressure in the reservoir is no longer influenced by fast temperature changes at the end of the condenser. Thus the gas buffer is not affected by these variations, and does not harmfully influence the operating temperature by undesirable shifts of the vapor/gas front.

Accumulation of working fluid in the reservoir can also be caused by an accidental spilling of liquid before the start of operation. Special precautions during mounting and transportation, as well as launch and orbiting maneuvers of the satellite (until the GLHP reaches the place of operation), must be taken to avoid this unfavorable situation.

Heat conduction from the heat pipe wall to the reservoir can be effectively stopped by mounting a cold trap at the entrance of the feed tube. If it is held at a certain temperature, temperature variations at the condenser end can be prevented. However, this device means active regulation. It requires auxiliary energy, and was therefore not chosen for space missions. A further reduction of heat conduction usually has been achieved by a tube made of two materials joined by friction welding, with the less conductive material on the reservoir side (e.g. aluminum to stainless steel).

The best temperature control is achieved by external (feedback) control. Especially when the heat source is very delicate, in case of a large variation of heat load and a large thermal resistance between heat source and vapor, an additional element that controls the gas expansion is indispensable.

If the contact to the evaporator is weak, the temperature at the heat source rises considerably with higher heat dissipation, and it diminishes with decreasing heat dissipation, even if the vapor temperature stays constant. The thermal resistance is the reason, why the temperature difference between source and vapor, ΔT , is linearly dependent. Here the control system ensures that the vapor temperature falls with rising heat flux according to the apparent temperature gradient ΔT .

Two types of external control have been designed, a mechanical system (passive control) and an electrical system (active control).

The passive control is realized by an expandable bellow-type reservoir whose volume is adjusted by a control fluid with a high coefficient of expansion. This fluid is sealed within a thin duct that at one end is mounted into the heat source and at the other presses against the reservoir end cap. Thus an increase of temperature at the heat source, for instance, is transformed in a forward movement of the end cap, which means an increase of reservoir volume. The gas in the condenser is sucked into the reservoir and opens more area in the condenser for heat transfer. At the same time the vapor temperature diminishes. Hence the evaporator can absorb a higher heat flux because of a higher temperature gradient between heat source and vapor.

Although this system has worked quite well under laboratory conditions, it has not been used in space missions, as it makes use of delicate moving parts with a high failure probability.

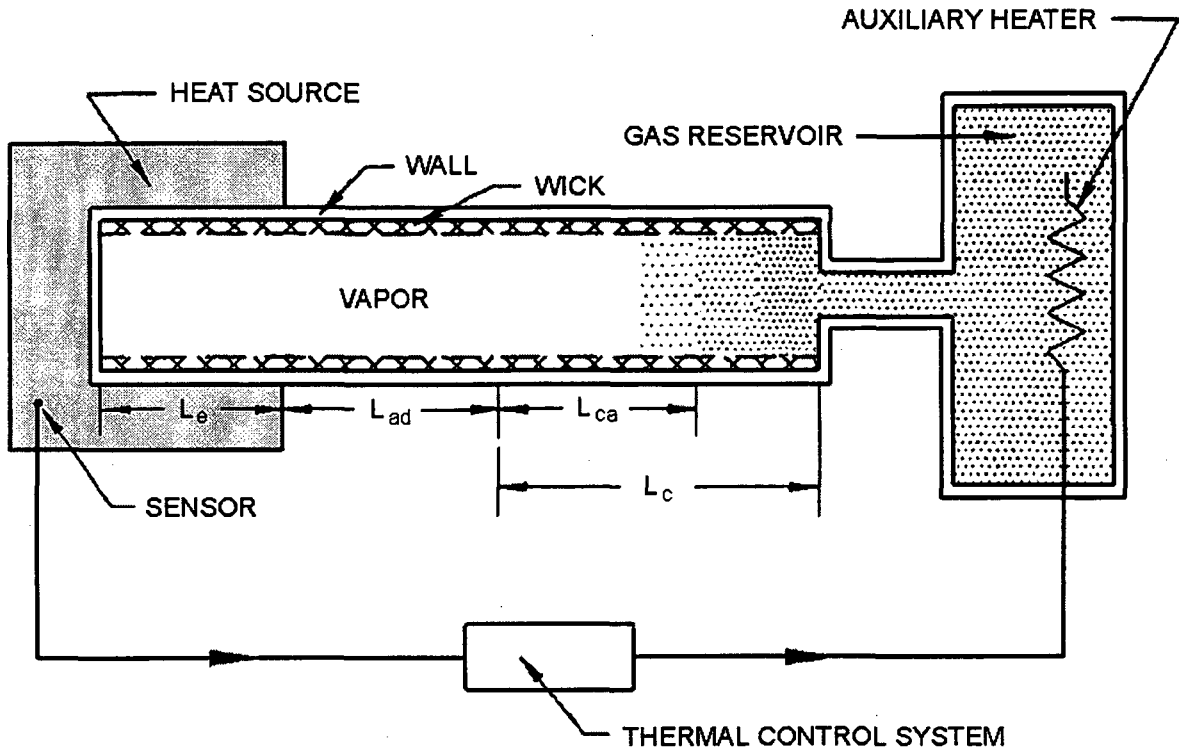


Fig. 2.4 - Actively controlled GLHP

The active control (Fig 2.4) is realized by electronic feedback. The temperature of the heat source is measured by a thermistor. An electronic controller processes the transducer signal and activates or deactivates a resistance heater inside the reservoir. If heat dissipation diminishes and the heat source temperature falls, the controller switches on the heater. With the temperature rise in the reservoir the gas expands and shuts off more condenser area. The vapor temperature increases and the temperature gradient flattens due to less heat dissipation. If more heat is released at the source, the temperature rises at this point, and the controller turns off the heater.

This system provides precise controllability of the operating temperature (below 0.5 K or better), but requires an external control system with auxiliary electrical power which is about 5 % of the nominal thermal energy transmitted by the GLHP [22].

All GLHP's mentioned so far have one thing in common: their sensibility towards ambient temperature variations which in some cases can be quite harmful to temperature controllability. For this reason, in space missions, the reservoirs which are exposed to the environment have to be protected by shields against radiation from outside.

The reservoir can be placed next to the evaporator. If good thermal contact between the two sections is provided, or the reservoir is even introduced into the evaporator (maintaining its connection to the condenser end of course), temperature variations can be minimized. The reservoir will always be at evaporator temperature which in principle is almost constant. This type of GLHP has a hot reservoir that must not be coated by a wick. A wick inside the reservoir would mean the presence of liquid, and this makes the reservoir itself a heat pipe that forces the gas out into the condenser.

As in the reservoir the working fluid only exists in the state of vapor, the partial pressure of the vapor there is exclusively conditioned by the vapor pressure in the gas-blocked condenser section, where the fluid exists in liquid form. Being independent of ambient conditions the reservoir vapor pressure follows temperature changes in the condenser with a considerable delay. This has a detrimental effect on the controllability of the GLHP in the case of large variations of the condenser temperature, unless it is very much lower than the operating temperature [5].

In space applications, where radiating plates rather than long condensers are used for cooling, it is quite awkward and weighty to bring the reservoir close to the evaporator and establish good thermal contact between them. Therefore, although GLHP's with hot reservoirs did successfully pass tests under microgravity conditions, they were finally not installed in radiators for satellite thermal control.

Charging a heat pipe with noncondensable gas also leads to temperature control in other respects: The heat pipe is able to work as a **thermal diode**. Due to solar impinging radiation during launch or while adjusting the orbit position for instance, the nominal condenser may reach a temperature higher than the nominal evaporator. The direction of the vapor stream is inverted, and the gas is now carried to the evaporator. But as soon as the evaporator is completely filled up with gas, it is blocked against heat transfer, the heat pipe is "switched off", and the electronic equipment is protected against heating by opposite heat fluxes.

According to publications about GLHP's coupled to radiator panels and intended for operation in space, preference was given to heat pipes with cold wicked reservoirs [2, 24-27]. The heat pipe container is made of aluminum or stainless steel, and the wick is usually formed from a stainless steel meshwork. To enhance the heat transport capacity, the wick is often moulded as slabs or arteries which are arranged within the vapor space of the heat pipe. In this way the resistance for the liquid return flow decreases considerably.

Aluminum pipes are axially grooved and contain ammonia as the working fluid in combination with nitrogen as the noncondensable gas. Stainless steel pipes generally combine methanol with nitrogen or argon. With all of the systems cited, temperature variations in the evaporator could be kept from $\pm 3 \text{ K}$ to $\pm 10 \text{ K}$ around the desired value.

The first GLHP's appeared in the early 70's, urged by the necessity to control the temperature of measuring systems in scientific satellites. At that time the heat dissipation of the electronic equipment was relatively low (up to 30 W); one heat pipe was sufficient to meet the requirements. With the condenser fixed to the panel by clamps the heat radiated to space from one surface, whereas the backface was isolated against the satellite body by multi-layer insulation (MLI).

Fig. 3.1 shows a radiator that was used aboard the satellite OAO (Orbiting Astronomical Observatory) [24]. The temperature of the measuring equipment was kept between 21 and 26 °C over the whole range of heat generation and ambient heat load variations.

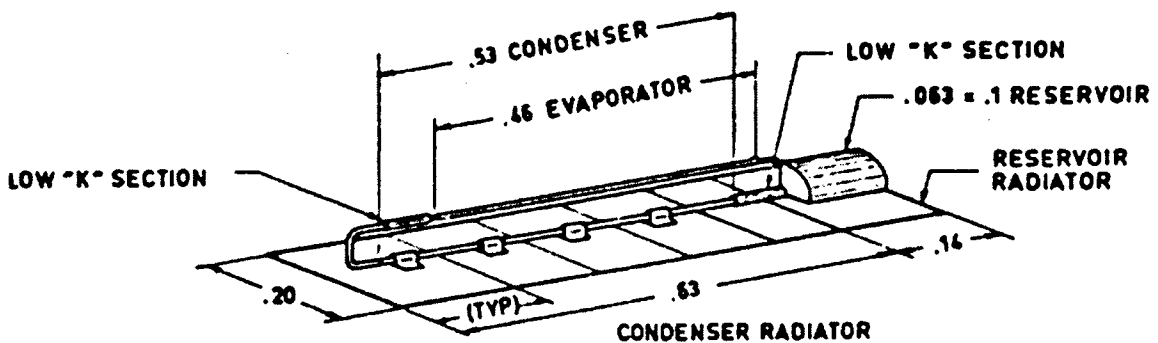


Fig. 3.1 - Radiator configuration with one GLHP on the astronomical satellite OAO (dimensions in m)

In another astronomical satellite mission, OAO-C, an experiment called AHPE (Ames Heat Pipe Experiment) was mounted, with the GLHP featuring a hot reservoir. In Fig. 3.2 the reservoir is seen to be bent back to the dissipating platform and positioned in front of the evaporator. The platform whose temperature was kept between 14 and 20 °C accommodated a board processor (OBP) with a heat dissipation of between 10 and 30 W.

As shown in Fig. 3.1 also, a technique of slitting the radiator panel perpendicularly to the heat pipe axis can be clearly noted. In AHPE the panel strips are additionally separated by intermediate

fiberglass. This type of segmentation is a quite common measure to reduce the thermal conductivity in the axial direction, thus achieving a sharper vapor/gas front.

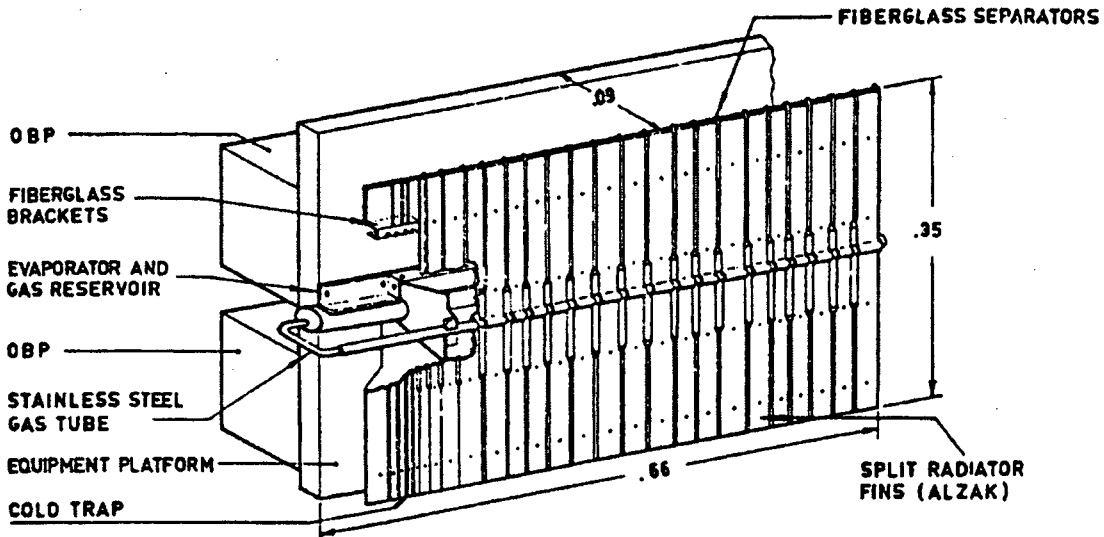


Fig. 3.2 - Configuration of the AHPE experiment with a hot reservoir GLHP on the astronomical satellite OAO-C (dimensions in m)

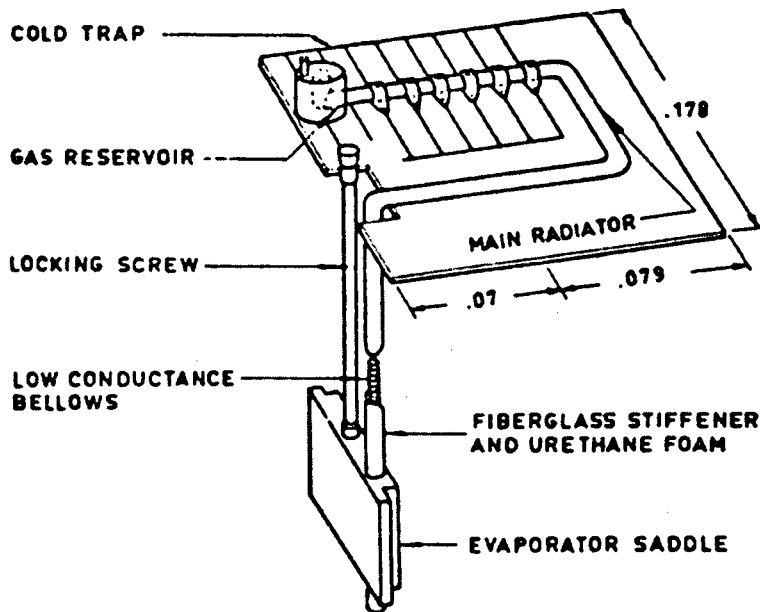


Fig. 3.3 - GLHP radiator of the lunar magnetometer LSM (dimensions in m)

The radiator in Fig 3.3 was designed to supplement the cooling system of the Lunar Surface Magnetometer (LSM) of Apollo mission 16 [25]. Although the heat dissipation was quite

constant, around 5.6 W, the equipment had to be protected against extreme changes of the lunar environment. In this application the GLHP also undertakes the task of a thermal diode. The on/off ratio was 2150:1. The extremely low conductance of 0.0026 W/K during the switched-off condition was achieved by an additional blockage of the conductive path along the heat pipe, realized by a low conductance bellow right in the adiabatic zone. The temperature of the measuring equipment was adequately controlled between -12 and +21 °C.

With the tendency of increasing heat dissipation in communication satellites the radiators became larger and heavier to provide sufficient radiating surface. To distribute the heat uniformly over the radiator, heat pipe arrays that were fixed to the panel at optimized positions became inevitable.

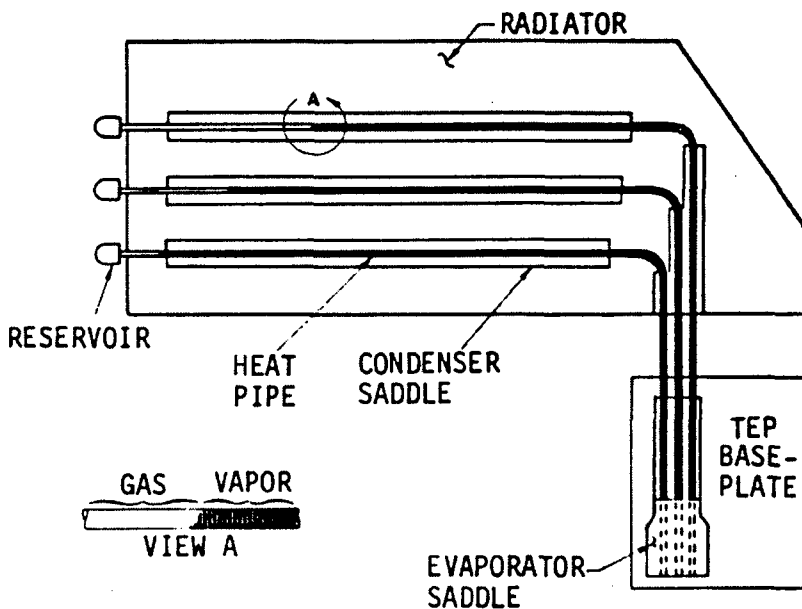


Fig. 3.4 - Multiple GLHP radiator of the communication satellite CTS

One of the first examples of a main thermal control system based on GLHP's was on the CTS (Communication Technology Satellite) [26]. Fig 3.4 shows an arrangement of 3 pipes connected to the panel by saddles to provide a better heat entrance into the panel. The panel consists of a 1 mm thick aluminum plate with silverized teflon coatings on both surfaces. Installation limitations on the satellite allowed only a small elevation of the radiator out of the satellite, so that the heat pipes had to be bent. For this reason each heat pipe had different heat transport capacities. To enable that every heat pipe transfers a heat load proportional to its capacity, the corresponding gas inventories were adjusted to stagger the vapor/gas fronts. The system was designed to remove

196 W at worst case, that is, with one of any of the 3 GLHP's being non-operational (failed) and submitted to maximum insolation. The controllable temperature range on the base-plate was from 21 to 48 °C.

Fig 3.5 presents an array of 6 GLHP's for the European satellite MAROTS [27]. The radiator is formed by 4 segmented panels and a central base-plate that carries 8 SSPA type transmitters. The base-plate contains conventional fixed conductance heat pipes (FCHP's) to distribute the heat equally. The GLHP's run directly into the panels on both sides without forming adiabatic zones. To decouple the reservoirs from temperature variations on the panels, they protrude and are connected to their respective condensers by small tubes with small diameter and wall thickness. The dissipation capacity of this system was 185 W at temperatures between 30 and 40 °C.

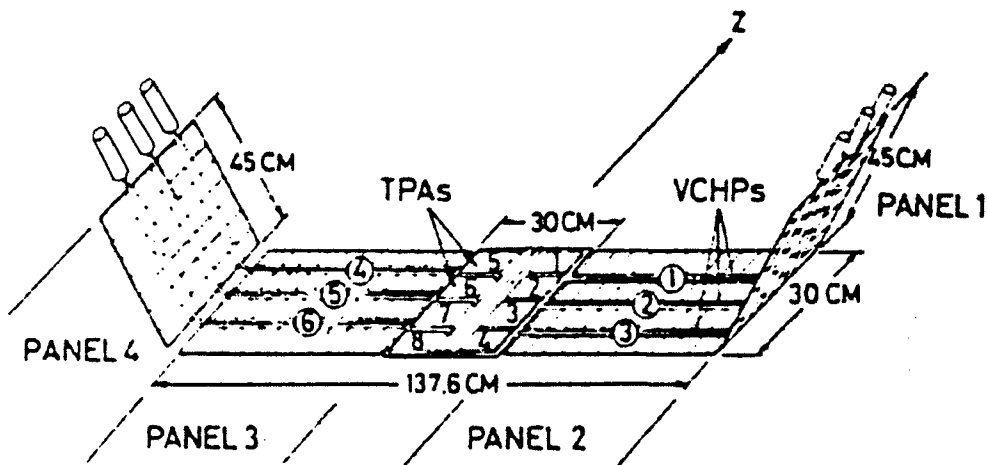


Fig. 3.5 - Base-plate with GLHP radiators of the communication satellite MAROTS

A GLHP radiator that constitutes a wall of the satellite body was used on the Japanese satellite ETS-5 [2]. Here all the heat pipes are incorporated into a 15 mm thick honeycomb panel. The panel is made up from two outer 0.3 mm thick aluminum skins embracing and bonded to an array of hexagonal cells with a width of 3.2 mm. The cells are shaped by extremely thin ($\cong 0.02$ mm) aluminum profiles [28] in a side-by-side arrangement. In this way a very light, but stiff and conductive structure is feasible. The radiator called TCM (Thermal Control Module) has 6 gas-loaded VCHP's and 6 FCHP's. Two fixed conductance pipes in the central part of the panel (Fig. 3.6a) are intended to cool 8 medium power TWTA (20 W) whose dissipation does not vary much due to constant operation. As an operating temperature of between 0 and 45 °C was tolerated, a strictly controlled temperature was not important. At the lower part of the radiator

wings two other U-shaped FCHP's can be seen on both sides. They are joined to the GLHP evaporators, as shown in Fig. 3.6c. These two edges which are isolated against space by MLI indicate the locations where two high power TWTA (100 W) with variable operating characteristics were mounted. Here the FCHP's act like secondary heat paths coupling two GLHP evaporators in order to distribute the thermal load equally.

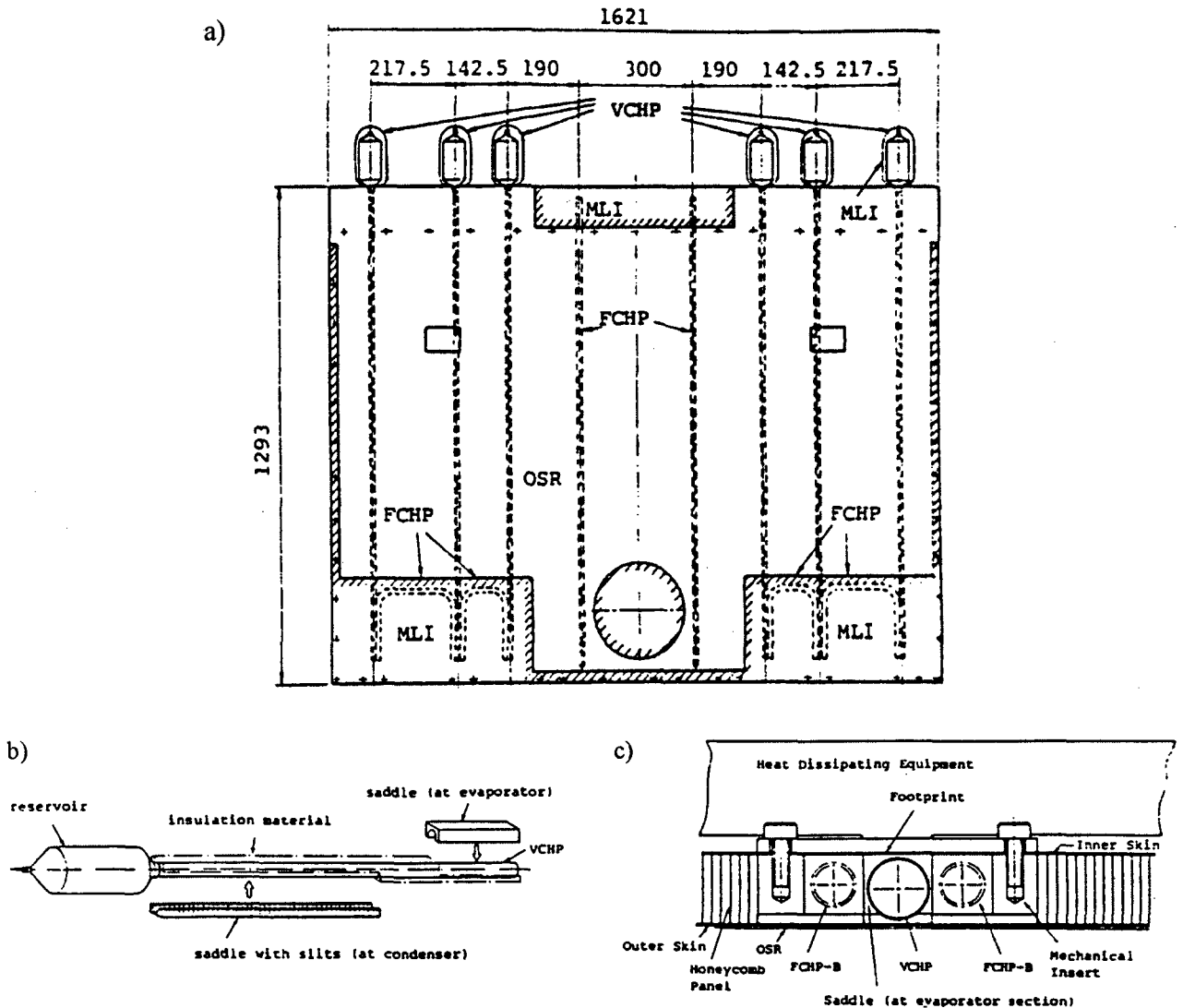


Fig. 3.6 - Thermal control module of the communication satellite ETS 5

a) View from space, b) Configuration of the incorporated GLHP, c) Cross section below the TWTA

In this way each high power TWTA, cooled by 3 GLHP's, could be kept at a temperature between 25 and 45 °C. It is easy to understand that a radiator, which at the same time contributes to the main satellite structure, cannot be cut in strips to reduce thermal conductance in direction

of the heat pipe axes. It also cannot offer two faces of radiation. Fig. 3.6b shows that, instead of the panel, the saddle that connects the condenser to the radiating surface was slitted abundantly in order to block that undesired heat path. It can also be seen there, how the thermal contact to the internal aluminum skin was avoided by intermediate insulation material.

Panels based on honeycomb structure are also used for radiators with large extension and cantilever systems [29]. They guarantee a better stability and damp possible vibrations.

Modeling a GLHP, by a set of mathematical expressions, helps the designer to predict how a certain heat pipe, with its geometry, properties of associated materials, a defined noncondensable gas inventory and its condenser exposed to a certain thermal environment, will react to a certain heat flux applied at the evaporator. The solution of the problem is presented as an axial distribution of the heat pipe wall temperature, where particular interest is taken in the vicinity of the vapor/gas front.

In principle, energy propagates through the heat pipe by two paths, latent heat and enthalpy flow through the vapor space and sensible heat by conduction through the pipe wall. Thus two domains have to be modelled and linked mutually at the interface where heat and mass are exchanged. In complete models which consider this interface between vapor and liquid the link is established by creating a source (in the evaporator) and a sink (in the condenser) as boundary conditions for the vapor space. The terms can be derived from energy balances across the interface. Simpler models only link the domains by a heat transfer coefficient h . Once the coupling is defined, the mass diffusion equation in the vapor space and the heat conduction equation in the pipe wall can be solved simultaneously to obtain the desired temperature profile. The solution is found through an iterative procedure, since the equations for temperature are transcendent with respect to the phase-equilibrium and also non-linear regarding the heat transfer to the environment in the usual case of radiation.

To avoid excessive numerical expenses the models are generally based on suitable assumptions or simplifications. This rather idealized handling of the problem allows simple algorithms and sometimes even solutions in closed form. The authors of the models verify the validity of the respective assumptions by the aid of a GLHP with appropriate characteristics. It can be stated that the applicability of certain assumptions depends on:

- range and level of the operating temperature
- type of condenser cooling
- mutual diffusivity of vapor and gas
- condenser length and its ratio to the pipe diameter and

- thermal properties of the container material.

In the following section the main features of altogether 15 steady-state and transient GLHP models found in literature are outlined. Later some models are presented in a more detailed way, as they show convenience and applicability for the use in the present case of study.

4.1 Chronological survey

The first GLHP model to be widely published was a steady-state flat front model by Marcus and Fleischmann (1970) [4]. Though founded on a phenomenon that is not realistic at all, this model until nowadays has been taken as a starting point, reference and comparison by many GLHP researchers. For several heat pipes with low thermal wall conductivity and low rates of diffusion between vapor and gas, solutions obtained by this model have been verified. The model strictly separates the GLHP into two sections by a sharp interface, the flat vapor/gas front. The interface is impervious to mass transport in both directions. In the active section, where the vapor-liquid cycle takes place, the temperature is equal to the evaporator temperature, and there is no gas present. As axial heat conduction in vapor space, wick and heat pipe wall is neglected, the temperature value shows a sudden discontinuity, when crossing the front position, falling to the value of the ambient temperature. Applying the ideal gas law on the partial gas pressure in the inactive section, it is possible to determine the temperature of the active section as well as the front location, if heat flux and gas quantity are given.

Edwards and Marcus (1972) [5] allow for a diffuse front, where the composition of the vapor-gas mixture and therefore the temperature changes gradually along the heat pipe axis. The shape of the front depends on axial heat conduction together with mass diffusion in the front vicinity. With the gas and the front being at rest (steady state) a one-dimensional distribution of the gas concentration is obtained by applying Fick's law of binary diffusion. In the transition region of vapor space to the heat pipe wall the heat and mass transfer is conjugated by a mass balance of the working fluid. Assuming that the total pressure does not vary along the pipe, further neglecting a pressure drop in the condenser (absence of inertial effects) and setting the gas concentration in the condenser entrance zero, it becomes sufficient to just model the condenser. Heat dissipation to the environment is included by a heat transfer coefficient that considers the heat path from the vapor up to the agent which cools the condenser. Taking a high wick and wall conductance in order to linearize the wall temperature T_p around the vapor temperature $T_{v,c}$ (as

$T_{v,c} - T_p \ll T_{v,c}$) the model even accounts for the heat that is leaving the condenser by radiation. The behavior of GLHP's with relatively small pipe diameters is well represented by this kind of one-dimensional model.

To analyze the radial distribution of the temperature and mass composition Rohani and Tien (1973) [6] developed the first two-dimensional steady-state model for the whole vapor space. The main aim of this model was to demonstrate the importance of heat and mass transfer between vapor and gas in high temperature GLHP's. As axial wall heat conduction is not considered, the wall is simply taken to be a radial boundary condition with constant heat transfer coefficients, though different for evaporator and condenser. The available area for the heat output is determined by the calculation of the inactive condenser length based on the flat front model. This standard model also serves as a convergency criterion for the numerical solution of 4 equations of conservation, regarding mass, momentum (including viscous terms), energy and species of a vapor-gas mixture. With radial and axial velocities expressed by the stream function the equations appear in elliptical form. The formation of the radial temperature profile near the wall is directed by a gradient that is assumed to be parabolic. In doing so a non-linear boundary condition at the wall is avoided and a numerical solution in this region is facilitated.

An opposite principle was sought in the model of Sun and Tien (1975) [7], where an analytical solution of the wall temperature profile is obtained for the whole heat pipe. The model deals with pure conduction; hydrodynamic phenomena are ignored. This model is directed to GLHP's that present large Biot numbers, where the two ends of the heat pipe are in contact with solid bodies, or where the condenser is exposed to an environment that causes a high external heat transfer coefficient. In this case the temperature drop between vapor and wall is comparable to the temperature drop between wall and heat sink. The heat pipe is divided into 4 functional sections: evaporator, adiabatic zone, active condenser and inactive condenser. For each section a heat balance over an element dz is made. Appropriate boundary conditions connect the respective sections in the axial direction. The vapor space temperature is included in the model by an internal heat transfer coefficient at the evaporator and an energy balance across the heat pipe wall. The noncondensable gas effect contributes to the model by the definition of an inactive length similar to that of the flat front model. At this point the model requires, for each simulated case, the introduction of two experimental values that are necessary to localize the flat front. These are the evaporator pressure, $p_{v,e}$, and the temperature at the condenser end, $T_g(L)$, where $T_g(L) > T_\infty$. A closed form solution of the problem becomes possible by two arrangements: by transforming

the sectional heat balances into dimensionless form and by relating the sectional temperatures to the vapor space temperature. By this means the 4 differential equations appear in a generic form, where only the coefficients, the non-homogeneous terms and boundary conditions vary according to the respective sections.

The first transient model, presented by Rice and Azad (1976) [8], used the lumped capacity approach to establish an energy balance over the active heat pipe section (evaporator, adiabatic zone and active condenser). The balance considers the heat absorbing capacity of the lumped heat pipe wall and the lumped liquid working fluid column until the position of the (flat) vapor/gas front, the latent heat variation of the active vapor space and the heat losses from adiabatic zone and active condenser. All parts of the system that are situated downstream of the front are neglected. Despite its simplicity the model is able to predict quite well the temperature of the active section and the transient response of the system.

Shukla's transient model (1981) [9] is the simplest model to consider the reciprocal action between vapor and the diffuse front inside the heat pipe. Simplifying the vapor momentum equation for the one-dimensional case, without considering compressibility and viscosity of the fluid, the model couples the vapor velocity to the momentary front position. Two heat balances over the two parallel heat paths connect the model to the external thermal conditions. The first one covers the vapor space in the active GLHP region, neglecting axial heat conduction in the vapor. The second one considers the entire wall of the condenser, but ignores evaporator and adiabatic zone by assuming a constant temperature there. The link to the inactive vapor space region is made by a diffusion process due to Fick's law (with apparent steady-state temperatures and constant pressure) and by an average molar fraction for each time step of simulation. It is supposed that gas only exists in condenser and reservoir.

To analyze GLHP's which are run by fluids at low saturation pressure conditions (especially during start-up from low temperatures), Delil and van der Vooren (1981) [10] published a steady-state, one-dimensional model that specifically cares about inertial effects. The model is restricted to the condenser vapor space and therefore does not account for axial conduction, but considers a diffuse front. With the mass balance expressed in terms of mass flow density, the equation of motion, the ideal gas law and Fick's law for the vapor-gas mixture, a system of equations is set up that determines velocity and molar fraction of the vapor as well as concentration and temperature of the binary mixture. The model becomes a flat front model, if the diffusion coefficient \mathcal{D} approaches zero, because then the equations show a discontinuity at the supposed flat front

position. Therefore solutions are given in two directions, one upstream with χ_g approaching 1 and one downstream with v_v approaching 0. As remarkable by-products the model renders information about the linear vapor deceleration in the active condenser and a criterion that indicates, when it is possible to assume constant pressure along the entire heat pipe.

Kimura *et al.* (1981) [11] present a transient model that is based on the lumped capacity philosophy, yet manages to link the characteristics of one-dimensional diffusive mass transport to the sectional balances. The model stands out because of its completeness, covering more details of the system and its performance relative to other one-dimensional models. Since in transient operation the heat source itself adds further thermal inertia to the system, especially when heating is due to metallic blocks, the authors provide a heat balance that specifically refers to this effect. Further the model considers a non-wicked reservoir and its connection to the condenser end, the feed tube. Though regarded thermally separated from the heat pipe (zero thermal capacity and conductivity), the reservoir together with its feed tube has a significant influence on the simulated behavior with respect to the gas front dynamics. Moreover it should be noted that with practically the same equations the authors resolve both the so-called ordinary transient operation as well as the start-up performance. Three heat balances appear: one for the heat source, one for the combined section of evaporator, adiabatic zone and active condenser and the last one for the gas-blocked section that in case of the start-up involves the whole condenser. The set of equations is completed by the ideal gas law applied to the molar flow of the mixture into the reservoir, the gas mass balance along the feed tube and the conservation of the total gas mass. During start-up the gas is distributed in all parts of the GLHP, with a partial pressure that corresponds to the temperature in each section. As soon as the vapor pressure in the evaporator equals the total pressure, start-up is said to be concluded and the algorithm continues with the normal transient operation with a front already formed in the heat pipe. Axial heat conduction between active and inactive zones is incorporated in the model by a fin efficiency factor that artificially shortens the length of the blocked section.

A steady-state conduction model, yet more detailed with respect to condensation and gas-blocked regions, was presented by Bobco (1983) [12]. A peculiarity of this model is that condensation is allowed to take place in the adiabatic zone, when the heat throughput is lower than 20 % of the maximum one. Moreover heat conduction is also admitted in the connection between condenser and reservoir. Heat balances are placed in 4 sections: the part of adiabatic zone that takes part in condensation, the active condenser, the inactive condenser and a secondary adiabatic zone which

is the reservoir feed tube. The condensation process in the first two sections is replaced by a local heat flux specified by a distribution parameter. Thus the application of an internal heat transfer coefficient that is hardly palpable is avoided, but this parameter still has to be determined empirically. To find the front position Bobco performs a gas mass balance using, as an approximation, the flat front model, but based on all averaged temperatures of the contributing sections. In dimensionless form and joined by continuity conditions, implicit closed form relations are possible between the sectional temperatures, the heat load and the front position. Although the evaporator is not included in the model, its temperature is obtained by setting a zero gradient at the beginning of the first section. Additional mathematical manipulations on the equations led to a different, more flexible determination of the gas inventory than in the classical formulation shown in section 6.4. Now the gas can occupy a larger volume in the case of small heat fluxes, since L_{ca} is allowed to fall below zero. Comparing the hot case (no condensation in the adiabatic zone and the front shifted to the entrance of the feed tube) to the cold case (start of liquid freeze-out at a certain minimum temperature location in the inactive condenser) a more sophisticated optimized relation between the volumes of the reservoir and the condenser is obtained. Bobco modified his model in a complementary work [30] to cover the range of heat fluxes between 0 and 50 % of Q_{max} . The special contribution of this publication is the introduction of additional, parasitical heat transfer coefficients in order to evaluate heat losses in every GLHP section, when the heat fluxes are very low. In comparison with Sun and Tien's heat conduction model Bobco's model has a clearer formulation of the axial temperature profile with a higher resolution. On the other hand the necessity remains to introduce empirical values into the model, such as a parameter that describes the distribution of the condensation heat flux and the location where the adiabatic zone begins to show condensation. The author finds these parameters by means of a validity analysis, where the temperature profiles are fitted by published experimental data.

A model that is easy to compute and based on the rigid assumptions of the flat front model was outlined by Antoniuk (1987) [13]. This model actually presents a vapor space module, a subroutine, destined to be incorporated in a general thermal analysis program. The model itself is steady-state, but renders time-dependent results by the fact, that during each time step the values for vapor temperatures and the vapor-to-wall conductances are updated. The conductances are treated as boundary nodes for the discretized external GLHP structure. From the instantaneous axial temperature distribution the model determines the gas-blocked length and the active vapor temperature by solving simultaneously the equation of gas mass conservation in the inactive

section together with the heat balance over the active section. Two definitions distinguish the two sections: The active section is free of noncondensable gas, and the inactive section has no heat transfer to the surrounding wall. The vapor space equations do not have transient terms, because the thermal inertia of the vapor is neglected. The model was expanded to discover the start of ice block formation. If the working fluid freezes in some location of the inactive section and forms a block, the reservoir can be separated from the active section, and this would mean complete loss of controllability. Further the case of spilling of liquid out of an artery after thawing of the ice block is examined.

Two-dimensional diffusion, though symmetric to the heat pipe axis, was investigated by Peterson and Tien's steady-state model (1989) [14]. The problem involves the condenser and the adiabatic zone and is mounted by 3 equations. The first postulates gas mass conservation in two dimensions, the second takes advantage of the gas concentration gradient to perform an energy balance at the vapor/wall interface, and the third gives a relation between the temperature at the interface and the mixture composition there. In dimensionless form and expressed in terms of a new variable (the ratio between gas diffusion rate and condensation rate) a convergent solution can be obtained. If wall conduction is negligible, the new variable has a low value and obeys a parabolic distribution in radial direction for large distances from the condenser end. All the 3 types of cooling can be included: forced convection, natural convection and radiation. If the parabolic distribution is assumed to be valid for the entire domain of integration, the number of equations can be reduced to two by an integral formulation. Then a numerical solution is available for both cases, for negligible axial conduction and for dominant axial conduction. In the latter case wall conduction has more influence than diffusion, and the equations derived for two dimensions coincide with the one-dimensional equations. The authors further proceed to an analytical solution of the axial temperature distribution in the case of low diffusion and forced convection cooling (with constant h_{ext}). The important contribution of Peterson and Tien's analysis is the fact that it offers criteria that check under which circumstances two-dimensional effects must be considered by a GLHP researcher. That is the case, when low diffusion, low latent heat, high heat fluxes and low wall conductivity are crucial and the gas quantity is relatively low.

Semena *et al.* (1990) [15] presented a transient model where non-linear wall heat conduction equations describe each of the three GLHP sections. The wall is taken as the combination of container and wick. The link to the vapor space with negligible diffusive and convective effects is made by means of thermal resistances which depend on position and temperature. The thermal

properties of capacity and conductivity are also variable. Empirical functions for the vapor/wall interface resistances are derived from an analysis of sensitivity coefficients of the source temperature with respect to the applied heat flux. The model is completed by corresponding integral balances for the gas mass and the heat flux that is transported by vapor. Analytical solutions are given for a steady-state evaporator temperature profile and also for the time that the evaporator takes to become gas-free during start-up. The transients are modelled by means of discrete elements with variable capacities. Thermal links (variable resistances) that depend on the gas buffer length interconnect these elements.

The most comprehensive transient model was developed by Harley and Faghri (1994) [16]. It comprises two-dimensional equations regarding mass, momentum and energy conservation for a compressible vapor-gas mixture, a gas mass conservation equation and an ideal gas law relation for the vapor. Inertial and viscous effects in the vapor space, heat transfer between vapor and gas as well as variable thermal properties are included. The heat conduction equations for the wall and the wick respectively are also two-dimensional. Heat convection by the liquid flow was neglected, as the liquid is assumed to be highly conductive and the wick to be very thin. A model with this degree of precision is especially favorable for the investigation of high temperature GLHP's with radiative cooling, since assumptions used in former models show significant errors.

The same authors published a transient lumped capacity model in 1994 [17] to offer a rapid and convenient tool in GLHP projects. The transient condenser length and thus the thermal capacities of active and inactive sections are found, assuming that the vapor/gas front is flat. However, the model was extended to permit axial heat conduction in the condenser wall under the condition of radiative cooling. For this purpose constant temperatures for the active as well as the inactive section are initially determined from heat balances over the respective sections. In a fictitious steady-state heat conduction process these values are used as boundary conditions at the border to the adiabatic zone and at the condenser end respectively. This means that during every time step the condenser achieves a steady-state temperature distribution spanned between those two boundary values.

How the axial temperature profile changes due to the motion of the vapor/gas front, was examined by Chung and Edwards in their moving-front theory [18]. A transient heat balance over the active section of the GLHP reveals a term that describes the portion of heat that is conducted from the active into the inactive zone. This portion is analytically evaluated from the temperature gradient at the position of a discrete (or flat) gas front. The axial temperature profile changes are

derived from a heat balance on a pipe wall element that is moving with respect to a resting gas front. When, in reality, the front advances, the wall element moves in direction to the hot heat pipe end, while exchanging heat with the vapor space. When the front retreats, the wall element moves towards the cold end at sink temperature. The novelty of this work is that it explains theoretically, why temperature profiles in the front vicinity steepen or flatten according to direction and magnitude of the front velocity during heat pipe transients.

Authors	Regime	Dimension	Considered parts	Binary diffusion	Wall conduction	Compressibility	Inertial effects	Viscous effects	Variable properties	External reservoir	Radiative cooling	Peculiarities
Marcus, Fleischmann (1970)	steady state	1-D	condenser									flat front
Edwards, Marcus (1972)	steady state	1-D	condenser	•	•						•	
Rohani, Tien (1973)	steady state	2-D	entire heat pipe	•			•	•				
Sun, Tien (1975)	steady state	1-D	entire heat pipe		•							empirical coefficient necessary
Rice, Azad (1976)	transient	1-D	entire heat pipe		•							lumped capacity
Shukla (1981)	transient	1-D	condenser	•	•					•		gas absorption reservoir
Delil, van der Vooren (1981)	steady state	1-D	condenser	•			•					reducible to flat front model
Kimura <i>et al.</i> (1981)	transient	1-D	entire heat pipe	•	•					•		lumped cap., incl. heat source and start-up
Bobco (1987)	steady state	1-D	condenser + ad. zone		•					•		empirical constants necessary
Antoniuk (1987)	transient	1-D	vapor space		•					•		flat front
Peterson, Tien (1989)	steady state	2-D	condenser + ad. zone	•	•						•	analytical solution possible
Semena <i>et al.</i> (1990)	transient	1-D	entire heat pipe		•				•			
Harley, Faghri (1994)	transient	2-D	entire heat pipe	•	•	•	•	•	•		•	
Faghri, Harley (1994)	transient	1-D	entire heat pipe		•						•	lumped capacity, flat front
Chung, Edwards (1996)	transient	1-D	heat pipe wall		•							moving front

Table 1 - Overview of GLHP models with respect to their features and assumptions

4.2 Classical steady-state flat front model

Marcus and Fleischmann originally developed this basic model for a hot reservoir that is integrated into the core of the heat pipe [4]. For the case of interest it is slightly modified in order to consider an external cold reservoir.

For being flat the front strictly separates the section, where the working fluid circulates, from the gas-blocked section. The borderline between the two sections is extended to the heat pipe wall, where heat conduction into the inactive section is not allowed, thus letting the temperature be discontinuous at this position. The heat flux transferred by the heat pipe leaves the active condenser according to the following equation:

$$Q = h\pi D_{\text{ext}} L_{\text{ca}} (T_{\text{v,a}} - T_{\infty}) \quad (4.1)$$

The active length L_{ca} depends on the quantity of noncondensable gas in the GLHP that obeys the ideal gas law expressed by

$$N_{\text{g}} = \frac{P_{\text{g}}}{\mathfrak{R}T_{\text{g}}} \cdot \sum_j V_{\text{g},j} \quad j = \begin{cases} \text{ci} \\ \text{r} \end{cases} \quad (4.2)$$

As in the model the inactive section receives no heat by conduction, its temperature is assumed to be equal to the ambient temperature ($T_{\text{g}} = T_{\infty}$). The partial gas pressure at this point is the total pressure less the vapor saturation pressure at the temperature of the inactive section. The total pressure is identical to the vapor pressure in the active section, as there is no gas in that part of the heat pipe. Thus:

$$P_{\text{g}} = P_{\text{v,sat,a}} - P_{\text{v,sat},\infty}^* \quad (4.3)$$

The volume occupied by the gas is made up by the reservoir and the inactive condenser:

$$V_{\text{g}} = V_{\text{r}} + A_{\text{v}}(L_{\text{c}} - L_{\text{ca}}) \quad (4.4)$$

Now eqn. (4.2) assumes the following form:

$$N_{\text{g}} = \frac{P_{\text{v,sat,a}} - P_{\text{v,sat},\infty}}{\mathfrak{R}T_{\infty}} [V_{\text{r}} + A_{\text{v}}(L_{\text{c}} - L_{\text{ca}})] \quad (4.5)$$

* $P_{\text{v,sat},j} = P_{\text{v,sat}}(T_j)$ with $j = \begin{cases} \text{a} \\ \infty \end{cases}$

$$\Rightarrow L_{ca} = L_c - \frac{m_g R_g T_\infty}{A_v (p_{v,sat,a} - p_{v,sat,\infty})} + \frac{V_r}{A_v} \quad (4.6)$$

After substituting (4.6) into (4.1) a general expression for the heat transfer in the GLHP can be obtained:

$$Q = h\pi D_{ext} (T_{v,a} - T_\infty) \left[L_c - \frac{m_g R_g T_\infty}{A_v (p_{v,sat,a} - p_{v,sat,\infty})} + \frac{V_r}{A_v} \right] \quad (4.7)$$

$$\text{with } p_{v,sat,a} = f(T_{v,a}) \quad \text{and} \quad p_{v,sat,\infty} = f(T_{v,\infty})$$

The only unknown in eqn. (4.7) is the operating temperature, $T_{v,a}$, which is dependent on the heat flux and the external heat transfer coefficient; it is determined through iterations.

4.3 Transient lumped capacity model including start-up

Kimura *et al.* present the only GLHP model that explicitly covers the beginning of operation [11]. Here the time can be predicted that a certain heat pipe takes to reach the so-called ordinary transient operation which is the moment, when the whole heat pipe has reached operating temperature. To trace the thermal response of the system the authors divided the heat pipe in functional sections, where the thermal conductivity is assumed to be so large that there is no temperature gradient in that particular section (principle of lumped capacity). As a result not a temperature profile along the pipe is obtained, but distinct temperatures for each section with temperature steps at the borders between the sections, as was previously mentioned about the flat front model.

The heater block adjacent to the evaporator normally has such a significant thermal mass that it influences the transient response of the heat pipe. If the heat source is included in the analysis and mass distribution and temperature are uniform in evaporator and adiabatic zone, the sectional heat balances during **start-up** are:

$$\text{Heat Source} \quad C_{so} \frac{dT_{so}}{dt} = Q - K_{so} L_e (T_{so} - T_{e,ad}) \quad (4.8)$$

$$\text{Evaporator and Adiabatic Zone} \quad C_{e,ad} \frac{dT_{e,ad}}{dt} = K_{so} L_e (T_{so} - T_{e,ad}) \quad (4.9)$$

$$\text{Condenser} \quad C_c \frac{dT_c}{dt} = K_{\infty} L_c (T_{\infty} - T_c) \quad (4.10)$$

$$\text{where} \quad C_j = \rho_j V_j c_j \quad (4.11) \quad \text{and} \quad K_j = h_{\text{ext},j} \pi D_{\text{ext}} \quad (4.12)$$

From these balances the sectional transient temperatures can already be determined: T_{so} and $T_{e,ad}$ by simultaneous solution of eqns. (4.8) and (4.9), and T_c from eqn. (4.10).

Start-up continues, until the gas is completely driven out of evaporator and adiabatic zone, and the vapor pressure in the evaporator becomes equal to the total pressure. The total pressure can be determined conveniently by the total quantity of vapor and gas in the reservoir. The total molar flux into the reservoir is

$$\dot{N}_r = \frac{V_r}{\mathfrak{R}T_r} \frac{dp_t}{dt} \quad (4.13)$$

Gas mass conservation in the feed tube (denoted by subscript f) between the condenser and reservoir requires that

$$\dot{N}_{g,r} = \chi_g \dot{N}_r - c D A_f \frac{d\chi_g}{dz} \quad (4.14)$$

Placing the origin of z at the condenser end, the boundary conditions for eqn. (4.14) are

$$z = 0 : \chi_g = \chi_{g,c} \quad z = L_f : \chi_g = \chi_{g,r}$$

The total gas quantity in the GLHP during start-up is given by

$$N_g = \frac{p_t - p_{\text{sat}}(T_{e,ad})}{\mathfrak{R}T_{e,ad}} V_{e,ad} + \frac{p_t - p_{\text{sat}}(T_c)}{\mathfrak{R}T_c} V_c + N_{g,r} \quad (4.15)$$

Since N_g does not vary with time, the time derivative of $N_{g,r}$ is

$$\dot{N}_{g,r} = -\frac{V_{e,ad}}{\mathfrak{R}} \left[\frac{d}{dt} \left(\frac{p_t}{T_{e,ad}} \right) - \frac{d}{dt} \left(\frac{p_{\text{sat}}(T_{e,ad})}{T_{e,ad}} \right) \right] - \frac{V_c}{\mathfrak{R}} \left[\frac{d}{dt} \left(\frac{p_t}{T_c} \right) - \frac{d}{dt} \left(\frac{p_{\text{sat}}(T_c)}{T_c} \right) \right] \quad (4.16)$$

The combination of the equations (4.13), (4.14) and (4.16) results in an implicit relation for the total pressure starting from an initial situation (p_0, T_0) at $t = 0$:

$$p_t = p_0 + \frac{H_2}{H_1} \left[E_1 \cdot e^{-\frac{t}{\tau}} \left(e^{\frac{t}{\tau}} - 1 \right) + E_2 t + (T_0 - T_\infty) e^{-\frac{K_{so} L_c t}{C_c}} \left(e^{-\frac{K_{so} L_c t}{C_c}} - 1 \right) \right] \quad (4.17)$$

$$\text{where } E_1 = \frac{C_{so} C_{e,ad} Q}{K_{so} L_e (C_{so} + C_{e,ad})^2}, \quad H_1 = \frac{V_{e,ad}}{\Re T_{e,ad}} + \frac{V_c}{\Re T_c} + \frac{V_r}{\Re T_r} \left[\chi_{g,c} + (\chi_{g,c} - \chi_{g,r}) \frac{e^{-\frac{\dot{N}_r}{cDA_f}}}{1 - e^{-\frac{\dot{N}_r}{cDA_f}}} \right],$$

$$E_2 = \frac{Q}{C_{so} + C_{e,ad}}, \quad H_2 = \frac{p_t V_{e,ad}}{\Re T_{e,ad}^2} - \frac{p_{sat}(T_{e,ad})}{\Re T_{e,ad}^2} V_{e,ad} \left(\frac{B_2}{T_{e,ad}} + \frac{2B_3}{T_{e,ad}^2} - 1 \right),$$

$$\frac{1}{\tau} = K_{so} L_e \frac{C_{so} + C_{e,ad}}{C_{so} C_{e,ad}}, \quad p_{sat}(T) = e^{-B_1 + \frac{B_2}{T} + \frac{B_3}{T^2}} \quad (B_1, B_2, B_3 \text{ are fitting constants})$$

The time constant τ defines the time the system takes to complete start-up.

The algorithm shifts to **ordinary transient operation**, when $p_{sat}(T_{e,ad})$ equals p_t in eqn. (4.17). Now it is assumed that the vapor/gas front is already developed into the condenser and that the entire active section, including the active condenser, is at a uniform temperature T_a . The sectional balances are:

$$\text{Heat Source} \quad C_{so} \frac{dT_{so}}{dt} = Q - K_{so} L_e (T_{so} - T_a) \quad (4.18)$$

Evaporator, Adiabatic Zone and Active Condenser

$$C_a \frac{dT_a}{dt} + C_{cl} \frac{d}{dt} \left(\frac{L_c - L_{cl} + L_{ca,ef}}{L_c} T_a \right) = K_{so} L_e (T_{so} - T_a) + K_{cso} (L_c - L_{cl} + L_{ca,ef}) (T_\infty - T_a) \quad (4.19)$$

$$\text{Inactive Condenser} \quad C_{cl} \frac{dT_{cl}}{dt} = K_{cso} L_{cl} (T_\infty - T_{cl}) \quad (4.20)$$

Since wall heat conduction into the inactive condenser is important in the case of spaceborne GLHP's, an additional active length $L_{ca,ef}$ is introduced into eqn. (4.19) to reduce the inactive length. To determine this effective length the inactive condenser is regarded to be a fin with length L_{ci} , a constant cross section and with the root temperature T_a . When defining a fin efficiency η_{ci} , this length can be expressed by

$$L_{ca,ef} = \eta_{ci} \cdot L_{ci} \quad (4.21)$$

Introducing $C_p = C_a + C_{ci}$, eqn. (4.19) becomes

$$C_p \frac{dT_a}{dt} + \frac{C_{ci}}{L_c} \frac{d}{dt} ((1 - \eta_{ci}) L_{ci} T_a) = K_{so} L_c (T_{so} - T_a) + K_{ceo} (L_c - (1 - \eta_{ci}) L_{ci}) (T_{\infty} - T_a) \quad (4.22)$$

The temperatures of the three sections in eqns. (4.18), (4.20) and (4.22) can be obtained, if the inactive length L_{ci} is known.

With the help of the flat front theory one can assume that the noncondensable gas remains in the blocked area with the length $L_{ci} \cdot (1 - \eta_{ci})$. The gas quantity according to eqn. (4.2) is therefore

$$N_g = A_v L_{ci} (1 - \eta_{ci}) \frac{p_{sat}(T_a) - p_{sat}(T_{ci})}{\mathfrak{R} T_{ci}} + N_{g,r} \quad (4.23)$$

$$\Rightarrow L_{ci} = \frac{N_g - N_{g,r}}{A_v (1 - \eta_{ci})} \frac{\mathfrak{R} T_{ci}}{p_{sat}(T_a) - p_{sat}(T_{ci})} \quad (4.24)$$

The gas quantity in the reservoir, after some time interval t , is the initial quantity added to the quantity that has passed through the feed tube during the interval t :

$$N_{g,r} = N_{g,r}(t_0) + \int_{t_0}^t \dot{N}_{g,r} dt \quad (4.25)$$

The molar gas flux into the reservoir, $\dot{N}_{g,r}$, is obtained from eqn. (4.14) using eqn. (4.13) and an exponential approximation for the saturation pressure as mentioned below eqn. (4.17):

$$\dot{N}_r = \frac{V_r}{\mathfrak{R} T_r} \frac{d[p_{sat}(T_a)]}{dt} = \frac{V_r}{\mathfrak{R} T_r} \frac{d[p_{sat}(T_a)]}{dT_a} \frac{dT_a}{dt} = \frac{V_r}{\mathfrak{R} T_r} \left[\frac{p_{sat}(T_a)}{T_a^2} \left(B_2 + \frac{2B_3}{T_a} \right) \right] \frac{dT_a}{dt} \quad (4.26)$$

$$\Rightarrow \dot{N}_{g,r} = \frac{V_r}{\mathfrak{R} T_r} \cdot \left[\frac{p_{sat}(T_a)}{T_a^2} \left(B_2 + \frac{2B_3}{T_a} \right) \right] \frac{dT_a}{dt} \cdot \left[\chi_{g,ci} + \left(\chi_{g,ci} - \chi_{g,r} \right) \frac{e^{-\frac{N_r}{cDA_t}}}{1 - e^{-\frac{N_r}{cDA_t}}} \right] \quad (4.27)$$

The length L_{ci} is determined simultaneously with η_{ci} from the equations (4.25) to (4.27).

4.4 Antoniuk's vapor space model

As it is a flat front model, Antoniuk's model adopts the same algorithm as the classical model in section 4.2. However, the position of the flat front in this case varies according to the transient axial temperature distribution which the external thermal heat pipe network imposes on the vapor space that is modeled here. Therefore the following assumptions continue to be valid:

- No noncondensable gas is present outside of the active GLHP section.
- The vapor temperature is constant throughout the active section.
- The vapor pressure at any location j is equal to the saturation pressure: $p_v(T_j) = p_{\text{sat}}(T_j)$.
- Heat is only released from vapor to heat pipe wall and only along the active condenser length.
- Hence there is no temperature difference between gas and wall in the inactive section.

The last statement, however, indicates that in this model the temperature of the vapor-gas mixture in the inactive section changes with respect to the z -direction, being $T_p(z)$ for the condenser and T_r for the external reservoir. Placing the origin of z at the end of the condenser, as shown in Fig. 6.4, the total gas distribution in the reservoir and condenser up to the vapor/gas front position L_{ci} is obtained by

$$N_g(L_{ci}) = \frac{p_t(L_{ci}) - p_v(T_r)}{\mathfrak{R}T_r} V_r + \int_0^{L_{ci}} \frac{p_t(L_{ci}) - p_v(T_p(z))}{\mathfrak{R}T_p(z)} A_v(z) dz \quad (4.28)$$

It should be noted that this equation was developed for an external wicked reservoir. As the working fluid is present in its liquid form, the partial vapor pressure in the reservoir is a function of the reservoir temperature.

If for convenience the vapor quantity up to position L_{ci} is treated separately, eqn. (4.28) becomes

$$N_g(L_{ci}) = N(L_{ci}) - N_v(L_{ci}) = p_t(L_{ci})F(L_{ci}) - N_v(L_{ci}) \quad (4.29)$$

$$\text{where } F(L_{ci}) = \frac{V_r}{\mathfrak{R}T_r} + \int_0^{L_{ci}} \frac{A_v(z)}{\mathfrak{R}T_p(z)} dz \quad \text{and} \quad N_v(L_{ci}) = \frac{p_v(T_r)V_r}{\mathfrak{R}T_r} + \int_0^{L_{ci}} \frac{p_v(T_p(z))A_v(z)}{\mathfrak{R}T_p(z)} dz$$

Applying the assumptions to the active section yields

$$p_t(L_{ci}) = p_v(T_{v,a}(L_{ci})) \quad (4.30)$$

The heat balance is made over the whole active section, where heat input and output are controlled by a variable heat transfer coefficient:

$$\int_{L_d}^L \pi D_v(z) h(z) [T_p(z) - T_{v,a}(L_{ci})] dz = 0 \quad (4.31)$$

$$\Rightarrow T_{v,a}(L_{ci}) = \frac{\int_{L_d}^L \pi D_v(z) h(z) T_p(z) dz}{\int_{L_d}^L \pi D_v(z) h(z) dz} \quad (4.32)$$

If the total gas quantity in the heat pipe, $N_{g,t}$, is known, L_{ci} , p_t and $T_{v,a}$ can be determined from eqns. (4.29), (4.30) and (4.32). As L_{ci} appears as an integration border, its solution is found in an iterative way, by evaluating $T_v(L_{ci})$, $F(L_{ci})$ and $N_v(L_{ci})$ until $N_g(L_{ci}) = N_{g,t}$.

A singularity will occur in eqn. (4.32), when L_{ci} approaches L , that is, when the gas blocks the whole GLHP length. In this case this equation and eqn. (4.30) are no longer valid, and eqn. (4.29) is replaced by the following:

$$N_g = p_t(L)F(L) - N_v(L) \quad (4.33)$$

4.5 Transient lumped capacity model with axial heat conduction

Similar to the lumped model in section 4.3 Faghri and Harley [17] divided in this model a GLHP (without external reservoir) into two functional portions, an active and inactive one, and provided each of them with a lumped thermal capacity that only represents liquid and solid masses with their respective uniform temperatures $T_{a,h}$ and $T_{ci,h}$. The presence of a noncondensable gas is also considered, that is, a quasi steady-state position of the vapor/gas front according to the flat front assumption is determined, but based on the prescribed temperatures of the two sections. The peculiarity of this model is the attempt to smooth out an abrupt temperature drop at the front position by allowing for axial wall heat conduction along the condenser.

Considering radiative condenser cooling the heat balance over the active section (evaporator, adiabatic zone and active condenser) is written as:

$$Q = C_a \frac{dT_{a,h}}{dt} + 2\sigma\epsilon\pi r_{ext} L_{ca} (T_{a,h}^4 - T_{\infty}^4) \quad (4.34)$$

The active condenser length is determined similarly to eqn. (4.6) in the classical flat front model:

$$L_{ca} = L_c - L_{ci} = L_c - \frac{m_g R_g T_{ci,h}}{A_v (p_{v,a,sat} - p_{v,ci,sat})} \quad (4.35)$$

However, as the inactive condenser shall receive heat by wall conduction from the active section, its temperature is higher than the ambient temperature. Thus heat exchange between the inactive portion of the condenser and the environment is taking place according to the following condition:

$$C_{ci} \frac{dT_{ci,h}}{dt} + 2\sigma\epsilon\pi r_{ext} \frac{m_g R_g T_{ci,h}}{A_v (p_{v,a,sat} - p_{v,ci,sat})} (T_{ci,h}^4 - T_\infty^4) = 0 \quad (4.36)$$

The model now allows that at every instant the condenser reaches a steady state, where the temperature profile spreads between the two boundary temperatures $T_{a,h}$ at the entrance of the condenser and $T_{ci,h}$ at its end.

A condenser that conducts heat axially and at the same time loses heat by radiation to the surroundings with a temperature T_∞ obeys the following heat balance:

$$k\pi(r_{ext}^2 - r_v^2) \frac{d^2 T_c}{dz^2} - 2\epsilon\sigma\pi r_{ext} (T_c^4 - T_\infty^4) = 0 \quad (4.37)$$

As an analytical solution is wanted, an effective heat transfer coefficient, h_{ef} , is defined to avoid non-linear terms in the differential equation

$$h_{ef} = \frac{\epsilon\sigma(T_c^4 - T_\infty^4)}{T_c - T_\infty} = \epsilon\sigma(T_c + T_\infty)(T_c^2 + T_\infty^2) \quad (4.38)$$

and further a parameter \bar{m}^2 is introduced which is a kind of diameter related condenser Biot number

$$\bar{m}^2 = \frac{2r_{ext} h_{ef}}{k(r_{ext}^2 - r_v^2)} \quad (4.39)$$

Now eqn. (4.37) can be simplified:

$$\frac{d^2 T_c}{dz^2} - \bar{m}^2 (T_c - T_\infty) = 0 \quad (4.40)$$

The temperature profile that results from this equation is not realistic, as the second term includes the heat output that has already been considered in the two transient heat balances (4.34) and (4.36). A conclusive result, however, is obtained by excluding the heat fluxes that determined the uniform temperatures of the two sections from the heat conduction equation (4.40). The equation dissolves in equations for the two heat pipe sections in the following way:

Active Condenser

$$\frac{d^2 T_{ca}}{dz^2} - \left[\bar{m}^2 (T_{ca} - T_\infty) - \bar{m}^2 (T_{a,h} - T_\infty) \right] = 0 \Rightarrow \frac{d^2 T_{ca}}{dz^2} - \bar{m}^2 (T_{ca} - T_{a,h}) = 0 \quad (4.41a)$$

Inactive Condenser

$$\frac{d^2 T_{ci}}{dz^2} - \left[\bar{m}^2 (T_{ci} - T_\infty) - \bar{m}^2 (T_{ci,h} - T_\infty) \right] = 0 \Rightarrow \frac{d^2 T_{ci}}{dz^2} - \bar{m}^2 (T_{ci} - T_{ci,h}) = 0 \quad (4.41b)$$

The general solution is given by

$$T_{ca} - T_{a,h} = A e^{-\bar{m}z} + B e^{\bar{m}z} \quad 0 \leq z \leq L_{ca} \quad (4.42a)$$

$$T_{ci} - T_{ci,h} = C e^{-\bar{m}z} + D e^{\bar{m}z} \quad L_{ca} \leq z \leq L_c \quad (4.42b)$$

The boundary conditions are

$$z = 0 : \quad T_{ca} = T_{a,h} \quad z = L_c : \quad T_{ci} = T_{ci,h}$$

$$z = L_{ca} : \quad T_{ca} = T_{ci}; \quad \frac{dT_{ca}}{dz} = \frac{dT_{ci}}{dz}$$

With these boundary conditions the following solutions for the condenser temperature are obtained:

$$T_{ca} = T_{a,h} + \frac{1}{2} (T_{a,h} - T_{ci,h}) \frac{(e^{-\bar{m}(L_{ca}-2L_c)} + e^{\bar{m}L_{ca}})(e^{\bar{m}z} - e^{-\bar{m}z})}{1 - e^{2\bar{m}L_c}} \quad (4.43a)$$

$$T_{ci} = T_{ci,h} + \frac{1}{2} (T_{a,h} - T_{ci,h}) \frac{(e^{-\bar{m}L_{ca}} + e^{\bar{m}L_{ca}})(e^{\bar{m}z} - e^{\bar{m}(2L_c-z)})}{1 - e^{2\bar{m}L_c}} \quad (4.43b)$$

The authors of this model (Faghri and Harley) published a different solution, that does not satisfy the third boundary condition of equal temperatures at the transition between the two sections:

$$T_{ca} = T_{a,h} + \frac{1}{2}(T_{a,h} - T_{ci,h}) \left(e^{\bar{m}(L_{ca}-2L_c)} + e^{-\bar{m}L_{ca}} \right) \left(e^{-\bar{m}z} - e^{\bar{m}z} \right) \quad (4.44a)$$

$$T_{ci} = T_{ci,h} + \frac{1}{2}(T_{a,h} - T_{ci,h}) \left(e^{\bar{m}L_{ca}} + e^{-\bar{m}L_{ca}} \right) \left(e^{-\bar{m}z} - e^{\bar{m}(z-2L_c)} \right) \quad (4.44b)$$

At the position L_{ca} the two parts of the solution drift apart by

$$T_{ca}(L_{ca}) - T_{ci}(L_{ca}) = (T_{a,h} - T_{ci,h}) e^{-2\bar{m}L_c}$$

This difference can be neglected in the case of a large value of \bar{m} , which means a large Biot number, or long condensers. If radiation is the cooling mechanism, the value of \bar{m} is in the range of 4 (for aluminum pipes) to 8 (for stainless steel pipes).

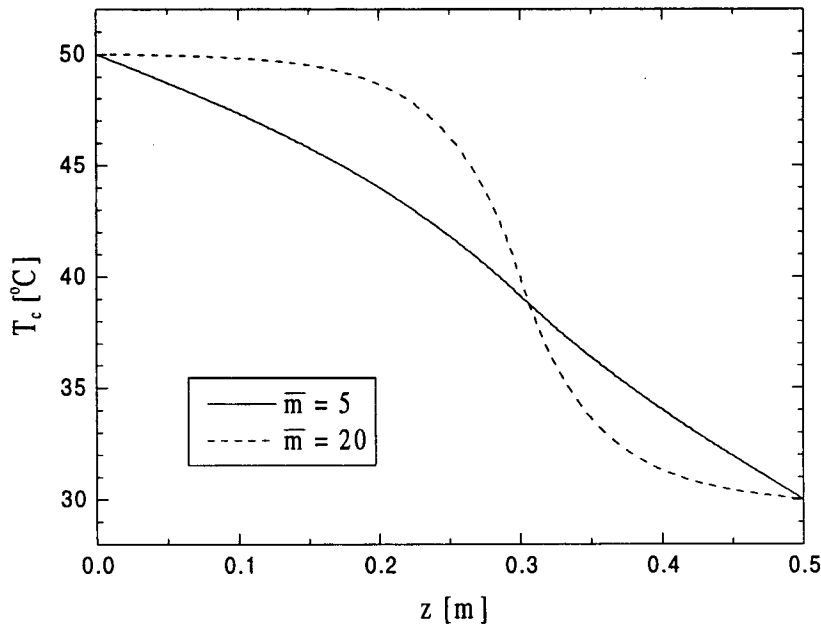


Fig. 4.1 - Solutions for the quasi steady-state condenser temperature profile from eqn. (4.43) with $L_{ca} = 0.3$ m, $L_c = 0.5$ m, $T_{ca} = 50$ °C, $T_{ci} = 30$ °C for radiative cooling ($\bar{m} = 5$) and convective cooling ($\bar{m} = 20$)

In Fig. 4.1 two condenser temperature distributions are plotted for values of \bar{m} that can be expected for the cases of radiative cooling and convective air cooling respectively. In the first case pronounced temperature gradients at both condenser boundaries can be noted. At $z = 0$, the end

of the adiabatic zone, the inclination of the curve is physically plausible, as it is the region from which the condenser receives heat. But at $z = L_c$ the inclination opposes the common practice to provide a zero derivative at the end of the condenser, as at this point there is no heat flux leaving the heat pipe in axial direction. For larger Biot numbers the curve smoothes down at both boundaries, so that for this case the implementation of the model becomes more reasonable.

4.6 Verification of the applicability of GLHP model assumptions

As mentioned in the beginning of this chapter, the applicability of a certain model for GLHP simulation depends on the physical and operational characteristics of the heat pipe. It is rarely necessary to apply a model such as that presented by Harley and Faghri [16] which attempts to cover so many real effects. The precision that might be gained by such comprehensive modeling does not diminish the usefulness of simpler models, if the assumptions used are carefully checked. Further the increased precision may not justify the disproportionate expense of programming and computation time. Well-known dimensionless characteristic numbers, as well as critical numbers established by the authors of the models, offer criteria for the validity of certain assumptions.

In heat pipes that work at moderate temperatures, defined as being in the range of -150 up to 300 °C [31], the Mach number is much lower than 0.3, even if the heat pipe is submitted to maximum heat load. In this case the vapor flow can be considered incompressible. Checking further the critical Reynolds number for flow in ducts ($Re_{crit} = 2300$) gives a notion, if the flow can be considered laminar or turbulent. In the case of laminar flow viscous effects have little contribution to the pressure distribution inside the vapor space. In cases that are comparable to the present one the pressure drops due to vapor flow friction are less than 6 % of the total pressure drop [32].

The characteristic numbers, parameters and their threshold values encountered in the GLHP literature are enumerated below. At the same time these values are compared to those of the GLHP's that take part in the experiments, thus providing evidence of the applicability of the model that will be used in the simulations of chapter 5.

According to the findings of Delil and van der Vooren [10] the pressure throughout a gas-loaded heat pipe can be assumed constant, if the following critical number is sufficiently small:

$$\upsilon = \frac{k_{pw} R_v T_{v,e}^2}{A_v h_{lv}^2 p_{v,e}} \quad (4.45)$$

The assumption of constant pressure means that, besides the viscous pressure drop in the vapor space, the pressure loss due to vapor acceleration along the evaporator and the subsequent recovery due to deceleration along the condenser are negligible. These are inertial effects that the authors claim to be significant, if the critical number υ exceeds the value 10^{-3} and the ratio Q/Q_{sonic} is larger than 0.15. Q_{sonic} is the magnitude of heat flux which must be applied to the heat pipe in order to induce the vapor velocity to become sonic. In heat pipes that work at moderate operating temperatures this value is so high that it is disregarded when verifying the operational limits of heat pipes (section 6.2). In the present case Q/Q_{sonic} would be around 0.02 and the number υ around $3 \cdot 10^{-5}$. Spatial pressure variations as well as inertial vapor effects therefore can be neglected for the case of interest.

In their two-dimensional analysis Peterson and Tien [14] present two characteristic parameters that verify, if in a GLHP two-dimensional vapor flow effects are to be expected. The first one, called the diffusion parameter E , is related to the vapor condensation rate at the liquid/vapor interface and indicates the relative importance of radial diffusion. Diffusive energy transport, $\rho_v h_{lv} \bar{D}/r_v$, is compared to convective energy transport, $h(T_{v,e} - T_s)$. The second one, the wall conduction parameter W , evaluates the axial wall heat transport in the condenser with respect to the convective one. There is no difference with the results of one-dimensional modeling, if the following expressions are valid:

$$E = \frac{\rho_{v,e} h_{lv} \bar{D}}{h r_v (T_{v,e} - T_\infty)} > 1 \quad (4.46)$$

$$W = \frac{\bar{kA}}{2\pi r_v^3 h} > 10 \quad (4.47)$$

The heat transfer coefficient h is based on the area, where liquid and vapor are in contact, and includes the external thermal contact resistance and the resistances of heat pipe container, wick and liquid/vapor interface. The total axial conductance \bar{kA} comprehends thermal conductivities and effective cross sections of heat pipe wall and wick.

In the case of cooling by radiation or by an air stream, all other thermal resistances are negligibly

small if compared to the external. Using experimental values from the test runs, values of 1.5 and 8.7 for the parameter E and values of 197 and 4084 for the parameter W are obtained. The first of the values refers to radiation to an environment at -50 °C, the second to convection inside a cooling jacket to a 1.5 g/s air stream at 25 °C inlet temperature. This shows above all that, if a large thermal resistance to the cooling agent is provided, two-dimensional effects become less important.

When the heat pipe has a high thermal conductivity and the heat flux encounters a large resistance at the interfaces, where it enters and where it leaves the heat pipe, a lumped capacity model can be a very simple alternative to simulate heat pipe transients. This type of model has a rather macroscopic view. Thermal properties are accumulated (lumped) and uniformly distributed over the whole heat pipe (in the case of fixed conductance heat pipes [33]) or functional sections (in the case of GLHP's [8, 11, 17]) which are treated like solids. In the extreme case [33, 17] the model does not care about the vapor inside the heat pipe nor about phase change processes. It should be remarked that lumped capacity models for GLHP's intrinsically presuppose the flat front assumption, as the active section is sharply separated from the inactive section.

When the length of the heat pipe is relatively long, it should be verified, whether the thermal resistance of the vapor space is to be considered. Colwell and Modlin [34] present a correlation that estimates the vapor resistance for a given pipe geometry. This resistance is important, when the effective length is approximately 100 times the vapor space diameter. In the present case this relation is much smaller: $L_{ef}/D_v = 44.7$.

A uniform temperature distribution in each section can be assumed, if the Biot number is

$$Bi = \frac{h_{c,ext} L_{char}}{k} < 0.1 \quad [35] \quad (4.48)$$

The characteristic length, L_{char} , refers to a dimension of the conductor where the highest temperature difference can be noted. In this case the total length of the heat pipe can be used, as it is the longest possible length available for heat transfer from and to the surroundings, if the condenser is completely open. In the present case the equivalent external heat transfer coefficient for radiation (eqn. 4.38) is very low. In the case of convective air cooling, that is applied in the heat pipe tests in section 7.7, the coefficient is approximately 85 W/m²K. The thermal conductivity k which is attributed to the heat pipe as a lumped conductor can be estimated according to the remarks made in the beginning of section 2.1. Reference [20] as well as reference

[32] compare the conductances of water filled copper heat pipes to those of copper rods of equivalent cross section:

$$k_{HP} = 90 \cdot k_{Cu} \text{ with } L_{char} = 1 \text{ m [20];}$$

$$k_{HP} = 34.3 \cdot k_{Cu} \text{ with } L_{char} = 0.5 \text{ m [32].}$$

Thus the heat transfer coefficient due to conduction, k_{HP}/L_{char} , would be between 35000 and 27000 W/m²K. Having in mind that the transport of latent heat is responsible for superconductivity, estimates of k_{HP}/L_{char} for heat pipes driven by other fluids can be made by reducing or increasing the mentioned values relating the latent heat of evaporation of the working fluid to that of water. As h_{lv} of water is about 3.3 times that of acetone, the estimate for acetone consequently would be about 9000 W/m²K, and for the case of interest the following Biot number results: $Bi \cong 0.009$.

Kimura *et al.* [11] recognize in their lumped capacity model the importance of the thermal inertia of the heat source for the GLHP transient response. As in the experiments the heat will be generated through skin heaters with negligible thermal inertia, their burn-in time constants are of no importance.

So far the applicability of a one-dimensional model without consideration of compressibility, viscous and inertial effects has been proved to be appropriate to represent the GLHP that is going to be studied. It remains to check now, if a flat front approximation is tenable.

According to Sun and Tien [7] the interface between vapor and gas is sharper, the lower the vapor pressure is at ambient temperature, the lower axial wall conduction and the larger a parameter called gas control sensitivity factor. This factor is defined as

$$N_s = \frac{h_{lv}}{R_v} \tag{4.49}$$

Table 2 shows some values of this parameter for the most common working fluids of heat pipes. It can be noted that acetone shows a relatively low value. Fig. 6.1 and the observations about operational conditions made in section 6.4 confirm a low acetone vapor pressure, when the heat pipe is run under space conditions. Of course aluminum, a commonly used container material for axially grooved heat pipes, is quite conductive. But to some extent reduction of heat transfer through this sensible heat path can be achieved by slitting the condenser saddle as well as the segmentation of the radiating sheets, as depicted in the figures of chapter 3 and 5.2.

Acetone	Ammonia	Methanol	Water
3800	2343	4445	5260

Table 2 - Gas control sensitivity factors at 30 °C for common heat pipe fluids

In a comparative analysis Bobco [36] discovered, that in GLHP's with external reservoirs the flat front model predicts that much higher heat fluxes can be absorbed by the heat pipe, before the front actually reaches the condenser end. He recommends that the use of a flat front model should be restricted to situations where the heat flux does not induce the front to exceed 90 % of the condenser length: $L_{ca} < 0.9 \cdot L_c$!

A comprehensive numerical analysis of a set of gas-loaded heat pipes coupled to a radiator panel cannot yet be found in the literature. The demand for the investigation of such a system was expressed by Peterson and Tien [19] in their introductory work that is based on a simplified steady-state analysis. They show, how the spacing between the heat pipes influences the temperature distribution on the radiating sheet, and further, how high the nodal resolution (or degree of discretization) of the system must be in order to sufficiently fulfill the conservation of energy and noncondensable gas mass. With respect to the GLHP's their model is rather limited: Only the axially heat conducting heat pipe wall of the condenser and the adiabatic zone is considered, and the vapor temperature of the active zone, $T_{v,a}$, is given as an internal boundary condition. The active length, L_{ca} , that distinguishes the active part of the condenser from its gas-blocked part is also fixed. The cross section of the heat pipes shows a quadratical outer contour to enable a plane connection to the inner face of the radiating sheet. The heat pipes are bonded to only one sheet.

In section 5.2 this partial model is used to illustrate the temperature fields on radiators of three different widths and to compare them to radiators of the same dimensions but with their sheets cut in perpendicular strips, as it is common practice for space GLHP radiators. Moreover the model was adapted to the heat pipe profile that is used in this study. For the subsequent simulations the metallic structure of the radiator is extended to form the complete system, the capacitive terms are added and a model, whose applicability was verified in section 4.6, is applied to represent the vapor space, thus enabling transient modeling.

5.1 Discretization of the radiator

The radiator is, strictly speaking, the part of the system where the heat leaves the system's core, the vapor space, in the direction of the environment. It comprises therefore of the condensers, the condenser saddles and the radiating sheets. When these elements are discretized, the condensers (in common GLHP models treated as one-dimensional domains) form an interface to a domain which is at least two-dimensional. Sometimes the saddles are included in one-dimensional models

and are referred to by a fin efficiency [5]. This decreases heat resistance in the direction of heat flow. The saddles can also be automatically incorporated in the model, if the lumped capacity formulation is employed. In the following the saddles as well as the sheets are handled as two-dimensional structures. In doing so they are represented by a network with a single layer of nodes. However, a structure can be assumed two-dimensional only, if its thickness is much smaller compared to its width and length, as the temperature gradient in the third dimension is negligible.

With the discretization of the two-dimensional objects by a regular network, generating rectangular meshes, they appear as a succession of parallel node strings. Apart from a simple numerical algorithm that can be applied when sweeping line-by-line through the two-dimensional domain, this kind of array permits the connection of a one-dimensional condenser string to a string of the adjacent two-dimensional structure. For convenience heat transfer between elements belonging to domains of different dimensions is usually expressed by a heat transfer coefficient h .

Fig. 5.1 shows a cut-out of the radiator with the nodal arrangement that is going to be used in the simulations. The image represents a radiator configuration with a width of 30 cm which corresponds to a spacing of 10 cm between the GLHP's.

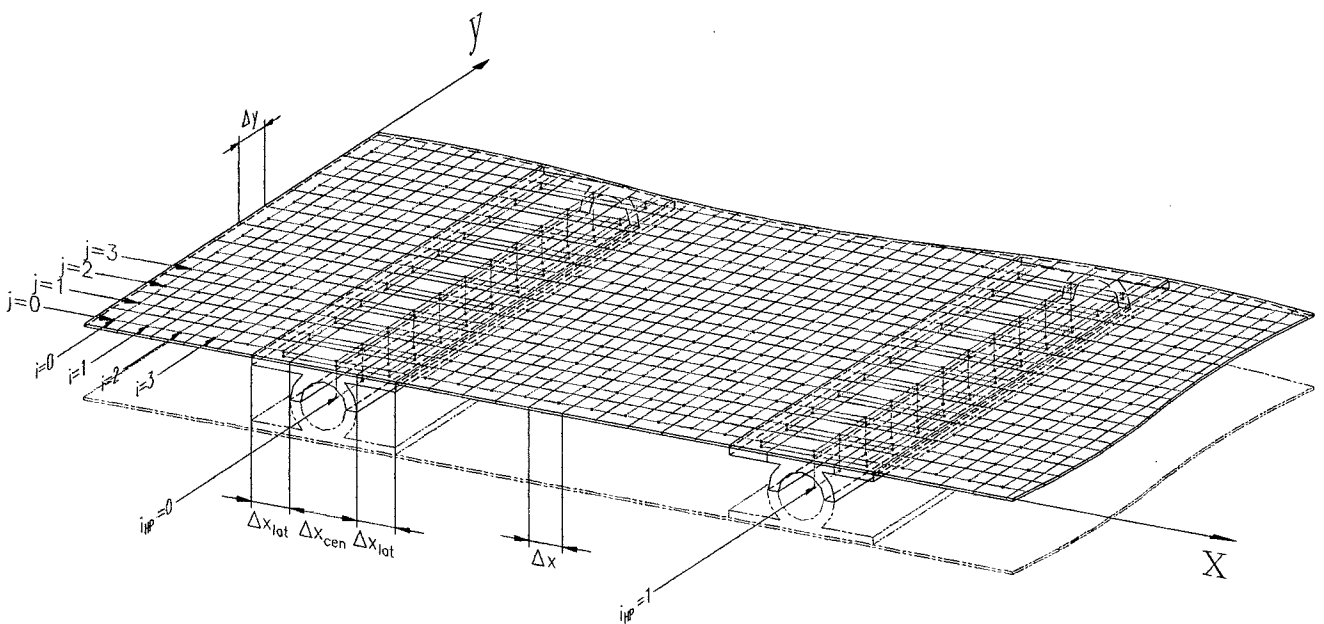


Fig. 5.1 - Cut-out of a 30 × 50 cm radiator showing the nodal network in heat pipes, fins and radiating sheet

The nodal network can be characterized by 3 levels which are successively swept by the numerical algorithm during each iteration. The low level is formed by the 3 GLHP strings that actually are

the vapor space nodes. The intermediate level contains nodes which represent the condenser wall. They receive the heat flux through a film coefficient, h_i , referred to the liquid/vapor interface. The same level accommodates saddle (or fin) nodes in the side strings. Here the heat flux is opened to the second dimension enabling a better, because broader, heat diffusion into the sheet. At the high level the radiating sheet receives heat from 3 heat sources made up by 3 node strings of the intermediate level respectively. The heat transfer between these levels is specified by the saddle-sheet joint conductance, h_b , which is dependent on the thermal characteristics of the thermal cement or grease that fills the gap between saddle and sheet. Because of the partition of the algorithm in 3 levels three-dimensional modeling can be avoided. The heat portions that the corresponding node neighbors exchange vertically are included in the respective heat source terms of the discretization equations. Due to the small thickness the thermal resistance within the aluminum in vertical direction is negligible in relation to the heat transfer coefficients mentioned before.

According to the node density in Fig. 5.1 the radiator sheet is transversely divided into 39 parts (x-axis) and axially into 50 equal parts (y-axis). Thus the standard sheet element ($\Delta x \times \Delta y$) has dimensions of 7×10 mm in this illustrative example. For reasons that are explained in the next section, the applied element length will actually be much shorter. At the GLHP positions, i_{HP} , the width of the sheet elements is different, as it corresponds to the element width of the lower level. The width Δx_{cent} of the central elements is taken equal to the dimension of the external heat pipe diameter, D_{ext} , that is 14 mm. For simulation these elements are transformed in numerical artefacts of the condenser wall, as they will not be related to the form of the object they represent. They are created distinctly to join different heat transfer areas in the vertical direction, and they have a relatively smaller thermal resistance in the direction of the heat pipe axis because of a considerably larger cross section. As the width of the saddle elements is inevitably fixed, later the transverse node density will also be characterized by the number of border standard sheet elements, being 5 in this case.

The radiator network described so far indicates that the simulation can be reduced to just a half of the system. The other half, in the figure drawn as contours of contiguous parts, need not be considered, as the system is symmetrical with respect to the plane that contains all heat pipe axes. This simplification is only possible, if the heat flux that is introduced at the evaporator is uniformly distributed over the heat pipe perimeter when entering the condenser section. In other words: The preceding adiabatic zone must be made long enough to ensure that the peripheral

temperature gradient caused by one-sided heat input has been overcome. Heat leaves the system only in the upside direction by radiation from the sheet. All other surfaces are considered to be isolated. Radiative heat transfer between the condensers through the gap and border heat losses from the gap to the surroundings are taken to be impeded and are not included in the simulation. The sheet margins are also assumed to be isolated by setting a zero temperature gradient at the borders of this domain.

The numerical method that is used in all simulations is based on a finite control volume formulation [37]. The temperatures of one axial network string ($i = 0$ to $i = n-1$) can be calculated simultaneously, if a Tridiagonal-Matrix Algorithm (TDMA) is applied to a set of finite-difference equations. These equations result from integration of the differential equations (5.1) to (5.3) over each control volume that surrounds a grid point. The processing sequence of the simulation algorithm is from low to high level. In this way the information diffuses gradually from the GLHP's through the saddles to the sheet by each iteration. The TDMA is actually restricted to one-dimensional equations, but two-dimensional structures can be treated by the so-called line-by-line scheme which is used for both the saddles and the sheet. Sweeping from left ($i = 0$) to right the TDMA solves the temperatures on one string $i = k$, assuming that the temperatures along the neighbor strings $i = k-1$ and $i = k+1$ are known from their previous values. Due to the sweep direction the string $k-1$ already keeps the temperature values of the current iteration, whereas the string $k+1$ contributes the values of the previous iteration. In this way the method quickly brings the information from the left borders and, each time a GLHP position is crossed, from the lower borders to remote regions on the sheet.

As the TDMA requires linear equations, radiation to the environment has to be linearized. The linearization is realized by applying a truncated Taylor series expansion around the sheet temperature value taken from the previous iteration. Thus the heat flux that emerges from each element is related to its derivative with respect to temperature. In the discretization equations radiation is included in the heat source term. For the transient simulations the capacitive terms that have to be added to the equations obey an implicit scheme. This method has the advantage of being unconditionally stable. The approximation of the temperature derivative with respect to time is made by "backward" differences. The determination of the element temperatures is based on new time values $t+\Delta t$, which means that in each iteration the new temperature values predominate during the current time step. The derivation of the transient finite-difference equations applied to the radiation sheet can be found in detail in appendix A1.

5.2 Simple steady-state analyses of various radiator configurations

The analyses performed in this section take the work of Peterson and Tien [19] as a pattern. They aim to find, for the present radiator system, the spacing between the GLHP's that ensures an interaction between the heat pipes considering mere steady-state heat conduction through the radiating sheets. For this purpose the radiator is checked with three different widths, named as narrow, medium and broad radiator. Each of the configurations is also compared to that with segmented sheets, henceforth called as the slitted radiator configuration.

The original heat conduction model was formulated for heat pipes that have the same cross section in both the adiabatic zone and condenser. In the present case the cross section of the adiabatic zone is circular, but its geometry changes abruptly at the beginning of the condenser. In order to provide a broad area for mechanical connection and a better heat entrance to the sheets, the cross section expands to form the saddles. The heat transfer equations are therefore written for three domains, that is, the sheet, the condenser saddles and the adiabatic zones. As indicated in section 5.1 the first two domains show a two-dimensional temperature distribution. The equations refer to one half of the system.

The partial differential equation for the sheet with a thickness s is

$$k_R s \left[\frac{\partial^2 T_R}{\partial x^2} + \frac{\partial^2 T_R}{\partial y^2} \right] = \varepsilon \sigma (T_R^4 - T_\infty^4) - h_b (T_f - T_R) \quad (5.1)$$

With all four sheet margins isolated the boundary conditions are

$$x = 0, x = w_R : \frac{\partial T_R}{\partial x} = 0 \quad y = 0, y = L_c : \frac{\partial T_R}{\partial y} = 0$$

At the contact plane between condensers and sheet the transfer coefficient h_b accounts for the thermal resistance.

For the condensers ($m = 1, 2, 3$) with fin thickness e the partial differential equations are:

$$k_f e \left[\frac{\partial^2 T_f^m}{\partial x^2} + f_{\text{curv},1} \frac{\partial^2 T_f^m}{\partial y^2} \right] = f_{\text{curv},2} h_i (T_{v,a}^m - T_f^m) - h_b (T_f^m - T_R) \quad (5.2)$$

At the central element of the condenser profile the cross section for axial heat conduction is larger than at the lateral elements. There also exists a larger transfer area for heat coming from

the vapor space than the external area in contact with the sheet, where heat leaves the element. Taking this geometrical difference into consideration, while maintaining a two-dimensional and plane element for discretization, two weighting factors, $f_{curv,1}$ and $f_{curv,2}$, are introduced into eqn. (5.2). These factors enhance heat conduction in the y -direction and the transfer coefficient h_i at the vapor/wall interface respectively:

$$f_{curv,1} = \frac{\pi(D_{ext}^2 - D_v^2)}{8D_{ext}e}, \quad f_{curv,2} = \frac{\pi D_v}{2D_{ext}} \quad (\text{note: } D_{ext} = \Delta x_{cen})$$

For the lateral elements (fins) the following values are applied: $f_{curv,1} = 1$ and $f_{curv,2} = 0$.

When assuming the flat front principle for the vapor space a discrete location L_{ca} can be found in y -direction, where the condensing rate, expressed by the first term on the right hand side of eqn. (5.2), changes abruptly from a finite value to zero. Hence the inactive section of this domain is separated from the active one by setting $h_i = 0$ for $L_{ca} < y < L_c$.

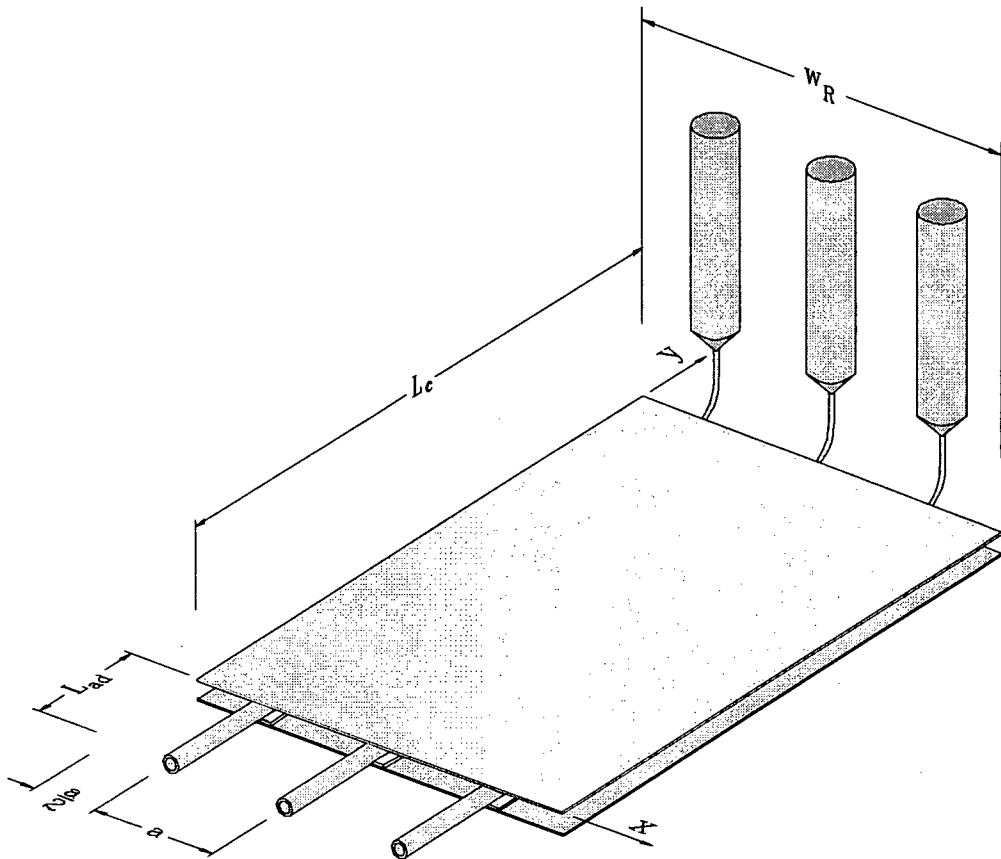


Fig. 5.2 - Main dimensions of the GLHP radiator as used in the steady-state partial model

The condenser ends ($y = L_c$) and the fin borders ($x = 0, x = B$) are assumed to be isolated. At the transition to the adiabatic zones ($y = 0$) heat conduction through the wall is considered as a boundary condition:

$$x = 0, x = B : \frac{\partial T_f^m}{\partial x} = 0; \quad y = 0 : q = k_f f_{\text{curv}} \frac{\partial T_f^m}{\partial y}; \quad y = L_c : \frac{\partial T_f^m}{\partial y} = 0$$

For the adiabatic zones the temperature is given by

$$\overline{kA} \frac{d^2 T_{\text{ad}}^m}{dy^2} = \pi \frac{D_v}{2} h_i (T_{\text{ad}}^m - T_{v,a}^m) \quad (5.3)$$

$$y = 0 : q = k_f \frac{dT_{\text{ad}}^m}{dy}; \quad y = -L_{\text{ad}} : \frac{dT_{\text{ad}}^m}{dy} = 0$$

The primary purpose of the following numerical analysis is to show the effect of placing heat pipes with high heat loads next to a heat pipe at a low power level. For all of the tested configurations the panel length is fixed at 50 cm and the panel width is varied according to heat pipe spacings of 5, 10 and 20 cm. The active condenser length, L_{ca} , of the middle heat pipe was set to 20 cm, with that of the outside heat pipes being 40 cm. All heat pipes are kept at the same operating temperature, $T_{v,a}$, of 50 °C.

Radiating sheet size, $w_R \times L_c$	
Broad radiator ($a = 20$ cm))	60 × 50 cm
Medium radiator ($a = 10$ cm)	30 × 50 cm
Narrow radiator ($a = 5$ cm)	15 × 50 cm
Sheet thickness, s	0.8 mm
Width of sheet/saddle contact area, B	30 mm
Total metallic heat pipe cross section, A_p	
Adiabatic zone	0.57 cm ²
Condenser	1.31 cm ²
Evaporator temperature, $T_{v,a}$	50 °C
Ambient temperature, T_∞	-50 °C
Sheet emissivity, ϵ	0.86
Metal thermal conductivity, k_s	
Sheet	222 W/mK
Heat pipe	163 W/mK
Vapor-to-wall interface conductance, h_i	4000 W/m ² K
Saddle/sheet joint conductance, h_b	3000 W/m ² K

Table 3 - Input data and parameters as used in the steady-state analysis

Special attention must be paid to the axial and transverse node resolution. For fear of misevaluating the radiated heat the node density should be higher in the direction, where larger temperature gradients are expected. Fig. 5.3 shows the effects of node resolution on the calculated total heat flux dissipated by the two sheets for a heat pipe spacing of $a = 10$ cm (medium radiator). For the normal and slitted radiator configurations the transverse node resolution has been varied discretely in four steps: 21, 27, 39 and 51 nodes with numbers of border standard sheet elements equal to 2, 3, 5 and 7 respectively.

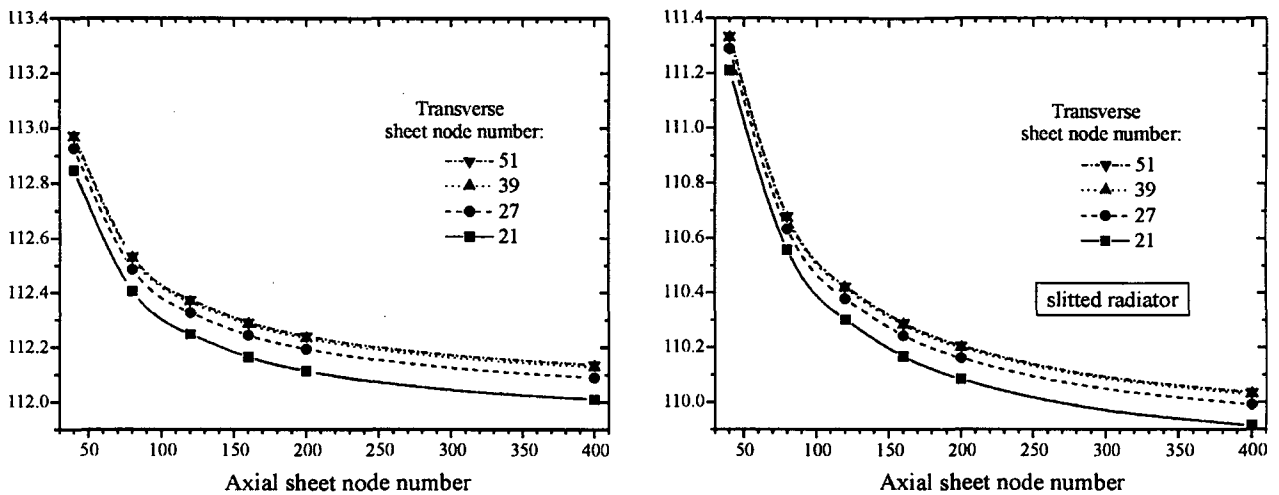


Fig. 5.3 - Effect of node density on calculated radiator heat output

It can be noted that an increase in transverse resolution beyond 39 does not bring any benefit, whereas an increase in axial resolution continually does. For the same extension of active lengths the radiator in the slitted configuration dissipates about 2 W less. This means that for the same heat input the slitted radiator opens more condenser length than the normal one. When scaling the figures the size of the depicted heat flux interval was intentionally made equal to illustrate the importance of appropriate gridding especially for the slitted radiator. Nevertheless the range of uncertainty falls below 0.5 %, if the axial node number exceeds 150. Hence for the following simulations a grid density of 39×160 (with reference to medium radiator size) was regarded as a suitable compromise between numerical heat output precision and reasonable computing time.

Figs. 5.4 to 5.9 show axial heat pipe temperature profiles and sheet temperature fields that resulted from the steady-state simulations. For a better comparison the figures always show pairs of charts for normal and slitted radiator configurations. The segmentation is indicated in the respective figures by black transverse lines. Not only the sheets but also the condenser fins are considered as being cut in 10 segments of 5 cm. In the simulation program the separation

between the segments is taken as complete by postulating a zero conductivity ($k = 0$) across all gaps. For all cases the temperature of the environment is set as $-50\text{ }^{\circ}\text{C}$. Heat transfer to the environment merely occurs by radiation.

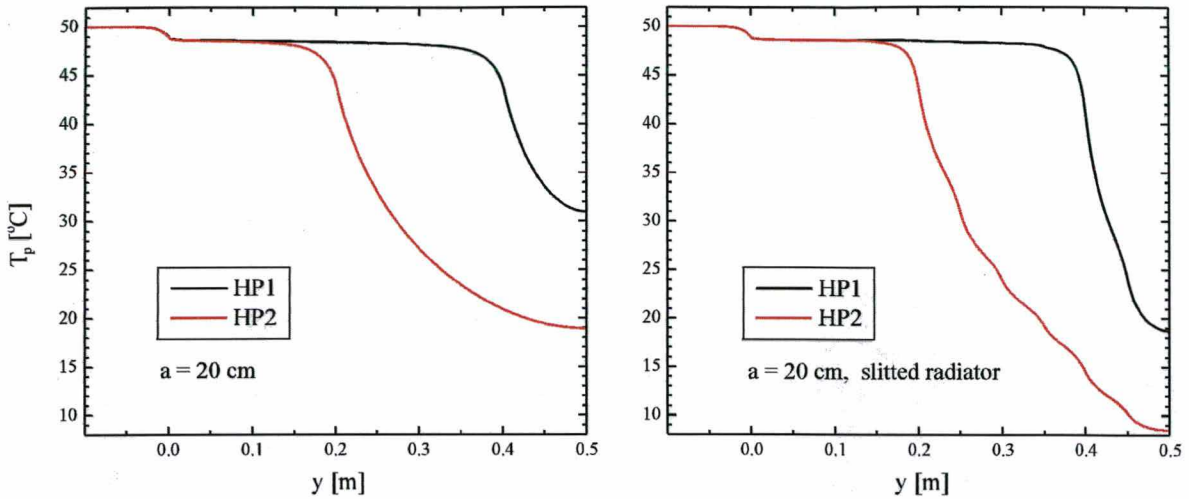


Fig. 5.4 - Wall temperature profiles of two GLHP neighbors in the broad radiator

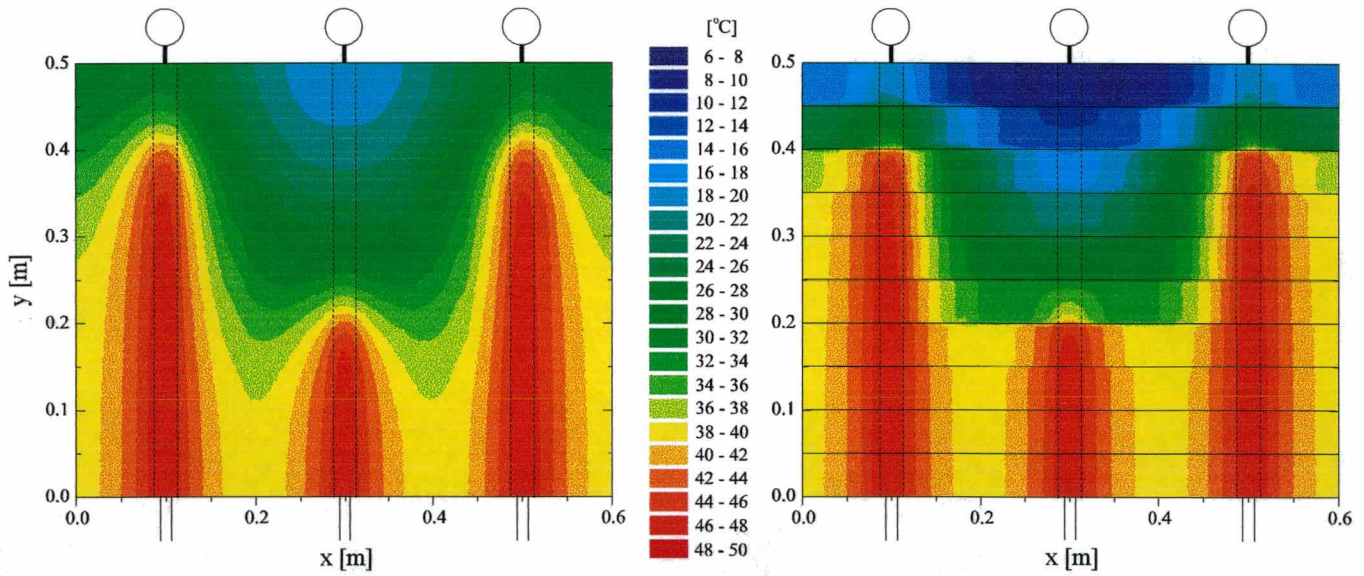


Fig. 5.5 - Sheet temperature fields of normal and slitted broad radiator

In the colored images a strong contrast can be noted in the regions close to GLHP positions, especially when the spacing between the heat pipes is large. Although the sheet has a relatively high conductivity these two-dimensional effects are pronounced in the case of radiative cooling. In Fig. 5.5 a temperature drop of $13\text{ }^{\circ}\text{C}$ can be observed over a distance of 6 cm transversely to the heat pipe axis. In the y -direction the temperature gradient is smoothed due to the highly

conductive heat path formed by the condenser wall together with the fins. With segmented sheets and condenser fins the temperature gradient is also intense in the y-direction. The active lengths can be perceived more clearly, as heat conduction in the axial direction is about 50 % less.

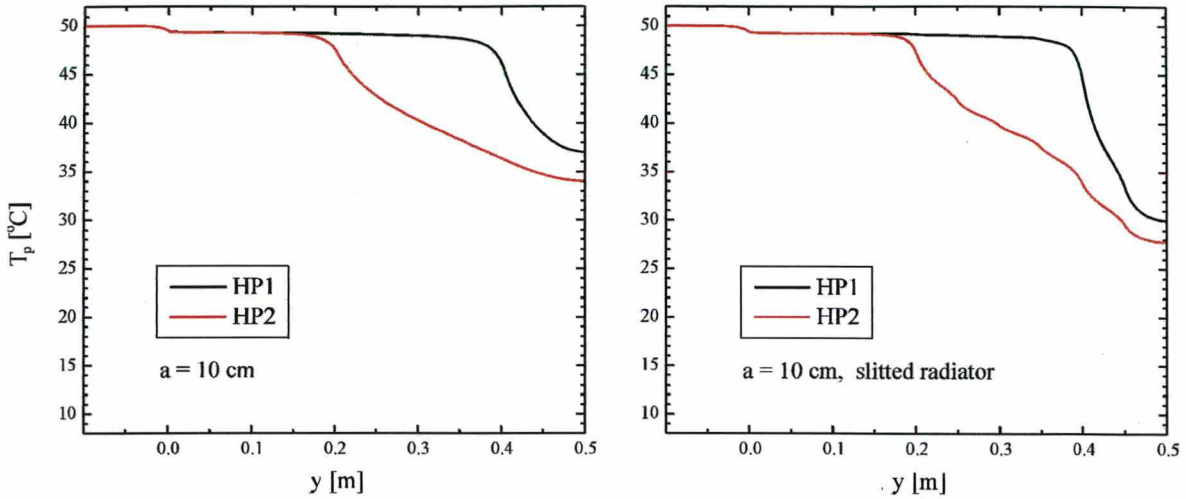


Fig. 5.6 - Wall temperature profiles of two GLHP neighbors in the medium radiator

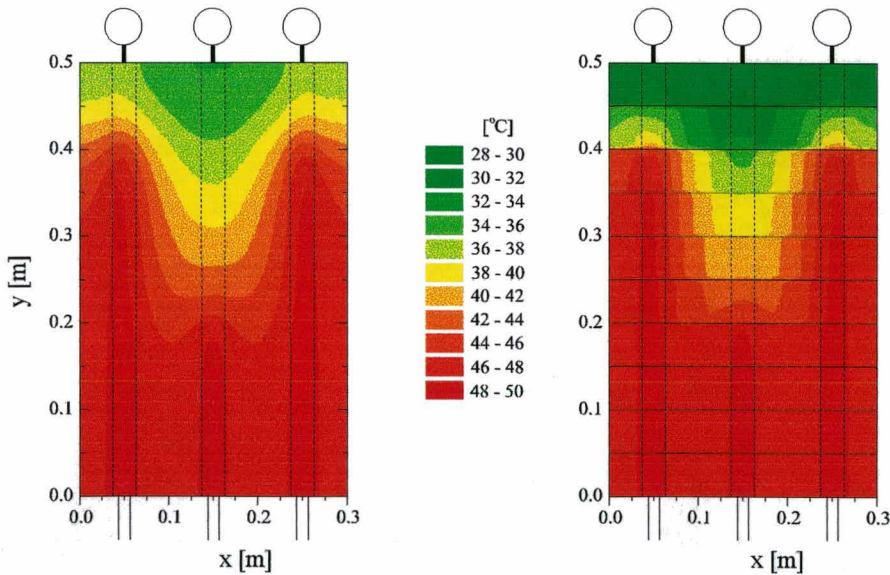


Fig. 5.7 - Sheet temperature fields of normal and slitted medium radiator

When the heat pipe spacing is large, the GLHP's can be observed as single, isolated objects, even if the active lengths are quite different. The temperature distribution of each heat pipe is not dependent on that of the neighboring pipes. When the spacing becomes closer, transverse conduction smooths the gradients, and thermal interaction between the heat pipes through the common sheet is visible. In the case of a spacing of 5 cm the highly charged heat pipe (HP1)

heats the inactive zone of its neighbor (HP2) to a temperature only 2 or 3 degrees lower than its own value. Radiator slitting here only takes effect for sheet lengths that are generally larger than the active lengths of the GLHP's at high power level. The consequence of heating the inactive zone of the low power GLHP is an increase of vapor pressure in this section which in turn reduces the noncondensable gas concentration at that point. The surplus gas amount is driven into both directions of the heat pipe, thus inducing the vapor/gas front to retreat and raising the evaporator temperature. The partial model with the rigid prescriptions of $T_{v,a}$ and L_{ca} fails to describe the real situation so far. A more comprehensive model that includes the interior reactions of the GLHP's is required.

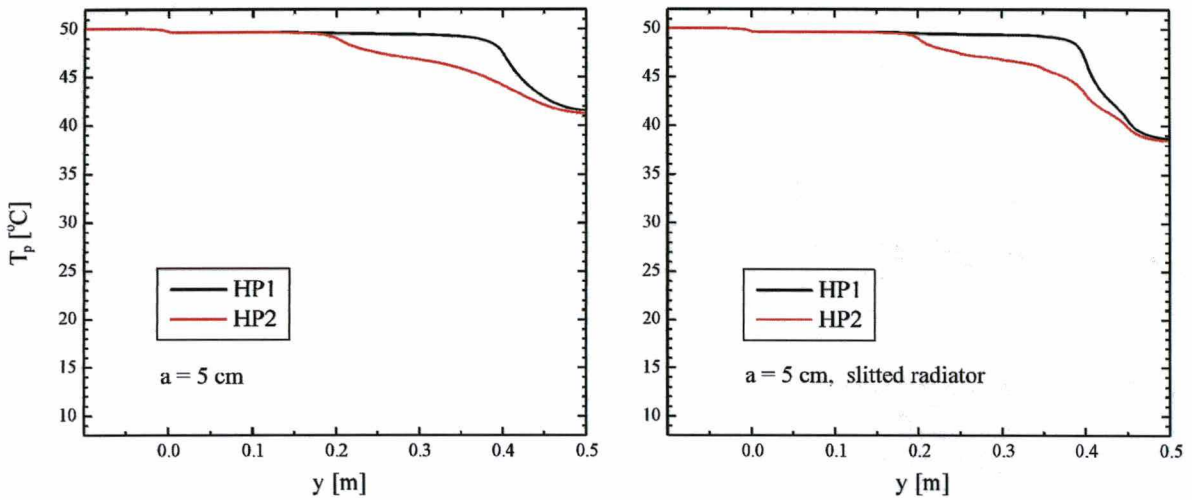


Fig. 5.8 - Wall temperature profiles of two GLHP neighbors in the narrow radiator

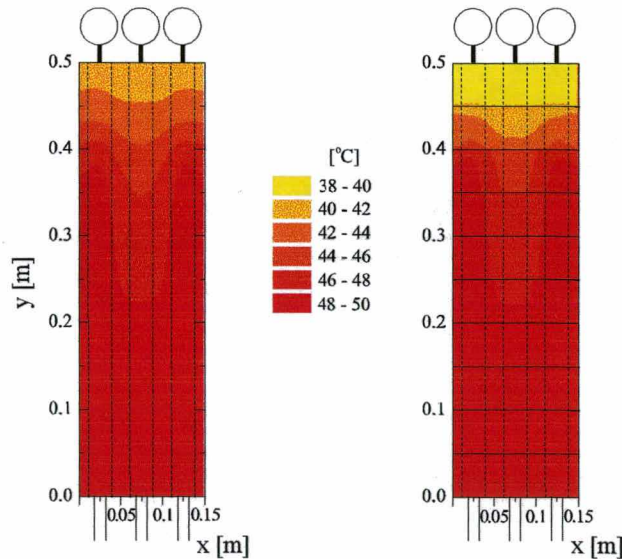


Fig. 5.9 - Sheet temperature fields of normal and slitted narrow radiator

5.3 Transient radiator analyses based on Antoniuk's vapor space model

In transient modeling the heat transfer equations include the thermal capacity of all metallic components and the working fluid in its liquid state. As an immediate temperature accommodation can be presupposed for vapor and noncondensable gas, their thermal capacity can be neglected with respect to the others. After introducing the transient terms the eqns. (5.1) to (5.3) take the following form:

For the sheet

$$k_{RS} \left[\frac{\partial^2 T_R}{\partial x^2} + \frac{\partial^2 T_R}{\partial y^2} \right] = C \frac{\partial T_R}{\partial t} + \varepsilon \sigma (T_R^4 - T_\infty^4) - h_b (T_f - T_R) \quad (5.4)$$

$$x = 0, w_R : \frac{\partial T_R}{\partial x} = 0; \quad y = 0, L_c : \frac{\partial T_R}{\partial y} = 0; \quad t = 0 : T_R = T_\infty$$

For the condensers

$$k_f e \left[\frac{\partial^2 T_f^m}{\partial x^2} + f_{\text{curv}} \frac{\partial^2 T_f^m}{\partial y^2} \right] = C \frac{\partial T_f^m}{\partial t} + h(T_{v,a}^m - T_f^m) - h_b (T_f^m - T_R) \quad (5.5)$$

$$x = 0, B : \frac{\partial T_f^m}{\partial x} = 0; \quad y = 0 : q = k_f f_{\text{curv}} \frac{\partial T_f^m}{\partial y}; \quad y = L_c : \frac{\partial T_f^m}{\partial y} = 0; \quad t = 0 : T_f^m = T_\infty$$

The domain that represents the heat pipe wall upstream of the condenser is extended into the negative y-direction to form the zone where an external heat flux, q_{ext} , is to be introduced, defined as the evaporator. The corresponding equation for evaporator and adiabatic zone is

$$\overline{kA} \frac{d^2 T_{e,ad}^m}{dy^2} + \delta \cdot \pi \frac{D_v}{2} q_{\text{ext}}^m = (\rho_s c_s A_s + \rho_l c_l A_l) \frac{\partial T_{e,ad}^m}{\partial t} + \pi \frac{D_v}{2} h_i (T_{e,ad}^m - T_{v,a}^m) \quad (5.6)$$

$$y = 0 : q = k_f \frac{dT_{e,ad}^m}{dy}; \quad y = -L_{ad} - L_e : \frac{dT_{e,ad}^m}{dy} = 0; \quad t = 0 : T_{e,ad}^m = T_\infty$$

where $\delta = 0$ for $-L_{ad} < y < 0$

and $\delta = 1$ for $-L_e - L_{ad} < y < -L_{ad}$

Just as in the steady-state model the heat pipe wall is coupled to the vapor space through a heat transfer coefficient, h_i , which is supposed to be constant over the whole active heat pipe section.

The variation of the parameters $T_{v,a}$ and L_{ca} with time, however, is now determined by a heat balance over the whole heat pipe, a gas mass balance including the reservoir and an equation for the vapor saturation pressure, corresponding to the equations in section 4.4.

For numerical convenience the axial coordinate should point to the same direction that the heat flux takes when passing through the system. Hence the origin of the vapor space coordinate z is placed at the beginning of the evaporator (Fig. 5.10) and the transformation of coordinate $z = y + L_e + L_{ad}$ is made with respect to the other domains of the system.

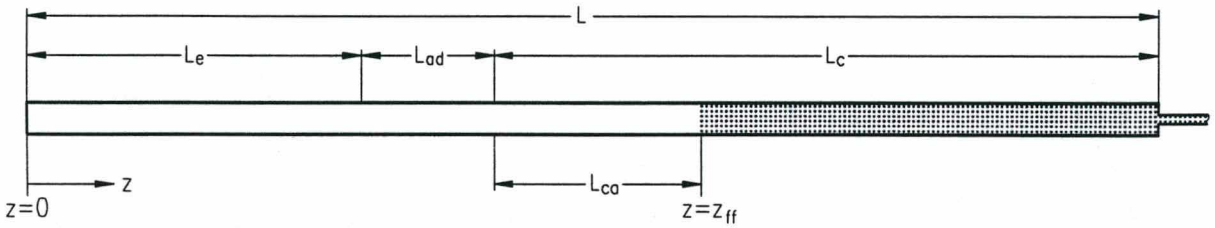


Fig. 5.10 - Relevant GLHP dimensions for the vapor space model

With reference to the new origin for z , and with h_i and A_v being constant along the heat pipe, the eqns. (4.28), (4.29), (4.30) and (4.32) now are written as follows:

$$N_g(z_{ff}) = p_t(z_{ff}) \left[\frac{V_r}{\mathfrak{R}T_r} + A_v \int_{z_{ff}}^L \frac{dz}{\mathfrak{R}T_p(z)} \right] - \left[\frac{p_{v,r} V_r}{\mathfrak{R}T_r} + A_v \int_{z_{ff}}^L \frac{p_v(T_p(z))}{\mathfrak{R}T_p(z)} dz \right] \quad (5.7a)$$

$$\Rightarrow N_g(z_{ff}) = p_t(z_{ff}) F(z_{ff}) - N_v(z_{ff}) \quad (5.7b)$$

$$p_t(z_{ff}) = p_v(T_{v,a}(z_{ff})) \quad (5.8)$$

$$T_{v,a}(z_{ff}) = \frac{1}{z_{ff}} \int_0^{z_{ff}} T_p(z) dz \quad (5.9)$$

Contrary to section 4.4 the reservoir vapor pressure in eqn. (5.7a), $p_{v,r}$, is left unspecified here, as its determination for the present type of reservoir turned out to be somewhat dubious.

As one of the unknowns, that is z_{ff} , represents one of the integration borders in (5.7) and (5.9), the equations have to be evaluated numerically, where $F(z_{ff})$, $N_v(z_{ff})$ e $T_{v,a}(z_{ff})$ are determined by an iterative solution procedure. The front position at every time step is found by comparison of

$N_g(z_{ff})$, obtained at each vapor space node position, with the known total noncondensable gas inventory, $N_{g,t}$. Beginning with the last condenser node the algorithm steps backwards to the evaporator in increments of Δz which correspond to the length of the discrete wall element Δy . At a certain value of z the front position will be passed, and $N_g(z_{ff})$ exceeds $N_{g,t}$, which means that z_{ff} is situated between z and $z-\Delta z$. Now a refined searching algorithm goes on bisecting continuously the length of the detected element with simultaneous adjustment of active vapor temperature and noncondensable gas contents, until the exact front position is determined.

After dissolving the integrals in eqns. (5.7a) and (5.9) into sums over the element lengths Δz , the expressions on which the refined algorithm is based are derived as follows:

$$N_{g,t} = N_{g,prev} + \frac{p_t(T_{v,a}) - p_v(T_{p,j_{ff}})}{\Re T_{p,j_{ff}}} A_v (1 - U) \Delta z \quad (5.10)$$

$N_{g,prev}$ denotes the gas content as determined for the previous step at node $j_{ff}+1$

$$N_{g,prev} = \frac{p_t(T_{v,a}) - p_{v,r}}{\Re T_r} V_r + \sum_{j_{rr}+1}^{j_{lc}} \frac{p_t(T_{v,a}) - p_v(T_{p,j})}{\Re T_{p,j}} A_v \Delta z \quad (5.11)$$

U was introduced as a kind of weighting factor (Fig. 5.11) characterizing the portion of Δz at j_{ff} that still contributes to the active zone until the position z_{ff} :

$$z_{ff} = \sum_{j=0}^{j_{rr}-1} \Delta z + U \cdot \Delta z \quad (5.12)$$

where U results from the rearranged eqn. (5.10)

$$U = 1 - \frac{(N_{g,t} - N_{g,prev}) \Re T_{p,j_{ff}}}{(p_t(T_{v,a}) - p_v(T_{p,j_{ff}})) A_v \Delta z} \quad (5.13)$$

This weighting factor is also required to adjust the heat transfer area of the front wall element by correspondingly weakening its internal film conductance, which was found important to achieve better convergence during simulation. Finally the exact active vapor temperature that corresponds to z_{ff} is

$$T_{v,a} = \frac{\sum_{j=0}^{j_{ff}-1} T_{p,j} \Delta z_j}{\sum_{j=0}^{j_{ff}-1} \Delta z_j} - U \cdot T_{p,j_{ff}} \quad (5.14)$$

As can be seen from eqns. (5.13) and (5.14) the bisection method is necessary to determine $T_{v,a}$ from an implicit definition.

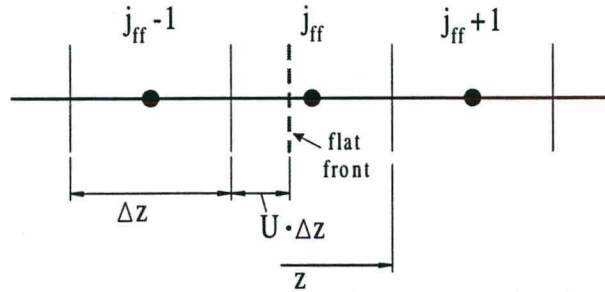


Fig. 5.11 - Numerical consideration of exact flat front position through weighting factor U

The transient analysis was performed for the three radiator sizes that were already treated in the steady-state analysis. The input data are also the same (Table 3), but with the addition of reservoir volume, $V_r = 150$ ml, and gas inventory, $m_g = 200$ mg, in order to provide data for the vapor space module. The heat flux is applied at $t = 0$ in form of a sudden step change. It is maintained constant at 60 W for the outside GLHP's and at 20 W for the middle one. It has to be emphasized at this point that the simulated radiator remains coupled only on the heat exit side; the evaporators still receive their heat fluxes independently from each other.

The amount of vapor in the reservoir strongly conditions the gas-blocked length in the condenser, as it controls the volume of the gas buffer. As explained in chapter 2, the gas buffer volume will respond in a progressive or regressive way to sink temperature changes, if the partial vapor pressure in the reservoir is substantial, whereas it will change linearly, if $p_{v,r}$ is negligible. If applying Antoniuk's vapor space model to the present configuration, with a non-wicked reservoir at sink temperature and separated by a long and narrow feed tube, this crucial parameter has to be imposed arbitrarily, as the model is not capable of giving reliable information about the transient evolution of the vapor-to-gas ratio in the reservoir.

Two simple situations which are border cases can be distinguished. If a non-wicked liquid-free reservoir has an immediate connection to the condenser, there is hardly any diffusion barrier on the way to the reservoir, so that its vapor pressure will be entirely controlled by the vapor pressure at the end of the condenser and independent of the reservoir temperature:

$$p_{v,r} = p_v(T(L_c)) \quad (5.15)$$

If the reservoir has a wick and liquid is present there, the vapor pressure will settle to the saturation pressure at reservoir wall temperature:

$$p_{v,r} = p_v(T_r) \quad (5.16)$$

Test simulations using condition (5.15) have resulted in excessive evaporator temperatures and led to convergence problems, in cases when the vapor/gas front was approaching the condenser end. Looking at the shaping of the reservoir-to-condenser connection one has to admit that this condition is far too rigid for the present case. The diameter of the connection is intentionally made small and its length rather large in order to hinder the flow of vapor at condenser end temperature into the reservoir.

When condition (5.16) was used, the simulation results showed a premature utilization of the whole condenser length at relatively low heat loads. For the present case this situation also is rather hypothetical, as the vapor will not adjust its pressure according to the reservoir temperature due to the lack of liquid there. However, at the beginning of operation, before heat is introduced, vapor actually can be found in the reservoir corresponding to the initial reservoir temperature. This state predominates for some time, as the situation changes due to diffusion with a considerable delay.

The transient profiles actually develop according to an unknown intermediate situation. Nevertheless it is worth while to have a look at the performance of Antoniuk's model to get an idea about operating temperatures at different heat loads for different radiator sizes. In the simulations represented by Figs. 5.12 to 5.14 a simple linear mean value between $p_v(T_{Lc})$ and $p_v(T_r)$ has been taken for the reservoir vapor pressure.

As can be seen in the figures, only the broad radiator offers a sufficient radiation area to absorb 60 W from each of the outside GLHP's without causing a complete condenser opening of any of the heat pipes. Further a tight temperature control can be seen in this case (Fig. 5.12), as the middle heat pipe remains unaffected by the neighbors and the outer heat pipe condensers are only half open. Each heat pipe adjusts its active length according to its own heat load, and the system reaches steady-state after about 70 min. When neighbor heating takes place and the whole condenser length is used up, the operating temperature shows a significantly higher level (15 °C more in Fig. 5.13). An interesting phenomenon of interaction appears for the narrow

radiator in Fig. 5.14. The rapid advances of the vapor/gas fronts towards the condenser end in the heat pipes with 60 W heat load stops the front motion of the low level heat pipe, when the latter reaches slightly more than half of the condenser. The front even retreats for about 5 cm, until the thermal inertia of the system has been exhausted. Now the overload propels the middle pipe quickly to the overdriven mode.

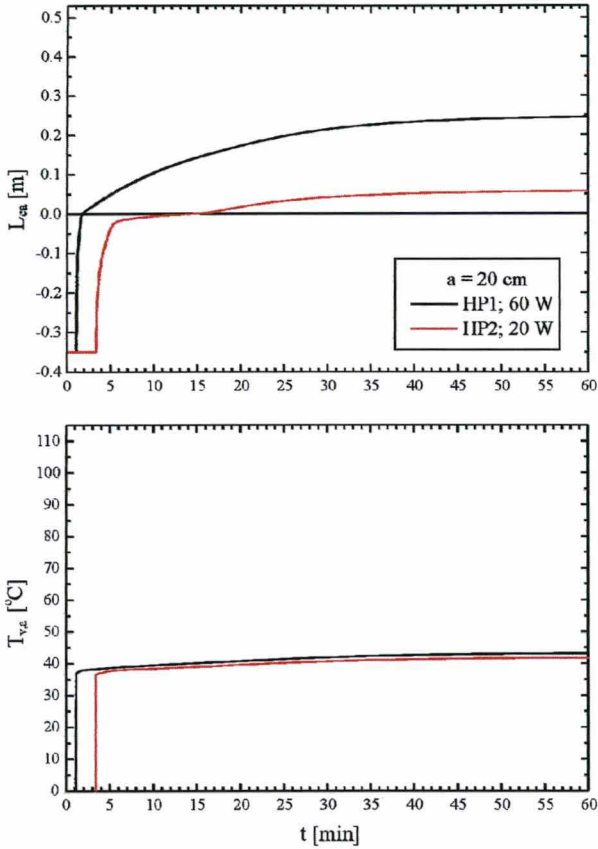


Fig. 5.12 - Broad radiator simulation results for active lengths and operating temperatures

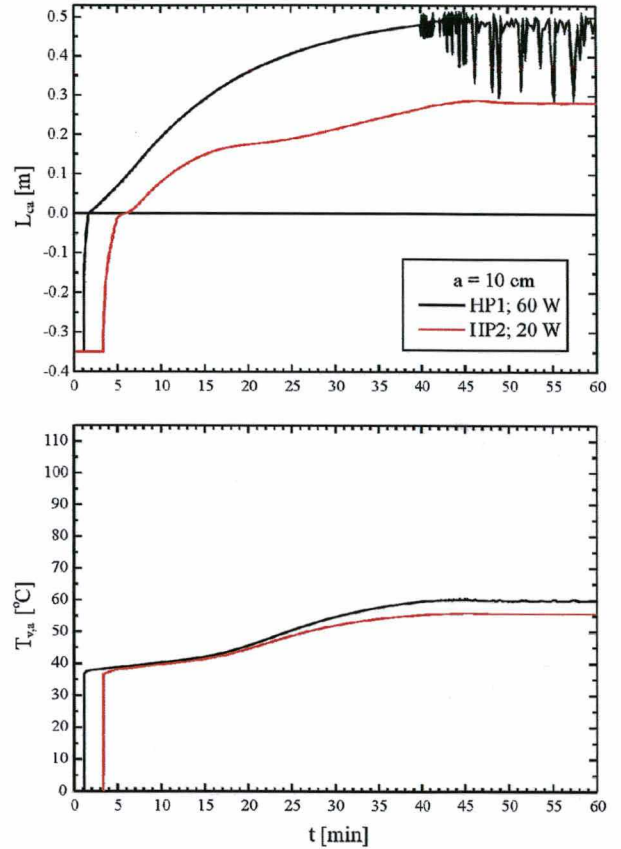


Fig. 5.13 - Medium radiator simulation results for active lengths and operating temperatures

The heat pipes obviously complete their start-up independently of the radiator size. Their start-up times depend only on the heat load, being 3 min 25 s for the heat pipes at low power level and 1 min 5 s for the highly charged ones.

In Fig. 5.13 the chosen heat load spectrum induces the fronts in the outside heat pipes to approach the condenser slowly. However, when the front reaches a value of 0.485 m, the simulation becomes unstable, as the pre-established temperature residual of 0.001 K can no longer be achieved. After that the values for the active length begin to oscillate and continue to change between 0.3 and 0.5 m. Due to this numerical defect the front of the middle heat pipe is

not able to develop to its final value and remains suppressed to 0.28 m. Fig. 5.15 reveals that this situation leads to an infringement of energy conservation. While the output-to-input ratios for the broad and narrow system approach unity after having completely exhausted the system's thermal capacity, the medium system loses 5 % of the supplied heat flux.

The observed instability was anticipated, as it is reported in the literature for flat fronts that approach full condenser length [36]. Though it has to be emphasized that this effect only appeared, when the approach was at low rate. A front that advances quickly, reaches full length without instabilities.

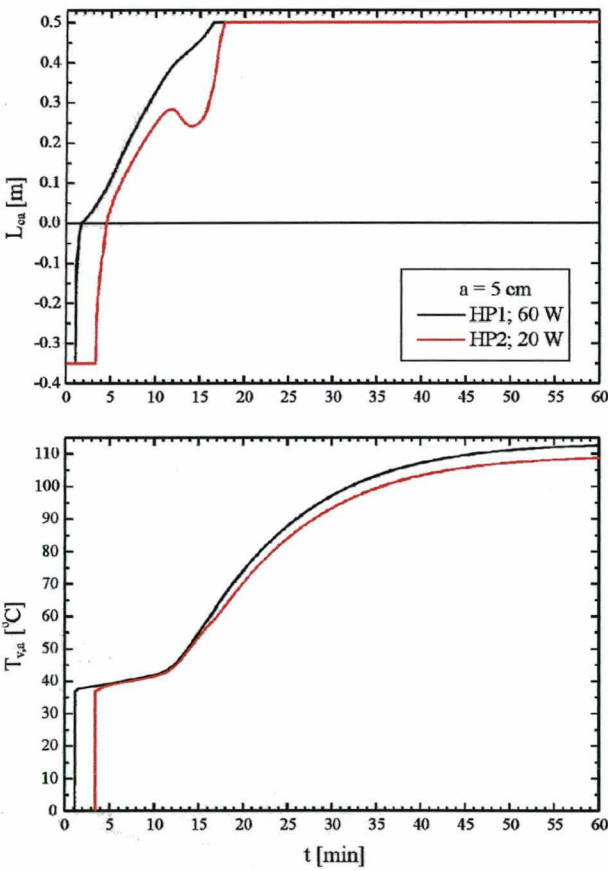


Fig. 5.14 - Narrow radiator simulation results for active lengths and operating temperatures

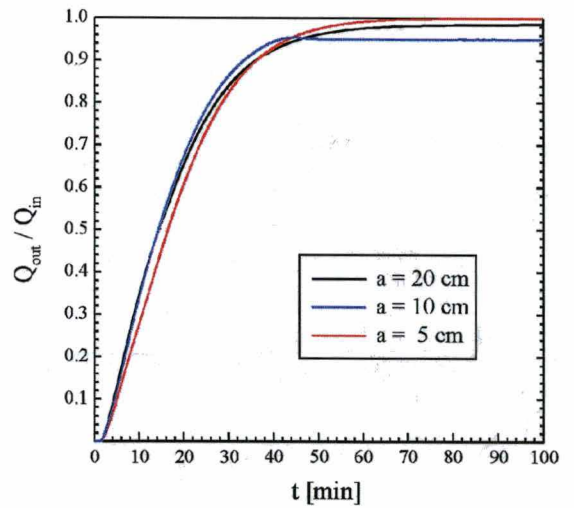


Fig. 5.15 - Heat-out to heat-in ratio for the 3 simulated radiator sizes

5.4 Transient vapor space model considering start-up and feed tube mass flow

The analyses in the preceding section have shown that, without reliable information about the amount of vapor in the reservoir, neither the vapor/gas front location nor its movement can be determined satisfactorily. It also remains vague, when and how the heat pipes pass over to operation under overload. The reservoir vapor pressure depends on the history of operation in which two mechanisms of mass transfer through the feed tube continuously contribute to its value. A spontaneous change is caused by the convective mass transport that directly obeys variations of heat load or temperature at any location of the GLHP. The other mechanism is the diffusive mass transport that tries to balance concentration gradients in the vapor-gas mixture of the gas buffer according to the surrounding temperature. The latter process is very lengthy and only becomes apparent a relatively long time after a condition has changed.

The above suggests that the vapor space model should be extended to get an insight about what is happening on both sides of the feed tube during operation.

First of all eqn. (5.7) is written in a different form to distinguish the reservoir gas portion that is going to be modified for the new vapor space model:

$$N_g(z_{ff}) = N_{g,c}(z_{ff}) + N_{g,r}(z_{ff}) \quad (5.17)$$

with
$$N_{g,c}(z_{ff}) = \frac{A_v}{\mathfrak{R}} \int_{z_{ff}}^L \frac{p_t(z_{ff}) - p_v(T_p(z))}{T_p(z)} dz$$

and
$$N_{g,r}(z_{ff}) = \frac{V_r}{\mathfrak{R}} \frac{p_t(z_{ff}) - p_{v,r}}{T_r}$$

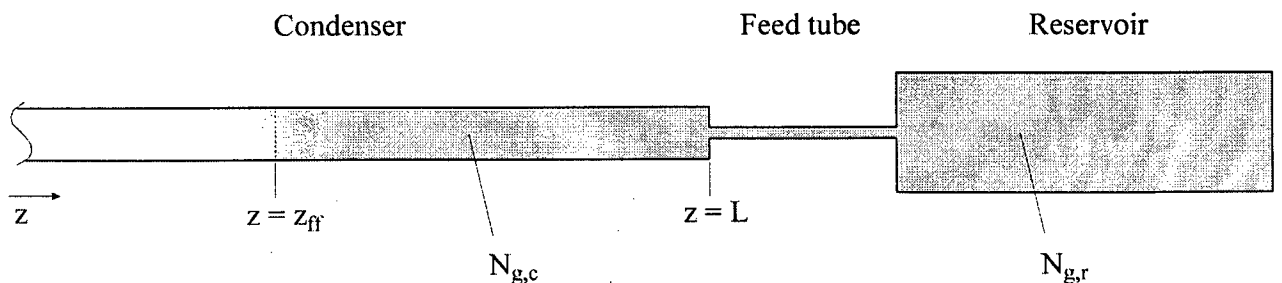


Fig. 5.16 - Gas-blocked part of a GLHP with feed tube (z_{ff} : centroidal position of a hypothetical flat front within a real diffuse front)

According to this equation the total gas mole number, N_g , is divided into the portion existing between the flat front position z_{ff} and the condenser end, $N_{g,c}$, and the portion in the reservoir, $N_{g,r}$. Because of the inaccessible reservoir vapor pressure in the reservoir gas term this portion is now derived from mass conservation for the molar gas flow through the feed tube.

If the total pressure p_t is assumed to be constant at any position inside the GLHP, the gas flow follows from eqns. (4.13) and (4.14):

$$\dot{N}_{g,r} = \chi_g \frac{V_r}{\mathcal{R}T_r} \frac{dp_t}{dt} - c\mathcal{D}A_f \frac{d\chi_g}{dz} \quad (5.18)$$

In this equation appear the terms that are attributed to the two aforementioned convective and diffusive transport mechanisms which are responsible for the gas flow.

Using the ideal molar gas law $p = \mathcal{R}cT$ and substituting the gas mole fraction χ_g by $1 - \chi_v = 1 - p_v/p_t$ the gas flow into the reservoir can be expressed in terms of the partial vapor pressure:

$$\dot{N}_{g,r} = \frac{V_r}{\mathcal{R}T_r} \left(1 - \frac{p_v(T_f)}{p_t} \right) \frac{dp_t}{dt} + \frac{\mathcal{D}A_f}{\mathcal{R}T_r} \frac{dp_v(T_f)}{dz} \quad (5.19)$$

Now the reservoir gas mole number in eqn. (5.17) can be specified more precisely after every time step:

$$N_{g,r} = N_{g,r}^0 + \int_t^{t+\Delta t} \dot{N}_{g,r} dt \quad (5.20)$$

This equation, however, contains the gas mole number which refers to the previous time step. As it is absolutely necessary to know the quantity of gas already present in the reservoir, the gas content history has to be traced to even the beginning of heat pipe operation, that is the start-up.

START-UP

At $t = 0$ the noncondensable gas and some vapor are homogeneously distributed all over the vapor space. The initial total pressure is

$$p_{t,0} = \frac{N_g \mathcal{R}T_0}{A_v L + V_r} + p_v(T_0) \quad (5.21)$$

When heating the evaporator the vapor pressure accommodates to the wall temperature profile $T_p(z)$, and the reservoir gas content, in general, is given by:

$$N_{g,r} = N_g - \frac{A_v}{\mathfrak{R}} \int_0^L \frac{p_t - p_v(T_p)}{T_p} dz \quad (5.22)$$

As N_g is constant, the time derivative of this equation yields:

$$\dot{N}_{g,r} = \frac{A_v}{\mathfrak{R}} \frac{d}{dt} \left[\int_0^L \frac{p_v(T_p) - p_t}{T_p} dz \right] \quad (5.23)$$

This expression for the gas flow into the reservoir is inserted into equation (5.20) to update the reservoir gas content after each time step during start-up. By equating with eqn. (5.19) an equation can be obtained that numerically determines the pressure rise Δp_t during each Δt . During simulation the increasing total pressure is compared to the vapor pressure calculated at the evaporator temperature at that time. As soon as this vapor pressure exceeds the total pressure, the gas is completely expelled from the evaporator and start-up is completed.

NORMAL TRANSIENT OPERATION

As the amount of gas in the reservoir is now known, eqn. (5.20) can be introduced into eqn. (5.17). The calculation continues with the consideration of a flat front position, as after conclusion of the start-up z_{ff} in fact yields a positive value. However, the total pressure during normal transient operation is governed by eqn. (5.8), so that the gas flow into the reservoir, expressed by eqn. (5.19), is now formulated as:

$$\dot{N}_{g,r} = \frac{V_r}{\mathfrak{R}T_r} \left(1 - \frac{p_v(T_f)}{p_t} \right) \frac{dp_v(T_{v,a})}{dT_{v,a}} \frac{dT_{v,a}}{dt} + \frac{\partial A_f}{\mathfrak{R}T_f} \frac{dp_v(T_f)}{dz} \quad (5.24)$$

Finally the original eqn. (5.17) can be substituted by the following extended molar mass balance at the time $t+\Delta t$:

$$N_g = A_v \int_{z_r}^L \frac{p_v(T_{v,a}) - p_v(T_p(z))}{\mathfrak{R}T_p(z)} dz + N_{g,r}^0 + \int_t^{t+\Delta t} \left[\left(1 - \frac{p_v(T_f)}{p_v(T_{v,a})} \right) \frac{V_r}{\mathfrak{R}T_r} \frac{dp_v(T_{v,a})}{dT_{v,a}} \frac{dT_{v,a}}{dt} + \frac{\partial A_f}{\mathfrak{R}T_f} \frac{dp_v(T_f)}{dz} \right] dt \quad (5.25)$$

The third term in this equation is treated numerically by an implicit formulation, and the feed tube temperature, T_f , is averaged by the values at the condenser end and in the reservoir.

Just as in the original vapor space model in section 5.3 the heat balance over the active heat pipe zone, eqn. (5.9), completes the algorithm, and the flat front position and active vapor temperature are determined iteratively in the same manner as described there.

5.5 Main features of the simulation program

After preliminary analyses with incomplete models in sections 5.2 and 5.3 the simulation from now on is directed to the complete geometry of the real object of experimentation, as shown in Fig. 5.17. The heat conduction model for the metallic structure comprises all the parts that can be seen there, except for the reservoirs and feed tubes whose thermal masses and conductivities have been assumed to be zero. Nevertheless the contents of the feed tube and reservoir contribute substantially to the simulated structure as a part of the vapor space model developed in the preceding section.

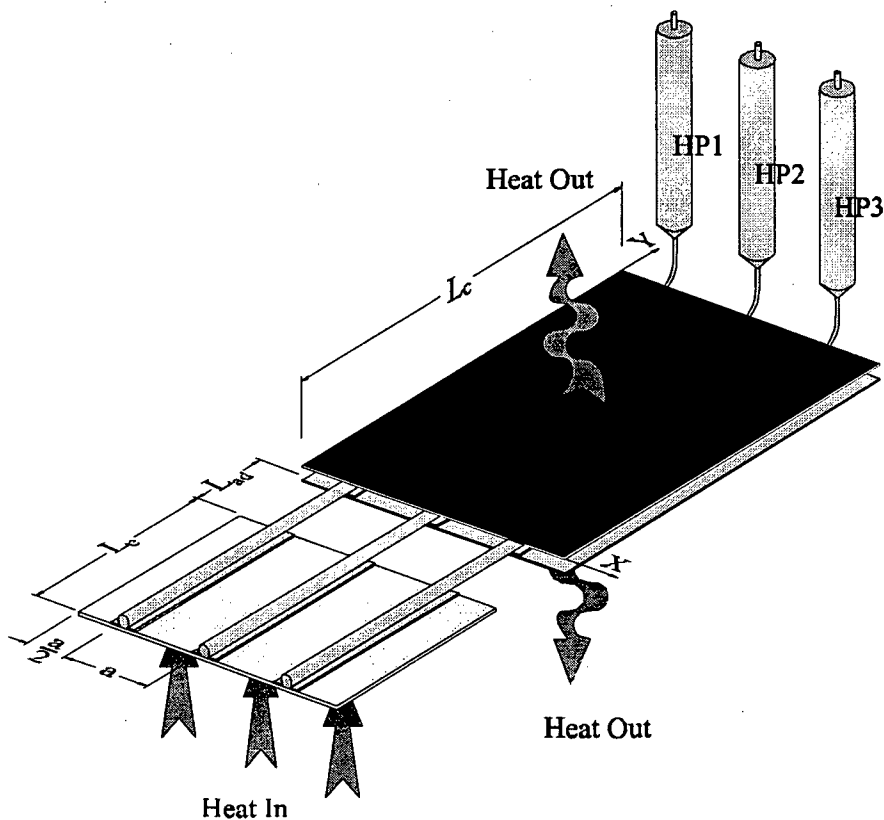


Fig. 5.17 - View of the complete GLHP radiator and its function

A sample case computed for Fig. 5.18 demonstrates clearly, that the new vapor space model is able to represent the evolution of active condenser length and active vapor temperature, better than the rigid formulation in Antoniuk's vapor space model with the two limiting cases due to the reservoir vapor pressure conditions in eqns. (5.17) and (5.18). When using the original model the condenser opens prematurely after about 2 minutes, whereas according to the extended model it takes more than 11 minutes to expel the gas from the evaporator. In the first case the temperature jumps unrestrictedly to a value that corresponds to a flat front position at the beginning of the condenser. In the second case the temperature develops more slowly into the adiabatic zone. Both the active length and active temperature increase to values within the interval defined by the limiting cases of the original model. In the further transient evolution both approach, in a slightly regressive way, the case of a non-wicked reservoir controlled by the vapor pressure at the condenser end.

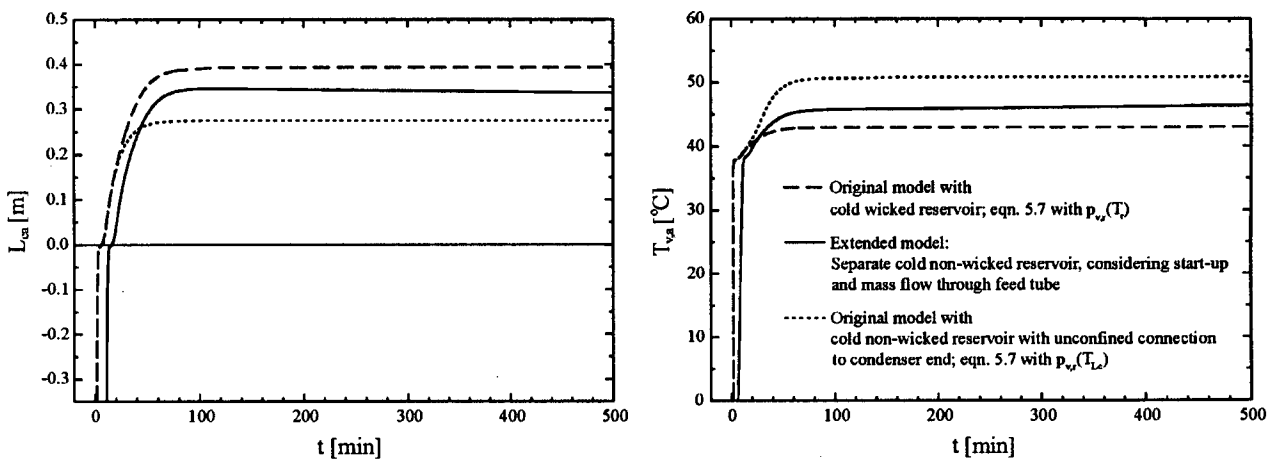


Fig. 5.18 - Comparison of original and extended vapor space models at 34.5 W heat input

As the radiator system presents an asymmetry in the x-y-plane at the heat input side, the previous general consideration of one (lower or upper) half of the system was now dropped. The discretization for the system up to the cooling section became more complex, as additional differently shaped domains had to be treated. These are the base-plate, the evaporator fins, the upper halves of evaporator and adiabatic zone from $y = -L_e - L_{ad}$ to $y = 0$, and the lower adiabatic zone halves from $y = -L_{ad}$ to $y = 0$. Yet the use of one domain for the radiating sheet and one for each condenser fin was maintained, as the symmetry for the cooling section still applies. All six domains were connected by appropriate boundary conditions at the junctions. The boundary conditions are formulated as external heat fluxes to the respective elements, resulting from

temperature gradient and compound thermal resistances between boundary nodes of the involved domains. This heat portion is included in the source term of the discretization equation.

Apart from the heat exchanging surfaces the whole system is supposed to be insulated against the surroundings. The heat fluxes are applied to areas at the lower base-plate surface which correspond to the flat contacted saddle areas, exactly below the positions of the saddles. On the sink side all the heat leaves the radiator by linearized radiation.

The nodal network of the whole system is generated by the program on the basis of 6 input parameters: radiator width, w_R ; the lengths of the heat pipe sections, L_e , L_{ud} and L_c ; the node numbers in x- and y-direction, n_x and n_y . The longitudinal node resolution which is fixed by L_c and n_y is maintained for the negative y-direction. Although the relatively small axial temperature gradients in this region would allow a coarser grid, the uniform axial node density over all the length of the system facilitates the coordinate transformation to the vapor space domain and gives the necessary precision when tracing the evolution of the flat front after completion of start-up. The mesh generation for sheet and base-plate in x-direction presupposes the existence of 3×3 elements with fixed widths at the positions of the heat pipe saddles (Δx_{lat} , Δx_{cen}). The remaining non-contacting area is divided equally according to the given node number n_x . The base-plate has the same width as the radiator and a length equivalent to that of the evaporator.

The simulation starts from the condition that all nodes are at the sink temperature, T_∞ . The flowchart in Fig. 5.19 shows that the computing process is governed by two loops. The outer loop increments the time, until a variable that is activated after initiation of the failure mode, t_{fail} , reaches a certain maximum value. The inner loop is controlled by a general temperature residual. Here all temperatures of all domains in the system converge gradually to values that correspond to the conditions at linearized radiative heat transfer to the surroundings. If any of the temperatures changes by more than 10^{-4} K from one iteration to another, the loop is repeated. This rather tight tolerance was found to be necessary to keep the error of radiated heat output lower than 0.25 % with respect to heat input.

As soon as the required convergence is achieved, the program releases important results into a data output stream during every time step and returns to the beginning of the time loop. Due to the very long transients of the involved diffusive mass transport process, at least double precision processing is required in order to keep the deviation of the results due to rounding errors small. An additional measure is the adaptation of the time step to the variation of the active condenser lengths.

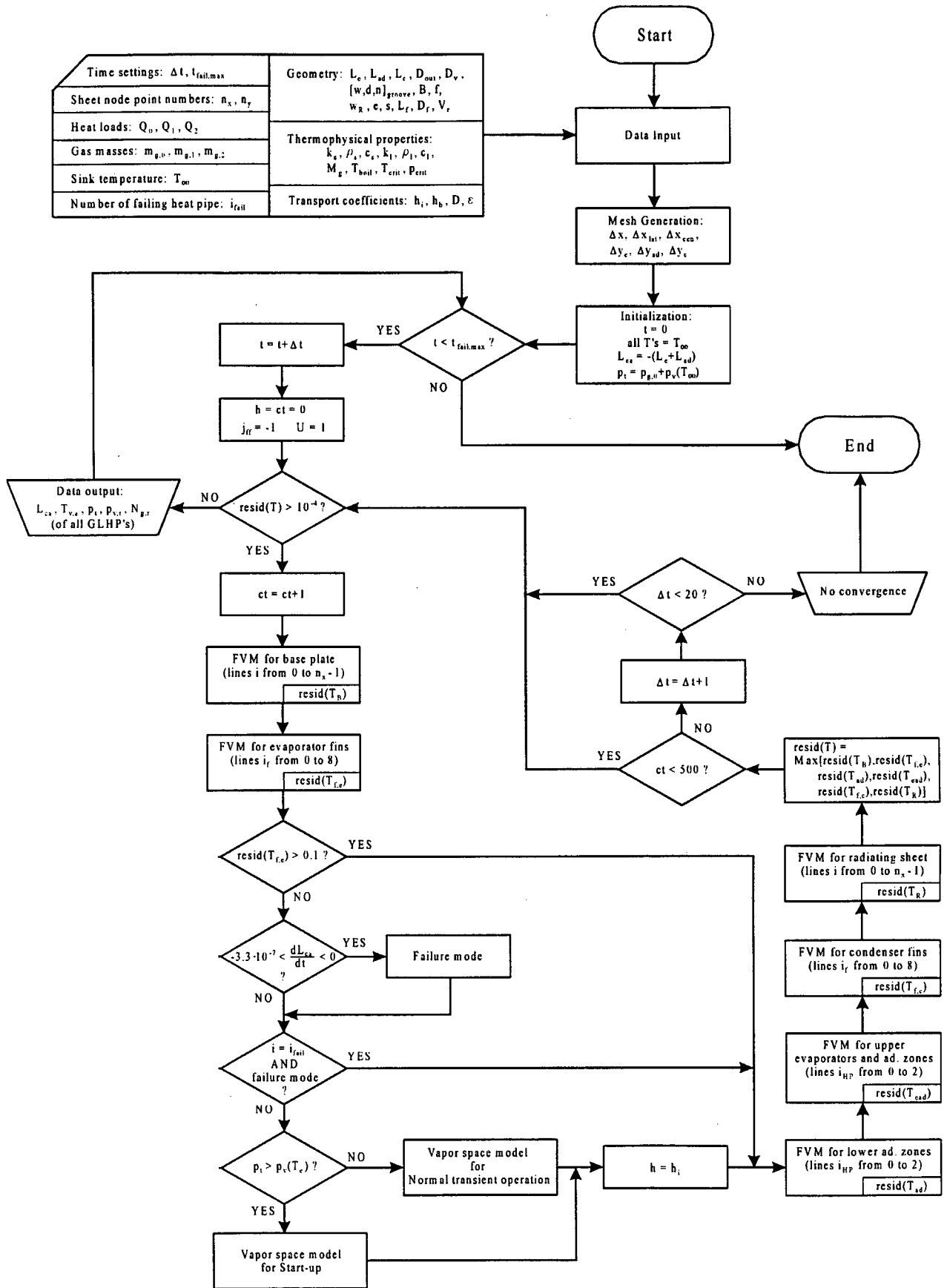


Fig. 5.19 - Simulation program flowchart

Before entering the inner or temperature iteration loop the number of the element that lodges the flat front, j_{ff} , is set to -1 , as in the computer program the first element of any domain is indexed with zero. Further the variable h that is reserved for the value of the internal heat transfer coefficient, h_i , is set to zero. In doing so the evaporator wall nodes are decoupled from the vapor space during the first iterations, as sometimes in consequence of a vehement heat flux change at the wall elements the difference to the vapor space temperature is so large that the program becomes unstable. Thus the program waits for the evaporator wall residual, $resid(T_{f,e})$, to become sufficiently low, before the vapor space is coupled to the metallic structure of the system by h . Furthermore h is held zero in case of an activated failure mode, when the numerical algorithm is about to compute the temperatures that belong to the failed heat pipe. As in the model the phase change heat transfer through the heat pipe is expressed by the internal heat transfer coefficient, a zero coefficient eliminates this crucial transfer mode and converts the affected heat pipe into a simple wall conductor.

Inside the temperature iteration loop the six domains are processed successively by proper finite volume model (FVM) subroutines according to the direction of the heat flow, that is from the bottom to the top and in positive y-direction. When the turn of the vapor space comes, a condition is verified that separates the situation, where the gas is distributed among vapor all over the heat pipe, from the situation, where an active pure vapor zone can be distinguished according to an established flat vapor/gas front ($p_t > p_v(T_e)$?). The transition from the first situation to the second marks the completion of start-up, but the transition is also possible in the contrary sense, when the heat load becomes so low that the front finally dissolves. This latter case actually occurred in radiator test run A (section 7.5). For the completion of start-up it is sufficient that just the **first** evaporator element reaches a temperature that induces the vapor pressure to become higher than the total pressure. When this happens, the program immediately renders a theoretical flat front situated behind at least one fifth of the evaporator length.

During start-up the total pressure has to be evaluated iteratively from an implicit definition that results from equating eqn. (5.23) with eqn. (5.19). This definition which is fully implicit with respect to the values of the new time value has the following form:

$$p_t - p_t^0 + \frac{A_v \Delta z \left[p_t \left(\sum_{j=0}^{n_{y,e}-1} \frac{1}{T_{pj}} - \sum_{j=0}^{n_{y,e}-1} \frac{1}{T_{pj}^0} \right) - \sum_{j=0}^{n_{y,e}-1} \frac{p_v(T_{pj})}{T_{pj}} + \sum_{j=0}^{n_{y,e}-1} \frac{p_v(T_{pj}^0)}{T_{pj}^0} \right] + \frac{\partial A_f}{\bar{T}_f} \frac{p_v(T_{L_f}) - p_v(T_{f,0})}{L_f} \Delta t}{\frac{V_r}{T_r} \left(1 - \frac{p_v(\bar{T}_f)}{p_t} \right) + A_v \Delta z \sum_{j=0}^{n_{y,e}-1} \frac{1}{T_{pj}}} = 0$$

During execution of each of the vapor space model subroutines an updated temporary node string for the adjacent wall temperatures is created that comprises the whole heat pipe length L . The values that contribute to this profile are the temperatures of the one-dimensional evaporator and adiabatic zone domains, and those of the central elements of evaporator and condenser fins. In the evaporator and adiabatic region, where the structure is divided in lower and upper halves, a corresponding mean temperature value is taken. As the internal heat transfer coefficient is assumed spatially constant, the vapor space subroutines that appeal to the energy balance according to eqn. (5.9) do not require a value for h . So its definition is made afterwards ($h = h_i$).

The time that the system passes to reach steady state is dependent on the set of input parameters. A particular influence was noted with respect to heat load, gas inventory and slitted or non-slitted configuration. The steady-state criterion was chosen to determine the starting point of the failure mode. This occurs when all active lengths do not change more than $3.3 \cdot 10^{-7}$ m per second.

In some cases, when the heat pipes were about to complete start-up, and also when active lengths came close to the condenser end, a pre-established time step of $\Delta t = 3$ s did not lead to the convergence postulated by $resid(T)$. In this case the program was scheduled for a time step augmentation. If the iteration counter registers a value higher than 500, the iteration process is restarted with a time step $\Delta t+1$. For the calculation of the current temperature values of all domains, however, the values of the previous time step are maintained. As observed, generally an increase to a time step of 5 s at the most was sufficient to conclude the iteration process successfully.

When the simulation was performed for the radiator in slitted configuration, the transverse borders of the sheet strips were treated, as if they were common sheet borders. This means that they were numerically isolated from each other by imposing a zero temperature gradient at the respective border elements. The same was done with the lateral condenser fin elements to impede axial heat conduction also at this location.

5.6 Parametric study of a simulated transient failure behavior

The following study intends to provide an insight into the vapor/gas front dynamics of a uniformly charged radiator after malfunction of one of the GLHP's. At the same time the influences of different heat loads, gas inventories, working fluids, feed tube diameters and the effect of radiator slitting on the transient response of the system are investigated. The modeling

conditions are somewhat simplified with respect to the heat and mass transport coefficients, as they are taken to be constant. For the internal film heat transfer coefficient, h_i , a value of $4000 \text{ W/m}^2\text{K}$ has been adopted, as this value is often used in heat pipe literature [38]. The coefficient of the saddle-to-plate junctions was estimated to be $3000 \text{ W/m}^2\text{K}$, in comparison to $4500 \text{ W/m}^2\text{K}$ of a similar joint configuration that was experimentally evaluated with 95 percent-by-weight silver Eccobond 56C as thermal glue [28]. The binary diffusion coefficient of the vapor-gas mixture was also given a constant value, determined from eqn. (6.22) for a mean feed tube temperature of $0 \text{ }^\circ\text{C}$ and a pressure that corresponds to vapor at $55 \text{ }^\circ\text{C}$. Moreover the reservoir temperature is held constant at the sink temperature of $-50 \text{ }^\circ\text{C}$.

The failure mode is activated by switching off the vapor space domain of one of the GLHP's. Before doing so the system is charged by equal heat loads applied at each of the evaporator positions on the base-plate. It runs through the start-up and normal transient operation until reaching steady-state. Because of the long and narrow feed tube connection to the reservoir the preparation of the system for the failure mode takes a long time (more than 18 hours), especially when the heat load is dimensioned in such a way that the condenser opens more than 80 % of its heat transfer area. The active condenser lengths change slowly with gradually decreasing rates for quite a while due to diffusive adjustments. The closer the maximum value of the active length has approached the condenser end, the more time it takes to reach a steady state.

In the failure mode symmetric and asymmetric sudden overcharges are simulated. In the first case one outside heat pipe ceases operation, and in the other case the middle heat pipe is affected. After the heat pipe failure the system is overcharged, as the heat loads from the preceding operation mode are maintained. Consequently the neighboring heat pipes have to take over virtually the full heat load of the failed one.

The parametric studies are directed to one radiator size with a heat pipe spacing of 10 cm. The analyses in sections 5.2 and 5.3 showed that in this medium-sized radiator heat pipe interactions turned out to be significant. The geometry and property data are the same as those presented in Table 3. The new element that completed the system, the base-plate, is projected to be of a rather less conductive aluminium alloy with a thermal conductivity of 137 W/mK , yet is four times as thick as the radiating sheet. According to preliminary simulation runs the adiabatic zone was determined to be 10 cm long. This length was found to be sufficient to overcome the temperature difference between upper and lower adiabatic zone domains at the border to the cooling section due to one-sided heat input at the evaporator.

One case of a slitted radiator is treated, where as before the radiating sheet is cut into 10 strips of 5 cm transverse to the heat pipe axes. In one case a gas mass overload has been simulated increasing the gas inventory by 20 %. This case really appeared without intention when preparing radiator test run C due to unexpected difficulties during heat pipe filling. In another case methanol instead of acetone was chosen as the working fluid in match with its appropriate noncondensable gas partner nitrogen. The nitrogen inventory was determined using eqn. (6.31) in such a way that the same evaporator temperature control performance as with the acetone/argon combination was assured. In order to ease the diffusion process through the feed tube one case is simulated with a tube diameter three times larger than the standard one.

The results of the simulation runs are presented in a compact form in the Figs. 5.20 through 5.26. The standard case to which all the parameter variations are compared is the following:

- Heat input per heat pipe: 38 W
- Gas inventory: 200 mg
- Internal feed tube diameter: 2 mm
- Acetone/argon filling
- Radiating sheets non-slitted

Deviations from this case are explicitly mentioned in the diagrams. Figs. 5.20 to 5.25 depict the behavior of the active condenser lengths for both kinds of failure, that is the failure of an outside heat pipe (1st HP failed) and the failure of the middle heat pipe (2nd HP failed). Fig. 5.26 gives a survey of the active zone vapor temperatures of the heat pipes that remain in operation for all cases in study. However, the graphical representation is reduced to the case of an outside heat pipe failure, because the temperature profiles for the other failure case appeared to be slightly lower (~ 0.5 K) than the profiles of the third heat pipe and for the slitted radiator 1.7 K below it.

In all cases an initial drawback of the vapor/gas front of more than half a centimeter can be noted inside the near heat pipe within the first 2 minutes. After this there is a fast increase of the active lengths caused primarily by heat conduction from the overheated zone below the evaporator of the failed heat pipe. Obviously the near neighbor shows the fastest front movement, about 0.08 mm/s for 38 W in the Figs. 5.20 and 5.23. The distant heat pipe has a front progression velocity about 30 % lower. The radiator in the slitted configuration shows a faster response to overload: The front in the immediate neighbor advances with a velocity of 0.12 mm/s. Also the case of heat pipes with gas overcharge shows a rather sensitive reaction to the overload. As in

the slitted case the distant heat pipe reaches the overload condition by touching the condenser end. It becomes obvious that the failure of an outside heat pipe always is the far more critical one, as even the distant heat pipe reacts more intensely than both heat pipes in case of the middle heat pipe failure, where overload can be dampened better, because it is distributed more uniformly. An exception to this can be seen for the slitted radiator. Here it does not depend which heat pipe fails, the close neighbor reacts with the same front velocity in both failure cases.

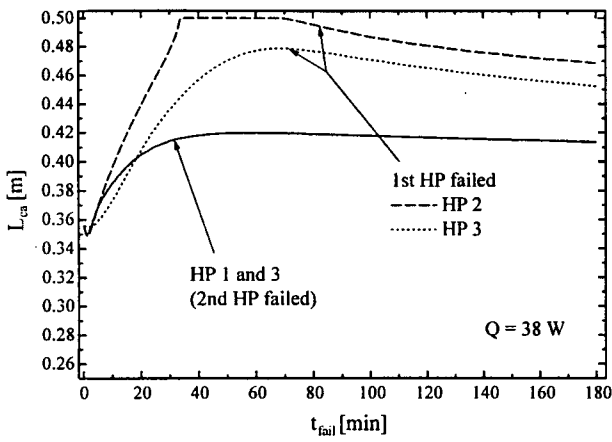


Fig. 5.20 - Front behavior, standard case (t_{ss} at $t_{fail,0}$: 32.1 h)

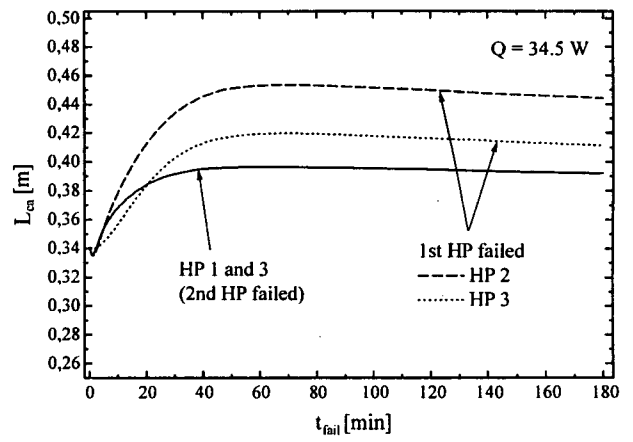


Fig. 5.21 - Front behavior, variation: lower heat input (t_{ss} at $t_{fail,0}$: 5.1 h)

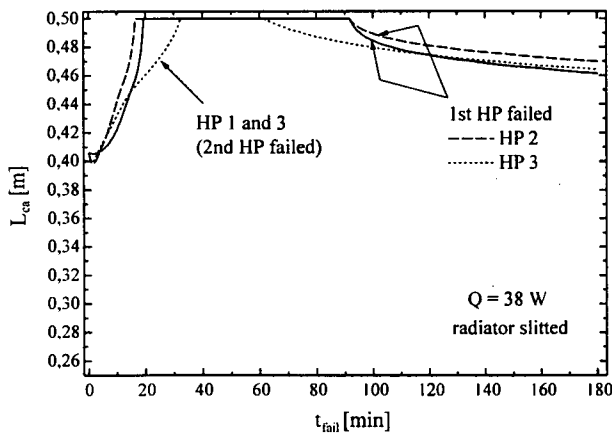


Fig. 5.22 - Front behavior, variation: slitted radiator (t_{ss} at $t_{fail,0}$: 18.5 h)

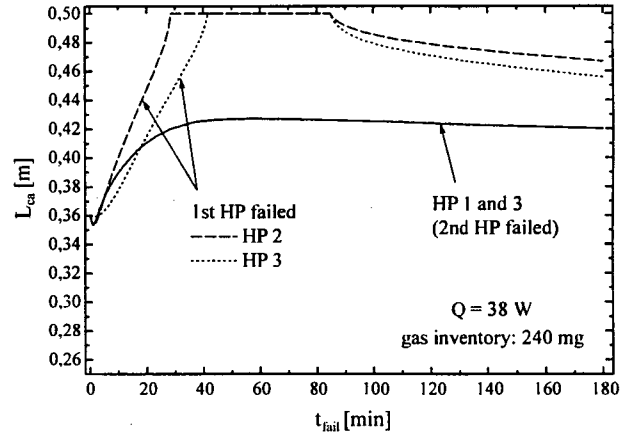


Fig. 5.23 - Front behavior, variation: higher gas inventory (t_{ss} at $t_{fail,0}$: 6.2 h)

In general all active lengths present a retreat after reaching their maximum extension. The smaller this value is, the less the front moves back. A similar back flow behavior of the front appears during the phase that leads to steady-state, not shown in the diagrams, though indicated by the times t_{ss} until initiation of the failure mode at $t_{fail,0}$. If the front touches the condenser end quickly, the rebound is also intense accompanied by a stronger increase of vapor temperature.

The back flow effect can be explained by the vapor flow into the reservoir which enhances the volume of the noncondensable gas buffer, and to some extent by neighbor heating across the radiating sheet, when a large part of the condenser length is open. During the movement of the fronts the total pressure increase rate of the whole GLHP is superior to the vapor pressure increase in the reservoir. When the front reaches the entrance of the reservoir, these rates become equal; and when the front moves back, the situation is inverted: The rate of increase of the vapor pressure is higher than that of the total pressure. The system responds with a delay due to the barring feed tube. If the diffusion barrier is diminished because of a larger feed tube diameter (Fig. 5.25), the vapor pressure equilibrates faster, the reaction is immediate, and the GLHP shows the features of the well connected non-wicked reservoir according to the lowest active length curve in Fig. 5.18 with the highest vapor temperature evolution in Figs. 5.18 and 5.26.

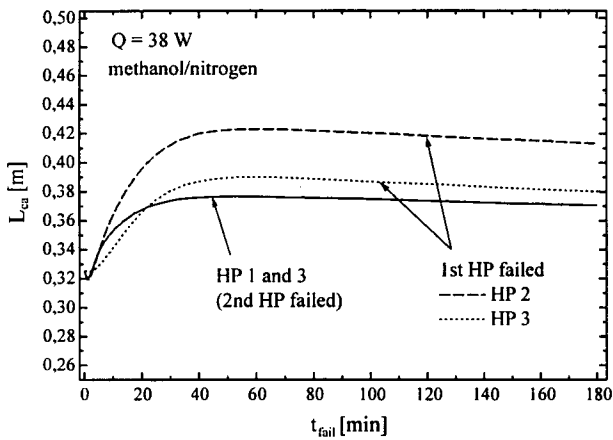


Fig. 5.24 - Front behavior, variation: methanol as working fluid (t_{ss} at $t_{fail,0}$: 28 h)

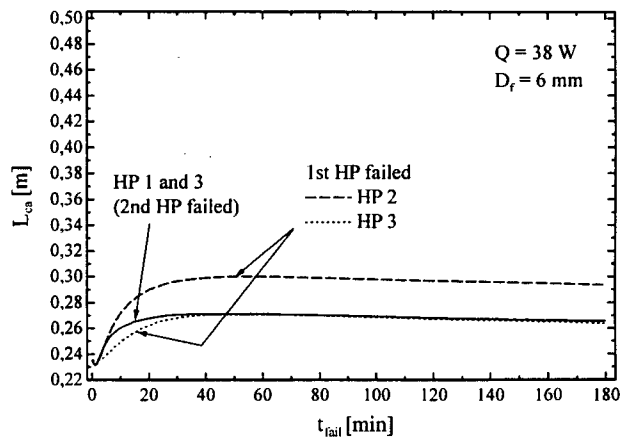


Fig. 5.25 - Front behavior, variation: large feed tube diameter (t_{ss} at $t_{fail,0}$: 26.9 h)

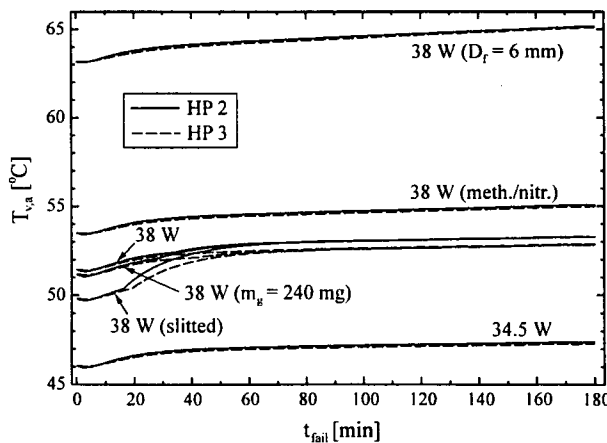


Fig. 5.26 - Active zone temperature behavior for all variations (Failure mode: 1st HP failed)

The most sensible case in investigation appears to be the slitted radiator. Already during the preceding phase ($t < t_{\text{fail},0}$) the active lengths are longer than for the entire radiator. During the failure mode the heat distribution to the neighbors is more intense, and the heat cannot be dispersed as easily over the radiating sheets, because each condenser section is bound to its isolated cooling sheet strip. The methanol filled GLHP evidently sustains higher heat loads without being overcharged, but at the cost of a higher evaporator temperature.

In a former similar numerical study [39] the heat transfer coefficients h_i and h_b were assumed with values more than twice as large as the present ones. The aim was to carry the heat flux information faster to the heat sink and to accelerate the transients during the simulations. In fact the steady-state condition was reached more quickly, but the main feature is that higher heat fluxes could be accommodated in a radiator of the same size. Due to the lower all-over heat resistance the heat flux could be brought to the heat sink with a much lower temperature drop. Thus more heat could be dumped to the sink because of a better radiative cooling efficiency. These findings show the importance of a good thermal contact between radiator components and also of an improved film coefficient in order to increase the heat transfer capacity of the radiator system. On the other hand the system appeared more sensible to overload due to failure, as the front velocities in general showed a higher value as in the present case.

Hitherto simulations with simplified input parameters have confirmed that a 3-GLHP radiator with a width of 30 cm is appropriate to withdraw 3×40 W from the base-plate, even in case of a heat pipe failure. Of course the model that treats the device as a closed thermodynamic system can not predict, if the physical conditions in the process space are given to actually transfer the desired heat load. As probable level and range of operating temperature are known from modeling, the following steps of GLHP design will demonstrate the verification of material, components and shaping of the heat pipe to be able to manufacture the real system. Inherent heat pipe operating limits are checked against a required heat throughput capability of **60 W**, as this is the heat load that a heat pipe has to withstand at least, when a neighbor heat pipe fails.

Encouraged by documented successful long time radiator tests with axially grooved GLHP's [27] this light and simple alternative was also employed in the present case. The grooves are formed by extrusion of aluminum. The resulting profiles are very common for conventional heat pipes and are offered in commercial catalogs in various shapes and sizes for various heat transfer capacities. Axially grooved pipes have the advantage that the capillary structure is already formed by the interior surface itself, so that wick forming and insertion is superfluous. To some extent this kind of wick design is also benign concerning vapor bubble formation at high heat flux densities. Bubbles are not constricted inside the grooves, and can easily escape to the vapor space, as they do not encounter obstacles.

6.1 Selection of the working fluid

To be appropriate as a heat transfer agent in a GLHP the working fluid has to be judged by the same criteria that apply to conventional fixed conductance heat pipes. In addition the following items have to be taken into account: a good temperature controllability in view of the thermal behavior of the surroundings [25, 40] and low susceptibility to vapor bubble formation in the evaporator.

Thus the following general requirements apply:

1. Compatibility with heat pipe container and wick material;

2. High latent heat of evaporation, low viscosity of the fluid in its liquid and vapor state and high surface tension, altogether combined in a characteristic number called “Merit Number”;
3. High thermal conductivity;
4. Low freezing point.

Additionally GLHP’s in particular demand for:

5. Low operating pressure, but large pressure variation with temperature $dp/dT_{v,a}$;
6. Minimum sensibility to ambient temperature variations;
7. High superheat capacity before reaching initiation of bubble boiling.

In the following three of the most common working fluids for space applications – **Ammonia**, **Acetone** and **Methanol** – are checked with respect to the aforementioned criteria. For the thermophysical properties, as referred to in the second, third and last item, a reference temperature of 50 °C is presupposed.

1. COMPATIBILITY WITH CONTAINER AND WICK MATERIAL

If the working fluid reacts chemically or physically with the heat pipe or wick material, solid particles or gases can be generated. The particles are carried to the evaporator, where they block parts of the capillary structure and cause superheated zones (hot spots). The gases accumulate in the condenser and to some extent block the condensing heat transfer.

Ammonia presents long-time compatibility with aluminum heat pipes, which was certified by abundant flight experience. Yet some investigators [41, 42] point out that the wick material should have the same composition as that of the container. In various tests with periods of up to 2 years acetone was found to be compatible with aluminum [40]. Methanol in combination with aluminum is not recommended by literature; it matches well with stainless steel.

2. MERIT NUMBER

A high heat of evaporation, h_{lv} , favors an intensive heat transport with only a small quantity of working fluid, and therefore the pressure drop inside the heat pipe remains small. Low viscosities, μ_l and μ_v , reduce the flow resistance of the working fluid, and a high surface tension, σ , results in a high capillary pumping capacity for liquid transport.

A convenient number to classify the combination of these properties is the merit number, defined as $\sigma h_{lv} \rho_l / \mu_l$. It should be as high as possible.

	Ammonia	Acetone	Methanol
Merit number [kW/cm ²]	8024	4134	4700

3. THERMAL CONDUCTIVITY

The liquid thermal conductivity should be high, so that the radial temperature gradient across the wick becomes small and the probability of bubble formation between wall and wick remains negligible.

	Ammonia	Acetone	Methanol
Thermal conductivity [W/mK]	0.424	0.173	0.203

4. FREEZING POINT

The freezing point of the working fluid should be as low as possible, so that the liquid does not freeze out in the condenser, when the temperature of the surroundings falls excessively. If this happens, the heat pipe ceases to function.

	Ammonia	Acetone	Methanol
Freezing point [°C]	-78	-95	-98

5. VAPOR PRESSURE BEHAVIOR WITHIN THE RANGE OF OPERATION

The vapor pressure which actually is the saturation pressure at the corresponding operating temperature should be relatively low in order to permit a small thickness of the container wall and to avoid creeping of the wall material due to long-term thermal and mechanical load. The pressure response towards temperature changes, on the other hand, should be large (high dp/dT) in order to provide a good sensitivity of the GLHP to small variations of evaporator temperature. Fig. 6.1 shows the behavior of the saturation pressure curves of the three mentioned working fluids. The curves were computed from the semi-analytical expression by Riedel, Plank and Miller [43]:

$$\log \frac{P_{sat}}{P_c} = -\frac{G}{T/T_c} \left[1 - \left(\frac{T}{T_c} \right)^2 + g \left(1 - \frac{T}{T_c} \right)^3 \left(3 + \frac{T}{T_c} \right) \right] \quad (6.1)$$

where $G = 0.21 + 0.4605 \frac{T_b}{T_c - T_b} \cdot \log \frac{p_c}{p_{atm}}$ and $g = \frac{\frac{T_b}{G(T_c - T_b)} \cdot \log \frac{p_c}{p_{atm}} - \left(1 + \frac{T_b}{T_c}\right)}{\left(1 - \frac{T_b}{T_c}\right)^2 \left(3 + \frac{T_b}{T_c}\right)}$

$T_b \rightarrow$ Temperature of ebullition [K], $T_c \rightarrow$ Critical temperature [K],
 $p_c \rightarrow$ Critical pressure [bar]

6. SENSITIVITY TO AMBIENT TEMPERATURE VARIATIONS

A working fluid, whose vapor pressure at the temperature of the inactive GLHP section, $p_{v,\infty}$, is small compared to the vapor pressure at evaporator temperature, $p_{v,e}$, is less sensitive to variations of the thermal environment. Fig. 6.2 shows the variation of the ratio $p_{v,\infty}/p_{v,e}$ as a function of T_∞ for the three fluids at a temperature of 40 °C. Although for all fluids $p_{v,e}$ is negligible at low temperatures (< 70 °C, in shadow conditions), the differences of $p_{v,\infty}/p_{v,e}$ become considerable, when the heat pipe works under insolation.

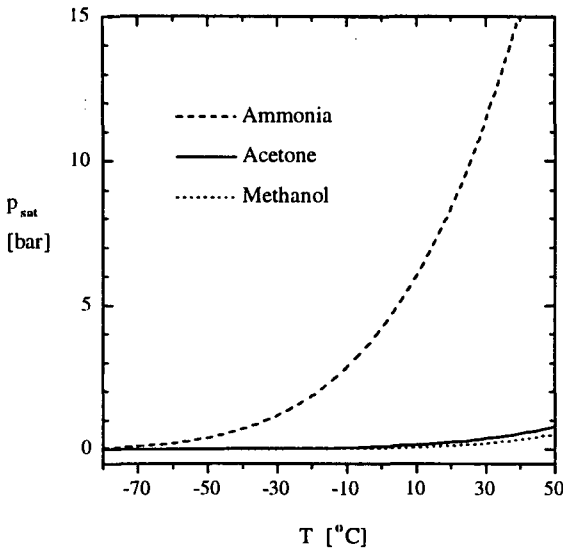


Fig. 6.1 - Vapor saturation pressure for 3 common heat pipe fluids

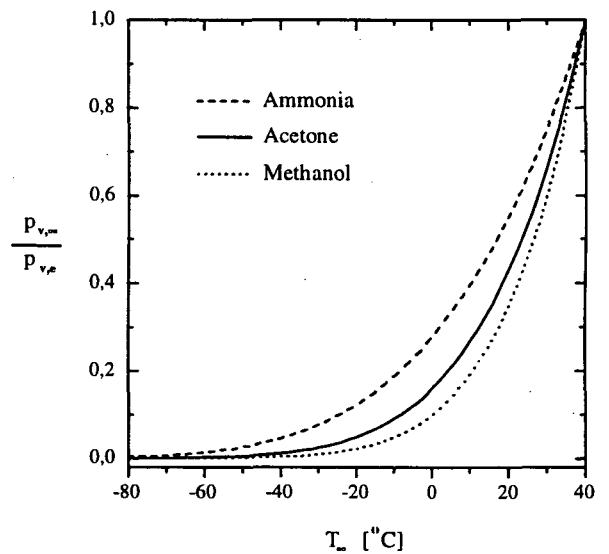


Fig. 6.2 - Sink to evaporator temperature vapor pressure ratio for 3 common heat pipe fluids

7. LIQUID SUPERHEAT NECESSARY FOR BUBBLE FORMATION

In the case of heat fluxes that are close to the designed maximum heat pipe capacity the liquid boundary layer next to the evaporator wall can reach a temperature so much higher than the

temperature of the saturated vapor, that ebullition germs are generated there. The difference between these temperatures, called superheat, depends on the wall surface conditions and is further affected by any noncondensable gas dissolved in the liquid. Since in GLHP's the gas is always in contact with liquid in the inactive condenser section, a small quantity may be dissolved and transported to the evaporator, where it can increase the nucleation radius of the bubble, r_n . To avoid premature ebullition the superheat ΔT_{sup} for a certain liquid should be as high as possible.

Acetone and methanol now shall be contrasted directly with ammonia by defining a relative superheat with respect to that of ammonia $\Delta T_{sup} / \Delta T_{sup,Am}$. If a spherical vapor bubble is in equilibrium with the liquid phase, the following Young-Laplace equation holds:

$$\Delta p = p_v - p_l = \frac{2\sigma}{r_n} \quad (6.2)$$

The approximation $\Delta p = (dp/dT) \cdot \Delta T$ brings eqn. (6.2) to the following form

$$\Delta T = \frac{2\sigma/r_n}{(dp/dT)} \quad (6.3)$$

so that the relative superheat can finally be obtained as

$$\frac{\Delta T_{sup}}{\Delta T_{sup,Am}} = \frac{\sigma}{\sigma_{Am}} \cdot \frac{(dp/dT)_{Am}}{(dp/dT)} \quad (6.4)$$

After performing derivation (dp/dT) of eqn. (6.1) the following values are calculated

	Acetone	Methanol
Superheat relative to ammonia	23.6	28.6

This shows very clearly the immense precautions that have to be taken, if ammonia that actually is a very powerful heat transfer agent is chosen as the working fluid. Due to the low allowable superheat the inner evaporating surface has to be very smooth and clean, and the heat flux has to be distributed over a sufficiently large area (low heat density \rightarrow long evaporators), so that the boiling limit will not be reached prematurely.

For the present GLHP acetone was chosen as the working fluid because of a low freezing point and the low sensitivity to the sink temperature. Furthermore acetone is very easy to handle when preparing experiments in laboratory, as it does not require special devices during the filling process. Methanol proves to be more attractive with respect to some items, but had to be disqualified because of the dubious compatibility with aluminum.

6.2 Selection of heat pipe dimensions and wick

The ducts for vapor and liquid in a heat pipe must be shaped and dimensioned in such a way that the pipe is able to transport the desired heat flux by means of the chosen working fluid. Regarding this task the following items are of fundamental importance: the cross section A_v of the void available for the vapor flow, the liquid flow cross section in the capillary structure and the heat pipe length.

If the maximum heat flux to be transported is prescribed, the dimensions are found in an iterative process, where commercially available pipe profiles with various void diameters, D_v , and groove geometries and various pipe lengths are examined for certain operational limits.

These limits establish a maximum heat transfer capacity that the respective heat pipe can achieve under certain operation conditions. For heat pipes that work at **moderate temperatures** (-150 up to 350 °C) the following limits apply [20]:

- Capillary limit
- Entrainment limit
- Boiling limit
- Frozen start-up limit

Capillary limit: This limit characterizes the maximum capillary pumping capacity of the wick, that enables the circulation of the working fluid inside the heat pipe, for a given combination of wick and fluid.

Entrainment limit: When the vapor velocity gets rather high, the vapor tears off droplets of liquid from the wick and carries them to the condenser. This phenomenon hinders the return flow of the liquid and finally leads to dry-out in the evaporator.

Boiling limit: If the heat flux density at the evaporator is too high, ebullition germs are formed in the wick or at the pipe wall. If the bubbles do not detach from the place of formation and further coalesce with others, they impede wetting of the evaporator surface and also reduce or even annihilate the capillary force.

Frozen start-up limit: During start-up with frozen working fluid the vapor that is released from the evaporator can freeze out in condenser and adiabatic zone. This causes depletion of fluid in the evaporator.

In the following the aforementioned operation limits are verified with respect to the present acetone/aluminum heat pipe and the prescribed heat flux. Fig. 6.3 shows dimensions and geometry of the heat pipe cross section. Evaporator, adiabatic zone and condenser have lengths of **25 cm**, **10 cm** and **50 cm** respectively.

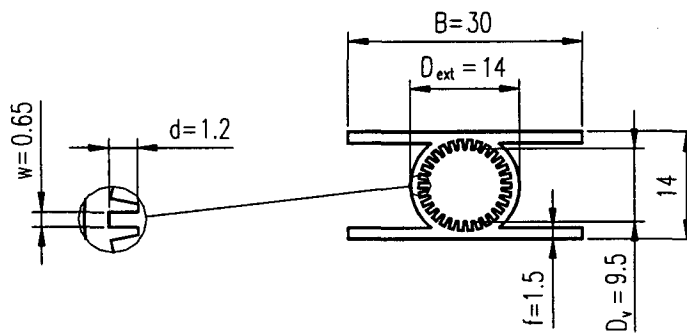


Fig. 6.3 Dimensions of the selected heat pipe profile (true to scale)

Relevant thermophysical properties of acetone at 50 °C [20] are the following:

Latent heat of evaporation	$h_{lv} = 527 \text{ kJ/kg}$
Liquid density	$\rho_l = 755 \text{ kg/m}^3$
Vapor density	$\rho_v = 1.67 \text{ kg/m}^3$
Liquid thermal conductivity	$k_l = 0.173 \text{ W/mK}$
Liquid specific heat	$c_l = 2250 \text{ J/kgK}$
Liquid viscosity	$\mu_l = 2.48 \cdot 10^{-4} \text{ Pa}\cdot\text{s}$
Vapor viscosity	$\mu_v = 8.8 \cdot 10^{-6} \text{ Pa}\cdot\text{s}$
Surface tension	$\sigma = 0.02 \text{ N/m}$

Material data of the aluminum alloy (AlMgSi0.5) that is used for the heat pipe container are: $k_s = 163 \text{ W/mK}$, $c_s = 900 \text{ J/kgK}$, $\rho_s = 2700 \text{ kg/m}^3$ [44].

In order to provide a liquid return flow to the evaporator, the capillary pressure, Δp_{cap} , generated by the evaporator wick, has to compensate for the total pressure loss in the evaporation-condensation cycle. The loss is due to friction of vapor and liquid flow, Δp_v and Δp_l . A pressure loss due to gravity effects, Δp_{grav} , appears in the case of an inclined heat pipe, with the evaporator elevated over the condenser. As in the present case the heat pipes will be horizontally aligned, the last item need not to be considered here.

The *capillary limit* thus is expressed as

$$\Delta p_{cap} \geq \Delta p_v + \Delta p_l \quad (6.5)$$

The maximum capillary pressure created by a groove with rectangular cross section is determined as follows:

$$\Delta p_{cap} = \frac{2\sigma}{w} = \frac{2 \cdot 0.02}{0.00065} = 61.5 \text{ [Pa]} \quad (6.6)$$

For a laminar and incompressible flow inside the pipe the Hagen-Poiseuille relation applies for the vapor pressure drop:

$$\Delta p_v = \frac{8\mu_v L_{ef} Q}{r_{h,v}^2 A_v \rho_v h_{lv}} \quad (6.7)$$

Vapor flow compressibility effects are negligible, as the Mach number is very much smaller than 0.3. The flow further can be considered laminar, as its pipe diameter related Reynolds number is smaller than 2300, a value commonly mentioned as being characteristic for the beginning of the laminar-to-turbulent transition.

$$\begin{aligned} \text{Ma} &= \frac{v_v}{\sqrt{\kappa R_v T_e}} = \frac{\dot{m}}{A_v \rho_v \sqrt{\kappa R_v T_e}} = \frac{Q}{A_v \rho_v h_{lv} \sqrt{\kappa R_v T_e}} \\ &= \frac{60}{7.088 \cdot 10^{-5} \cdot 1.67 \cdot 527000 \cdot \sqrt{1.33 \cdot 143.1 \cdot 323}} = 0.004 \end{aligned} \quad (6.8)$$

$$\text{Re}_v = \frac{\rho_v v_v D_v}{\mu_v} = \frac{4Q}{\pi \mu_v h_{lv} D_v} = \frac{4 \cdot 60}{\pi \cdot 8.8 \cdot 10^{-6} \cdot 527000 \cdot 0.0095} = 1734 \quad (6.9)$$

The effective length in eqn. (6.7), defined as

$$L_{ef} = 0.5 \cdot L_e + L_{ad} + 0.5 \cdot L_c \quad (6.10)$$

means the average distance that the vapor molecules overcome on their way from evaporator to condenser *. It is assumed in this case that both the evaporation rate and the condensation rate are uniform in axial direction.

Subsequently the vapor pressure drop amounts to

$$\Delta p_v = \frac{8 \cdot 8.8 \cdot 10^{-6} \cdot 0.475 \cdot Q}{0.00475^2 \cdot 7.088 \cdot 10^{-5} \cdot 1.67 \cdot 527000} = 0.0238 \cdot Q$$

The liquid pressure is obtained from the expression

$$\Delta p_l = \frac{\mu_l L_{ef} Q}{K A_w h_{lv} \rho_l} \quad (6.11)$$

where the permeability K for the liquid in open axial grooves [20] is determined by

$$K = \frac{2\varphi r_{h,l}^2}{f Re_l} \quad (6.12)$$

with φ being the groove width-to-pitch ratio, $r_{h,l}$ the hydraulic radius and $f \cdot Re_l$ a hydrodynamic parameter, given by

$$\varphi = \frac{w}{S} \quad (6.13)$$

$$r_{h,l} = \frac{2dw}{2d + w} \quad (6.14)$$

$$f Re_l = 24 \left(1 - 1.3553 \frac{w}{d} + 1.9467 \left(\frac{w}{d} \right)^2 - 1.7012 \left(\frac{w}{d} \right)^3 + 0.9564 \left(\frac{w}{d} \right)^4 - 0.2537 \left(\frac{w}{d} \right)^5 \right) \quad (6.15)$$

Evaluating $\varphi = \frac{0.00065}{\pi \cdot 0.0095/30} = 0.6534$, $r_{h,l} = \frac{2 \cdot 0.0012 \cdot 0.00065}{2 \cdot 0.0012 + 0.00065} = 5.11 \cdot 10^{-4}$ [m],

$$f Re_l = 15.3, \quad K = \frac{2 \cdot 0.6534 \cdot (5.11 \cdot 10^{-4})^2}{15.3} = 2.23 \cdot 10^{-8} \text{ [m}^2\text{]}$$

* For calculation it is assumed here that the noncondensable gas has completely retreated into the reservoir, so that the whole condenser length is open and takes part in the liquid transport.

$$\text{and } A_w = 30 \cdot 0.00065 \cdot 0.0012 = 2.34 \cdot 10^{-5} \text{ [m]}$$

the liquid pressure drop has the value of

$$\Delta p_l = \frac{2.48 \cdot 10^{-4} \cdot 0.475 \cdot Q}{2.23 \cdot 10^{-8} \cdot 2.34 \cdot 10^{-5} \cdot 527000 \cdot 755} = 0.5674 \cdot Q$$

Inserting the values for Δp_{cap} , Δp_v and Δp_l into eqn. (6.5) the conditional equation yields

$$61.5 \geq 0.0238 \cdot Q + 0.5674 \cdot Q$$

and the **capillary limit** turns out to be

$$Q = 104 \text{ W}$$

As the Reynolds number of 1734 is considerably large, the vapor that flushes through the adiabatic zone with a corresponding velocity of 0.96 m/s, may disturb the liquid flow at the interface. Therefore it is advisable to check for the maximum heat flux that can be transported by the vapor without liquid entrainment:

$$Q = A_v h_{lv} \sqrt{\frac{\sigma \rho_v}{2r_{h,l}}} \quad (6.16)$$

With the value already determined for the hydraulic radius the **entrainment limit** is given by

$$Q = 7.088 \cdot 10^{-5} \cdot 527000 \cdot \sqrt{\frac{0.02 \cdot 1.67}{2 \cdot 5.11 \cdot 10^{-4}}} = 213.5 \text{ [W]}$$

When compared to other fluids used in heat pipes, acetone has a rather low thermal conductivity. With an increase of heat flux the temperature gradient over the liquid layer therefore becomes more pronounced, so that evaporation no longer occurs at the liquid/vapor interface but at the heat pipe wall in the form of bubbles. If the heat flux further increases, the wall temperature will suddenly rise excessively and the *boiling limit* will be reached:

$$Q = \frac{2\pi L_e k_{w,ef} \Delta T_{crit}}{\ln(r_{int}/r_v)} \quad (6.17)$$

The critical superheat that causes vapor bubble generation at the wall

$$\Delta T_{\text{crit}} = T_p - T_v = \frac{2\sigma T_v}{h_{lv} \rho_v} \left(\frac{1}{r_n} - \frac{1}{w} \right) \quad (6.18)$$

is extremely sensitive to the nucleation radius r_n . In reference [31] a range is proposed for this radius that spans two orders of magnitude: $2.5 \cdot 10^{-7} \text{ m} < r_n < 2.5 \cdot 10^{-5} \text{ m}$. Experimental evidence of operation beyond the boiling limit, as presented in section 7.7, suggests a nucleation radius of 10^{-6} m for the present case.

The effective thermal conductivity of the liquid/wick combination, $k_{w,ef}$, can be determined for rectangular grooves by

$$k_{w,ef} = \frac{(w_f k_l k_s d) + w k_l (0.185 w_f k_s + d k_l)}{(w + w_f)(0.185 w_f k_s + d k_l)} \quad (6.19)$$

where w_f denotes the rib width between the grooves, being 0.47 mm here.

$$\text{With } \Delta T_{\text{crit}} = \frac{2 \cdot 0.02 \cdot 323}{527000 \cdot 1.67} \left(\frac{1}{10^{-6}} - \frac{1}{6.5 \cdot 10^{-4}} \right) = 14.66 \text{ [K]} \quad \text{and} \quad k_{w,ef} = 1.1 \text{ W/mK}$$

the following value for the **boiling limit** can be estimated:

$$Q = \frac{2\pi \cdot 0.25 \cdot 1.1 \cdot 14.66}{\ln(0.00595/0.00475)} = 112.5 \text{ [W]}$$

In space applications it is quite common that a heat pipe starts working from the frozen state. The heat flux that is applied at the evaporator first heats up the frozen working fluid locally until reaching its melting temperature. At this moment a melt front is formed at the end of the evaporator and starts to propagate through the grooves in direction to the condenser constantly fed by axial heat conduction. At the same time vapor is generated at the liquid/vapor interface. It flows to the adiabatic zone and condenser and is partly trapped on already liquefied material, but also on the still solid one. The first portion re-enters in the evaporation-condensation cycle, whereas the rest freezes out and is withdrawn from the cycle. If the mass rate of melted fluid is smaller than the mass rate of fluid condensed on frozen material, the amount of liquid decreases,

until the evaporator is finally depleted. When the two mass rates are compared, an equation can be formulated that defines the **frozen start-up limit**:

$$\frac{\varphi \rho_l A_w h_{lv}}{C_{pw} (T_{melt} - T_{\infty})} \geq 1 \quad (6.20)$$

($C_{pw} = \sum c_j A_j \rho_j$ is the heat capacity of pipe wall and liquid/wick matrix per unit length)

Taking a minimum ambient temperature of -100 °C, as projected for geostationary satellites [3,26], the result is

$$\frac{0.6534 \cdot 755 \cdot 4.03 \cdot 10^{-5} \cdot 527000}{357.8 \cdot (180 - 173)} = 4.2 > 1$$

After rearranging eqn. (6.20) the minimum ambient temperature can be determined, to which the heat pipe can be exposed without the risk of operation failure due to complete freeze-out of the working fluid:

$$T_{\infty, \min} = T_{melt} - \frac{\varphi \rho_l A_w h_{lv}}{C_{pw}} = 150.7 \text{ K} = -122.3 \text{ °C} \quad (6.21)$$

As is expected for moderate temperature heat pipes, the heat transport capability is generally limited by the liquid pressure drop [45]. The capillary limit appears to be the most critical. The relative insignificance of the vapor pressure drop can be noted here, as it makes up only 4 % of the total pressure drop.

With regard to the scheduled operating temperature it can be stated that the heat pipe with the chosen geometry of vapor space and wick is capable of transporting a heat flux of 60 W with a sufficient safety margin for all operating limits. This margin, however, diminishes easily, if the operating temperature becomes higher due to sink conditions or gas inventory other than that projected. Changing values of the temperature dependent fluid properties lower the maximal capillary pumping pressure and the critical superheat. If for instance the operating temperature rises by 10 °C to 60 °C, the capillary limit hardly changes, because the capillary pressure drop is compensated by smaller vapor and liquid pressure drops, but the boiling limit falls by 29 % to 80 W.

6.3 Selection of the noncondensable gas

When operating a GLHP on earth, the best match for the vapor is a noncondensable gas that has a molecular weight closest to that of the working fluid. With similar weights an axial stratification of the components inside the pipe due to gravitational force [26] can be avoided, when the heat pipe is working in the horizontal position. Additionally the diffusion coefficient can be kept small. Diffusion has a primary influence on the extension of the diffuse vapor/gas front. If the extension is large, the heat pipe capacity is reduced, as the local condenser temperature in the vicinity of the front is reduced.

In the temperature range of interest the following vapor-gas pairs are typical:

- Methanol ($M = 32$) with nitrogen ($M = 28.01$) or argon ($M = 39.9$);
- Ammonia ($M = 17.03$) with methane ($M = 16.04$) or nitrogen.

For the present case **argon** was chosen as the noncondensable gas, as it is easily available, and with its molecular weight it is the closest match to acetone ($M = 58.1$) among the inert gases.

Since experimental values for the acetone-argon pair were not available, in the following the diffusion coefficients for this and other combinations are calculated for 50 °C according to reference [46].

The approximation for a binary diffusion coefficient of two gases 1 and 2 that best corresponds to experimental data is given as:

$$D_{12} = 0.0018583 \frac{\sqrt{T^3 \left(\frac{1}{M_1} + \frac{1}{M_2} \right)}}{p \delta_{12}^2 \cdot \Omega_{D,12}(T_{12}^*)} \quad [\text{cm}^2/\text{s}] \quad p \text{ [bar]}, T \text{ [K]} \quad (6.22)$$

$$T_{12}^* = \frac{\kappa T}{\epsilon_{12}} \rightarrow \text{Reduced temperature}$$

Parameters of the Lennard-Jones potential:

$$\epsilon_{12}/\kappa = \sqrt{(\epsilon_1/\kappa) \cdot (\epsilon_2/\kappa)} \rightarrow \text{Energy of molecular interaction}$$

$$\text{and } \delta_{12} = 0.5 \cdot (\delta_1 + \delta_2) \rightarrow \text{Collision diameter}$$

$$\Omega_{D,12}(T_{12}^*) \rightarrow \text{Collision integral (tabulated)}$$

With the molecular diameters $\delta_{Ac} = 4.6 \text{ \AA}$, $\delta_{Ar} = 3.42 \text{ \AA}$, the energy parameters $\epsilon_{Ac}/\kappa = 560.2 \text{ K}$, $\epsilon_{Ar}/\kappa = 124 \text{ K}$, the collision integral $\Omega_{Ac,Ar}(1.226) = 1.3075$ and $p_{sat,Ac}(50^\circ\text{C}) = 0.8 \text{ bar}$ the diffusion coefficient of acetone in argon yields:

$$D_{AcAr} = 0.132 \text{ cm}^2/\text{s}$$

Vapor-gas pair	Pressure p_{sat} [bar]	Diffusion coefficient D_{12} [cm ² /s]
methanol-nitrogen	0.536	0.33
methanol-argon	0.536	0.305
ammonia-methane	19.9	0.015
ammonia-nitrogen	19.9	0.015

Table 4 - Diffusion coefficients for some vapor/gas combinations calculated by eqn. (6.22) at an operating temperature of 50 °C

Table 4 clearly shows the significance of the fact that the diffusion coefficient is inversely proportional to the pressure. At an operating temperature of 50 °C ammonia with its extremely high saturation pressure produces a rather sharp vapor/gas front because of a very low diffusion coefficient. If to the contrary the coefficient is high and a diffuse front spreads vastly, a premature condenser shut-off can occur at low operating temperatures.

The table also indicates that similar molecular weights do not necessarily mean small diffusion coefficients. More significant are larger collision diameters and intermolecular forces. Hence as a rule of thumb one should aspire for a larger molecular weight of the gas. In operation without gravity, for example, krypton ($M = 83.8$) with the acetone-related coefficient $D_{AcKr} = 0.095 \text{ cm}^2/\text{s}$ would be a better choice in the present case.

Besides stratification the gravitational force can cause natural convection in the region, where the hot active section changes to the gas-blocked inactive section of the heat pipe. The large temperature gradients that typically exist in that region lead to an additional mass transport due to the Marangoni effect. When an appropriate molecular weight for the gas or a mixture of gases is chosen, this undesirable convective transport can be eliminated [47]. For this purpose the gas density has to be kept equal at both margins of that region. The molecular weight that obeys this requirement is determined from the following expression:

$$M_g = \frac{\Re(\rho_v(T_a) - \rho_v(T_\infty))}{\frac{p_t - p_v(T_\infty)}{T_\infty} - \frac{p_t - p_v(T_a)}{T_a}} = M_v \frac{(T_\infty/T_a)p_{v,a} - p_{v,\infty}}{p_t - p_{v,\infty} - (T_\infty/T_a)(p_t - p_{v,a})} \quad (6.23)$$

With the assumption that there is no gas in the active heat pipe section ($p_{v,a} = p_t$) the equation can be further reduced:

$$M_g = M_v \frac{(T_\infty/T_a)p_{v,a} - p_{v,\infty}}{p_{v,a} - p_{v,\infty}} \quad (6.24)$$

and if for low sink temperatures the vapor pressure can be neglected ($p_{v,\infty} \cong 0$), the result becomes very simple:

$$M_g = \frac{T_\infty}{T_a} M_v \quad (6.25)$$

Considering an operating temperature of 50 °C and taking a sink temperature of -50 °C (that is planned for vacuum tests with radiative cooling) a value of 40.12 is obtained for the necessary molecular weight of the noncondensable gas. The close agreement with the value of argon shows that this gas excellently meets the requirements for the use in terrestrial experiments under aforementioned thermal conditions.

6.4 Selection of the gas reservoir volume

In a GLHP the reservoir volume has to be dimensioned in such a way that in any operational situation the whole condenser length is available for heat transfer area adjustments. The volume depends on the expected ranges of sink temperature (T_∞) and evaporator temperature (T_e). As the evaporator temperature, in principle, does not change much, the sink temperature is the primary criterion for reservoir dimensioning. The larger the range of T_∞ , the bigger is the volume.

To guarantee control over the whole condenser area, the gas should liberate the condenser completely in case of maximum operating and sink temperatures (limit case 1) and shut off the condenser completely in case of minimum operating and sink temperatures (limit case 2) [40]. If both limits are taken into consideration, a conditional equation for the reservoir volume can be derived.

According to Fig. 6.4, where a partially blocked condenser is shown, gas exists in reservoir and condenser up to a distinct position ($z = L_{ci}$) which marks the position of the vapor/gas front. As the front is assumed flat, the gas concentration shows a Heavyside type drop when passing this position: To the left the concentration has a value that is constant throughout the space occupied by the gas, and to the right it is zero.

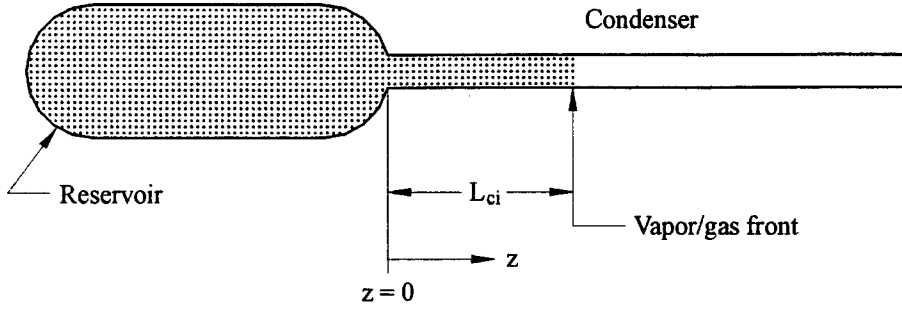


Fig. 6.4 - Partial schematic of a GLHP with a partially gas-blocked condenser (L_{ci} : flat vapor/gas front position)

In equilibrium, that is equality between total pressure and evaporator vapor pressure, the total gas mole number in non-wicked reservoir and inactive reservoir is

$$N_g = [p_v(T_e) - p_v(T_{ci})] \frac{V_r}{\mathfrak{R}T_\infty} + \frac{A_v}{\mathfrak{R}} \int_{z=0}^{L_{ci}} \frac{p_v(T_e) - p_v(T_{ci})}{T_{ci}} dz \quad (6.26)$$

Without liquid in the reservoir the vapor pressure there is exclusively conditioned by the partial vapor pressure in the inactive condenser and does not depend on the reservoir temperature. However, generally the reservoir and inactive condenser are exposed to the same sink conditions.

If subsequently setting $T_{ci} = T_\infty$ eqn. (6.26) is written in the form:

$$N_g = [p_v(T_e) - p_v(T_\infty)] \frac{V_r}{\mathfrak{R}T_\infty} + \frac{A_v}{\mathfrak{R}} \int_{z=0}^{L_{ci}} \frac{p_v(T_e) - p_v(T_\infty)}{T_\infty} dz$$

Resolving the integral and combining the two gas portions yields:

$$N_g = \frac{p_v(T_e) - p(T_\infty)}{\mathfrak{R}T_\infty} (V_r + A_v L_{ci}) \quad (6.27)$$

For limit case 1, that is $L_{ci} = 0$, holds

$$N_g = \frac{p_v(T_{e,max}) - p_v(T_{\infty,max})}{\mathfrak{R}T_{\infty,max}} V_r \quad (6.28)$$

and for limit case 2, that is $L_{ci} = L_c$, holds

$$N_g = \frac{p_v(T_{e,min}) - p_v(T_{\infty,min})}{\mathfrak{R}T_{\infty,min}} (V_r + V_c) \quad (6.29)$$

As N_g remains constant, eqns. (6.28) and (6.29) can be equated:

$$\begin{aligned} \frac{p_v(T_{e,max}) - p_v(T_{\infty,max})}{\mathfrak{R}T_{\infty,max}} V_r &= \frac{p_v(T_{e,min}) - p_v(T_{\infty,min})}{\mathfrak{R}T_{\infty,min}} (V_r + V_c) \\ \Rightarrow \frac{V_r + V_c}{V_r} &= \frac{p_v(T_{e,max}) - p_v(T_{\infty,max})}{p_v(T_{e,min}) - p_v(T_{\infty,min})} \cdot \frac{T_{\infty,min}}{T_{\infty,max}} \end{aligned}$$

For the relation between the volumes of condenser and reservoir now results

$$\frac{V_c}{V_r} = \frac{p_v(T_{e,max}) - p_v(T_{\infty,max})}{p_v(T_{e,min}) - p_v(T_{\infty,min})} \cdot \frac{T_{\infty,min}}{T_{\infty,max}} - 1 \quad (6.30)$$

In addition a conditional equation for the gas inventory can be obtained from eqn. (6.28) or eqn. (6.29):

$$m_g = N_g \cdot M_g = \frac{p_v(T_{e,max}) - p_v(T_{\infty,max})}{R_g T_{\infty,max}} V_r \quad (6.31)$$

In Table 5 reservoir volumes and gas inventories of acetone filled GLHP's are calculated for three situations with different thermal boundary conditions. The first situation refers to a real space application found in literature and the second is based on laboratory conditions without special cooling requirements. The second and third situations represent the design results as adopted for the realized test objects, the single GLHP (section 7.6) and the radiator GLHP (section 7.4) respectively.

$$(V_c = \pi r_v^2 \cdot L_c = \pi \cdot 0.475^2 \cdot 50 = 35.44 \text{ [ml]})$$

	Space conditions as in ref. [26]	Lab conditions (convective cooling)	TVT conditions as scheduled
$T_{e,max}$	49 °C	60 °C	50 °C
$T_{e,min}$	29.5 °C	50 °C	38.5 °C
$T_{\infty,max}$	-12.2 °C	25 °C	-10 °C
$T_{\infty,min}$	-100 °C	16 °C	-50 °C
$p_{v,e,max}$	0.7727 bar	1.1367 bar	0.8014 bar
$p_{v,e,min}$	0.3588 bar	0.8014 bar	0.5185 bar
$p_{v,\infty,max}$	0.0436 bar	0.2955 bar	0.0497 bar
$p_{v,\infty,min}$	0.0009 bar	0.1961 bar	0.0028 bar
V_r/V_c	2.84	2.87	4.23
V_r	100.7 ml	101.8 ml	150 ml
m_g	135 mg	138 mg	205 mg

Table 5 - Reservoir size determination for 3 selected situations with acetone operated GLHP's
(TVT = Thermal Vacuum Test)

Fig. 6.5 delineates the design process that is governed through eqn. (6.30) by localizing the operating points in a sink temperature plane. The indicated dimensionless reservoir sizes would be 150 ml and 200 ml with respect to the present condenser volume. The curves are drawn for two evaporator temperature ranges (10 and 5 °C) at two levels each. The ranges are expressed by intervals between $T_{e,min}$ and $T_{e,max}$ in the legends. The diagrams should be used as follows: When choosing a minimum sink temperature, the point on one of the curves indicates to which value the ambient temperature can rise in order to keep the evaporator temperature controlled within the interval that corresponds to the curve.

The diagrams show that the reservoir size primarily limits the temperature range controllability. In the case of the smaller reservoir the evaporator temperature can only be maintained in a range of 10 degrees for sink temperatures below -20 °C. A finer control is only possible at higher sink temperatures, which means that only small heat fluxes can be transferred. In the case of the larger reservoir fine control can be achieved for all sink temperature levels, but the sink temperature must not vary much. The distance from the diagonal line characterizes the sink temperature range: The further the operating point is located from that line, the broader is the operative sink temperature interval. This is due to the fact that the vapor pressure becomes more sensitive to temperature variations at higher temperature levels. For the same reason the curve for the same range but higher temperature level stays closer to the diagonal.

So in situations, where a tight temperature control is desired and large sink temperature variations are encountered, the reservoir turns out to be rather large, and this can conflict with structural and weight restrictions in space applications.

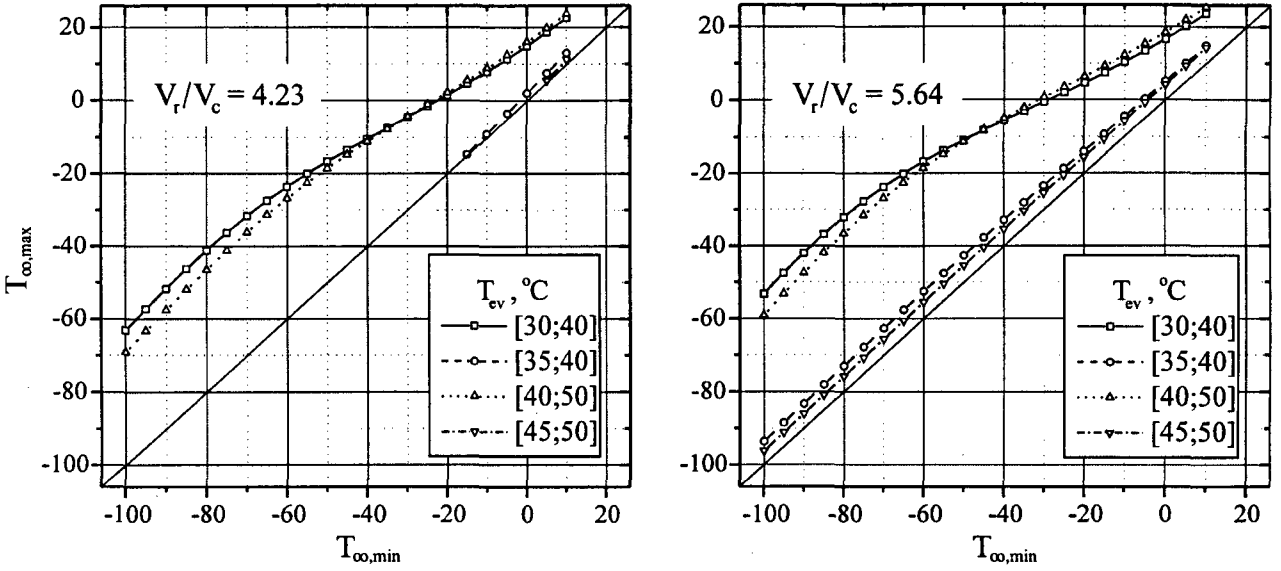


Fig. 6.5 - Temperature control capability diagrams for two reservoir sizes related to sink temperature and desired evaporator temperature level and range

The object of study, with its configuration and dimensions, so far has been qualified numerically for its task and has also fulfilled the criteria with view of the design process of a GLHP. The most challenging phase of the project now is to provide a real device that is capable to bear witness to the specially developed model and further to verify, if a relatively simple modeling is able to satisfactorily represent sensitive two-phase flow heat transfer domains which are embedded into a complex environment of scarcely tangible heat conductances. These are the contact conductances between the mechanically joined parts of the radiator and the film conductances across the interface where the phase change takes place. Quite a lot of intuition and a try-and-error procedure is needed to extract suitable values for these conductances to be used as data input for the simulations, as respective data for the present case were not available from freely accessible literature.

Before mounting the complete radiator system the operativeness of an acetone/argon driven axially grooved GLHP under terrestrial test conditions was verified. This convectively cooled prototype, referred to as the “single GLHP” hereafter, was first tested without gas charge as a conventional heat pipe (Run 0) and subsequently with a fixed gas charge, but with stepwise changing heat loads in a short test (Run 1) and two long-term tests (Run 2 and 3). The sequence of thermal vacuum tests performed with the radiator under space conditions comprised of five test runs in the normal (Runs A to E) and one in the slitted radiator configuration (Run F). For the purpose of documentation the data obtained from all tests are graphically presented in plots in appendices A3 and A4. These are the temporal evolutions of total pressure and evaporator temperature as well as wall temperature profiles acquired during both radiator and single GLHP tests, further the runs of the radiator reservoir temperature curves and the curves of the heat flux that was removed when cooling the single GLHP.

In the analyses of the test results in this chapter, however, the single GLHP is treated after the radiator. This is due to the fact that thermocouple measurements inside the vapor space of the radiator heat pipes provided some information about the internal film coefficients that were necessary to perform the single GLHP simulations. Moreover the validation analyses performed

with two single GLHP tests proved to be more unequivocal because of an immediate heat exchange to and from the heat pipe without bothersome joint resistances.

In general the behavior of the temperature at the evaporator, T_e , is the crucial criterion that approves the GLHP design with respect to the desired temperature controllability. This information is given in the appendices. In the following comparisons between experiment and simulation, however, the active zone vapor temperature, T_{va} , is chosen as the parameter of interest, since the vapor space forms the core of the system and, as a matter of fact, is the main component responsible for the highly effective heat transfer. If the experimentally found transients of T_{va} coincide with the simulated ones, it can be stated that the simulation can reproduce the real situation in a satisfactory way. The other parameter, of course, is the vapor/gas front position, L_{ca} , that proved to be an appropriate indicator to give an insight into the dynamics of the heat pipe interactions during simulation with a flat front model. In the real case of a diffuse front this now rather hypothetical parameter still should be suitable to represent front dynamics, as it transforms differently shaped temperature profiles at different levels into single characteristic values and thus helps to reduce a huge amount of measured values to a compact form. Two approaches of relevant transform functions are presented and discussed next.

7.1 Finding a hypothetical flat front position from experimental data

The position of the flat front is, by definition, the centroidal location of an axial non-condensable gas concentration distribution between two limits: a zero value upstream and a value downstream that corresponds to total pressure minus vapor saturation pressure at sink temperature. Presupposing the validity of the ideal gas law the gas concentration is inversely proportional to the temperature in the vapor space. As the wall temperature virtually follows the vapor space temperature, the temperature profile of the heat pipe wall can be graphically evaluated to find a flat front position as a first approximation. However, it has to be considered, that at the upstream end of the diffuse front the axial vapor space temperature profile is somewhat shifted towards the condenser end with respect to that of the wall temperature and the two profiles approach themselves at the downstream end. Hence an interpretation of the wall profile will always underestimate the active condenser length to an extent that depends on the radial temperature difference between vapor space and wall, which in turn is dependent on the internal condenser film coefficient. A graphical interpretation really becomes equivocal, when a spur of hot vapor within the diffuse front reaches the condenser end, and the temperature here starts to surpass the

sink temperature. The downstream margin of the diffuse front can no longer be allocated, as it vanishes into the feed tube and the centroidal front location loses one of its references.

For this reason the approaches that are going to be presented are based on a more physical background. The first one originates from energy conservation and can be extracted from Antoniuk's vapor space model, and the other establishes gas mass conservation and is based on a suggestion made by Sun and Tien [7]. The first alternative requires the knowledge of the temperature in the active zone, T_{va} . This is indirectly given by the measured total pressure through a Clausius-Clapeyron type relation and can be determined implicitly from eqn. (6.1) setting p_t instead of p_{sat} . Further the measured values of all temperatures along the heat pipe body, $T_{p,j}$, of course, are necessary. For the second approach the temperature values of the condenser are sufficient.

The first method simply assures the flat front to be located at the heat pipe length that the heat flux entering the pipe upstream needs in order to leave the pipe again towards at the condenser side. According to the energy balance over the active zone for a heat pipe with constant diameter follows according to eqn. (4.31)

$$T_{va} = \frac{\sum_{j=1}^k h_{i,j} T_{p,j} \Delta z_j + U h_{i,k+1} T_{p,k+1} \Delta z_{k+1}}{\sum_{j=1}^k h_{i,j} \Delta z_j + U h_{i,k+1} \Delta z_{k+1}} \quad (7.1)$$

j is counted from the first evaporator element, and k indicates the last heat pipe element Δz (in the direction to the condenser end) that still participates with its full length in the heat transfer process. The fraction U of the succeeding element that also belongs to the active zone hence is

$$U = \frac{\sum_{j=1}^k h_{i,j} T_{p,j} \Delta z_j - T_{va} \sum_{j=1}^k h_{i,j} \Delta z_j}{(T_{va} - T_{p,k+1}) h_{i,k+1} \Delta z_{k+1}} \quad (7.2)$$

and the flat front position z_{ff} is now determined by

$$z_{ff} = \sum_{j=1}^k \Delta z_j + U \Delta z_{k+1} \quad (7.3)$$

The index k is evaluated iteratively starting from $j = 1$, stepping in the direction of the condenser end and each time adding another element, until the absolute value of U falls below unity.

The second method suggests an inactive length to be defined as the length that the gas existing in the heat pipe container would occupy, if all of it was at the partial pressure and temperature of the gas at the condenser end. Since during normal heat pipe operation gas is only encountered in the condenser, all gas portions that are attributed to their respective condenser elements Δz_j are summed up and compared to a "gas piston" with a uniform partial gas pressure. Using this assumption and equating the total gas mass to the sum of gas portions due to experimental data

$$m_g = \frac{A_v}{R} \frac{p_t - p_v(T_p(L_c))}{T_p(L_c)} L_{ci} + m_{g,r} = \frac{A_v}{R} \sum_{L_c} \frac{p_t - p_v(T_{p,j})}{T_{p,j}} \Delta z_j + m_{g,r} \quad (7.4)$$

the following expression for the flat front position can be obtained

$$z_{ff} = L - \frac{T_p(L_c)}{p_t - p_v(T_p(L_c))} \sum_{L_c} \frac{p_t - p_v(T_{p,j})}{T_{p,j}} \Delta z_j \quad (7.5)$$

As the origin of the heat pipe coordinate z is placed at the beginning of the evaporator, the parameter L_{ca} that is employed in the analyses is given by subtracting the evaporator and adiabatic zone lengths from the result in eqn. (7.3) or (7.5).

In the analyses of the radiator and single GLHP test results (presented in sections 7.4 and 7.6 respectively) the second method was applied to extract the flat front transients from experimental data. Though the temperatures at the condenser end were not measured, these temperatures were approximated by a Lagrange type quadratic extrapolation considering the three measured wall temperature values closest to the condenser end, that is $T_{p,10}$, $T_{p,11}$ and $T_{p,12}$. With the distances being Δy between the measuring points and $\Delta y/2$ between the last temperature point and the end of the condenser, the Lagrange formula takes the following form:

$$T_p(L_c) = 0.375T_{p,10} - 1.25T_{p,11} + 1.875T_{p,12} \quad (7.6)$$

The first method was found not to be very suitable because of the uncertainty encountered with respect to the internal film coefficients that are crucial to determine the area where the heat leaves the vapor space. It was detected that the evaporator coefficient was different from the condenser coefficient and that at least the latter was not constant during operation. Nevertheless

a representative example of a radiator operating point at steady-state has been prepared for Fig. 7.1 to compare the two methods. In this case $h_{i,e}$ was set equal to $h_{i,c}$, so that the coefficients drop out in eqn. (7.2). In the series of graphs with one chart for each radiator heat pipe, the flat front positions are indicated as vertical lines; the dashed line corresponds to the first method and the solid line to the second.

Unless the flat front position reached about two thirds of the condenser length, both methods showed nearly identical results. The difference became rather large, when a situation near the condenser end was examined. Here the flat front according to the energy balance method always reached the condenser end prematurely and showed an even larger deviation, if compared to results from simulation. This originates from the relatively low level of the active vapor temperature that is determined from the measured total pressure. This temperature appears in the charts as a dotted line. The greater the difference between this temperature and the wall temperature profile, the more heat is considered to enter the vapor space (represented in the second chart by the upper 45°-hatched area), and this has to be counterbalanced on the heat output side. Hence the lower 45°-hatched area has to become equally large, and subsequently the flat front position is pushed forward excessively. This mismatch is inherent in the flat front model which the method is derived from. It postulates a constant temperature throughout the active zone which actually is an average temperature of a real vapor temperature profile spanned between the evaporator and the center of the diffuse front (indicated as a short-dashed line in the first chart). So an apparently paradoxical situation is visible in the charts, as a reasonable part of the condenser seems to act as an evaporator having a higher temperature than the active vapor temperature. For small active lengths and generally for heat pipes with a sharp vapor/gas interface, however, this method is acceptable, that is when the straight T_{va} -line intersects the wall temperature profile in the adiabatic zone section.

A further complication to the energy balance method appears, when the wall temperature profile is distorted between mid-evaporator and some initial portion of the condenser due to a high sink heat transfer coefficient. This occurred with the single GLHP experiment and can be seen in Fig. 7.2. According to the acceleration of the vapor flow at the evaporator end and its deceleration at the entrance of the condenser and the resulting pressure drop and recovery respectively, the temperature profile shows a strong indentation. This real gas-dynamic effect turns a simple heat transfer allocation impossible. The large temperature difference that already appears before the condenser temperature peak leads to absurdly small active lengths, not worthy to be displayed in this figure.

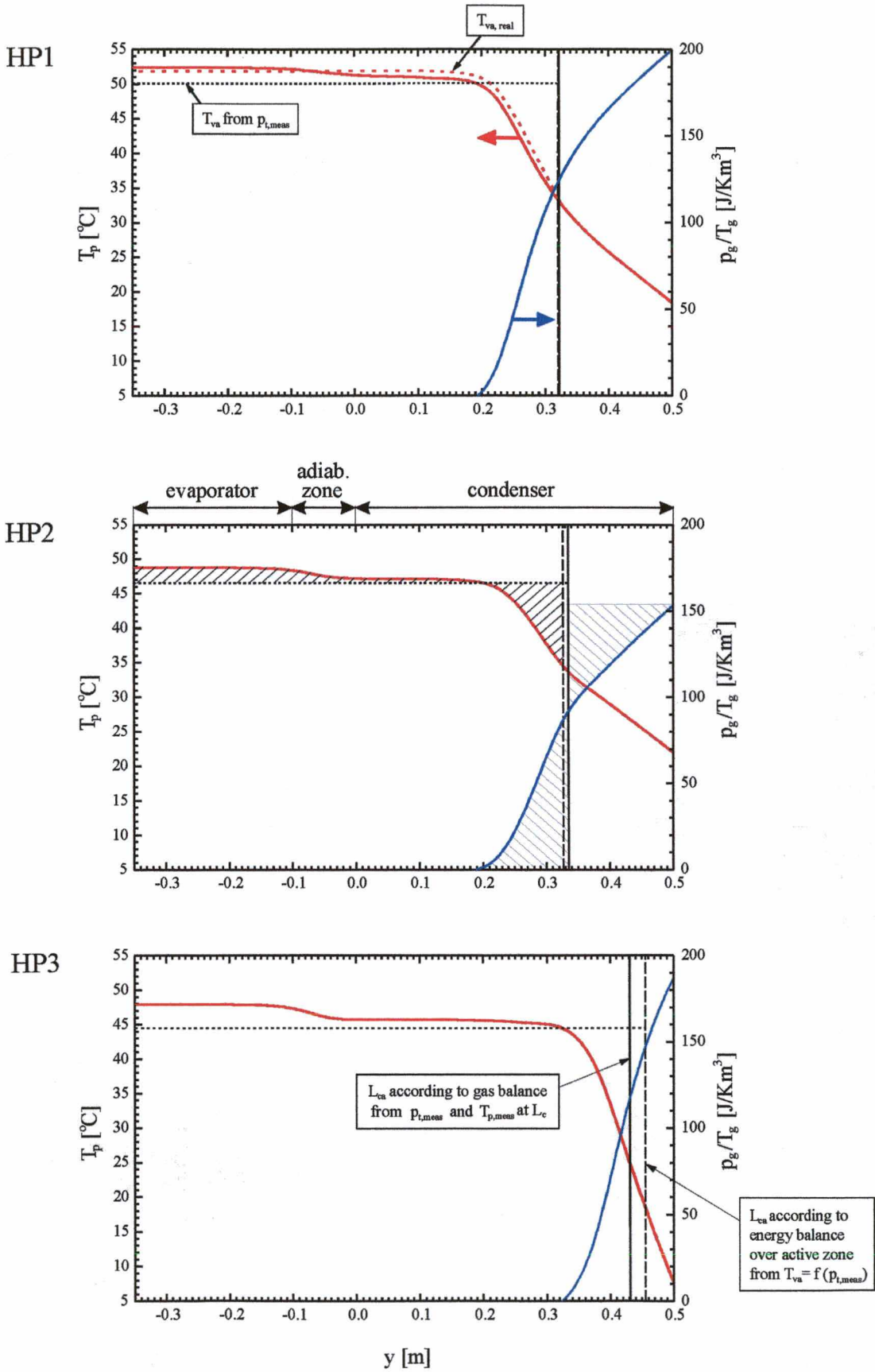


Fig. 7.1 - Steady-state wall temperature and gas concentration profiles of the radiator GLHP's and flat front positions according to energy balance and gas balance approaches (Run B with 40/20/40 W heat load)

The second method, on the other hand, proved to be rather insensitive to the rigid vapor temperature assumption, presumably as it merely considers condenser-related occurrences. According to this approach the areas below and above the gas concentration curve (p_g/T_g), which are 135°-hatched in the second chart of Fig. 7.1, have to become equal to reveal the flat front position, due to the aforementioned definition of a centroidal position in a diffuse front. When the axial evolution of the concentration in the radiator heat pipes is analyzed, the lower part of the hatched area actually is slightly smaller. This is due to the consideration of negative mass terms (that have been cropped in the charts) for some positions upstream of the flat front. In the single GLHP case a faulty accumulation of gas in the beginning of the condenser due to the indentation of the wall profile has been eliminated by intentionally lifting the profile of the upstream part of the condenser for the flat front computation. Thus somehow physical coherence was ensured, as the gas concentration until the highest condenser temperature value was at least maintained equal.

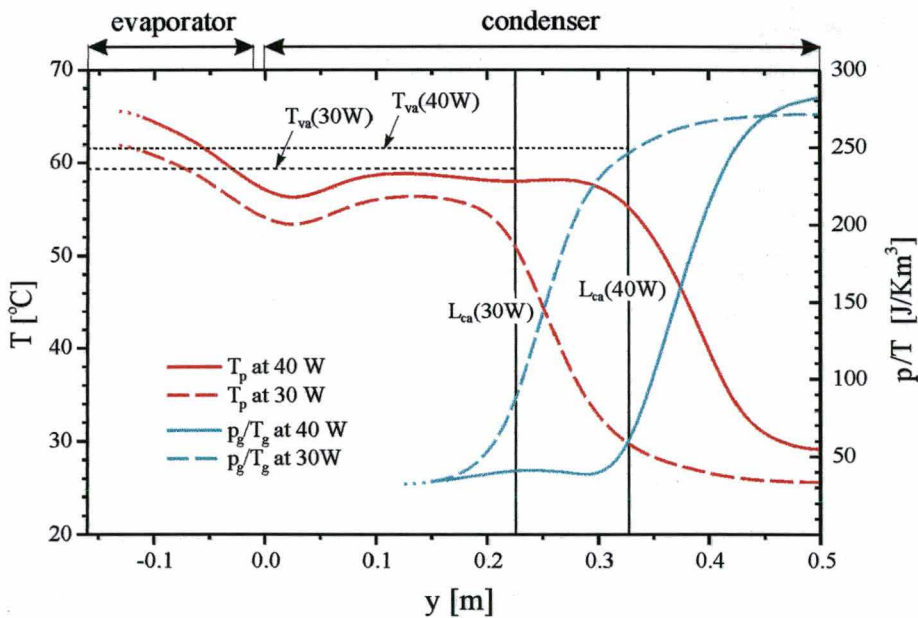


Fig. 7.2 - Steady-state wall temperature and gas concentration profiles of the single GLHP and respective hypothetical flat front positions according to the gas balance approach (taken from Run 3)

7.2 Correlation of the internal condenser heat transfer coefficient

The usability of the vapor space model is dependent on the knowledge of the internal film coefficients in the evaporator and condenser, as they are the boundary conditions that rule the

simulated heat transfer process through the heat pipe core. For this purpose temperature measurements in the vapor space have been attempted during the radiator tests to evaluate a parameter that is difficult to grasp. It is primarily conditioned by the type of working fluid and the shape and finish of the surface where the heat transfer takes place inside the heat pipe. However, it has been reported that seemingly identical GLHP's revealed a significant deviation of heat transfer characteristics when operating [48].

A work that, in a general way, tried to quantify the condenser film coefficient in GLHP's in function of a series of parameters was presented by Qin *et. al.* [49]. The objective was to find a correlation for a global condenser coefficient out of more than 300 measured values obtained in tests with 5 different GLHP's charged with different heat loads. The heat pipes were cooled by forced air convection and were operated without an adiabatic zone. The heat pipe configurations differed with respect to working fluid, condenser diameter-to-length ratio, tip angle (θ), gas inventory and liquid overcharge (Λ). The dimensionless non-linear correlation (with 5 regression coefficients C_0 to C_4) is related to the tubular condenser Nusselt number and was formulated as follows:

$$\text{Nu}_c = C_0 \left(\frac{g h_{lv} \rho_l D_v^3}{v_l L_c q_c} \right)^{C_1} \Lambda^{C_2} \left(\frac{\theta}{90^\circ} \right)^{C_3} \left(\frac{p_t}{p_t + p_g^*} \right)^{C_4} \quad (7.7)$$

$$\text{where } \text{Nu}_c = \frac{h_{i,c} D_v}{k_l} \quad \text{with } h_{i,c} = \frac{Q - Q_{\text{loss}}}{\pi D_v L_c (T_v - T_{p,c})}$$

The dependence of the condenser coefficient on operating temperature and gas inventory is expressed by the total pressure, p_t , and the so-called gas-loaded pressure, p_g^* , respectively. The latter signifies the pressure that is measured, when the noncondensable gas shuts off the whole condenser section, or in other words, the total pressure at the conclusion of start-up. A statistical analysis of variance (F-test) performed by the authors affirmed that the obtained data could be well attributed to a certain GLHP, although the comparison between experimental and regression condenser coefficients presented an error in the range of $\pm 27.5\%$.

Better results are hoped for in the case of a correlation for unique heat pipe geometry, working fluid, inclination and liquid overcharge, as in the case of the present radiator heat pipes. First of all eqn. (7.7) could be simplified by joining together all terms before the pressure ratio term to one constant 10^{C_A} . Further the condenser coefficient is maintained as a global value, but this

time it should be referred to a condenser **and** adiabatic zone length, as condensing heat transfer takes place in both sections. The new reference length is designated as L^* . The $h_{i,c}$ -correlation enters the simulation program with a value that is at least as long as the adiabatic zone length. This is necessary to avoid singularities that, for instance, occur after start-up conclusion.

After the mentioned rearrangements the new heat pipe specific correlation formula appears in the following form:

$$h_{i,c} \cdot L^* = k_1 \cdot 10^{C_A} \left(\frac{P_t}{P_t + P_g^*} \right)^{C_B} \quad (7.8)$$

After logarithmizing this equation the regression coefficients C_A and C_B can be determined by a simple linear regression algorithm.

7.3 Technological aspects of GLHP manufacturing and filling

Two materials were used for the GLHP: the aluminum alloy Al 6063 (AlMgSi0.5) for the heat pipe body and stainless steel for the reservoir. The two materials make contact midway along the feed tube in the form of an atomic bond. This kind of bond occurs when two rods of the dissimilar materials are pressed together with their faces and simultaneously twisted against each other under high contact pressure. The resulting friction heat welds the two parts together. The feed tubes were turned and bored out from these friction-welded samples. The best junction quality is achieved, when the material is taken from the region as far as possible from the rotation center of the bimetallic rod, as there the circumferential velocity is highest during twisting. Even with a wall thickness of 1 mm the feed tubes did not show any leakage at the aluminum-steel transition when tested with helium against vacuum.

The body of the radiator heat pipes was machined from a 85 cm long piece of extruded axially grooved profile, as shown in Fig. 6.3. At the adiabatic zone and at the upper side of the evaporator the fins were removed by lathe and slotting machine respectively to get a round shaping of the heat pipe at these sections. The fins on the condenser side were slitted with a distance of 5 cm in view of the tests with the radiator in slitted configuration. The resulting gaps have a width of 1 mm coinciding with the clearance between the sheet strips. The reservoir was made from a 34 mm outer diameter and 1.5 mm thick stainless steel tube. In the direction of the feed tube a conical taper was formed to provide a smooth transition to the very small orifice. The

tiny junctions of the feed tube to condenser end cap and taper on the other side were realized by electron beam welding. In this way a high welding reliability was assured, and the bimetallic transition could be protected against thermal strains, as the electron beam focusses the generation of heat very precisely. The feed tube enters into the end cap with an upward inclination of 30° . Below the bimetallic transition it is bent further upwards with a large-scale radius to enable a vertical orientation of the reservoir. This arrangement is aimed to testing on earth, as gravity will be able to drain off eventual working fluid condensate from the reservoir. The other junctions were TIG welded. First the fill tube with end cap and taper was welded to the reservoir cylinder. Then the heat pipe body and the reservoir with feed tube were brought into exact position with each other to accomplish the welding of the cap to the condenser end. A rigid positioning was achieved by bolted wooden clamps that hold the heat pipe body and reservoir together and maintain them in an orthogonal position to each other (Fig. 7.3). Due to the very fragile connection of the reservoir to the condenser this arrangement was maintained during all the following handling of the GLHP, until the moment they were to be assembled in the radiator. The fill tube on the reservoir cap is made from a quarter inch tube to facilitate swage lock tube fittings for the succeeding elements.

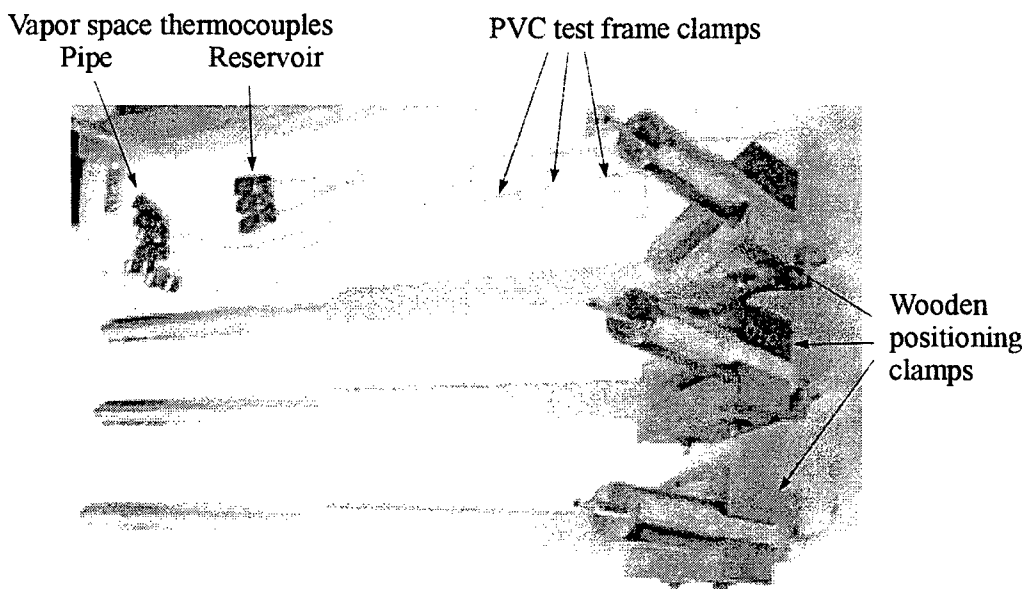


Fig. 7.3 - Radiator heat pipes after machining and connecting to the gas reservoirs (top view)

For the single GLHP experiment all the fins of the extruded profile had to be removed in order to get a round-shaped outer surface. A simple tube form was desired in order to apply the heat directly at the perimeter of the evaporator and to remove it by an air stream through a cylindrical

refrigeration jacket. Unfortunately it was not possible to machine a round pipe with a length of 85 cm to equal the length of the radiator heat pipes. Using the conventional lathes that were available, vibrations during the rotation of the workpiece, even after inserting a steel bar of appropriate diameter into the void of the profile, did not allow machining of a uniform wall thickness and sometimes even caused a disruption of the container. To better fix the workpiece a special tool was constructed, whose function is comparable to a pencil sharpener. This tool was clamped by the turning jaws of the lathe. As special features it presented a machining steel tip adjusted to perform a tangential cut with a diameter of 14 mm and just behind a drilled hole with the same diameter whose function was to accommodate the part of the pipe that has just been machined. While turning on the lathe the forward feed pushes the workpiece with its entire length through that tool. In doing so the already machined surface of the pipe served as a reference for the surface that had not been machined yet. Even with this technique a pipe with the desired length could not be achieved. The biggest length that could be obtained with a satisfactory surface quality was 66 cm. This length at least was sufficient to provide the scheduled condenser length and an evaporator length of 15 cm. A proper adiabatic length had to be omitted. The reservoir of the single GLHP that has only two thirds of the radiator pipe reservoir volume was made of a 24 mm outer diameter stainless steel tube with the same thickness.

For temperature measurements inside the vapor space of the radiator heat pipes 3 thin stainless steel sheathed ungrounded thermocouple probes were introduced into the heat pipe. One vapor space thermocouple was positioned at half height of the reservoir length and brazed into the reservoir cap (Fig. 7.5). The other two were introduced into the condenser void through an adapter in the evaporator end cap that facilitated a helium-proof fixation of a steel covered element inside the aluminum container (Fig. 7.4). This adapter is of the same geometry as an unbent feed tube, just shorter. The steel-to-aluminum transition is needed in this case, on one hand, to join the steel end to the jackets of the thermocouple probes by brazing, and on the other hand, to weld the aluminum end into the evaporator cap. All brazes were done with a silver filler.

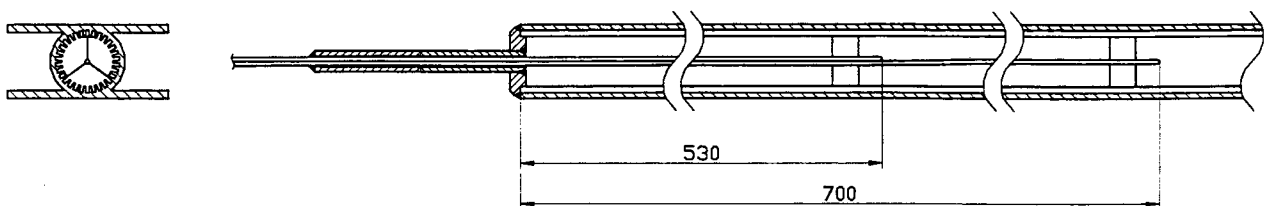


Fig. 7.4 - Fixation of vapor space thermocouples inside the heat pipe container

Near the sensor point the probes were centered inside the condenser by tripod type supports. They were formed from 0.03 mm thick and 5 mm broad stainless steel fillets, a common material used by dentists. Due to the orientation of the fillet width in axial direction and the tiny pedestals that press against the webs of the groove, the process space remains practically undisturbed.

As seen in Fig. 7.5 a pressure transducer was mounted into the fill line and finally a needle valve was attached to provide the closure of the vapor space.

Subsequently all internal surfaces of the GLHP's were cleaned with solvents to remove grease, welding residues and other impurities from inside. The aluminum part of the heat pipe was purged with acetone and the stainless steel part with trichlorethylene. The respective parts were alternately filled up and then immersed in a water filled ultrasonic bath at 50 °C. After the heat pipe part reached the water temperature, the sound field was activated for about 20 minutes. After draining of the solvent the purging process was repeated with another quantity of clean solvent.

Before the definitive filling the GLHP's have to be flushed with the same fluid that later is going to be the working fluid. This is recommended to better prepare the surface that is taking part in the evaporation and condensation process cycle. Water and air molecules are physically absorbed at the metallic surface and have to be eliminated as well as possible to ensure a good wetting angle which is important for the generation of the desired capillary pressure. A "pure" surface further diminishes the risk of a premature formation of nucleation germs. If instead of the parasitic molecules a monolayer of working fluid molecules can be achieved on the process surface, it is very well prepared for the intended operation. For the flush procedure the heat pipe body was filled up completely with acetone to ensure that the whole inner aluminum surface was wetted. Then the heat pipe was connected with the fill line to a high vacuum pump. A heater band was wrapped around all the heat pipe body with closer windings at the evaporator, since there a stronger cooldown takes place when evacuating. After switching on the heater band and opening the gas balast valve the backing pump was put into action. The gas balast deals with the big amount of liquid acetone that is sucked out of the heat pipe initially. Within the first minutes the evaporator, the feed tube and the lower part of the reservoir cool down violently (showing hoar-frost generation) because of strong acetone evaporation. To protect the bimetallic transition zone in the feed tube it was heated with a hot air fan. After reaching fine vacuum the high vacuum pump was switched on, and the heat pipe was degassed under constant heating for about 5 hours. A vacuum of lower than 10^{-3} mbar was reached. After closing the needle valve the GLHP was then ready for the filling procedure.

Normally GLHP's are filled by a special rig, in the succession of working fluid first and then the noncondensable gas [40]. The filling rig is used for commercially made heat pipes to specially take care of the inner surface and the working fluid to achieve very high purity and, especially in case of ammonia, to avoid contact between the fluid and the surroundings. However, in the present case that filling sequence led to gas overcharge of up to 25%, as the desired gas quantity could not be metered in, even under a controlled ambient temperature (± 0.1 K). For this reason the order was inverted, and in doing so the filling precision could be improved to $\pm 5\%$.

Argon was introduced directly from the compressed gas cylinder by joining the connecting hose to the muff of the needle valve. Initially this screwed connection was left loose to blow off the air in the line between gas cylinder and the needle valve face. After tightening the screw the valve actuator was turned very slightly to establish a small argon flow of about 0.2 mg/s. The pressure increase in the heat pipe was registered by the pressure transducer, and the corresponding gas mass was determined from the ideal gas law. The mentioned mass flow was maintained, until 90% of the desired gas mass was reached. Subsequently the mass flow was lowered by a factor 5 to 6 to reach the end of the filling procedure more slowly and avoid overshoot. Best filling results were achieved when the actuator was tightened after measured 99.97 % of gas mass, as retarded gas pressure adjustments inside the heat pipe always led to a slightly higher steady-state pressure.

Acetone was filled into the heat pipe by fixing the pipe in a slightly inclined position, that is with the evaporator below the condenser to ease the acetone stream through the feed tube. Above the closed needle valve an extension was mounted in order to enable the attachment of a graduated burette. First the extension was filled and eventual air bubbles were removed from inside it by gentle jerks. With the filled burette the desired quantity of acetone was released into the heat pipe according to the measuring scale divided into tenths of a milliliter. The acetone charge was determined from the volume that is formed by all the grooves. As during operation puddling of some acetone at the inferior part of the pipe because of gravity is usually taken into account, a liquid overcharge of 10 % was provided. During acetone filling some of the liquid may stick in the fill line or form a layer at the reservoir and feed tube wall. To be sure that all of it was evaporated into the heat pipe container the reservoir was heated up to 60 °C and the feed tube to 30 °C for about 20 minutes by means of a hot air fan, whereas the heat pipe, at the same time, was cooled in an ice bath.

7.4 Experimental radiator setup for thermal vacuum tests

The radiator tests were performed in a vacuum chamber with liquid nitrogen cooled shrouds. The available experiment space inside the shrouds was 1 m in length and 1 m in diameter. A special test frame composed of perforated columns was prepared to position the radiator in the center of the vacuum chamber and to achieve exact horizontal alignment with respect to x- and y-axes.

Before the integration of the GLHP's into the radiator 12 T-type wall thermocouples were fixed by thermal cement at the outer heat pipe surface of each heat pipe. As seen in Fig. 7.5 they were placed on half height of the perimeter, one on half length of the evaporator and adiabatic zone respectively and 10 in equal distances at the condenser. For the position of the condenser thermocouples the mid-point of each 5 cm long condenser section was chosen.

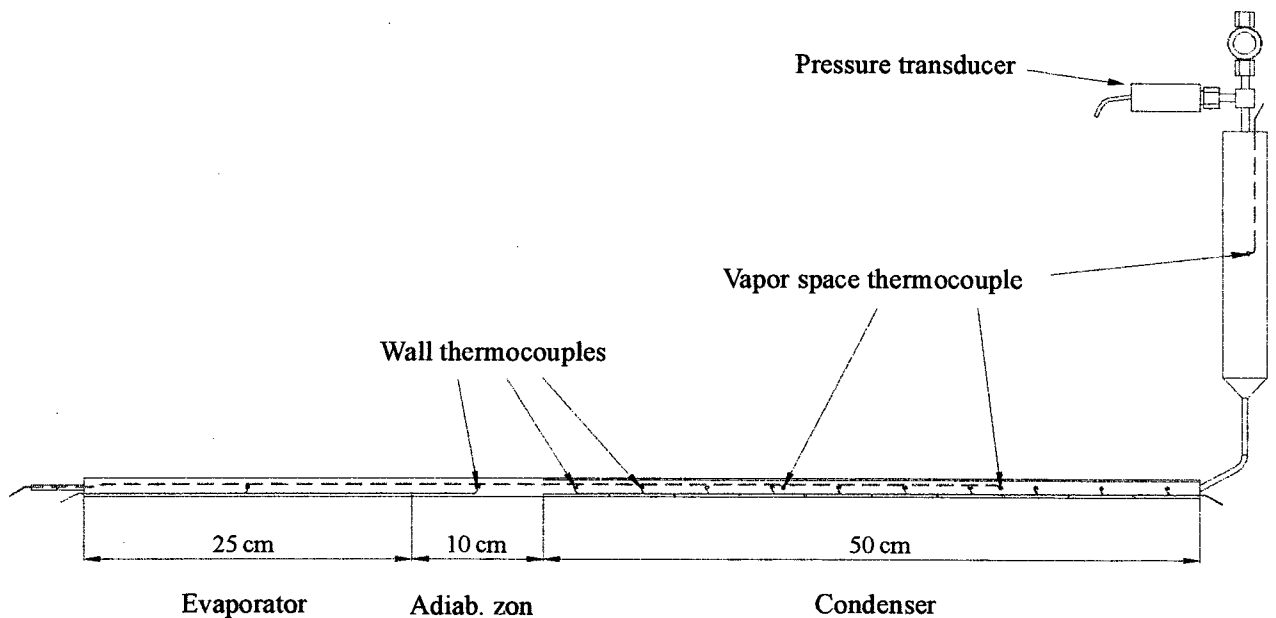


Fig. 7.5 - Sensor arrangement at each radiator GLHP

The outer surfaces of the sheets were coated with a black paint ("Solarlack M40 Li") with a measured emissivity of 0.86. The paint could be applied directly on a clean surface. Best emissivity results were obtained when repeating the spray process three times. A sheet thickness of 0.8 mm was chosen, since it gave sufficient mechanical stability of the sheets during machining and assembling.

The radiator was fixed to the test frame at the reservoirs by PVC clamps (shown in Fig. 7.3), and at the base-plate it was sustained on the tips of two adjusting screws. The GLHP's were screwed on the radiating sheets and the base-plate. Long and tiny screws press the radiating sheets onto

the condenser fins. Below the screw head on the upper face and above the nut on the lower face washers with an outer diameter of 7 mm were put to better distribute the pressure acting against the sheets. Recommendations made about bolted joints [50] have been followed with respect to the longitudinal screw spacing. They state that, if the ratio of the half-distance between the screw axes to the washer radius is smaller than 10, the spatial variation of contact resistance between the joined planes is insignificant. Hence a spacing of 5 cm was found to be enough to maintain good thermal contact between the joined parts. Between sheet and saddle a thermal grease (“Omegatherm 201”) was distributed to enhance this contact.

For tests in a one-g environment the heat transfer performance of asymmetric heating of axially grooved heat pipes is almost equal to that of uniformly heating the evaporator perimeter, if the heat enters from the bottom and the heat pipe has a liquid overcharge of more than 5 % [51]. For this reason the base-plate was arranged below the evaporators. Three 0.2 mm thick skin heaters were fixed by thermal grease below the respective evaporator positions to simulate the heat dissipation of high power amplifiers. A low conductive aluminum alloy was intentionally chosen as the material of the 3.15 mm thick base-plate to compensate for the highly conductive sheets.

The base-plate together with the dummy heaters was wrapped in 15 layers of multilayer insulation. The same was done separately for each of the adiabatic zones. As the upper sheet represents a considerable shape factor with respect to the reservoirs, they had to be protected against radiative heating by a multifoil shield. Conventional insulation material was inserted between the condenser fins (see detail in Fig. 7.6) to block radiation heating of neighboring condensers through the gap inside the sheets and between the sheet edges to avoid border heat losses from the gap to the surroundings.

During cool down of the shrouds it was noted that it took considerably more time to get all parts of the system to the ambient temperature of $-50\text{ }^{\circ}\text{C}$, because of the poor emissivity coefficient of the untreated stainless steel reservoir surface. Moreover, for the same reason, the reservoirs reached relatively high temperatures when the overload condition of the GLHP was approached during the test. Subsequently, for test runs C to F, the emissivity was increased by sheathing the reservoirs with kapton tape.

Fig. 7.6 presents a general overview of all sensor positions and a scheme of all power supply lines that were needed to perform the tests inside the vacuum chamber. Altogether 48 channels were scanned in intervals of 10 seconds by a HP 34970A data acquisition system. Before starting the test program an in-situ calibration of all thermocouples was made at ambient temperature and

pressure with reference to the indication of a calibrated thermometer inside the vacuum chamber. All the pressure transducers were put into one supply line in order to spare two power supply units. This was possible, since the transducers showed equal resistances in the megaohm range, so that they in fact divided a threefold supply voltage equally among them when connected in series.

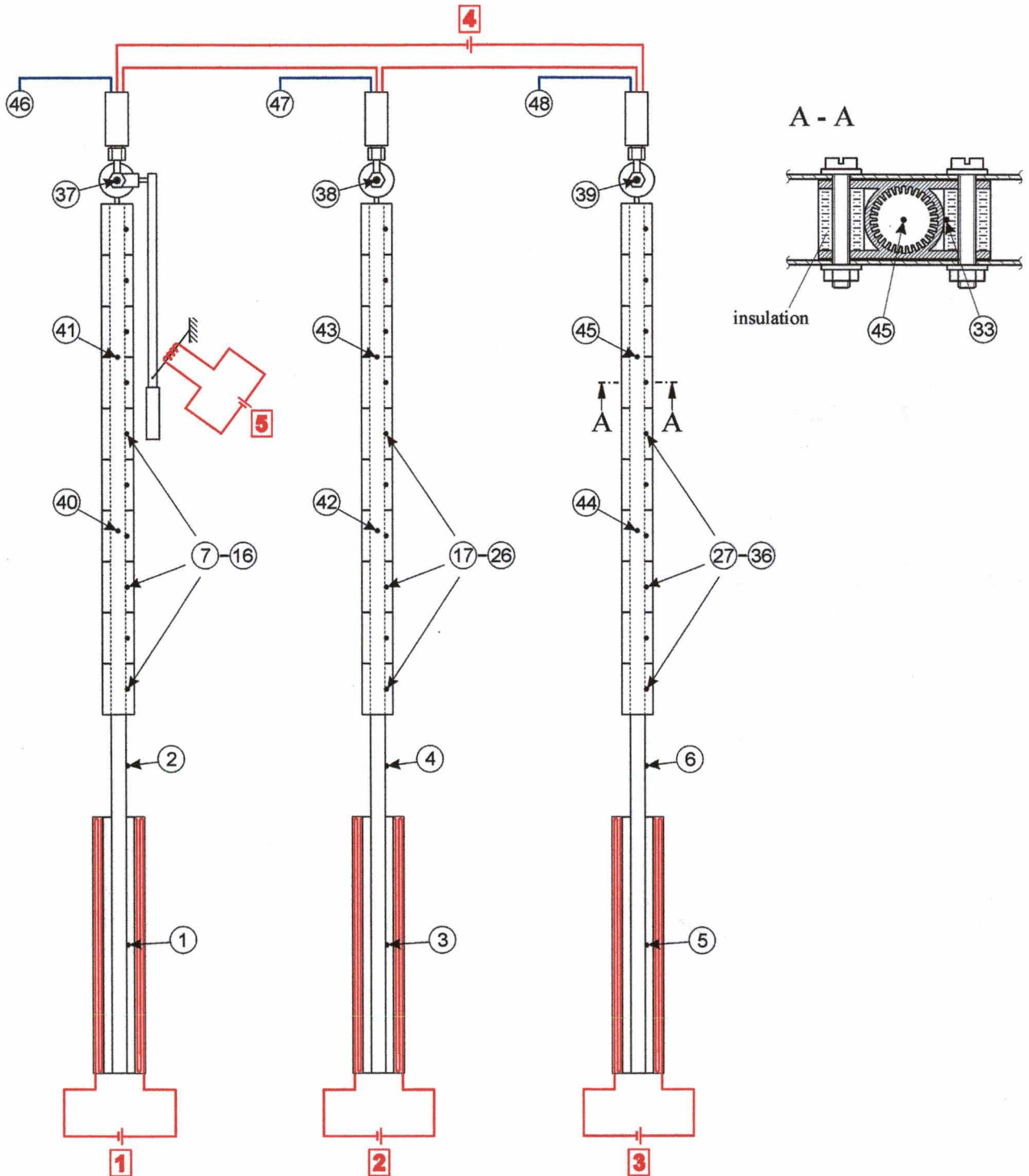


Fig. 7.6 - Layout of temperature and pressure sensor channels and power supply lines for the radiator tests

Each of the dummy heaters was linked to its own power supply to adjust precisely the respective amount of dissipated heat. To be sure that the correct voltage was fed at the heater terminals the heater resistances and also those of the supply lines were measured. Then the voltage that had to be generated at the terminals of the power supply, G , could be determined due to the following formula:

$$G = (R + R')\sqrt{Q/R}$$

R and R' signify heater and supply line resistances respectively and Q the dissipated ohmic heat. In order to reduce uncertainties in the amount of supplied power all terminals of the power sources 1 to 3 were permanently monitored with recently calibrated volt meters, so that voltage oscillations and shifts could be corrected manually. An exact supply voltage for the pressure transducers was provided by the precision power source HP 6111A.

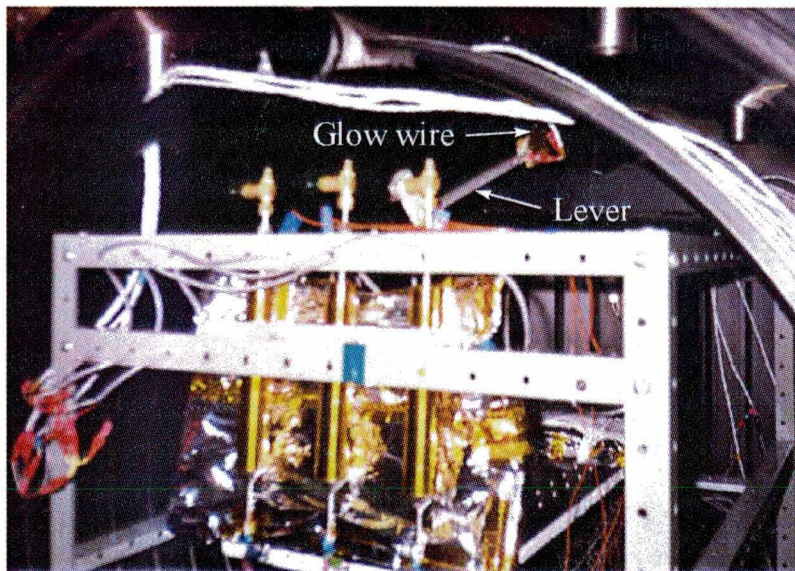


Fig. 7.7 - Close-up view at the mounting of the lever responsible for the simulated failure of HPI

The failure of one heat pipe during radiator operation was simulated by a sudden opening of the valve at the first heat pipe. The opening inside the vacuum chamber was achieved by a lever with sufficient weight and length connected directly to the valve actuator. For this purpose the valve knob was removed, when the test frame was brought in final position inside the chamber. The lever then was pushed over the actuator pin and fixed with a locking screw. The other end was fixed to a nylon thread that was tied to the upper end of the cooling shroud, so that the lever

could be kept in a slightly upward position (Fig. 7.7). Then a glow wire was twisted around the nylon thread and connected to a power supply. At a determined time during test the power was switched on, the wire burned the thread and released the lever that unseated the valve actuator.

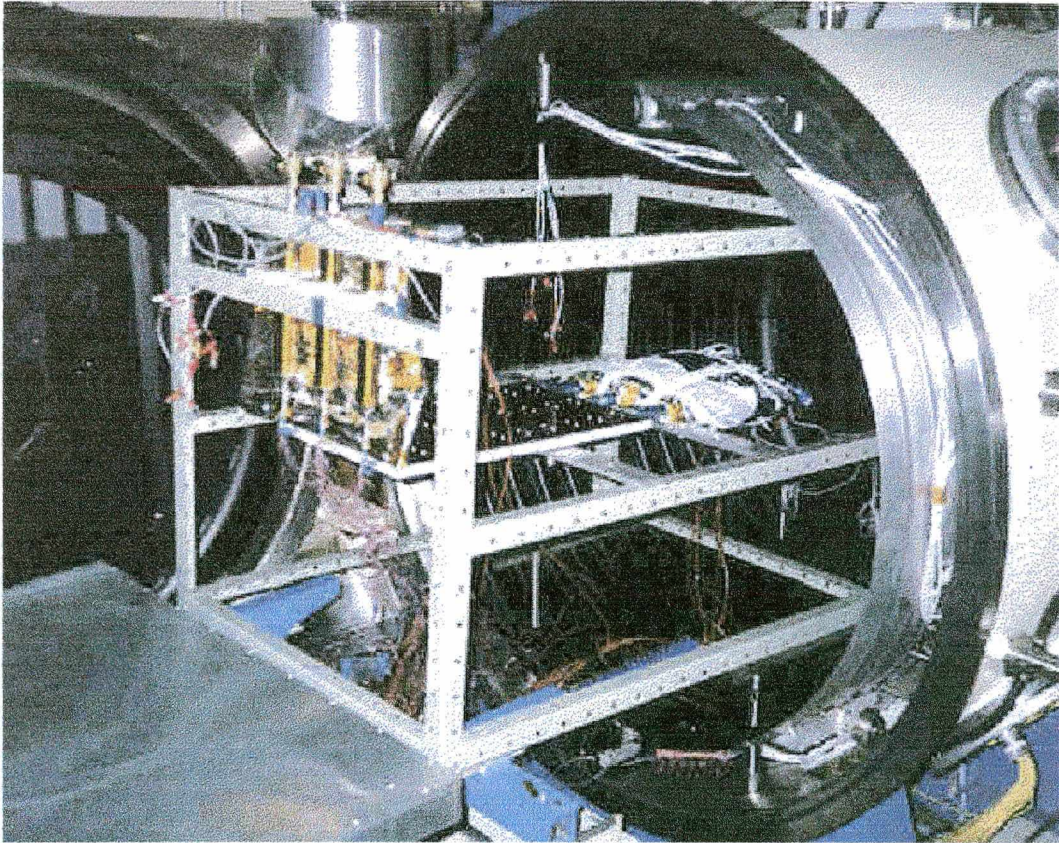


Fig. 7.8 - Fully assembled radiator test frame before insertion into the vacuum chamber

Radiating sheets	
area	0.3 x 0.5 m
thickness	0.8 mm
conductivity	193 W/mK
material	Al 6063
Base-plate	
area	0.3 x 0.25 m
thickness	3.15 mm
conductivity	137 W/mK
material	Al 5052
Adiabatic zone length	0.1 m
Reservoir-to-condenser volume ratio	4.23
Feed tubes	
inside diameter	2 mm
outside diameter	4 mm
length	90 mm
Sheet emissivity	0.86
Ambient temperature	-50 °C

Table 6 - Summary of radiator design details

7.5 Radiator test results and comparison with simulation

Altogether 6 radiator tests with different and intermittently changing heat loads were conducted according to the test program shown in Table 7. In some of the test runs, during some phases of the cycle, the heat load of the outside heat pipes differs to that of the middle one in order to induce heat pipe interactions before a heat pipe failure. In run A for instance the power supply to the outside pipes was simply switched off to observe what a restart of these pipes would look like. For visibility reasons the heat load spectrum was also indicated within the test result diagrams (Figs. 7.11, 7.13, 7.15 to 7.18). Small boxes list the heat loads in the order of heat pipe number, next to a dashed line placed at the time a change occurred. After any of the stepwise heat load changes a steady state was awaited taking the evaporator temperatures as reference. Regarding test runs A to C the gas inventories change from test to test due to the in section 7.3 mentioned initial difficulties when filling the heat pipes. Later the inventories were controlled better, so that the comparability between the last test runs became more feasible.

	min	HP 1	HP 2	HP 3
<u>Run A</u>	↓	232 mg	229 mg	218 mg
	0	40 W	20 W	40 W
	126	0 W	20 W	0 W
	147	40 W	20 W	40 W
<u>Run B</u>		235 mg	220 mg	195 mg
	0	40 W	20 W	40 W
	108	40 W	40 W	40 W
	192	40 W	40 W	40 W
<u>Run C</u>		244 mg	252 mg	235 mg
	0	40 W	20 W	40 W
	310	40 W	40 W	40 W
<u>Run D</u>		200 mg	210 mg	198 mg
	0	40 W	40 W	40 W
	149	35 W	35 W	35 W
	270	35 W	35 W	35 W
<u>Run E</u>		198 mg	210 mg	198 mg
	0	35 W	35 W	35 W
	151	40 W	40 W	40 W
	228	40 W	40 W	40 W
<u>Run F</u>		197 mg	210 mg	198 mg
slitted radiator!	0	35 W	35 W	35 W
	151	40 W	35 W	40 W
	208	40 W	20 W	40 W
	268	40 W	40 W	40 W
	345	40 W	40 W	40 W

Table 7 - Radiator test run scheme featuring gas inventories and heat load cycles

In four of the runs the first heat pipe was induced to fail. With the abrupt opening of the valve at the heat pipe concerned an outlet with a diameter between 0.5 and 1 mm² was formed, and a fast decompression took place, as the contents surged out into the vacuum within a few seconds. This resulted in a strong cooldown of the whole radiator. At the position of the failed heat pipe the sheet temperature dropped for about 15 degrees. The variation in time of the wall temperatures at various axial heat pipe positions is depicted in the left hand chart of Fig. 7.9. The most striking decline can be seen at the temperature of the adiabatic zone, partly because of its relatively low thermal capacity. But the main reason is that in this region most of the acetone present in the heat pipe evaporated in about 20 seconds. This and other effects could be estimated during a heuristic search for the cooldown transients that had to be included in the simulation. Previous simulations made in section 5.6 did not consider this real incident. A proper gas-dynamic treatment of the phenomena inside the heat pipe and reservoir was not attempted, as it would be beyond the scope of the present project.

A prior energy balance over a control volume including the vapor space and the vacuum stated that virtually all the energy loss of the failed heat pipe during decompression resulted from the evaporation of the working fluid. As the liquid charge was known, the stored latent energy could be estimated (8.64 kJ). The following task was to distribute and adjust fictitious time-dependent heat sinks along the discretized heat pipe elements and to run the simulation again and again, until the simulated transients approached the real ones. The best adjustment that was achieved is seen in the right hand chart of Fig. 7.9.

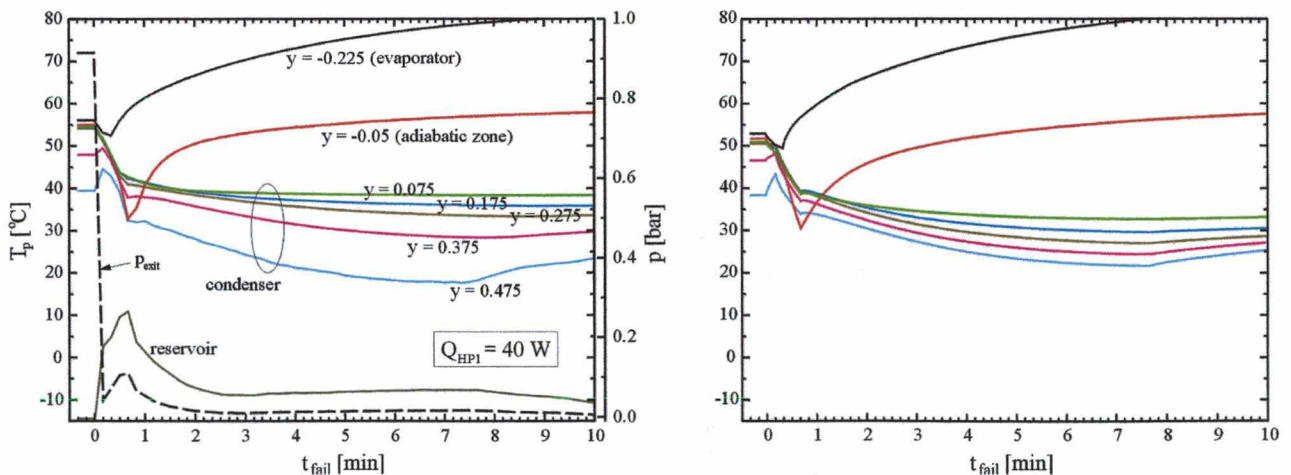


Fig. 7.9 - Cooldown behavior of HP1 during failure: experiment and numerical counterpart (Run B)

The systematic search revealed that during decompression most of the liquid is sucked into the evaporator and especially into the adiabatic zone by capillary forces and that during about 40 seconds a part of it was returned by condensation along the former inactive condenser length. During this time an addition of a linearly increasing heat source from the front position to the condenser end showed the best coherence. After about 20 minutes the perturbation due to the cooldown faded away and the still operating heat pipes recovered the temperature levels they had before the failure mode.

The experimental internal heat transfer coefficients were deduced from the measurements of the first vapor space thermocouples (channels 40, 42 and 44 in Fig. 7.6). At these positions it could be assumed that at certain steady-state operating points no gas would reduce the condensing heat transfer and that the local vapor space temperature would virtually not be different from that in the evaporator. The measurements were taken in situations where the diffuse front was close to the condenser end with the gas expelled from most of the condenser. Moreover only situations with symmetric heat loads were considered, so that neighboring heat pipe effects were avoided. The coefficients thus were obtained from the following 8 steady-state situations with equally charged heat pipes: Run B - 40 W, Run C - 40 W, Run D - 35 and 40 W, Run E - 35 W, Run F - 35 and 40 W. The results were determined through the following relations:

$$h_{i,e} = \frac{Q}{\pi D_v L_e (T_{p,e} - T_v)} \quad \text{and} \quad h_{i,c} \cdot L^* = \frac{Q}{\pi D_v (T_v - T_{p,c})}$$

On the condenser side the axial position of the vapor space thermocouple tip did not coincide with that of the wall thermocouple, so that for $T_{p,c}$ a weighted mean of the closest measurements was taken. The evaporator coefficient did not show a perceptible dependence on heat load or gas inventory. Mean values of 6500, 9000 and 5000 W/m²K were evaluated for HP1, HP2 and HP3 respectively. For the simulations an overall value of 6500 W/m²K was adopted, as the numerical results proved to be insensitive to the value of the evaporator coefficient, if compared to the other heat transfer coefficients. The condenser coefficient, on the other hand, accurately followed the tendency described by the correlation proposed in equation (7.8). This could be certified by the comparison of experimental and regression values shown in Fig. 7.10, as the error did not surpass a range of ± 10 %. It has to be mentioned, however, that the regression was made for each of the heat pipes. A common regression for all heat pipes was not applicable, as identical GLHP's can hardly be manufactured. The agreement, however, is very good, if one considers the uncertainty that involved the measurements of pipe and vapor temperature as well as the

determination of the gas-loaded pressure. In the first case small low-frequency oscillations were observed for vapor and wall temperatures, so that mean values over 4 to 5 minutes of scanning time were used. In the second case the moment of start-up conclusion generally was hidden between two successive sensor channel scans, so that an interpolation between the last measured pressure before the switch point and the first measured after was necessary.

The regression coefficient pairs (C_A ; C_B) are (4.52691; 2.51371), (4.58162; 3.19086) and (4.464235; 2.36286) for HP1, HP2 and HP3 respectively.

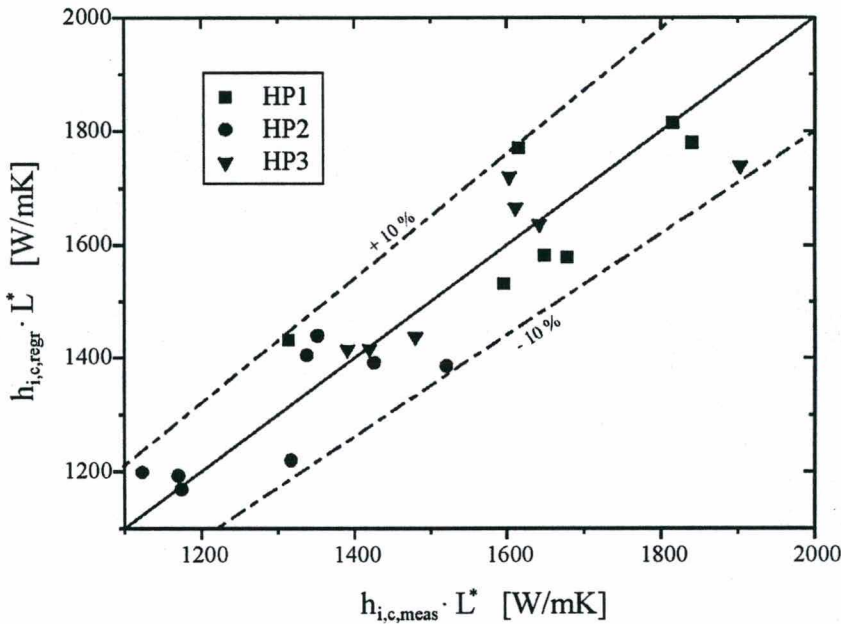


Fig. 7.10 - Comparison of experimental and regression values for the condenser film coefficient

For the simulations of the radiator system nearly the same program as described in section 5.5 has been used, yet some features concerning the data input have been improved or extended to better account for the real situation. During innumerable tentative simulation runs it became possible to bound probable real values for input parameters that formerly were simply estimated according to information found in literature. In successively improving these parameters experimental and numerical results gradually approached themselves to an extent that is believed to be satisfactory. Briefly speaking, the most crucial parameters are in sequence of their importance: the contact conductance of the bolted joints between sheets/plate and the heat pipe saddles, h_b ; the diffusion coefficient for the acetone/argon mixture, \mathcal{D}_{AcAr} ; the gas reservoir temperature, T_r ; the internal condenser film conductance, $h_{i,c}$.

The reservoir temperature could actually not be kept close to the sink temperature, especially during test phases when the hot vapor approached the feed tube. The poor emissivity of the polished stainless steel surface of the reservoir cylinders did not allow an accommodation to the ambient temperature. The situation was improved by sheathing the cylinders with kapton tape, as in doing so the emissivity could be raised to about 0.4. Nevertheless the reservoir temperature reached 0 °C in the close GLHP after the failure occurrence (against 10 °C for the blank reservoir case). As the in fact considerable reservoir vapor pressure has a high influence on the front position and active zone temperature, the simulation program had to account for this time dependence. After each time step the reservoir temperature in the simulation was updated by measured values of the respective test run from an external data file.

Because of the large reservoir temperature variation the diffusion coefficient could also no longer be assumed to be constant. On the contrary: It was verified that this value differed by a factor 3. Consequently eqn. (6.22) was introduced as a subroutine to update the coefficient according to the momentary total pressure and the mean value between condenser end and reservoir temperatures. The variable condenser film coefficients for each heat pipe entered the simulation through the given correlation. The gas-loaded pressure was stored for each heat pipe at the moment the respective simulated start-up was concluded. For the few moments that the simulated front needed to reach the condenser, correlated experimental values $h_{i,c}$ were temporarily used to avoid initial singularities after start-up conclusion.

Great effort was needed for the estimation of an appropriate contact coefficient for the bolted flat joints treated with thermal grease. This coefficient proved to be **much lower** than the value of 3000 W/m²K assumed in chapter 5. Moreover it was realized that it could not be taken as constant for all phases of a test run. As the temperature at the concerned joints generally increased during a test run, it is believed that the change in contact resistance originates from dilatation differences of the aluminum parts with respect to the steel bolts and also from changes in thermal conductivity of the thermal grease. During operation under initial heat load a value of about 500 W/m²K proved to be the best approximation for all test runs. After heat pipe failure this value increased to about 1500 W/m²K. Hence a cyclic adjustment of the contact coefficient was included in the simulation process.

The essence of the experimental and numerical results is presented in the following figures, with each test run represented by a set of two charts. Variations in time are shown for the active condenser length and the vapor temperature. The experimental parameters were evaluated according to the gas balance approach and from the measured total static pressure respectively.

In the charts the (solid) experimental curves of all the three heat pipes are collated together with the (dashed) simulated ones.

For scale reasons the charts omit the start-up periods of the GLHP's. The time to conclude start-up diminishes with higher heat load and with smaller gas inventory. In the experiments the start-up duration varied from 10.9 minutes for the outside heat pipes in run D up to 15.2 minutes for the middle heat pipe in run C.

When analyzing the experimental curves the following observations can be made:

1. The larger the gas inventory of a heat pipe, the faster is the temperature increase for the same power step increase. The level of the operating temperature is also correspondingly higher.
2. The more the active length has previously approached the condenser end, the more intense is its backward shift and following gradual retreat after the period of radiator cooldown due to heat pipe failure. The reduction of available heat transfer area is compensated by a proportionate temperature rise.

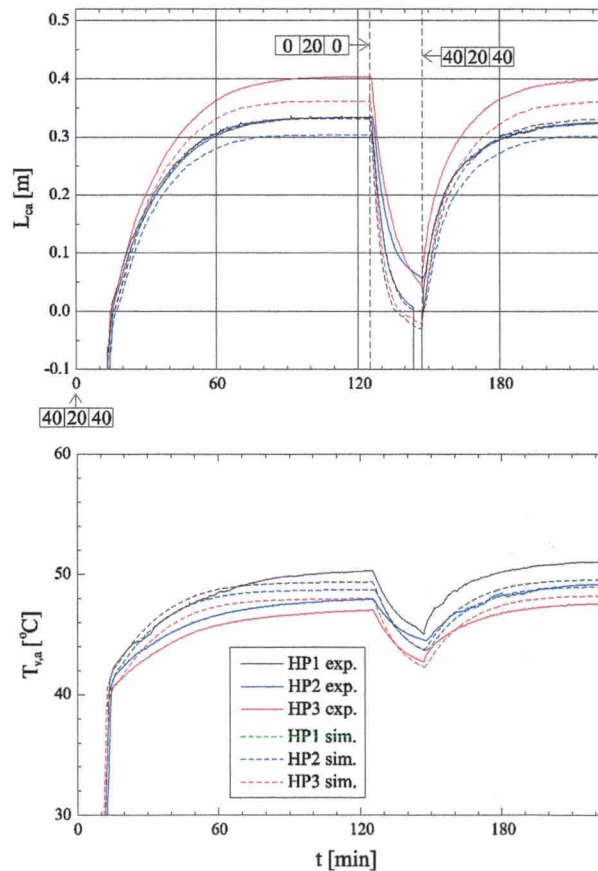


Fig. 7.11 - Test performance Run A

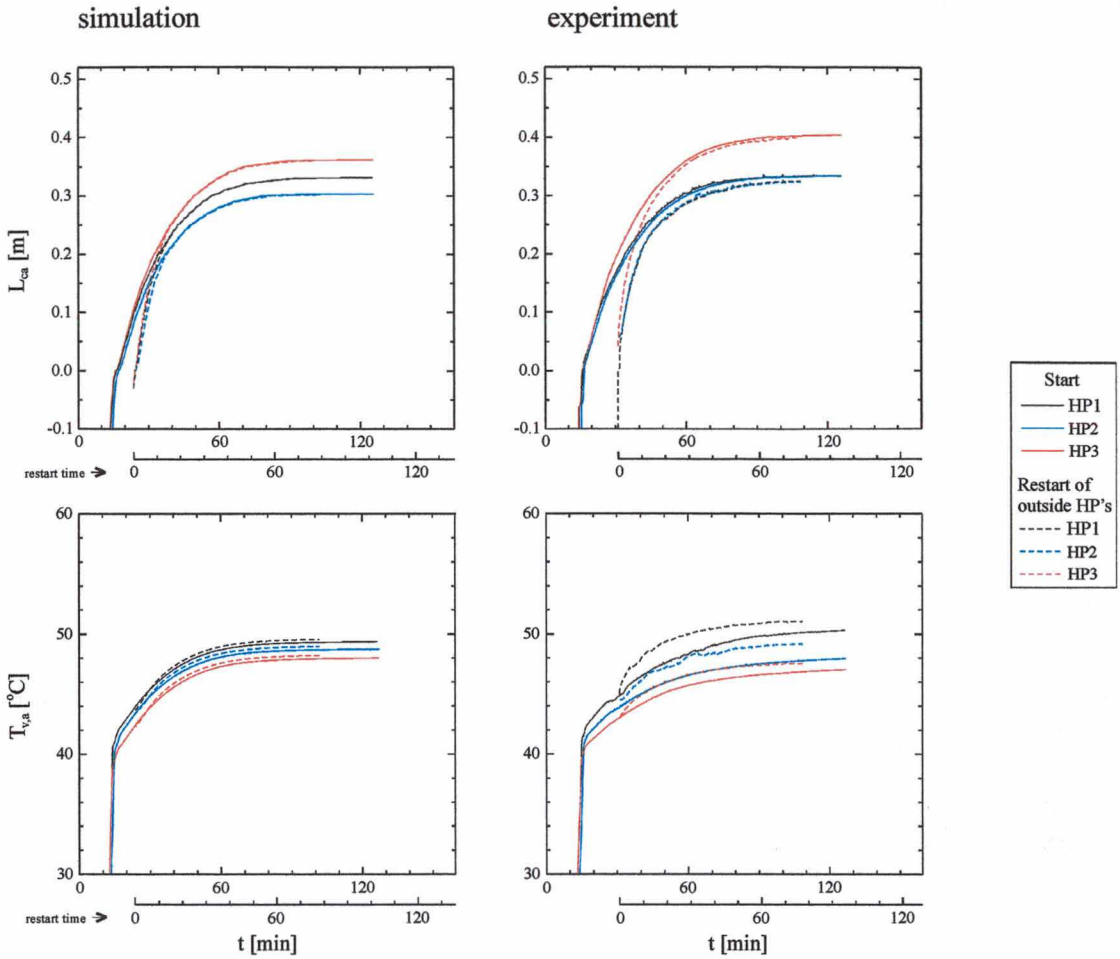


Fig. 7.12 - Operating point hysteresis between the start of all heat pipes and the restart of the outside heat pipes (HP1 and HP3) after temporary switch-off of their heat loads

3. If the front retreats because of a heat load reduction as in run A, the re-established operating point under the same heat load conditions will be different. The operating temperature will be higher (1 to 2 °C in Fig. 7.12), and the active length will be somewhat lower. Hence a kind of hysteresis can be stated. To a lower extent the simulation results confirm this phenomenon.

4. The still operative heat pipes show opposite reactions to the failure of the first heat pipe. The reaction of the near pipe is a pronounced once-through oscillation: at first a retreat of about one fifth of the former length, then an advance of three fourths of the initial amplitude, followed by a smaller retreat. The front continues fluctuating with a relatively high frequency of about 0.0125 Hz around a gradually decreasing mean value. The front in the distant heat pipe, however, pushes forward initially. The temperature evolution after failure, obtained at the last measuring points before the condenser end (Fig. 7.14), confirms this opposed behavior. This effect, again, is more pronounced, if the fronts were previously close to or at maximum length.

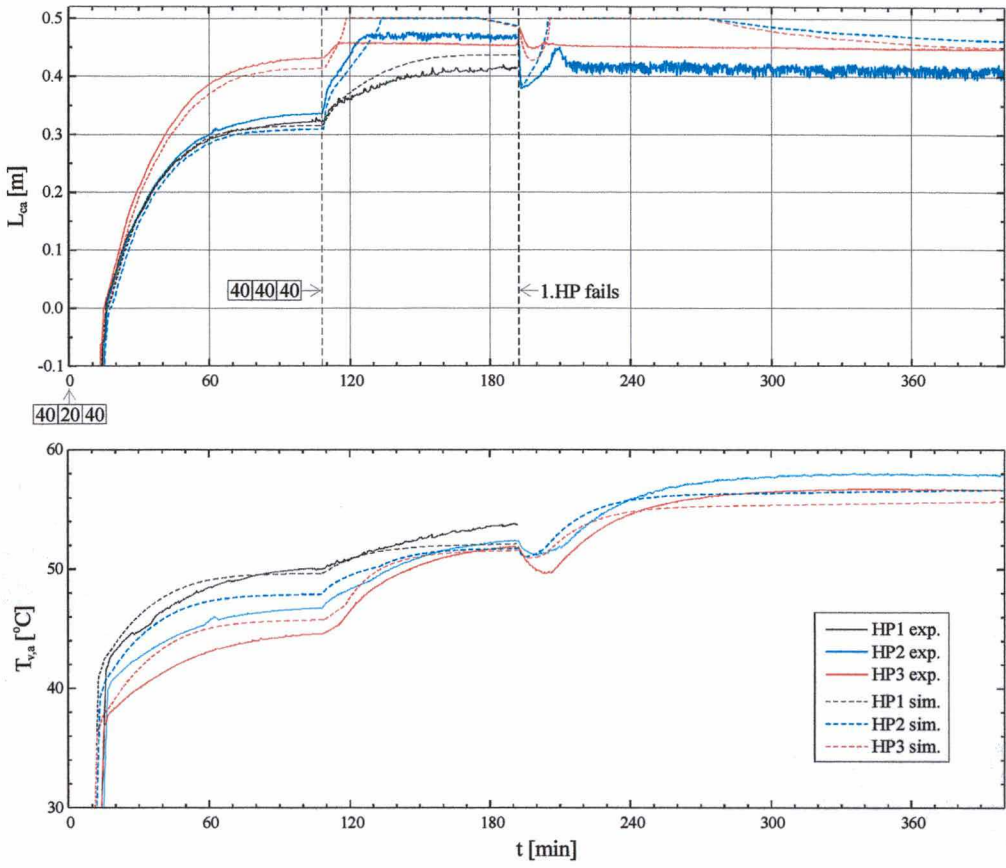


Fig. 7.13 - Test performance Run B

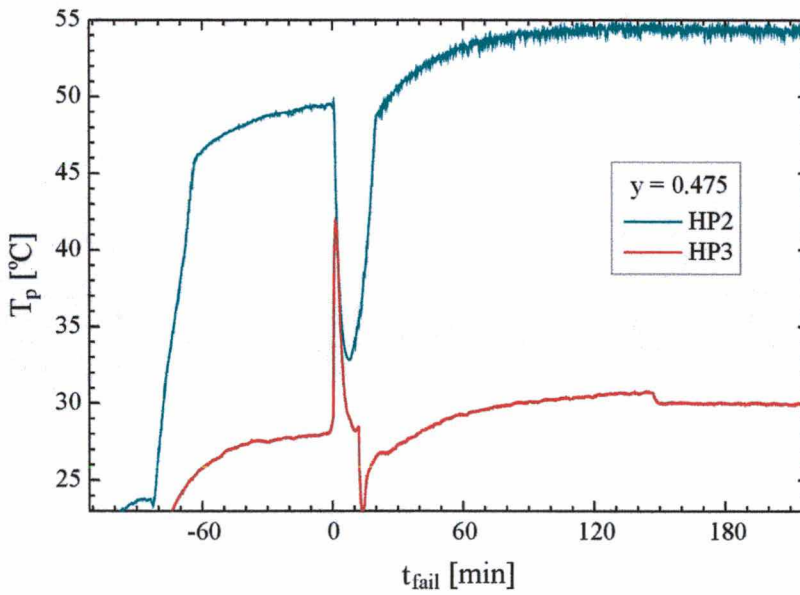


Fig. 7.14 - Condenser end temperature responses of HP2 and HP3 to the failure of HP1 (Run B)

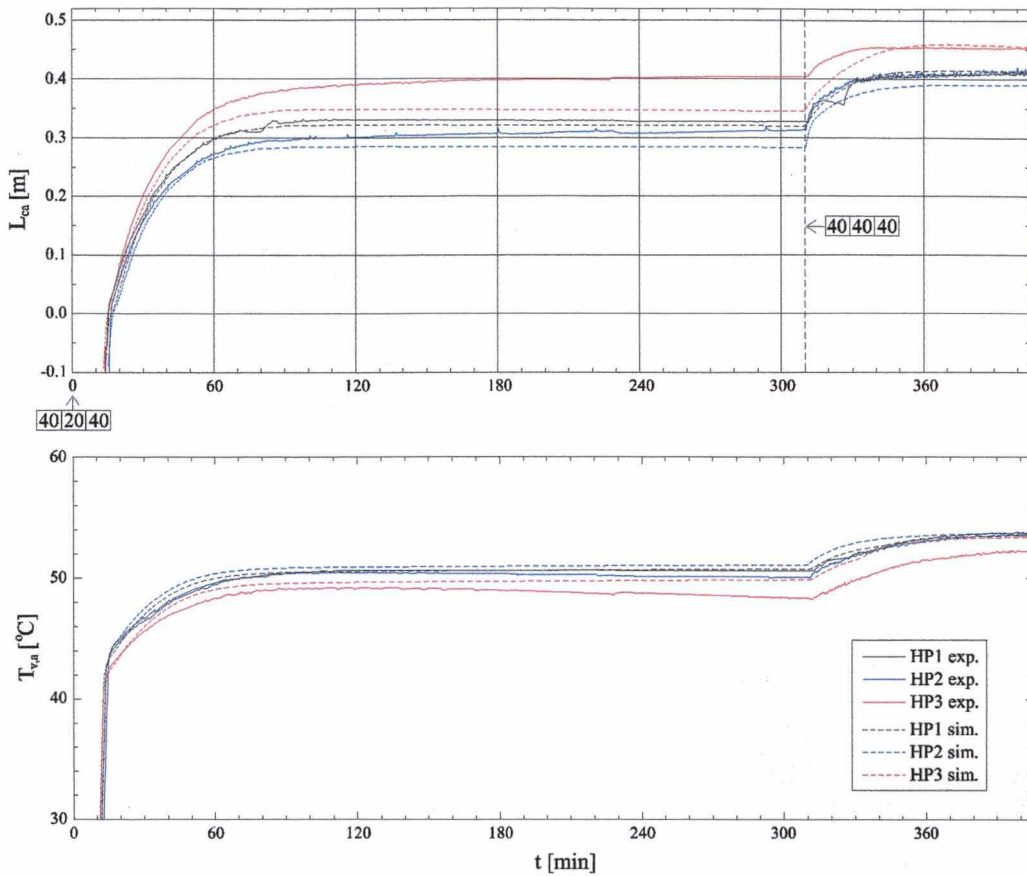


Fig. 7.15 - Test performance Run C

5. A remarkable heat dissipation capability of the radiator shows run D, where the failure occurs at a uniform heat load of 3×35 W. After the failure both operative heat pipes present a shorter active length than during the previous normal operation with all three pipes at 40 W, but at the same time a lower operating temperature. This is evidence of a time-consuming, but benign diffusive adjustment inside the vapor space. It shows that, depending on the history of operation, an apparently overcharged system can reach a satisfactory and stable operation after some time.

6. Direct comparison between runs E and F show that in the case of the slitted radiator the fronts approach the condenser end more rapidly under the same heat load conditions. The values of active lengths **and** operating temperatures are larger and stay closer together, at least before the maximum extent is reached. Enhanced thermal coupling between the heat pipes through the transversal sheet strips homogenizes the conditions in the active zones for unequal heat loads, but on the other hand turns the operation more critical, as the effective radiating area is reduced. The critical behavior of the slitted radiator can also be noted from all the responses of operating temperature and front location to any kind of heat load changes, as they are more pronounced.

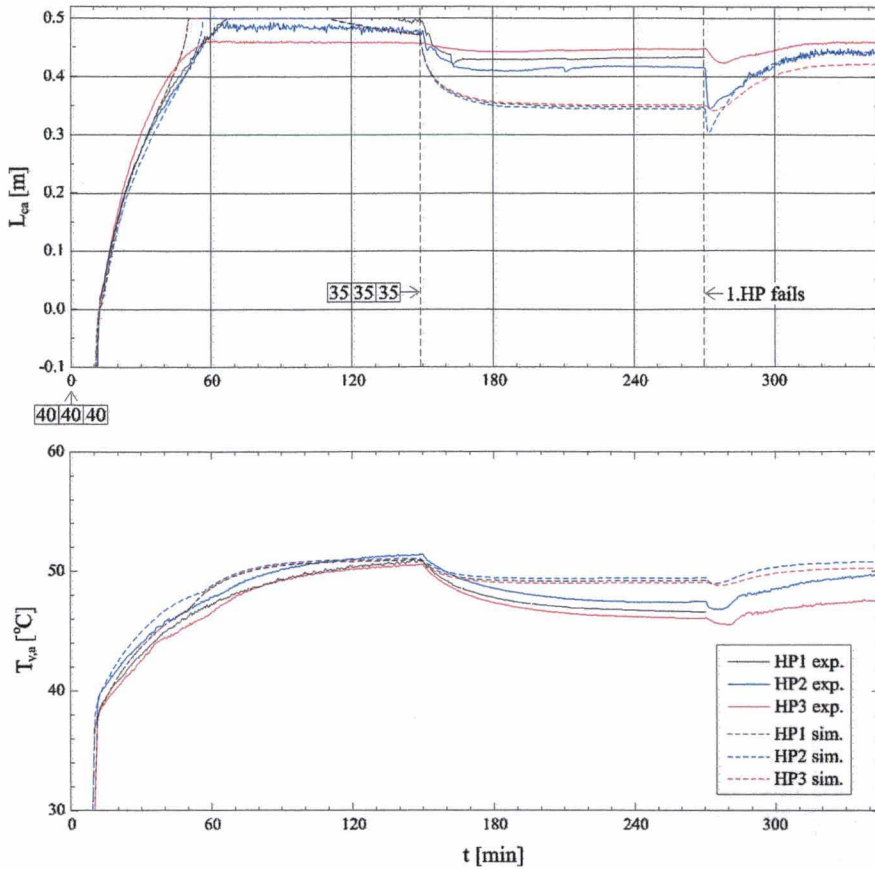


Fig. 7.16 - Test performance Run D

7. In most cases shunting of heat to the neighbor through the radiating sheets, when different heat loads were applied, was camouflaged by the different gas inventories. Yet one situation reveals this effect clearly, that is when the middle heat pipe in the slitted radiator run was lowered to 20 W. The heating of the inactive condenser zone by the neighbors induces the middle front to retreat unproportionally. The operating temperature of the concerned heat pipe is clearly higher than the other operating temperatures, although the applied heat load is only half.

On making a general comparison between simulation and experiment it can be stated that the numerical results represent well all features that were observed in the real system. The simulation shows a more flexible and straightforward dynamic behavior, when the vapor/gas front is close to the condenser end. Apart from the distinctive peaks the experimental curves show a certain stiffness in this region, though accompanied by pronounced oscillations especially when the radiator is slitted.

A relatively strong discrepancy was noted in the performance of the third heat pipe (HP3). The deviations from the predicted active lengths and operating temperatures are considerably larger

compared to the other heat pipes. But a clear abnormality appears in all test runs, when the transient wall temperature profiles of this heat pipe are observed. An example is given in Fig. 7.19. For any heat load the profiles show a much stronger and progressive decline after 40 cm of condenser length, even when the maximum condenser length has obviously been reached, so that these curves show a convex runout in the direction of the condenser end, in contrast to the concave curve behavior of the other heat pipes. It seems as if there is a heat loss at the end of HP3, though not to the reservoir, as can be generally certified by a relatively lower reservoir temperature (see appendix A3). So the hot vapor is obviously not able to reach the condenser end, especially when the gas inventory is relatively low.

Fig. 7.19 primarily aims to illustrate numerical and experimental wall temperature profiles for the overload condition. Run E was chosen, as it has a succession of increasing power steps per heat pipe, virtually no delay between experiment and simulation during start-up, and it shows the front reaction in the failure mode.

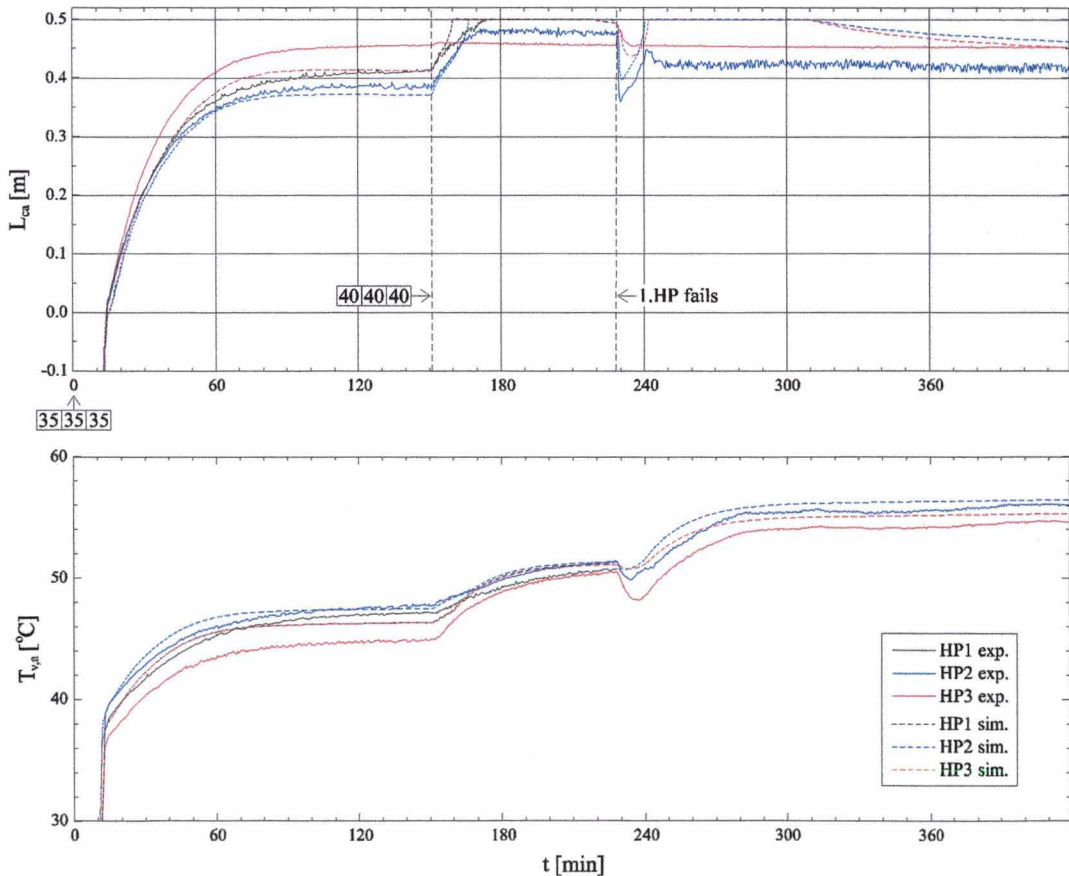


Fig. 7.17 - Test performance Run E

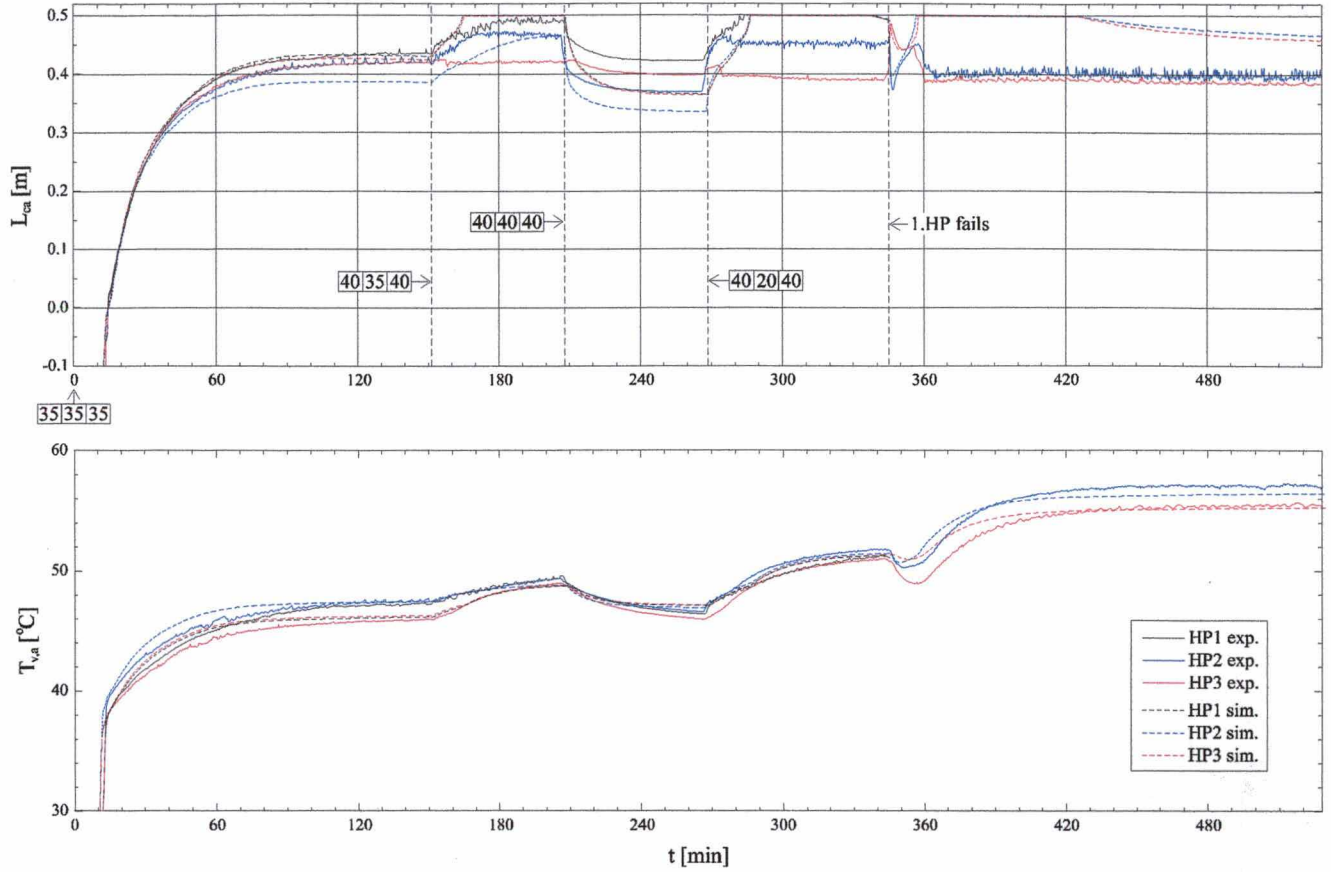


Fig. 7.18 - Test performance Run F (slitted radiator)

For active lengths of up to 40 cm the numerical profile agrees well with the experimental one. A slight anticipation exists due to fact that the numerical flat front causes a stronger initial decline of the wall temperature gradient further downstream. The greater this anticipation, the lower is the evaporator temperature, which is coherent, as more heat transfer area is exposed and the thermal conductance increased. The gradual dislocation and flattening of the temperature drop leads to a finally flat line, when the numerical active length touches the condenser end. In the real case the profile never becomes completely flat. A certain final curvature near the condenser end is reached and maintained in the following. Just the temperature level of the whole profile rises. This is the reason for the typical level below the maximum condenser length that the experimental active length reaches at overload conditions. The larger the wall temperature gradient, the bigger the observed amplitude of a longitudinal oscillation of the profile. The movement of the profiles during the characteristic peak after the failure event is shown in a fine time resolution and with guiding marks in the appendix, including the minimum level for each heat pipe. When after some time the numerical front starts to return from the condenser end, the real wall temperature profile is seen to coincide with the again steepening numerical profile at a

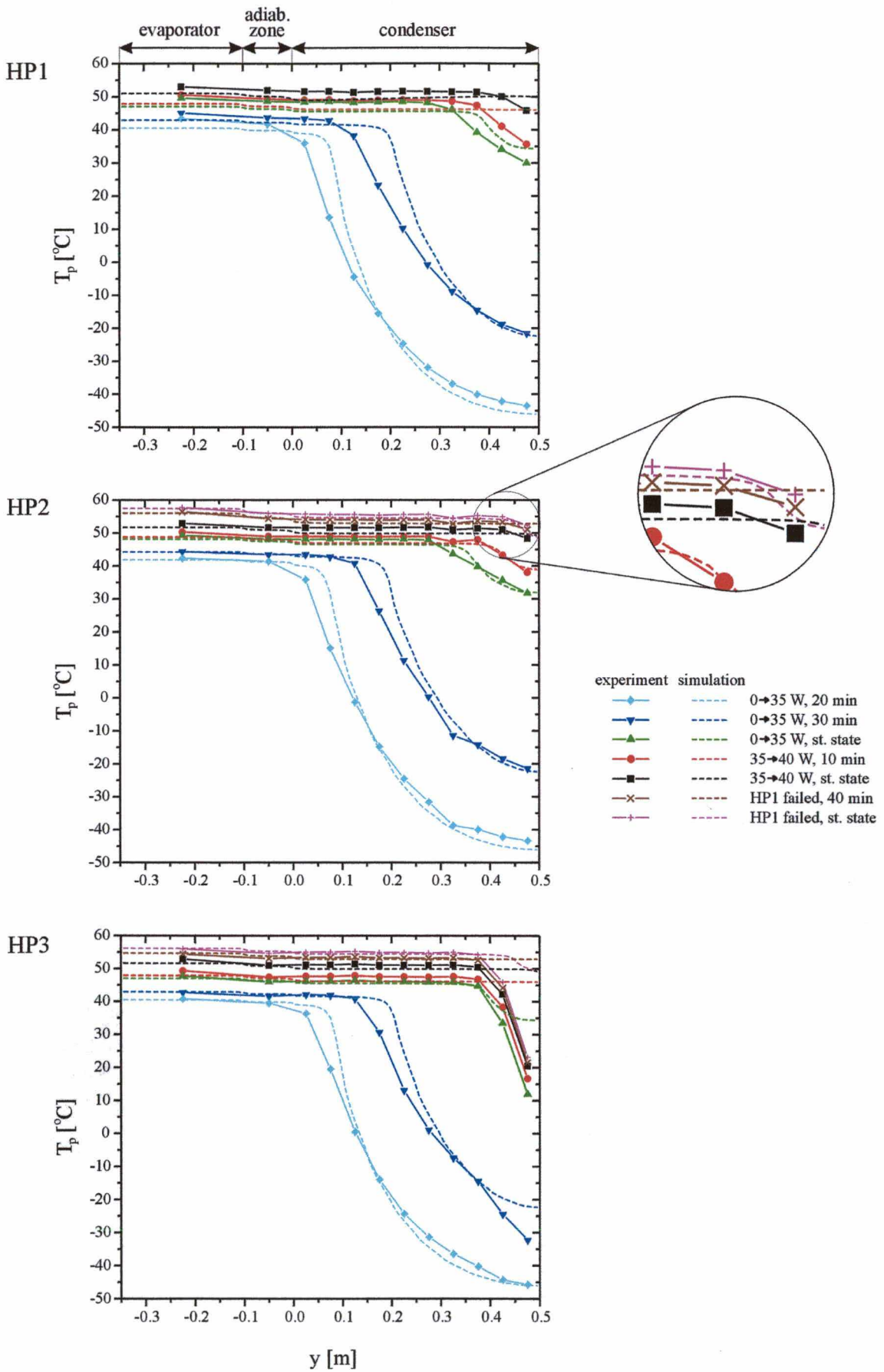


Fig. 7.19 - Comparison of experimental and numerical wall temperature profiles of the radiator heat pipes (Run E)

correspondingly higher temperature level. The agreement continues thereafter. Even in the experimental profile an increase of the gradient is perceptible in the uppermost curve of the HP2 chart (see detail in Fig. 7.19). If the test runs had been continued for more time, this factual front retreat would certainly have been identified more clearly.

The interpretation of results near the condenser end generally has to be taken with some benevolence, as the numerical curves as well as the computed experimental active lengths inherit their uncertainty from a flat front model. As related in literature and also detected earlier in the present investigation, phenomena occurring in the last 10 % of the condenser length are hardly explainable by such a simple model and certainly need a two-dimensional diffuse front model. In the following the validity of the developed theoretical tool will be confirmed by a more accessible analysis of the single GLHP test results.

7.6 Experimental single GLHP setup for tests with convective cooling

A setup for a single GLHP, similar to the those in the radiator, has been prepared in laboratory in order to get an insight into the dynamic vapor/gas front behavior under forced convection. The differences are a 40 % shorter evaporator, the lack of an adiabatic zone and a smaller gas reservoir in accordance with the different boundary condition. The design criteria for the reservoir are the parameters cited in Table 5. The gas inventory was unintentionally surpassed by 4.3 %, so that the real value during the tests is **144 mg**. The reservoir-to-condenser volume ratio here is only 2.82.

The heat pipe was heated by a skin heater that was bonded by thermal cement directly onto the evaporator surface and completely wraps up this section. On the condenser side the heat is removed by a stream of compressed air that is guided through a tight refrigeration jacket made of stainless steel. Fig 7.20 shows details of the assembled parts in the vicinity of the heat pipe. A supporting structure was especially designed to lift the heat pipe and align it in horizontal position by four nylon screws.

The heat pipe was equipped with 17 thermocouples that had been previously calibrated in an insulated water-filled stirred mug, at ambient temperature, at 60 °C and at the ice point. At the evaporator 4 thermocouples were located at two axial positions below the skin heater, as an axial distortion of the axial evaporator temperature profile was expected due to a relatively high external condenser heat transfer coefficient and the short distance from evaporator to condenser.

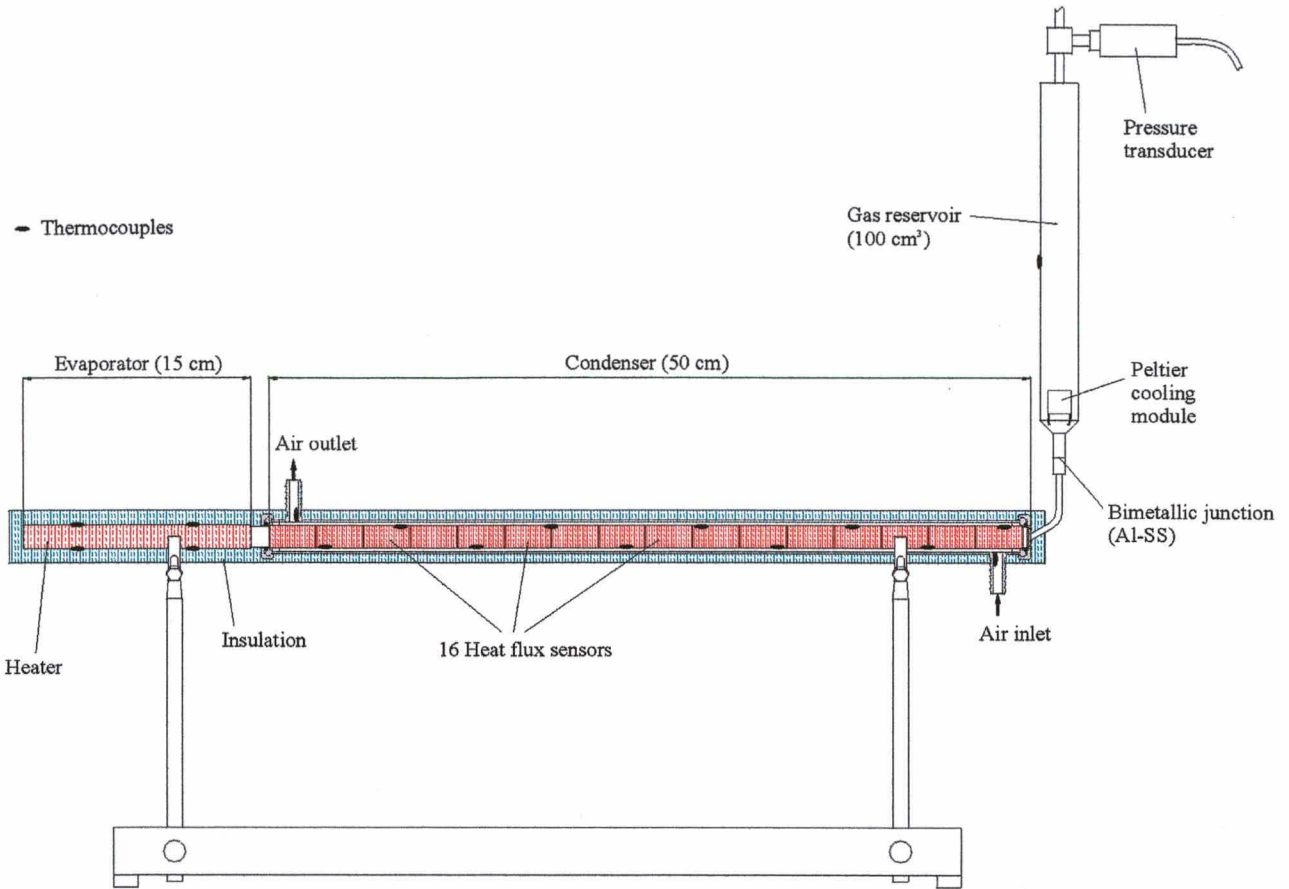


Fig. 7.20 - Assembly of temperature and heat flux sensors, heater and cooling devices for the single GLHP experiment

Two thermocouples were fixed on top of the evaporator in order to detect incipient dry-out. Another 10 thermocouples were fixed at equidistant positions, alternately at the bottom and at the top of the condenser surface. This arrangement was provided to reveal gravitational influence on the liquid columns in the axial grooves by monitoring temperature differences between top and bottom positions. Puddling of liquid at the bottom part of the pipe was expected, but this effect was hardly perceptible. One thermocouple was bonded on the outer surface midway on the gas reservoir, and one thermocouple was introduced through a small drilled hole into the channels of air inlet and air outlet muff respectively.

The entire condenser (together with the condenser thermocouples) was covered by 16 thin embracing heat flux meters. These sensors work due to the principle of the tangential thermoelectric effect [52]. They are laminates produced in a photolytic process and are approximately 0.5 mm thick. In this way the whole heat flux that left the condenser could be recorded, and furthermore an additional indicator for the detection of the diffuse front position was provided. The flux meter and thermocouple wires were guided through the jacket at two

feed-through locations near the extremities of the jacket. They were connected directly together with the pressure transducer output to two slots of the HP 34970A data acquisition system.

A Peltier type cooling module with a cooling power of 3.7 W was bonded by thermal cement at the entrance of the reservoir cylinder. Normally the action of a simple ventilating fan was sufficient to maintain the reservoir at constant (controlled) ambient temperature, unless hot vapor approached the condenser end. In this case the module was switched on to assist at the cooling of the reservoir.

The cooling jacket was constructed in such a way that it could be removed from the heat pipe. Further a minimal and low conductive contact to the heat pipe surface was assured. The jacket actually is a simple steel cylinder with two flanges welded on both sides. The flanges have pipe threads on the outer surface and a 45°-chamfered hobbed sealing surface inside. Knurled nuts press O-rings against these sealing surfaces and at the same time against the perimeter of the heat pipe, thus closing the annular refrigeration channel and fixing the jacket on the pipe.

With the heat flux meters bonded on the condenser a gap of only 2 mm was formed to the inner wall of the cooling jacket. The intention was to guarantee a turbulent air stream (Re about 3000) inside the annular channel and a temperature difference between air inlet and outlet of at least 10 K even at the lowest scheduled heat load. This difference is sufficient to allow the uncertainty of the air thermocouple measurements (up to ± 0.2 K) to be neglected. With the temperature difference between the two jacket muffins and the measured air flow rate it was possible to determine the outgoing condenser heat flux in a conventional way. However, it is important to mention that the rather high air velocity led to a temperature drop at the air outlet, as it forms a throat in the cross section of flow. At the design air throughput of 80.6 liter/min this drop was measured to be 0.75 K. Consequently this value was added to all scanned values of the air outlet temperature. As the air was introduced at the condenser end, the condenser was cooled according to the countercurrent flow principle. This means that the air stream was opposite to the direction of heat propagation through the heat pipe. This type of cooling is a lot more favorable, as it facilitates a more uniform convection heat transfer with an increasing air temperature next to an increasing wall temperature in flow direction. Co-current flow cooling is also not recommended for GLHP's for the following reason: It enhances the axial conductivity across the vapor/gas front by providing an additional (convective) heat path from the active to the inactive zone.

The airflow was measured by an airflow meter with a floating indicator disc, as shown in Fig. 7.21. It was placed in the line between the compressed air valve and the air inlet of the

jacket. The airflow could be controlled in the range of $\pm 2\%$. The indication of the flow was in normal-liters per minute, referring to $20\text{ }^\circ\text{C}$ and sea level. As the tests were carried out at higher temperatures and under ambient pressures of around 950 mbar, a correction had to be made to get the real air throughput \dot{V} according to the following formula:

$$\dot{V}_1 = \dot{V}_0 \sqrt{\frac{p_0 \rho_1}{p_1 \rho_0}} \quad (\text{index 0: normal conditions; index 1: real conditions})$$

In order to keep heat losses to the environment low the heater was sheathed by a layer of epoxy resin, and the whole heat pipe body including the refrigeration jacket was enveloped by 15 mm of polyurethane foam.

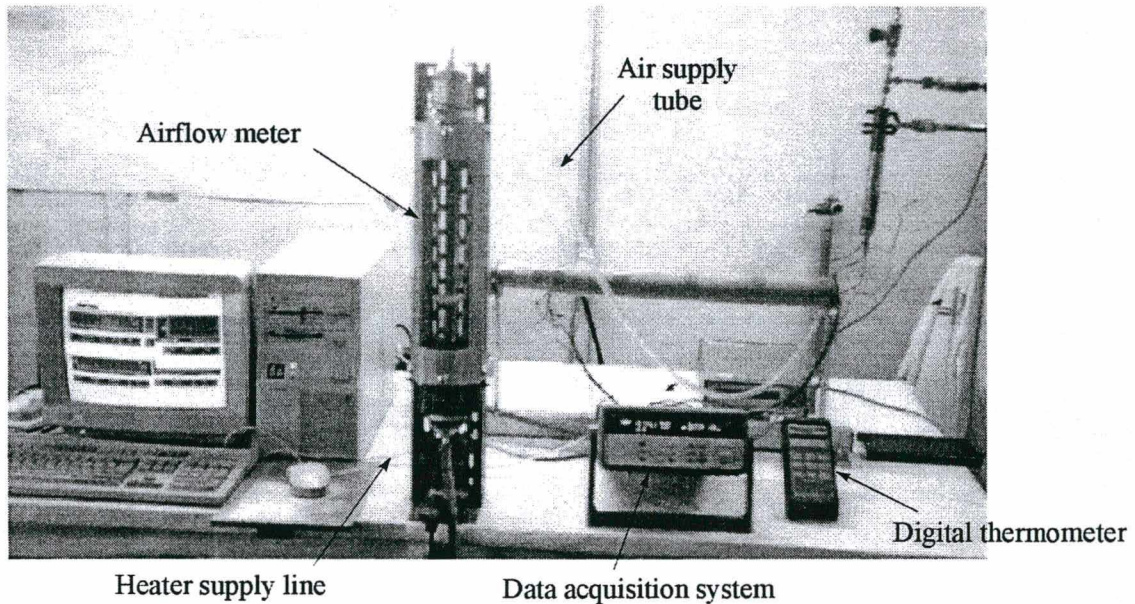


Fig. 7.21 - Front view of the experimental setup for single GLHP tests

7.7 Single GLHP test results and comparison with simulation

Unlike the radiator tests in vacuum, where the heat entrance area and adiabatic zones could effectively be protected against heat losses by multi-layer insulation, in the present case the heat flux that was actually transferred by the heat pipe differed appreciably from the power applied by the heater. The system also lost heat through the walls of the cooling jacket, so that the heat flux obtained from the measurements of air inlet and outlet temperatures was always less than the

heat flux that actually left the condenser, according to how much the active zone developed into the condenser. These two heat leaks had to be evaluated carefully in order to assure boundary conditions for the simulation program that were comparable to the real ones.

Initially it was planned to determine the first heat leak from the sum of heat portions obtained by the heat flux meters which would give the total heat emerging from the condenser. Unfortunately the precision of these sensors was not good enough (uncertainty of approximately 5 % of the nominal value), and furthermore two of them ceased to function. However, by chance another method was discovered to estimate this heat loss, using some data from an early test that had been rejected for further analysis. In this test cold water was used as the cooling agent. The consequence was that the vapor/gas front was not able to develop into the condenser, even at maximum heat loads, because the external heat transfer coefficient was too high, roughly 10 times the value for air cooling. So the heat was already completely removed at the beginning of the condenser. But exactly this fact made it possible to determine the heat output from the water inlet and outlet temperatures, and consequently the first heat leak. The second leak was blocked, as water cooling was so effective that one could assume that there was no heat transfer from the condenser to the jacket. Measurements at different heat loads gave a heat loss estimate of 8 %. Hence the heat load that was established as data input for the simulation program was 0.92 times the nominal value.

A comparison of the air temperature related heat outputs at various steady-state regimes, for all runs 0 to 3, to the now corrected heat pipe throughputs revealed that the second heat leak was of the order of 7 %. As this leak was also seen to be proportional to the heat flux, it was considered in the simulation by simply enhancing the external heat transfer coefficient by the factor 1.07.

In order to avoid excessive effort to model the convective heat transfer, the simulation assumed that heat left each condenser wall element according to the boundary condition of the third kind. Hence this energy component could be included in the source term of every element balance, if the heat transfer coefficient as well as the temperature of the adjacent air flow element were known. For this purpose an algorithm had been developed that is able to estimate a discrete air temperature profile from given air inlet and outlet temperatures and $n+1$ wall temperatures at a series of equidistant measuring points. It is not required to know the value for h_{ext} ; the only condition is that it has to be constant. A detailed derivation of this algorithm that leads to a set of n quadratic equations for n air temperatures midway between two wall temperature positions is given in appendix A2. With the estimated air temperatures an external heat transfer coefficient for each steady-state could be determined according to the following expression:

$$h_{\text{ext}} = \frac{\dot{m}c_p(T_{\text{out}} - T_{\text{in}})}{P \sum_{j=3}^{12} (T_{pj} - \bar{T}_{\text{air},12-(j-1)})} \quad \text{with} \quad \bar{T}_{\text{air } i} = 0.5(T_{\text{air } i} + T_{\text{air } i-1})$$

As in the derivation of the algorithm the axial coordinate points in the direction of the air flow, in the equation above the indexing of \bar{T}_{air} is seen to be opposite.

Already corrected for the heat loss through the cooling jacket, the convection heat transfer coefficient was determined to be **97 W/m²K**. This value virtually did not depend on the heat load, so it was taken as a mean value for the following simulations of test runs 1 and 3 that were contrasted with the experimental results. For the evaporator film coefficient the same value was taken as in the radiator simulations (6500 W/m²K). For the condenser film coefficient a global mean value of all 3 radiator heat pipes was adopted (3700 W/m²K), since the single GLHP tests did not dispose of vapor space temperature measurements.

The test runs 1 and 3 were found to be sufficient to validate the vapor space model as well as the gas balance approach that extracts the flat front position from experimental data. The simulated operating points at various heat loads, that is 20 W, 30 W, 40 W and 50 W, further the transients due to the stepwise increased and reduced heat loads showed a good agreement with the experimental curves, as shown in Figs. 7.22 and 7.23. The figures present a set of four charts that include two additional parameters to be evaluated. In order to verify the applicability of the model in a more detailed way this time the simulated and experimental transients of dimensionless reservoir gas content and reservoir vapor pressure have tentatively been taken into consideration. The additional parameters could be determined, as in consequence of the computed active condenser length an estimate of the condenser gas content was available:

$$m_{g,c} = \frac{A_v}{R} \frac{p_t - p_v(T(L_c))}{T(L_c)} (L_c - L_{ca})$$

and consequently the gas mass and vapor pressure in the reservoir:

$$m_{g,r} = m_g - m_{g,c} \quad \text{and} \quad p_{v,r} = p_t - (m_g - m_{g,c}) \frac{RT_r}{V_r}$$

As the primary validation criterion, however, remains the operating temperature, T_{va} . The other parameters are derived from this value and an extrapolated condenser end temperature. Note, even T_{va} is not a directly measured value, but deducted from the measured total pressure.

Nevertheless it should be clearly stated at this point, that with the gas inventory being constant in all single GLHP tests the validity of the Riedel-Plank-Miller saturation pressure equation (6.1) could be affirmed, as well as the precision of the total pressure indicated by the pressure sensor. This was possible by measurements of the total pressure and comparative calculations of saturated vapor and gas pressures at different ambient temperatures (between 22 and 28 °C), when the heat pipe was not operating.

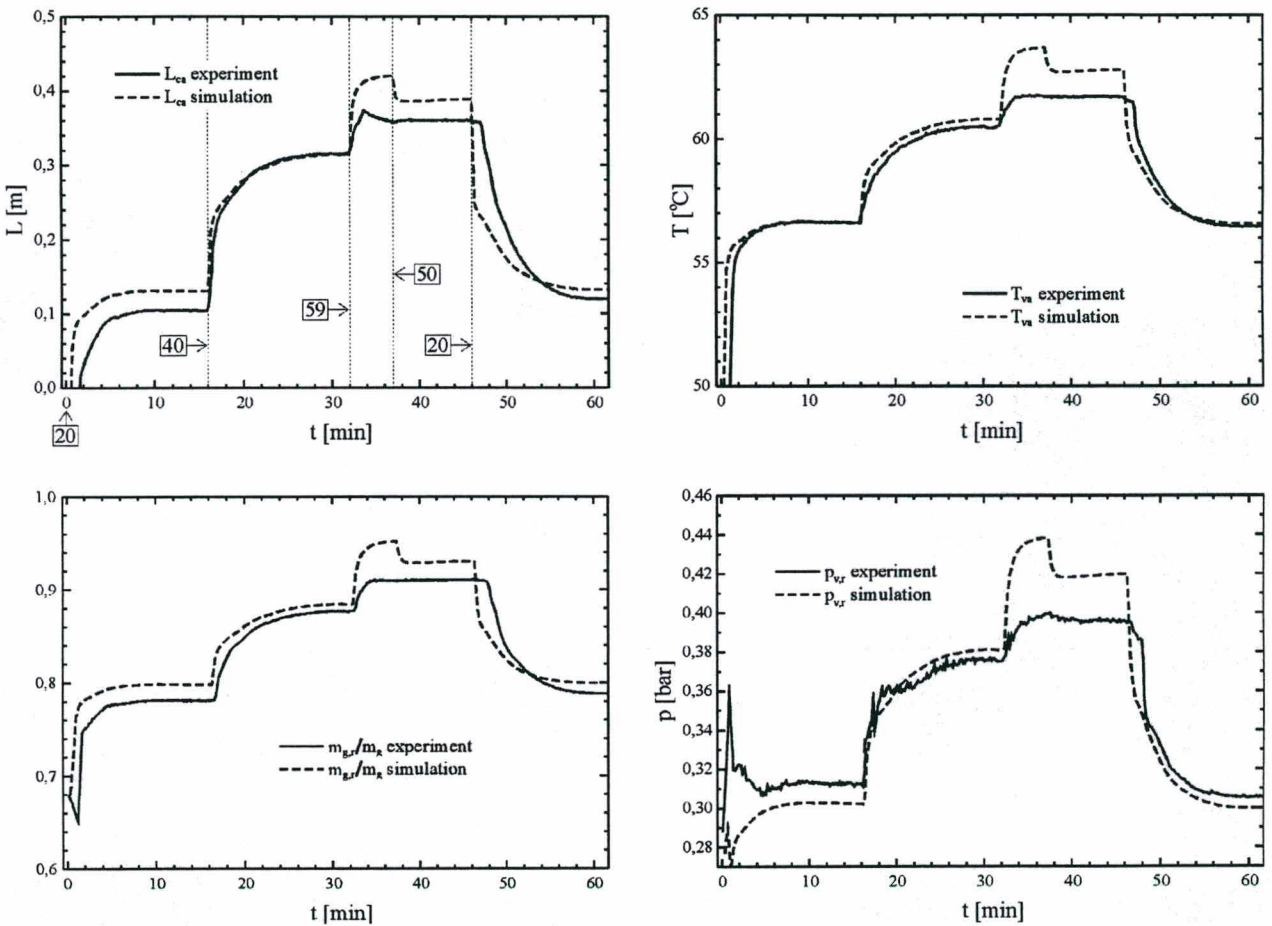


Fig. 7.22 - Test performance Run 1

On examining the figures the best conformity in both runs is noted at a heat load of 30 W. This is believed to be due to the best agreement with respect to the fixed value for the condenser film coefficient which for other heat loads is obviously different. If there had been a proper correlation for this coefficient, the result would have probably been better. An interesting detail can be observed for both numerical and experimental cases during start-up. Both curves show a peak, yet with different heights. As seen more clearly in Fig. 7.22 there was initially a rush of vapor into the reservoir accompanied by a reduction in reservoir gas content. However, at start-

up conclusion this temporary runaway behavior disappears from the curves, and they develop in the expected way.

Conspicuous deviations between experiment and simulation can be generally seen at the beginning of operation, and when the heat load rises to 59 W in run 1. In the first case, as usually expected, the real system needs more time to overcome additional thermal inertia, such as that of peripheral parts of the experimental assembly. In the latter case (seen in Fig. 7.22) the real system suffered dry-out, since the boiling limit has been surpassed. Of course, the model was not intended to cope with this phenomenon. So the numerical curves follow that heat increase in an undisturbed way. After the subsequent drop to 50 W (a heat load below the boiling limit) the heat pipe still seems to continue in a rather unstable operation mode, as the experimental curves remain on a relatively high level for some time, even after a distinct heat load drop to 20 W. This difficulty of the heat pipe to reprime and return to a stable operation after dry-out becomes more evident from the evaporator temperature behavior after the 59 W step (Run 1 in appendix A4).

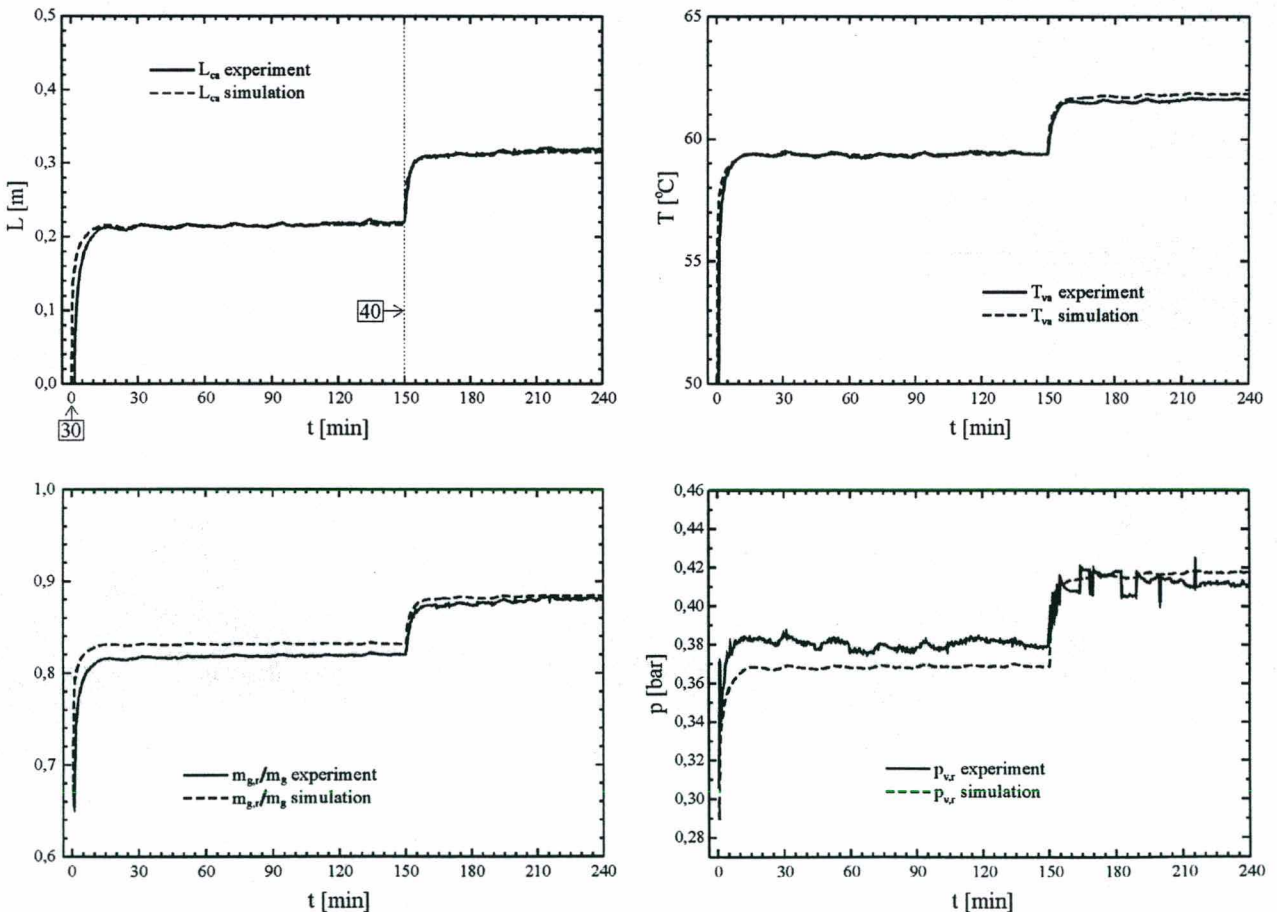


Fig. 7.23 - Test performance Run 3

Test run 2 succeeded to meet a heat load that corresponds to the boiling limit of this heat pipe, that is 54 W. That the “bull’s eye” was hit can be seen from a widely oscillating evaporator temperature around a nearly constant but much higher temperature than before; yet the temperature, during the time of observation, did not increase unboundedly. Note, on the basis of this evidence the initial nucleation radius, r_n , could be evaluated in section 6.2, and it in fact fitted in the interval between the values cited in literature. With the radiator heat pipes a dry-out at design conditions was not observed. Even with a heat flux certainly higher than 54 W that had to be accommodated after failure in the near heat pipe, the evaporator temperature remained at a stable value of 58 °C on an average. Hence the radiator heat pipe evaporators were long enough to avoid the critical heat flux density.

The test runs 2 and 3 revealed another interesting phenomenon that has been reported but not properly investigated in literature [53]. This phenomenon actually does not contribute to the scope of the present study, but is quite relevant for thermal control aspects of electronic equipment on the base-plate. According to these long-term test runs it can be stated that after applying a certain stepwise initial heat load operating pressure and evaporator temperature never remain stable, even at steady-state conditions. The higher this step, the bigger the amplitude of periodic oscillations of the two parameters and the smaller the frequency.

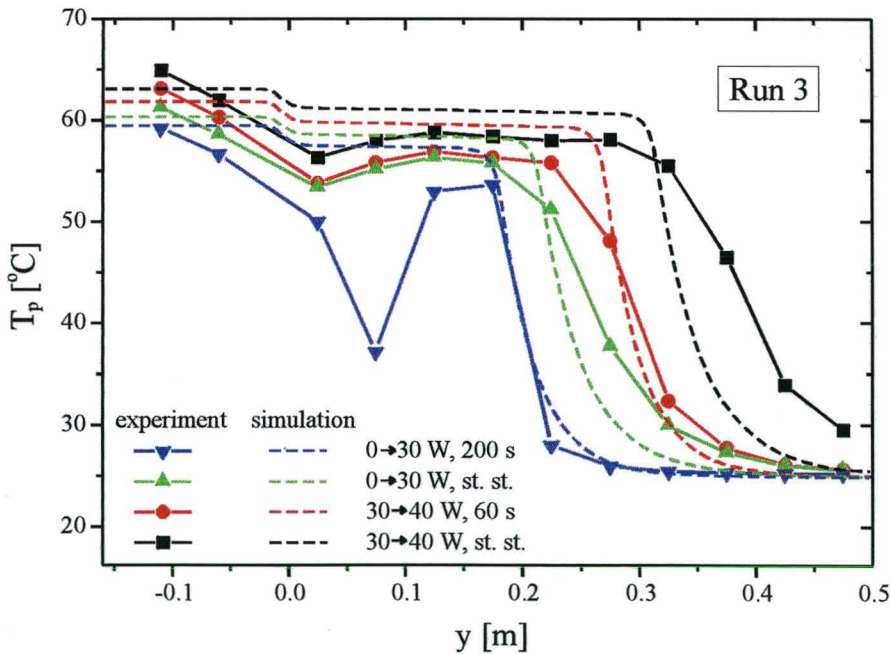


Fig. 7.24 - Experimental and numerical wall temperature profiles for two transient and two steady-state situations during single GLHP test run 3

Also for the single GLHP case an exemplary comparison between numerical and experimental wall temperature profiles has been selected in Fig. 7.24. A good agreement can be seen for the characteristic wall temperature drop close to the vapor/gas front, if the front is advancing. It has been mentioned earlier that a steepening of the front during its advance is typical and was explained by the moving front theory [18]. At steady state, however, the real drop is located further downstream, as the profile flattens and spreads more into the condenser. The distortion of the profile by the excessive temperature in the beginning of the evaporator and the following indentation at the transition to the condenser apparently has to be compensated in this way to maintain energy conservation over the whole heat pipe container.

7.8 Start-up characteristics in test and simulation

Since the model is capable of start-up simulation, it should also be validated in this respect. This particular operation mode can be made more visible, if the data are presented as shown in Figs. 7.25 and 7.26. There the evaporator temperatures and total pressures that are successively increasing are collected and related to each other. In this way the start-up gets especially enhanced against the rest of operation and the switch points become obvious. This is the point where the model switches from the start-up algorithm to that of the normal transient operation. In the figures it finally becomes visible that this happens at the moment, when the total pressure falls below the saturation pressure of the vapor at active zone temperature, or in other words, when the mean wall temperature of the evaporator exceeds its vapor temperature.

The idea for this way of representation originates from Sauciuc *et al.* [54], who in their experimental GLHP investigation realized that the operating or total pressure was developing due to two different consecutive characteristics. First the total pressure increases in a linear way according to the ideal gas law. After the switch point the total pressure follows the pressure curve of the saturated working fluid, yet with a certain horizontal shift. This shift is an indicator for the heat resistance of the evaporator. Furthermore it is inversely proportional to the internal evaporator heat transfer coefficient for a certain heat load in the case of a sharp vapor/gas front. That is the reason for the constant shift of the numerical curve, as long as the same heat load is applied, whereas it is larger and variable in the real case according to the width of a diffuse front.

The experimental curves show that in reality the transition is not as intermittent as the theory suggests. The gradually increasing importance of the vapor pressure gives the curves a hyperbolic like shape. Remarkable is the coincidence of experimental and numerical switch

points in the example taken from the radiator tests. The defined transition happens at exactly the same total pressure and evaporator temperature. In the single GLHP test the switch points differ by 22 mbar and 0.8 K because of the axial temperature profile distortion. Due to switching on in a cold space environment the radiator heat pipes take about 10 times longer to complete start-up.

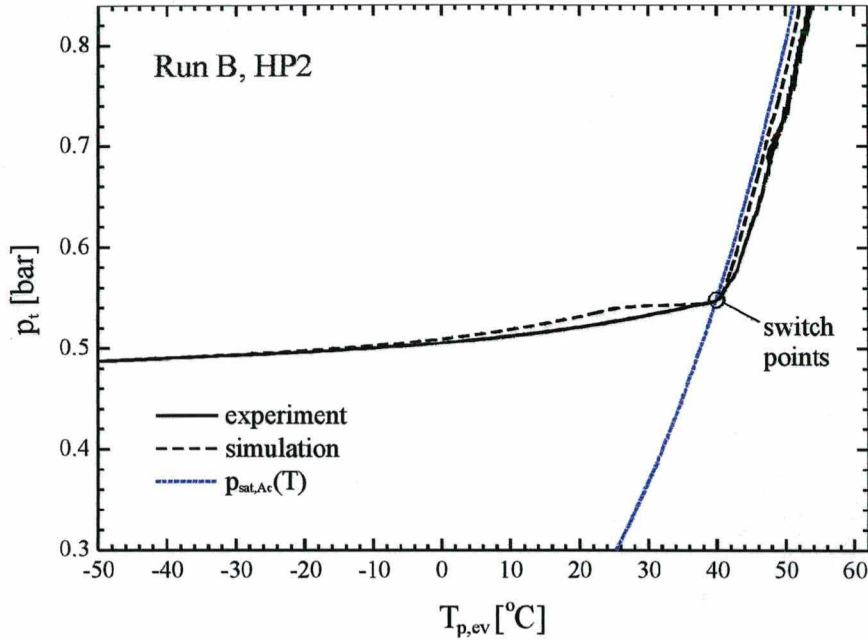


Fig. 7.25 - Start-up behavior of a radiator GLHP

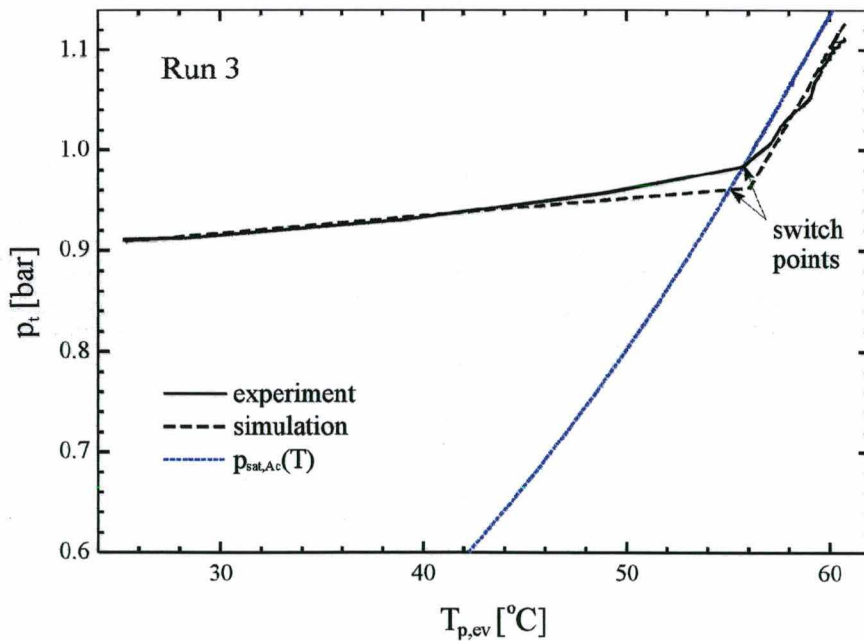


Fig. 7.26 - Start-up behavior of the single GLHP

Chapter 8

FINAL REMARKS

The results and discourses which have been compiled in this thesis reflect a 3 ½ year involvement in the theoretical and practical investigation of the dynamics of a gas-loaded heat pipe in particular and of a set of gas-loaded heat pipes functioning as crucial heat transfer elements in a satellite thermal control system. About half of the time was spent getting familiar with various theoretical aspects that nourish gas-loaded heat pipe models, to test some of the models, to tailor an appropriate one for the present case and finally to design a proper simulation program that was able to produce coherent results. Another 15 % of the time was taken up planning the experiments, about 20 % in the preparation and execution of the experiments and 15 % in the analyses of the read-out measurements.

During the theoretical phase it became clear that the designer of a gas-loaded heat pipe faces the problem of deciding which of the many models is the right tool to examine the object that he is about to create. So a checklist, that actually was a by-product of this project phase and is presented in a concise form in reference [55], is helpful to give more confidence in the choice of a simple GLHP model.

Nevertheless the present configuration of a GLHP with a separate non-wicked cold reservoir could not be sufficiently described by one of the available simple models. So an existent flat front model, developed only for the vapor space, was extended to consider mass transfer into a reservoir at prescribed temperature.

It was interesting to find out, that a simple flat front model, whose principle can be traced back to the first GLHP model ever developed, is able to describe well, what is happening inside the GLHP over a wide range of operation. It was in fact not necessary to know neither details about evaporation and condensation processes nor values of latent heat of vaporization of the working fluid to simulate this process of latent heat transfer. Just the vapor pressure saturation relation of the working fluid and empirically determined film coefficients were sufficient to fulfill the task. This shows that there actually is a relationship between the vapor pressure and the latent heat of a fluid (as for instance the Clausius-Clapeyron equation postulates), and that both are a function of the same parameter, the critical temperature.

When simulating the behavior of the radiator GLHP's, where special attention had to be paid to operation near and at overload condition, the feature of a vapor/gas front retreat was qualitatively represented. The model, however, showed a faster and stronger reaction of the front, when it was close to the condenser end. This is due to the limitations inherent in the flat front formulation itself. It became apparent that the experiment should have been continued for more time during the failure mode. The back flow effect was noted, yet quite weakly due to the restricted time of observation. Less costly future tests of a convectively air-cooled radiator will certainly provide the conditions to trace this effect better in a real situation. With radiator tests at ambient temperature the reservoirs including most of the feed tubes can be easily maintained at sink temperature. This is believed to be important to provide a better prediction by the simulation, as it was realized in the single GLHP tests.

Referring to the investigated axially grooved gas-loaded heat pipes in particular the following essential comments can be made:

- Among the operational limits of the heat pipe the boiling limit appeared to be the most critical one. Thus special attention has to be given to an appropriate length of the evaporator and also to a maximum allowable evaporator temperature, as these two parameters mainly condition that operational limit.
- The evaporator film coefficient of a certain GLHP did not reveal a dependence neither on heat load nor on noncondensable gas inventory. This confirms what had been found out by several investigators [56]. For the present case a mean value of $6500 \text{ W/m}^2\text{K}$ was determined. This value varied within $\pm 30 \%$ for the respective heat pipes.
- The condenser film coefficient showed a dependence on operating temperature and gas inventory, so that on the basis of these two parameters a correlation was formulated to consider this liability in the simulation. As an overall mean at medium heat load a value of $3700 \text{ W/m}^2\text{K}$ resulted from the analyses. Hence the evaporator film coefficient is about 1.8 to 2 times higher than the condenser coefficient. This result is in agreement with suggestions made in other investigations [57].
- The effective external heat transfer coefficient at convective cooling is more than 20 times higher than that at radiative cooling. This difference becomes evident from the shape of the wall temperature profiles in the respective test run sets. With a high external coefficient the temperature gradient near the vapor/gas front becomes larger, because the front itself gets sharper.

- As in the radiator tests the gas inventory of the same heat pipe changes from test to test, the following influence of gas amount could be detected: The lower the gas inventory, the lower is the evaporator temperature, but the stronger is the temperature response to heat load changes. Thus compared to the expected temperature control range, the evaporator temperature has a great sensitivity to deviations in gas inventory (T_{ev} 3 K higher, when m_g 12 % higher). This sensitivity, however, proved to be more pronounced with respect to the reservoir-to-condenser volume ratio. This was noted, when the evaporator temperature behavior of the radiator heat pipes was compared to that of the single GLHP.

The evaporator temperature control that could be obtained with the GLHP's in test was:

Radiator GLHP	between 44 and 60 °C for a heat load range between 10 and at least 60 W at a gas inventory of 220 mg (7.3 % overcharge)
Single GLHP	between 59 and 67 °C for a heat load range between 20 and 50 W at a gas inventory of 144 mg (4.3 % overcharge)

As far as the observed radiator performance is concerned, it can be stated that the system presented itself benign in the case of a failure of an outside heat pipe. When charging the system with 120 W, the heat load of the failed heat pipe was absorbed by the neighbors without a significant temperature rise of the still operative evaporators beyond the designed temperature range. Even additionally a slight ambient temperature rise of, let us say 10 °C, is possible. For a real application in satellites the base-plate with the dimensions used in this study, that is with the chosen heat pipe spacing, has to be made much more conductive. The temperatures that have been measured at the evaporator of the failed heat pipe exceeded 90 °C, which is not acceptable, if a real amplifier was mounted at this position. A solution to this problem would be a base-plate of the flat heat pipe type. This means not a solid plate, but a plate that contains a void with a working fluid and a wick to be able to quickly attenuate a hot spot in transverse direction.

REFERENCES

- [1] Agrawal, B.N.: Design of Geosynchronous Spacecraft; Prentice Hall, 1986.
- [2] Masumoto, H./ Kimura, H./ Ogushi, T./ Nakamaru, K./ Kanamori, Y.: Development of a VCHP/FCHP Radiator System for 3-Axis Stabilized Geostationary Satellite Application; *AIAA 20th Thermophysics Conference*, Williamsburg VA, Paper 85-1012, 1985.
- [3] Kelley, W.H./ Reisenweber, J.H.: Optimization of a Heat Pipe Radiator for Spacecraft High Power TWTAs; *Advances in Heat Pipe Technology, Proc. 4th Int. Heat Pipe Conference*, Pergamon Press, Oxford, pp. 505-516, 1981.
- [4] Marcus, B.D./ Fleischmann, G.L.: Steady-State and Transient Performance of Hot Reservoir Gas-Controlled Heat Pipes; ASME Paper 70-HT/SpT-11, 1970.
- [5] Edwards, D.K./ Marcus, B.D.: Heat and Mass Transfer in the Vicinity of the Vapor-Gas Front in a Gas-Loaded Heat Pipe; *ASME Journal of Heat Transfer*, Vol. 94, pp. 155-162, 1972.
- [6] Rohani, A.R./ Tien, C.L.: Steady Two-Dimensional Heat and Mass Transfer in the Vapor-Gas Region of a Gas-Loaded Heat Pipe; *ASME Journal of Heat Transfer*, Vol. 95, pp. 377- 382, 1973.
- [7] Sun, K.H./ Tien, C.L.: Thermal Performance Characteristics of Heat Pipes; *Int. Journal of Heat and Mass Transfer*, Vol. 18, No. 3, pp. 363-380, 1975.
- [8] Rice, G./ Azad, E.: Dynamic Characteristics of Heat Pipes; *2nd Int. Heat Pipe Conference*, Bologna, Italy, 1976.
- [9] Shukla, K.N.: Transient Response of a Gas-Controlled Heat Pipe; *AIAA Journal*, Vol. 19, No. 8, pp. 1063-1070, 1981.
- [10] Delil, A.A.M./ van der Vooren, J.: Uniaxial Model for Gas-Loaded Variable Conductance Heat Pipe Performance in the Inertial Flow Regime; *Advances in Heat Pipe Technology, Proc. 4th Int. Heat Pipe Conference*, Pergamon Press, Oxford, pp. 359-372, 1981.
- [11] Kimura, H./ Itagaki, H./ Sakurai, Y.: Transient Performance of Gas-Loaded Variable Conductance Heat Pipes with a Hot Reservoir; *Advances in Heat Pipe Technology, Proc. 4th Int. Heat Pipe Conference*, Pergamon Press, Oxford, pp. 589-600, 1981.
- [12] Bobco, R.P.: Variable Conductance Heat Pipes: A First Order Model; *Journal of Thermophysics and Heat Transfer*, Vol. 1, No. 1, pp. 35-42, 1987.
- [13] Antoniuk, D.: Generalized Modeling of Steady State and Transient Behavior of Variable Conductance Heat Pipes; *AIAA 22nd Thermophysics Conference*, Honolulu HI, Paper 87-1615, 1987.

- [14] Peterson, P.F./ Tien, C.L.: Numerical and Analytical Solutions for Two-Dimensional Gas Distribution in Gas-Loaded Heat Pipes; *ASME Journal of Heat Transfer*, Vol. 111, pp. 598-604, 1989.
- [15] Semena, M.G./ Baturkin, V.M./ Rassamakin, B.M./ Grechina, N.K.: Analytical and Experimental Study of Operating Characteristics of Low-Temperature Variable Thermal Resistance Heat Pipes; *7th Int. Heat Pipe Conference*, Minsk, Belarus, 1990.
- [16] Harley, C./ Faghri, A.: Transient Two-Dimensional Gas-Loaded Heat Pipe Analysis; *ASME Journal of Heat Transfer*, Vol. 116, pp. 716-723, 1994.
- [17] Faghri, A./ Harley, C.: Transient Lumped Heat Pipe Analyses; *Heat Recovery Systems & CHP*, Vol. 14, No. 4, pp. 351-363, 1994.
- [18] Chung, J.H./ Edwards, D.K.: Moving Gas Front Effects on Heat Pipe Transient Behavior; *Journal of Thermophysics and Heat Transfer*, Vol. 10, No. 1, pp. 76-82, 1996.
- [19] Peterson, P.F./ Tien, C.L.: Temperature-Distribution Analysis for Variable-Conductance Multi-Pipe Radiators; *9th Int. Heat Transfer Conference*, Jerusalem, Israel, 1990.
- [20] Faghri, A.: *Heat Pipe Science and Technology*; Taylor & Francis, 1995.
- [21] Nelson, L./ Sekhon, K.S./ Fritz, J.E.: Direct Heat Pipe Cooling of Semiconductor Devices; *3rd Int. Heat Pipe Conference*, Palo Alto CA, 1978.
- [22] Groll, M.: Heat Pipe Technology for Spacecraft Thermal Control; *Spacecraft Thermal and Environmental Control Systems*, ESA SP-139, 1978.
- [23] Hinderman, J.D./ Waters, E.D./ Kaser, R.V.: Design and Performance of Non-Condensable Gas Controlled Heat Pipes; *AIAA Progress in Astronautics and Aeronautics*, Vol. 29, pp. 445-462, 1972.
- [24] *Spacecraft Thermal Control Design Data*; ESA (TST-02), Revision 3, Vol. 2, 1986.
- [25] Kirkpatrick, J.P./ Marcus, B.D.: A Variable Conductance Heat Pipe/Radiator for the Lunar Surface Magnetometer; *AIAA 7th Thermophysics Conference*, San Antonio TX, Paper 72-271, 1972.
- [26] Mock, P.R./ Marcus, B.D./ Edelman, E.A.: Communications Technology Satellite - A Variable Conductance Heat Pipe Application; *AIAA/ASME Thermophysics and Heat Transfer Conference*, Boston MA, Paper 74-749, 1974.
- [27] Savage, C.J./ Aalders, B.G.M./ Kreeb, H.: A Variable Conductance Heat Pipe Radiator for MAROTS-Type Communications Spacecraft; *Journal of Spacecraft*, Vol. 16, No. 3, pp. 176-180, 1979.
- [28] *Thermal Control Handbook*; MBB-ERNO TB-TD3, Issue 2, 1985.

- [29] Moschetti, B./ Amidieu, M./ Tatry, B.: Design and Test of a Space Deployable Radiator; *15th Int. Conference on Environmental Systems*, San Francisco CA, Paper 851364, 1985.
- [30] Bobco, R.P.: Variable Conductance Heat Pipe Performance Analysis: Zero-to-Full Load; *Journal of Thermophysics and Heat Transfer*, Vol. 3, No. 1, pp. 33-41, 1989.
- [31] Chi, S.W.: Heat Pipe Theory and Practice - A Sourcebook; McGraw-Hill, 1976.
- [32] Peterson, G.P.: An Introduction to Heat Pipes – Modeling, Testing and Applications; John Wiley & Sons, 1994.
- [33] Beam, J.E.: Transient Heat Pipe Analysis; *AIAA 20th Thermophysics Conference*, Williamsburg VA, Paper 85-0936, 1985.
- [34] Colwell, G.L./ Modlin, J.M.: Mathematical Heat Pipe Models; *8th Int. Heat Pipe Conference*, Beijing, China, 1992.
- [35] Incropera, F.P./ DeWitt, D.P.: Fundamentals of Heat and Mass Transfer, 4th Edition; John Wiley & Sons, 1996.
- [36] Bobco, R.P.: VCHP Performance Prediction: Comparison of First-Order and Flat Front Models; *Journal of Thermophysics and Heat Transfer*, Vol. 3, No. 4, pp. 401-405, 1989.
- [37] Patankar, S.V.: Numerical Heat Transfer and Fluid Flow; Taylor & Francis, 1980.
- [38] Delil, A.A.M.: Limitations in Variable Conductance Heat Pipe Performance and Control Predicted by the Current Steady-State Model Developed at NLR; *5th Int. Heat Pipe Conference*, Tsukuba, Japan, 1984.
- [39] Edom, A./ Colle, S.: Simulation of a Transient Failure Behavior of a Space Radiator Based on Variable Conductance Heat Pipes; *28th Int. Conference on Environmental Systems*, Danvers MA, Paper 981582, 1998; also in: *SAE 1998 Transactions, Journal of Aerospace*.
- [40] Dunn, P.D./ Reay, D.A.: Heat Pipes; 4th Edition, Pergamon Press, Oxford, 1994.
- [41] Lapinsky, R.J./ Antoniuk, D.: Characterization of Aging Mechanisms in Aluminum/Ammonia Heat Pipes; *AIAA 26th Thermophysics Conference*, Honolulu HI, Paper 91-1361, 1991.
- [42] Delil, A.A.M.: Some Critical Issues in Developing Two-Phase Thermal Control Systems for Space; *11th Int. Heat Pipe Conference*, Tokyo, Japan, 1999.
- [43] Reid, R.C./ Prausnitz, J.M./ Sherwood, T.K.: The Properties of Gases and Liquids; 3rd Edition, McGraw-Hill, 1977.
- [44] Müller, R.: Personal Communication, Daimler-Chrysler Aerospace AG, Space Infrastructure Division, Bremen, Germany, 1999.

- [45] van Buggenum, R.I.J./ Daniels, D.H.W.: Development, Manufacture and Testing of a Gas-Loaded Variable Conductance Methanol Heat Pipe; *6th Int. Heat Pipe Conference*, Grenoble, France, 1987.
- [46] Bird, R.B./ Stewart, W.E./ Lightfoot, E.N.: *Transport Phenomena*; John Wiley & Sons, 1960.
- [47] Cima, R.M./ Ambrose, J.H.: Elimination of Natural Convection Heat Transport in Variable Conductance Heat Pipes; *9th Int. Heat Pipe Conference*, Albuquerque NM, 1995.
- [48] Heat Pipe Heat Rejection System – Final Report, NASA CR-144763, Dynatherm Corporation, Cockeysville, MD, 1965.
- [49] Qin, M./ Yuan-Guo, Ch./ Yi Y.: Performance of Heat Transfer in a Gas-Loaded Heat Pipe; *9th Int. Heat Pipe Conference*, Albuquerque NM, 1995.
- [50] Mantelli, M.B.H./ Yovanovich, M.M.: Parametric Heat Transfer Study of Bolted Joints; *Journal of Thermophysics and Heat Transfer*, Vol. 12, No. 3, pp. 382-390, 1998.
- [51] Kamotani, Y.: Effects of One-Sided Heat Input and Removal on Axially Grooved Heat Pipe Performance; *AIAA 15th Aerospace Sciences Meeting*, Los Angeles CA, Paper 77-191, 1977.
- [52] Gaviot, E./ Leclercq, D./ Machut, C./ Güths, S.: High Sensitive Thin Thermal Flowmeters; *4th Int. Symposium on Analytical Techniques*, Mandelieu la Napole, France, 1994.
- [53] Kobayashi, Y./ Okumura, A./ Matsue, T.: Effect of Gravity and Noncondensable Gas Levels on Condensation in a Variable Conductance Heat Pipe; *Journal of Thermophysics and Heat Transfer*, Vol. 5, No. 1, pp. 61-68, 1991.
- [54] Sauciuc, I./ Akbarzadeh, A./ Johnson, P.: Experimental Investigation on Variable Conductance Heat Pipes for Temperature Control; *9th Int. Heat Pipe Conference*, Albuquerque NM, 1995.
- [55] Edom, A.: Applicability Criteria for Simple Models of Gas-Loaded Heat Pipes; *11th Int. Heat Pipe Conference*, Tokyo, Japan, 1999.
- [56] Ferrel, J.K./ Davis, R./ Winston, H.: Vaporization Heat Transfer in Heat Pipe Wick Materials; *1st Int. Heat Pipe Conference*, Stuttgart, Germany, 1973.
- [57] Cardoso, H.P./ Colle, S.: Estimation of Heat Transfer Coefficient in Axially Grooved Heat Pipes; *10th Int. Heat Pipe Conference*, Stuttgart, Germany, 1997.
- [58] Hoffman, J.D.: *Numerical Methods for Engineers and Scientists*; McGraw-Hill, 1993.

APPENDICES

A1. IMPLICIT LINE-BY-LINE DISCRETIZATION METHOD APPLIED TO THE RADIATING SHEET

Heat balance for the radiating sheet at the condenser positions, considering constant material properties ρ , c and k within expected range of operating temperature:

$$\rho c s \frac{\partial T_R}{\partial t} = k s \frac{\partial}{\partial y} \left(\frac{\partial T_R}{\partial y} \right) + k s \frac{\partial}{\partial x} \left(\frac{\partial T_R}{\partial x} \right) - \epsilon \sigma (T_R^4 - T_\infty^4) + h_b (T_f - T_R)$$

Herein the source term:

$$S = S_{\text{rad}} + S_{\text{cond}} = -\epsilon \sigma (T_R^4 - T_\infty^4) + h_b (T_f - T_R)$$

(outside the regions that are in contact with the condenser fins: $h_b = 0$)

Linearizing the radiation term:

$$S_{\text{rad,lin}} = S_{\text{rad}}^0 + \frac{dS_{\text{rad}}^0}{dT_R} (T_R - T_R^0) = -4\epsilon \sigma T_R^{0^3} T_R + 3\epsilon \sigma T_R^{0^4} + \epsilon \sigma T_\infty^4$$

Rearranging the source term with respect to terms proportional to T_R and other constant terms:

$$S = -(4\epsilon \sigma T_R^{0^3} + h_b) T_R + \epsilon \sigma (3T_R^{0^4} + T_\infty^4) + h_b T_f$$

$$\text{with } S_{\text{prop}} = -(4\epsilon \sigma T_R^{0^3} + h_b) \quad \text{and} \quad S_{\text{cons}} = \epsilon \sigma (3T_R^{0^4} + T_\infty^4) + h_b T_f$$

$$\Rightarrow \rho c s \frac{\partial T_R}{\partial t} = k s \frac{\partial}{\partial y} \left(\frac{\partial T_R}{\partial y} \right) + k s \frac{\partial}{\partial x} \left(\frac{\partial T_R}{\partial x} \right) + S_{\text{prop}} T_R + S_{\text{cons}}$$

Integration over an element (finite control volume) and the time step Δt :

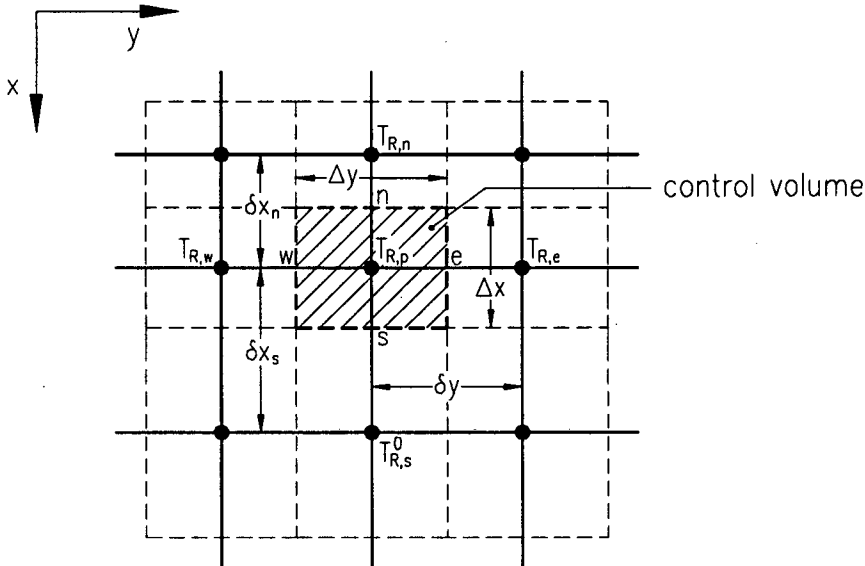
$$\begin{aligned} \rho c s \int_t^{t+\Delta t} \int_n^s \int_w^e \frac{\partial T_R}{\partial t} dx dy dt &= k s \int_t^{t+\Delta t} \int_n^s \int_w^e \frac{\partial}{\partial y} \left(\frac{\partial T_R}{\partial y} \right) dx dy dt + k s \int_t^{t+\Delta t} \int_n^s \int_w^e \frac{\partial}{\partial x} \left(\frac{\partial T_R}{\partial x} \right) dx dy dt \\ &+ \int_t^{t+\Delta t} \int_n^s \int_w^e (S_{\text{prop}} T_R + S_{\text{cons}}) dx dy dt \end{aligned}$$

$$\Rightarrow \rho c s \Delta x \Delta y \int_t^{t+\Delta t} \frac{\partial T_R}{\partial t} dt = k s \int_t^{t+\Delta t} \int_n^e \left(\frac{\partial T_R}{\partial y} \Big|_e - \frac{\partial T_R}{\partial y} \Big|_w \right) dx dt + k s \int_t^{t+\Delta t} \int_w^e \left(\frac{\partial T_R}{\partial x} \Big|_s - \frac{\partial T_R}{\partial x} \Big|_n \right) dy dt$$

$$+ \Delta x \Delta y \int_t^{t+\Delta t} (S_{\text{prop}} T_R + S_{\text{cons}}) dt$$

$$\Rightarrow \rho c s \Delta x \Delta y \int_t^{t+\Delta t} \frac{\partial T_R}{\partial t} dt = k s \Delta x \int_t^{t+\Delta t} \left(\frac{T_{R,e} - T_{R,p}}{\delta y|_e} - \frac{T_{R,w} - T_{R,p}}{\delta y|_w} \right) dt$$

$$+ k s \Delta y \int_t^{t+\Delta t} \left(\frac{T_{R,s} - T_{R,p}}{\delta x|_s} - \frac{T_{R,n} - T_{R,p}}{\delta x|_n} \right) dt + \Delta x \Delta y \int_t^{t+\Delta t} (S_{\text{prop}} T_R + S_{\text{cons}}) dt$$



Control volume $\Delta x \cdot \Delta y$ of the radiating sheet above the condenser (northern edge);

$$\Delta x = \Delta x_{\text{lat}}, \delta y = \Delta y$$

$$\text{As } \delta y|_w = \delta y|_e = \Delta y$$

$$\Rightarrow \rho c s \Delta x \Delta y (T_{R,p}^1 - T_{R,p}^0) = \int_t^{t+\Delta t} \left[\frac{k s \Delta x (T_{R,e} - T_{R,p})}{\Delta y} + \frac{k s \Delta x (T_{R,w} - T_{R,p})}{\Delta y} + \frac{k s \Delta y (T_{R,s} - T_{R,p})}{\delta x_s} \right. \\ \left. + \frac{k s \Delta y (T_{R,n} - T_{R,p})}{\delta x_n} + S_{\text{prop}} \Delta x \Delta y T_{R,p} + S_{\text{cons}} \Delta x \Delta y \right] dt$$

The subscripts 0 and 1 indicate previous (at t) and new (at $t+\Delta t$) values respectively.

In general the nodal temperatures $T_{R,k}$ ($k = w, p, e, n, s$) can vary with time during the interval Δt as follows:

$$\int_t^{t+\Delta t} T_{R,k} dt = [fT_{R,k}^1 + (1-f)T_{R,k}^0] \Delta t$$

where f represents a weighting factor between the times 0 and 1.

In the implicit method, it is assumed that the new time values predominate during the time step Δt .

Hence $f \equiv 1$ and

$$\begin{aligned} \int_t^{t+\Delta t} T_{R,k} dt &= T_{R,k}^1 \Delta t \\ \Rightarrow \rho c s \Delta x \Delta y (T_{R,p}^1 - T_{R,p}^0) &= \left[\frac{ks \Delta x (T_{R,e}^1 - T_{R,p}^1)}{\Delta y} + \frac{ks \Delta x (T_{R,w}^1 - T_{R,p}^1)}{\Delta y} + \frac{ks \Delta y (T_{R,s}^0 - T_{R,p}^1)}{\delta x_s} \right. \\ &\quad \left. + \frac{ks \Delta y (T_{R,n}^1 - T_{R,p}^1)}{\delta x_n} + S_{prop} \Delta x \Delta y T_{R,p}^1 + S_{cons} \Delta x \Delta y \right] \Delta t \end{aligned}$$

For the temperature to the south of the element, the previous value, $T_{R,s}^0$, is set deliberately, as during the line-by-line sweep the temperatures that are located to the right of the element of the line to be solved contribute with values of the previous iteration.

As a convention the temperatures that do not bear any superscript from now on are regarded as new temperatures to be solved in the current iteration at $t+\Delta t$, so that the superscript 1 will be omitted.

$$\begin{aligned} \Rightarrow \frac{\rho c s \Delta x \Delta y}{\Delta t} (T_{R,p} - T_{R,p}^0) &= \frac{ks \Delta x}{\Delta y} (T_{R,e} - T_{R,p}) + \frac{ks \Delta x}{\Delta y} (T_{R,w} - T_{R,p}) + \frac{ks \Delta y}{\delta x_s} (T_{R,s}^0 - T_{R,p}) \\ &\quad + \frac{ks \Delta y}{\delta x_n} (T_{R,n} - T_{R,p}) + S_{prop} \Delta x \Delta y T_{R,p} + S_{cons} \Delta x \Delta y \end{aligned}$$

$$\Rightarrow \left(\frac{ks\Delta x}{\Delta y} + \frac{ks\Delta x}{\Delta y} + \frac{ks\Delta y}{\delta x_s} + \frac{ks\Delta y}{\delta x_n} + \frac{\rho cs\Delta x\Delta y}{\Delta t} - S_{prop}\Delta x\Delta y \right) T_{R,p} =$$

$$= \frac{ks\Delta x}{\Delta y} T_{R,e} + \frac{ks\Delta x}{\Delta y} T_{R,w} + \frac{ks\Delta y}{\delta x_s} T_{R,s}^0 + \frac{ks\Delta y}{\delta x_n} T_{R,n} + \frac{\rho cs\Delta x\Delta y}{\Delta t} T_{R,p}^0 + S_{cons}\Delta x\Delta y$$

Introducing temperature coefficients:

$$A_e = A_w = \frac{ks\Delta x}{\Delta y}; \quad A_s = \frac{ks\Delta y}{\delta x_s}$$

$$A_n = \frac{ks\Delta y}{\delta x_n} \quad A_p^0 = \frac{\rho cs\Delta x\Delta y}{\Delta t}$$

$$B = A_p^0 T_{R,p}^0 + S_{cons}\Delta x\Delta y \quad A_p = A_e + A_w + A_s + A_n + A_p^0 - S_{prop}\Delta x\Delta y$$

$$\Rightarrow A_p T_{R,p} = A_e T_{R,e} + A_w T_{R,w} + A_s T_{R,s}^0 + A_n T_{R,n} + B$$

$$\Rightarrow -A_w T_{R,w} + A_p T_{R,p} - A_e T_{R,e} = B + A_s T_{R,s}^0 + A_n T_{R,n}$$

On the left hand side of the equation now appear known coefficients with unknown temperatures, being neighbors on the same line (or string) i . On the right hand side appear only known terms, among these the temperatures $T_{R,n}$, on line $i-1$, determined by the preceding solver traverse of the same iteration, and T_f (contained in S_{cons}) determined during the current iteration ($t+\Delta t$) as well as the temperatures of the previous iteration, $T_{R,s}^0$ on line $i+1$ and $T_{R,p}^0$.

In the case of steady-state simulation the same coefficients are used, provided that A_p^0 is removed from the terms B e A_p , as it becomes zero with Δt going to infinity.

To facilitate the notation in matrix form the indices of the unknowns are designated according to their succession in the line:

$$\text{With} \quad a_j = -A_w; \quad b_j = A_p; \quad c_j = -A_e; \quad d_j = B + A_s T_{R,s}^0 + A_n T_{R,n}$$

$$\text{follows} \quad a_j T_{R,j-1} + b_j T_{R,j} + c_j T_{R,j+1} = d_j$$

Matrix coefficients at the sheet margins, where thermal isolation is supposed

$$\left(\frac{\partial T_R(x,0)}{\partial y} = \frac{\partial T_R(x,l_c)}{\partial y} = 0 \quad \text{and} \quad \frac{\partial T_R(0,y)}{\partial x} = \frac{\partial T_R(w_R,y)}{\partial x} = 0 \right):$$

$$y = 0 : \quad a_0 = 0; \quad b_0 = A_p; \quad c_0 = -A_e; \quad d_0 = B + A_s T_{R,s}^0 + A_n T_{R,n}$$

$$y = l_c : \quad a_{n-1} = -A_w; \quad b_{n-1} = A_p; \quad c_{n-1} = 0 \quad d_{n-1} = B + A_s T_{R,s}^0 + A_n T_{R,n}$$

$$x = 0 : \quad a_j = -A_w; \quad b_j = A_p; \quad c_j = -A_e; \quad d_j = B + A_s T_{R,s}^0$$

$$x = w_R : \quad a_j = -A_w; \quad b_j = A_p; \quad c_j = -A_e; \quad d_j = B + A_n T_{R,n}$$

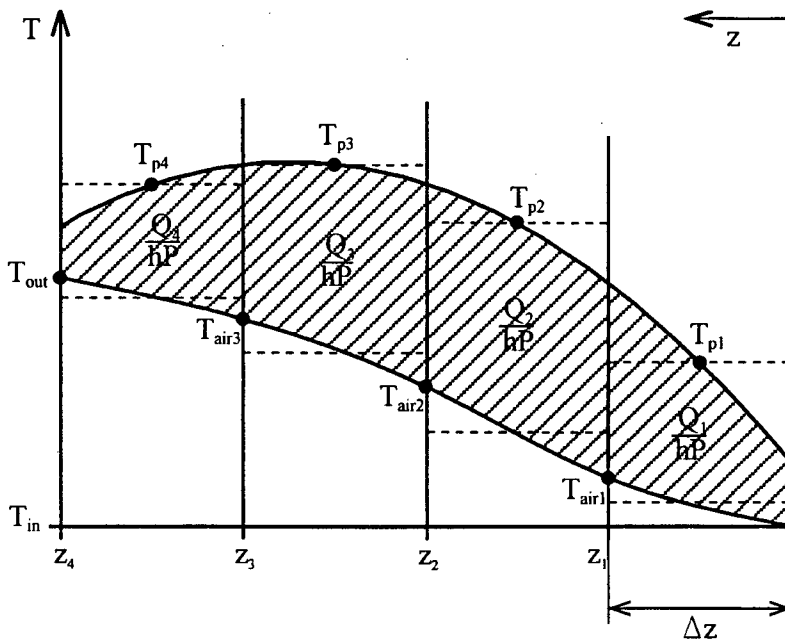
The final result is a system of linear equations for the simultaneous solution of all nodal temperatures on one line ($j = 0$ up to $j = n-1$):

$$\begin{bmatrix} b_0 & c_0 & 0 & \cdots & \cdots & \cdots & 0 \\ a_1 & b_1 & c_1 & & & & \\ 0 & a_2 & b_2 & & & & \\ \vdots & & & \ddots & & & \\ \vdots & & & & b_{n-3} & c_{n-3} & 0 \\ \vdots & & & & a_{n-2} & b_{n-2} & c_{n-2} \\ 0 & & & & 0 & a_{n-1} & b_{n-1} \end{bmatrix} \cdot \begin{bmatrix} T_{R,0} \\ T_{R,1} \\ T_{R,2} \\ \vdots \\ T_{R,n-3} \\ T_{R,n-2} \\ T_{R,n-1} \end{bmatrix} = \begin{bmatrix} d_0 \\ d_1 \\ d_2 \\ \vdots \\ d_{n-3} \\ d_{n-2} \\ d_{n-1} \end{bmatrix}$$

With all nonzero coefficients aligning themselves along three diagonals of the matrix a convenient and fast solver called Thomas algorithm [58], alias TDMA (TriDiagonal-Matrix Algorithm), can be applied.

A2. ALGORITHM TO ESTIMATE THE TEMPERATURE PROFILE OF THE COOLING AIR STREAM

The air temperature profile that the heat pipe model needs as the sink boundary condition for the condenser is estimated on the basis of measured experimental values. These are the heat pipe wall temperature profile, obtained at equidistant locations on the perimeter of the pipe, and the inlet and outlet air temperatures, T_{in} and T_{out} . In this way for n wall temperatures $n-1$ air temperatures at equidistant locations in the bulk stream can be determined. The algorithm is based on the assumption that the convective heat transfer coefficient h is constant along the heating surface. The following derivation is performed for a simple example with four measuring points on the pipe wall. As an approximation the heat portions transferred by each element Δz (hatched in the figure) are determined between constant values T_{pj} and linear mean values of T_{airj-1} and T_{airj} (dashed horizontal lines).



Evolution of the coolant temperature according to the wall temperature profile

$j = 1$:

Heat balance for the first element Δz closest to the air inlet:

$$Q_1 = hP \left[T_{p1} - \frac{1}{2}(T_{air1} + T_{in}) \right] \Delta z = \dot{m}c_p (T_{air1} - T_{in})$$

$$\Rightarrow T_{p1} - \frac{1}{2}T_{air1} - \frac{1}{2}T_{in} = \frac{\dot{m}c_p}{hP\Delta z}(T_{air1} - T_{in})$$

$$\Rightarrow T_{air1} = \frac{T_{p1} + T_{in}\left(\frac{\dot{m}c_p}{hP\Delta z} - \frac{1}{2}\right)}{\frac{\dot{m}c_p}{hP\Delta z} + \frac{1}{2}} \quad (1)$$

Heat balance for the whole condenser:

$$Q = \sum Q_j = hP\Delta z \left[\left(T_{p1} - \frac{1}{2}(T_{air1} + T_{in}) \right) + \left(T_{p2} - \frac{1}{2}(T_{air2} + T_{air1}) \right) \right. \\ \left. + \left(T_{p3} - \frac{1}{2}(T_{air3} + T_{air2}) \right) + \left(T_{p4} - \frac{1}{2}(T_{air3} + T_{out}) \right) \right]$$

$$= hP\Delta z \left[T_{p1} + T_{p2} + T_{p3} + T_{p4} - T_{air1} - T_{air2} - T_{air3} - \frac{1}{2}T_{in} - \frac{1}{2}T_{out} \right]$$

$$= \dot{m}c_p(T_{out} - T_{in})$$

With $\sum T_{pi} = T_{p1} + T_{p2} + T_{p3} + T_{p4}$

$$\Rightarrow \frac{\dot{m}c_p}{hP\Delta z} = \frac{\sum T_{pi} - T_{air1} - T_{air2} - T_{air3} - \frac{1}{2}T_{in} - \frac{1}{2}T_{out}}{T_{out} - T_{in}} \quad (2)$$

Introducing eqn. (2) into eqn. (1):

$$T_{air1} = \frac{T_{p1} + \left[\frac{\sum T_{pi} - T_{air1} - T_{air2} - T_{air3} - (T_{out} + T_{in})/2}{T_{out} - T_{in}} - \frac{1}{2} \right] T_{in}}{\frac{\sum T_{pi} - T_{air1} - T_{air2} - T_{air3} - (T_{out} + T_{in})/2}{T_{out} - T_{in}} + \frac{1}{2}}$$

$$\Rightarrow T_{air1} = \frac{T_{p1}(T_{out} - T_{in}) + (\sum T_{pi} - T_{air1} - T_{air2} - T_{air3} - T_{out})T_{in}}{\sum T_{pi} - T_{air1} - T_{air2} - T_{air3} - T_{in}}$$

$$\Rightarrow T_{air1}^2 - (\sum T_{pi} - T_{air2} - T_{air3})T_{air1} + T_{p1}(T_{out} - T_{in}) + (\sum T_{pi} - T_{air2} - T_{air3} - T_{out})T_{in} = 0$$

Carrying out the same procedure for the other unknown air temperatures, results in two more quadratic equations which together with the last one form a set of equations that solve the required air temperature profile:

$$j = 2: \quad T_{\text{air}2}^2 - \left(\sum T_{\text{pi}} - T_{\text{air}3} - T_{\text{in}} \right) T_{\text{air}2} + T_{\text{p}2} (T_{\text{out}} - T_{\text{in}}) + \left(\sum T_{\text{pi}} - T_{\text{air}1} - T_{\text{air}3} - T_{\text{out}} \right) T_{\text{air}1} = 0$$

$$j = 3: \quad T_{\text{air}3}^2 - \left(\sum T_{\text{pi}} - T_{\text{air}1} - T_{\text{in}} \right) T_{\text{air}3} + T_{\text{p}3} (T_{\text{out}} - T_{\text{in}}) + \left(\sum T_{\text{pi}} - T_{\text{air}1} - T_{\text{air}2} - T_{\text{out}} \right) T_{\text{air}2} = 0$$

In the general case of $j = 1..n$ the rule of formation for the set of n equations is:

$$T_{\text{air}j}^2 - \left(\sum_{i=1}^{n+1} T_{\text{pi}} - \sum_{\substack{i=0 \\ i \neq j, i \neq j-1}}^n T_{\text{air}i} \right) T_{\text{air}j} + T_{\text{p}j} (T_{\text{out}} - T_{\text{in}}) + \left(\sum_{i=1}^{n+1} T_{\text{pi}} - \sum_{\substack{i=1 \\ i \neq j}}^n T_{\text{air}i} - T_{\text{out}} \right) T_{\text{air}j-1} = 0$$

A3. RADIATOR TEST DATA PLOTS (RUNS A – F)

Test run A

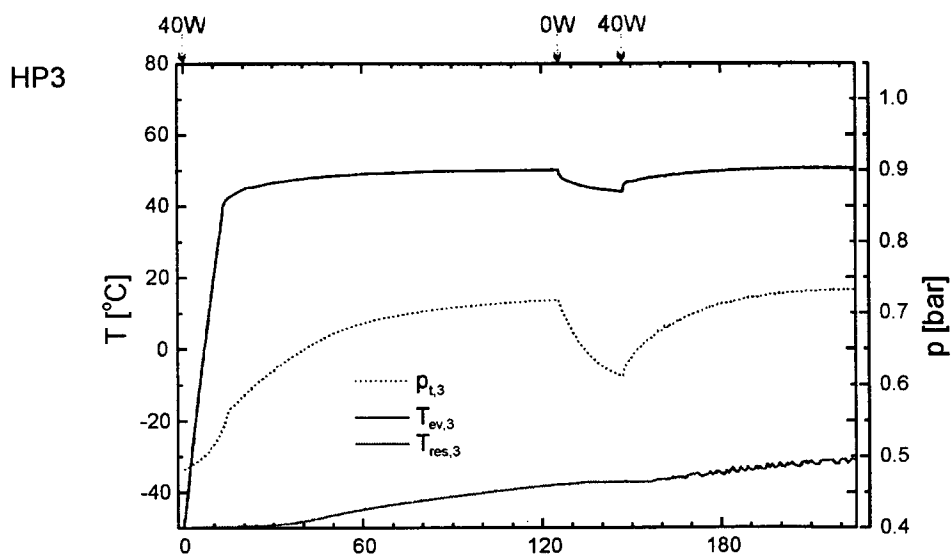
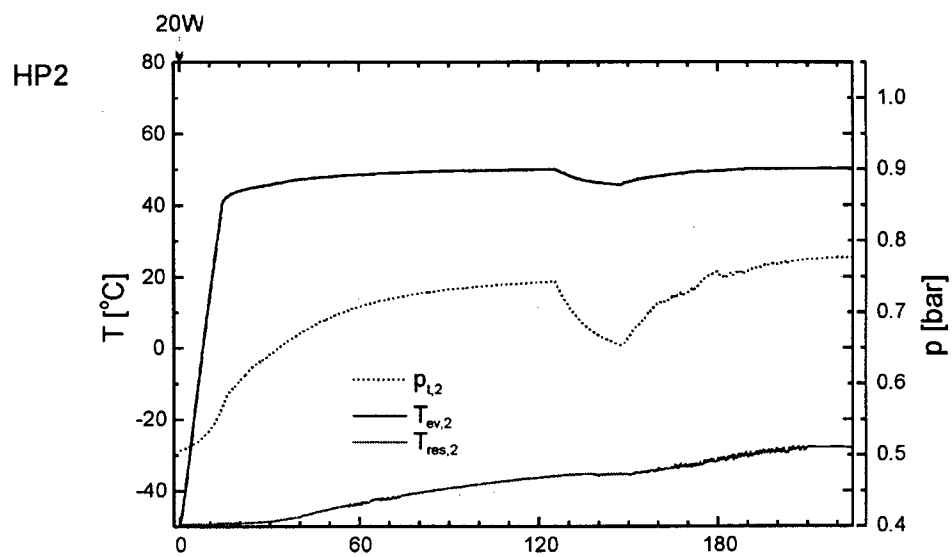
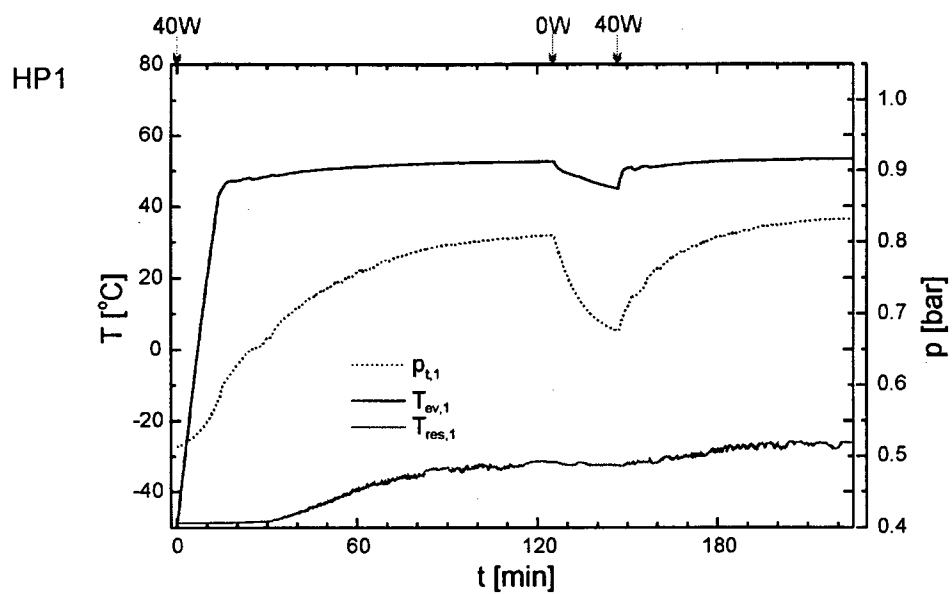
11/03/99

entire radiator, reservoirs unsheathed

argon masses: 232 mg, 229 mg, 218 mg

 T_{∞} : -50 °C

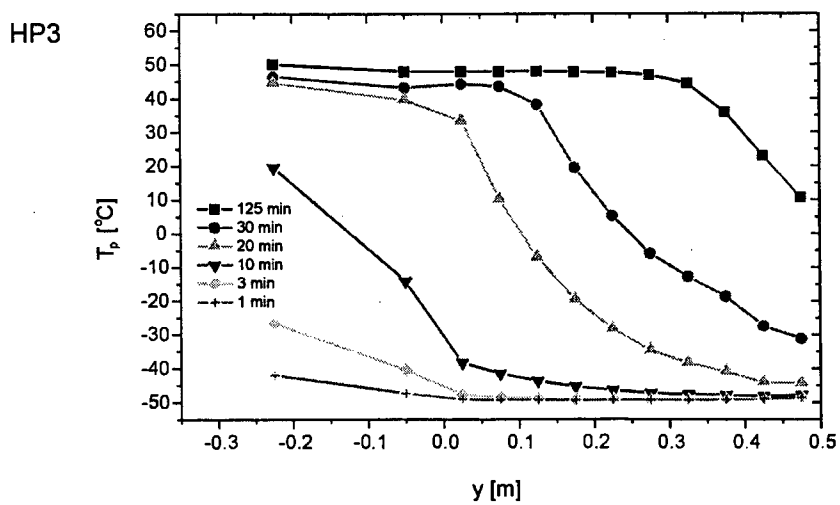
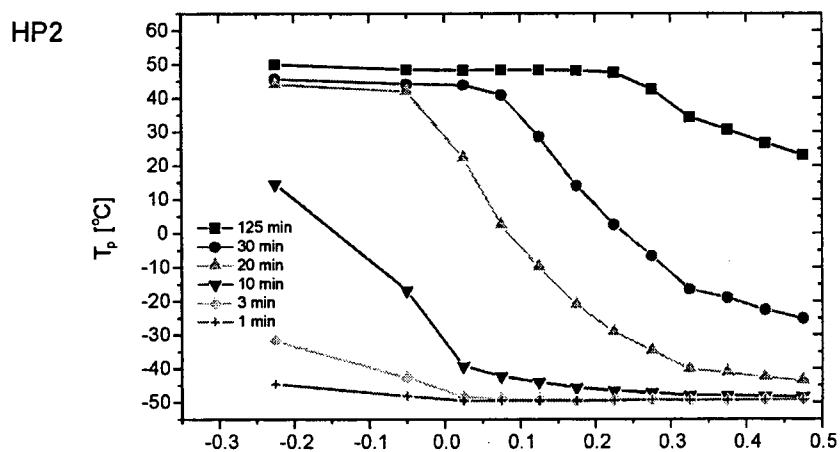
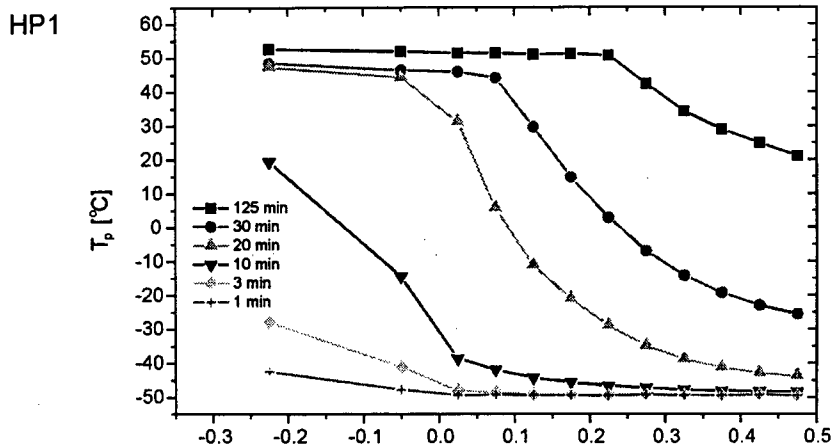
Time [min]	Power [W]
0	40/20/40
125.5	0/20/0
147	40/20/40
225	0 (all HP's) switch-off



HP1: 0 → 40 W

HP2: 0 → 20 W

HP3: 0 → 40 W

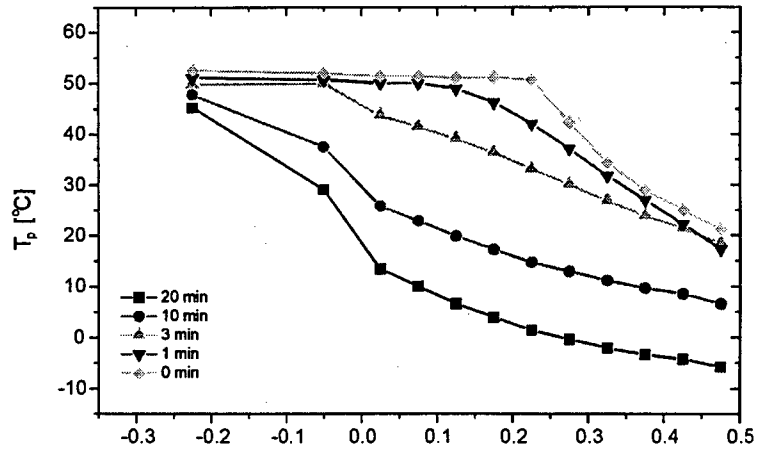


HP1: 40 → 0 W

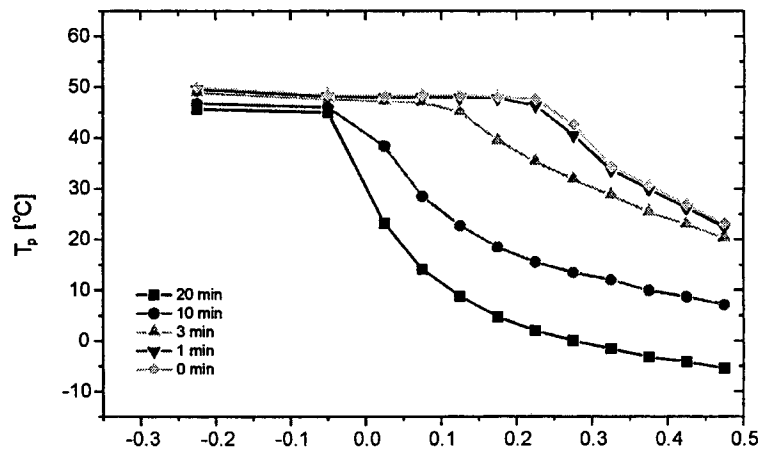
HP2: continues at 20 W

HP3: 40 → 0 W

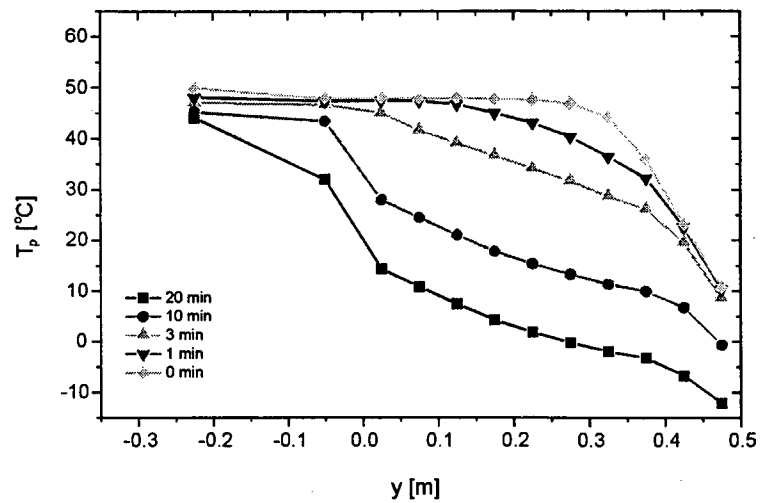
HP1



HP2



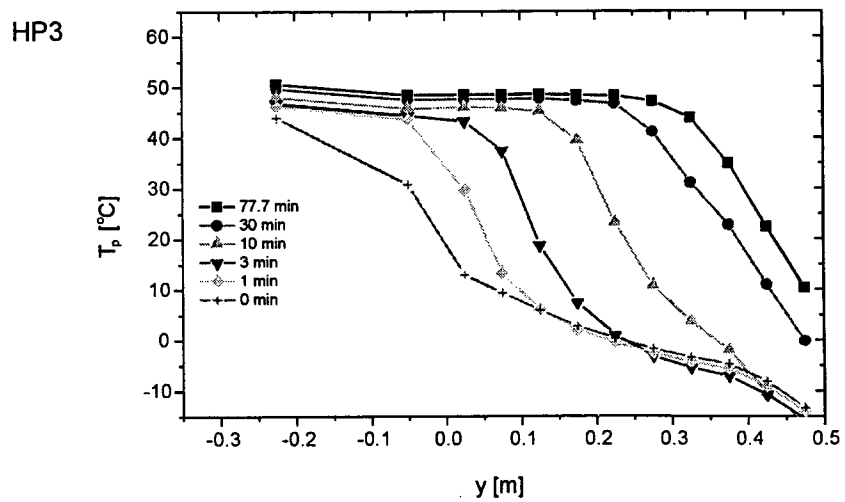
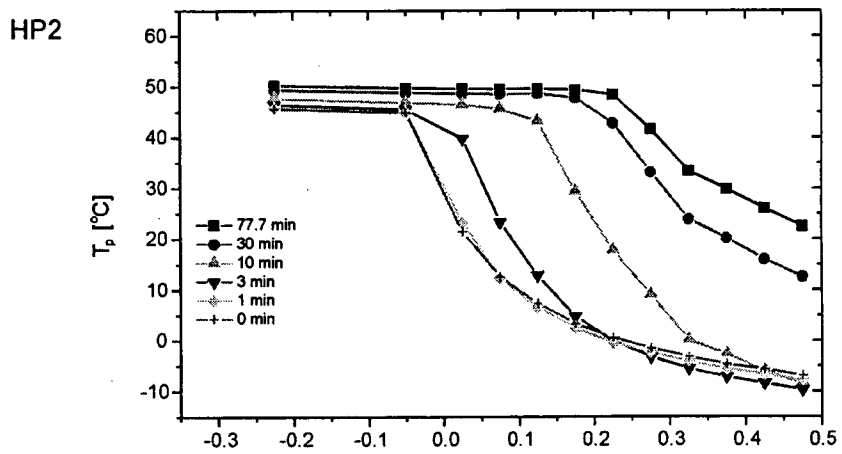
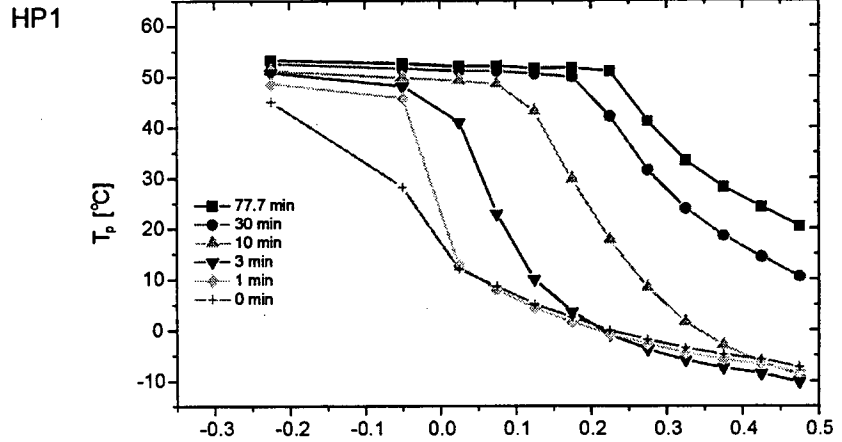
HP3



HP1: 0 → 40 W

HP2: continues at 20 W

HP3: 0 → 40 W



Test run B

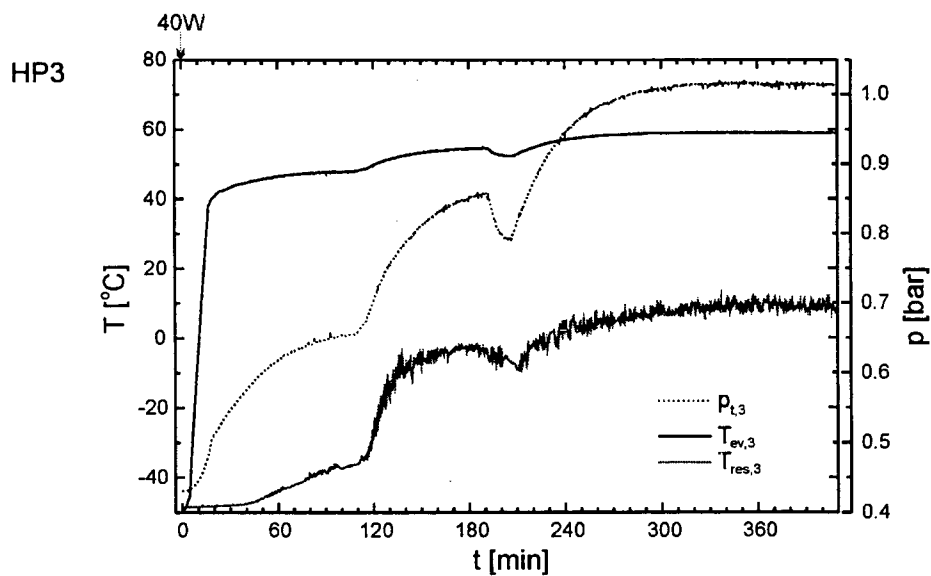
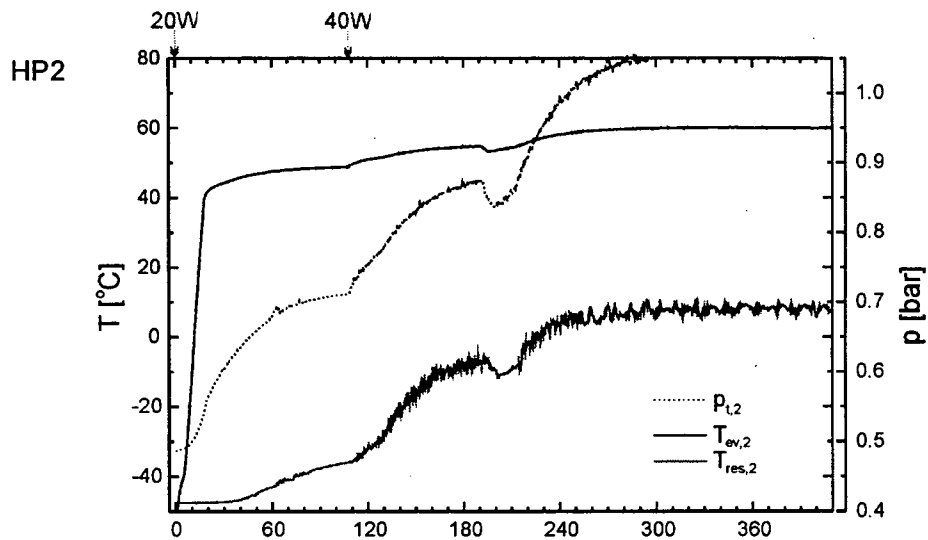
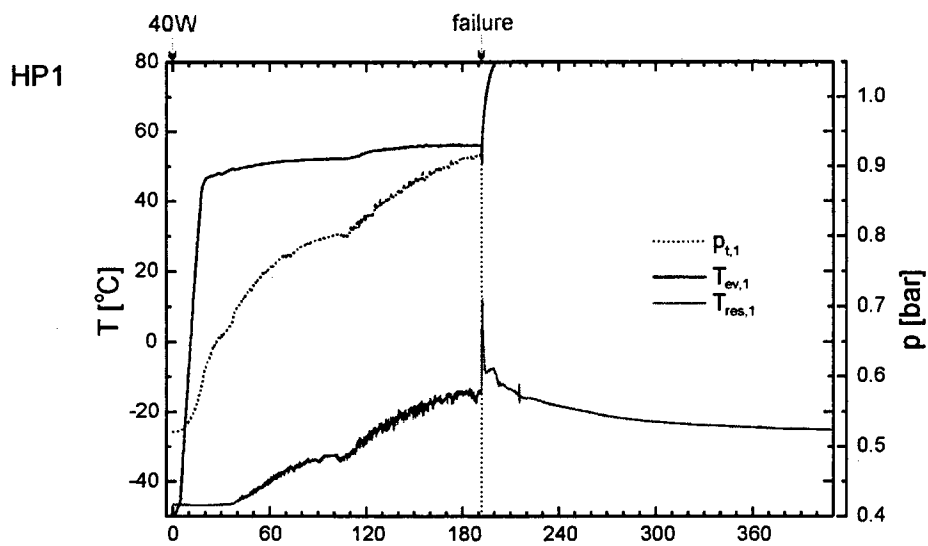
12/03/99

entire radiator, reservoirs unsheathed

argon masses: 235 mg, 220 mg, 195 mg

 T_{∞} : -50 °C

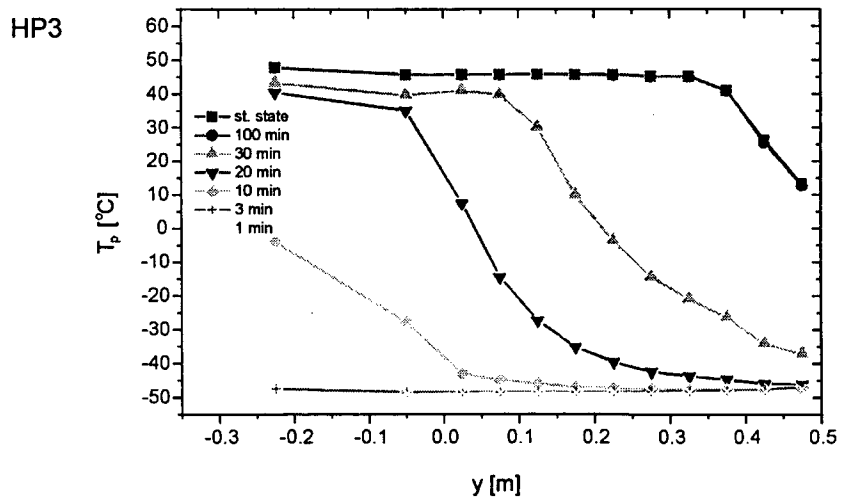
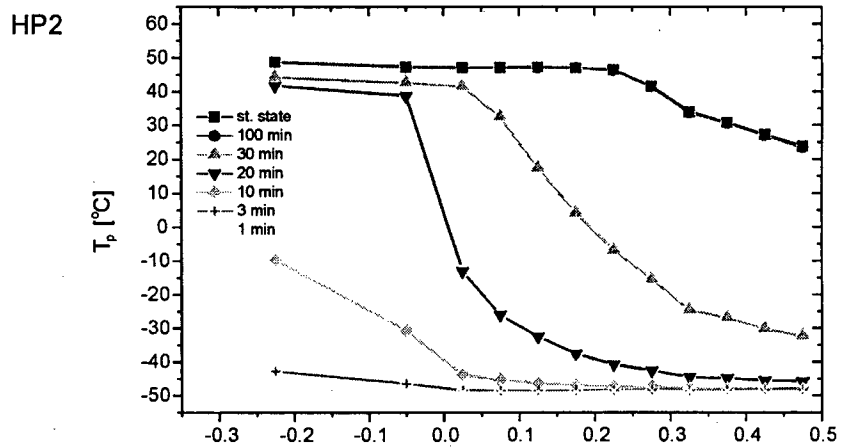
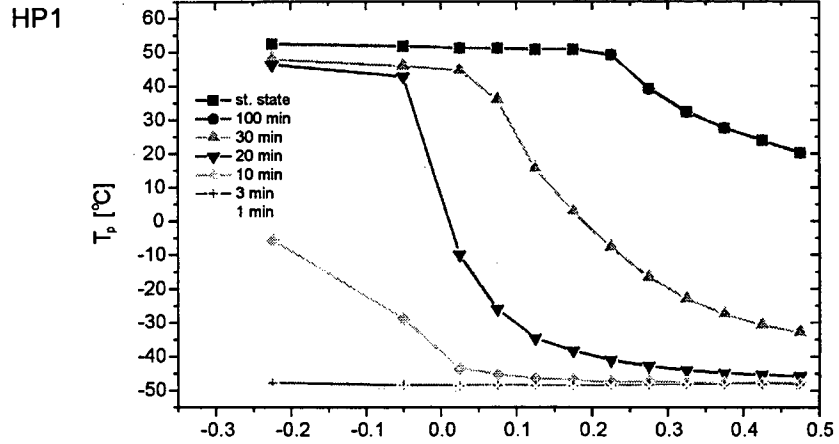
Time [min]	Power [W]	
0	40/20/40	
108	40 (all HP's)	
192	40 (all HP's)	HP1 fails
409	0 (all HP's)	switch-off



HP1: 0 → 40 W

HP2: 0 → 20 W

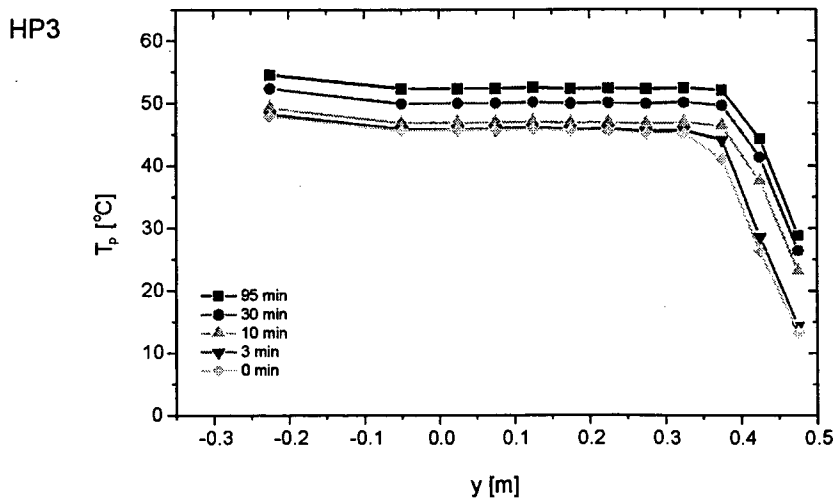
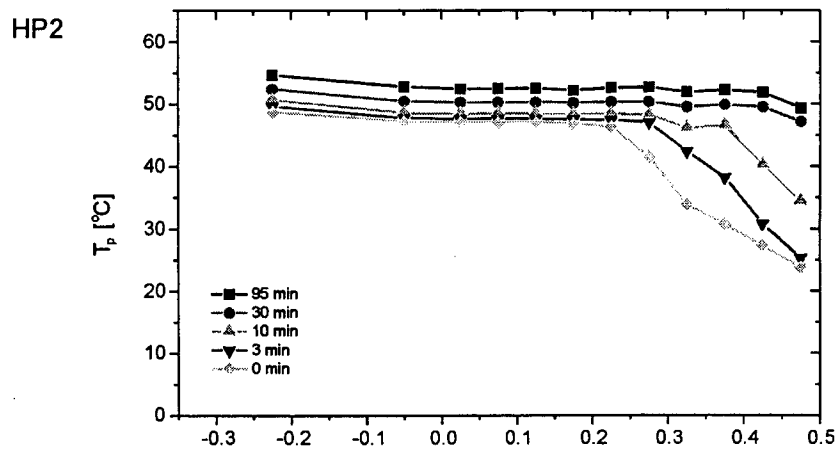
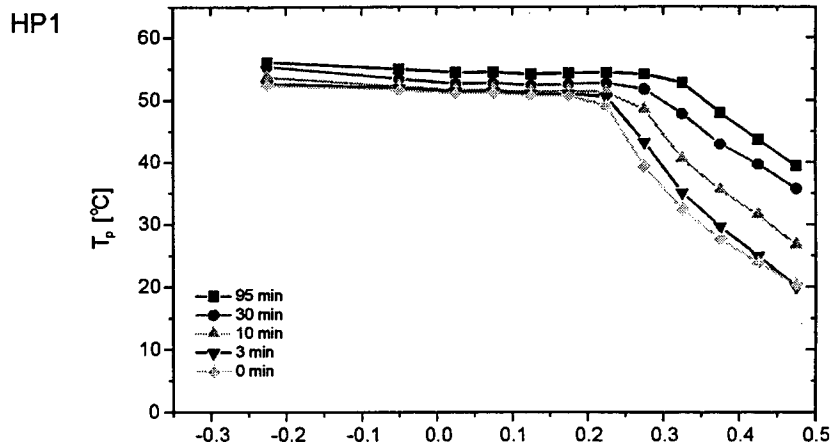
HP3: 0 → 40 W



HP1: continues at 40 W

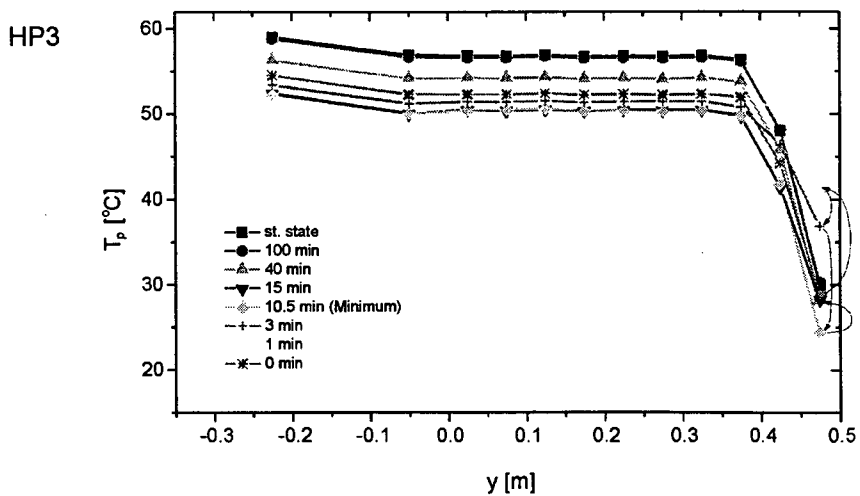
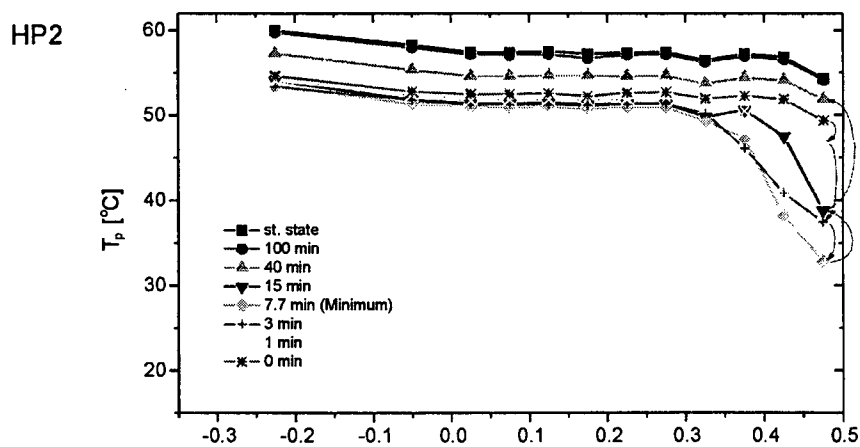
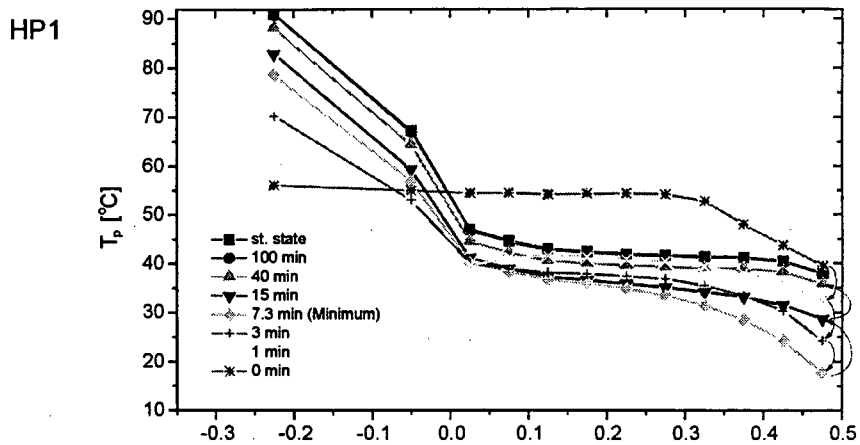
HP2: 20 → 40 W

HP3: continues at 40 W



HP1 fails

(all HP's continue at 40 W)



Test run C

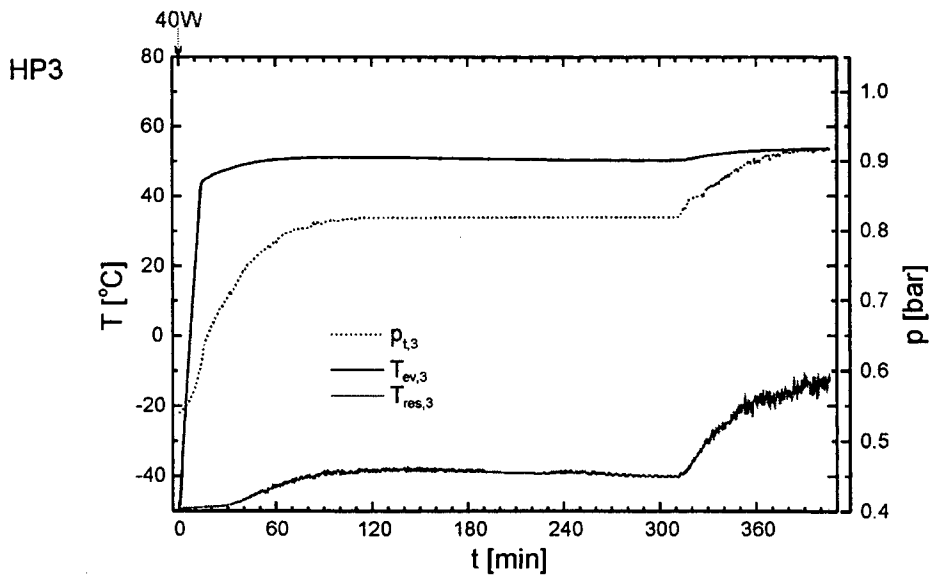
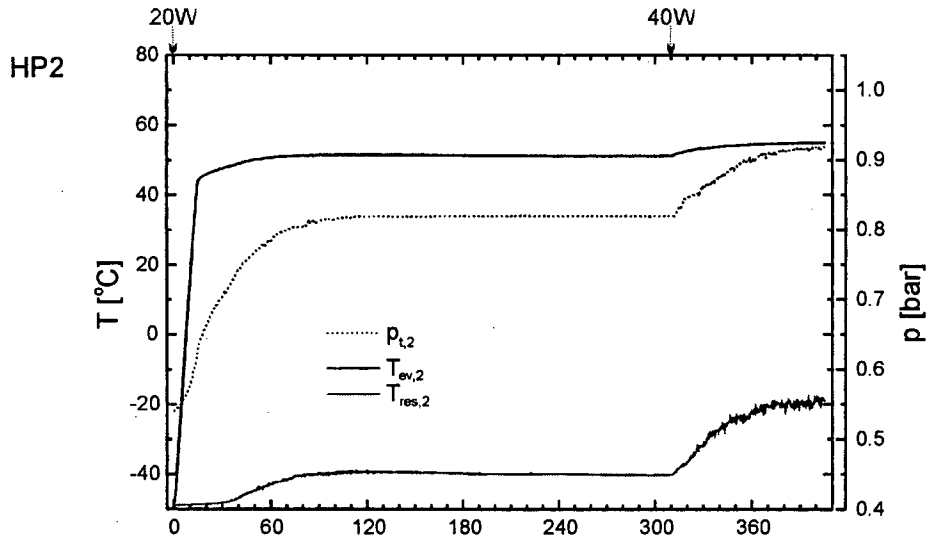
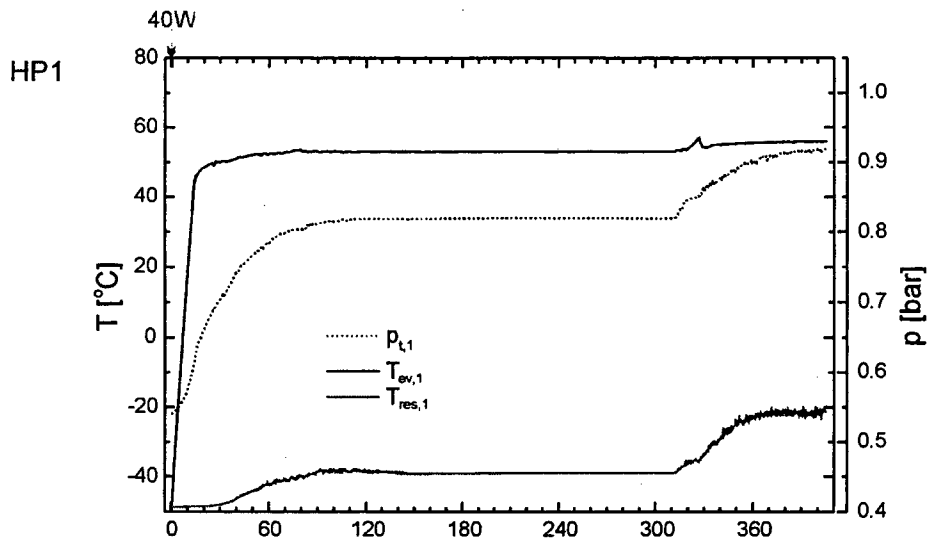
16/03/99

entire radiator, reservoirs sheathed with kapton tape

argon masses: 244 mg, 252 mg, 235 mg

 T_{∞} : -50 °C

Time [min]	Power [W]	
0	40/20/40	
310	40 (all HP's)	
405	0 (all HP's)	switch-off

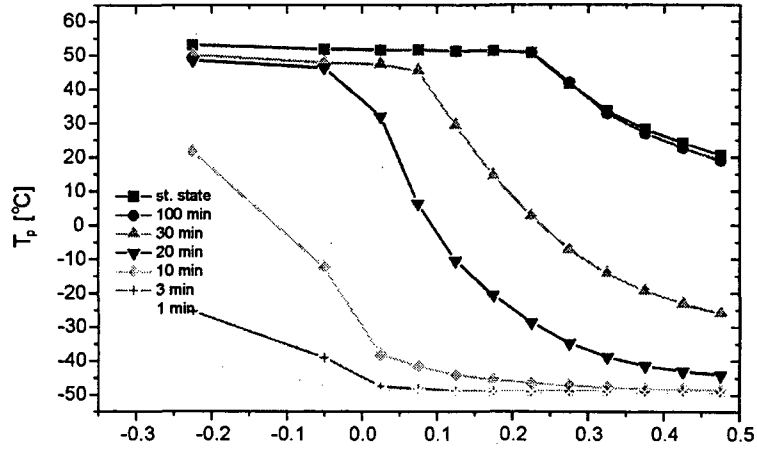


HP1: 0 → 40 W

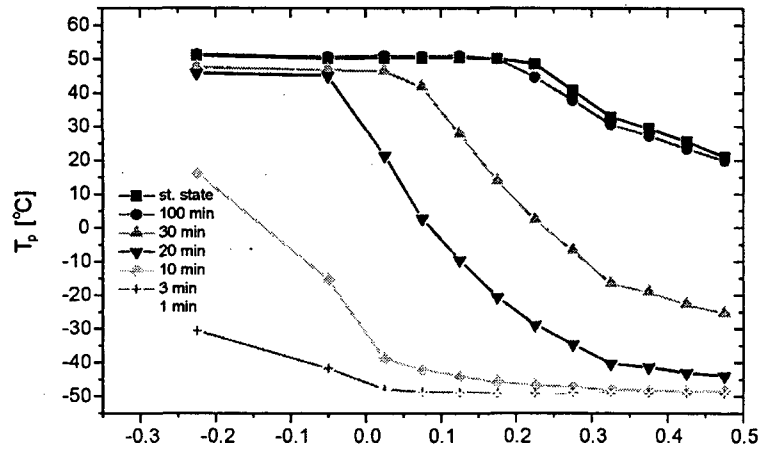
HP2: 0 → 20 W

HP3: 0 → 40 W

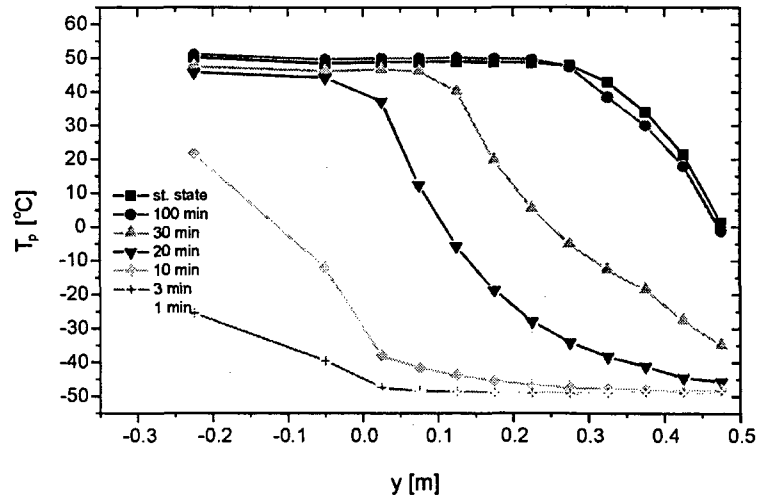
HP1



HP2



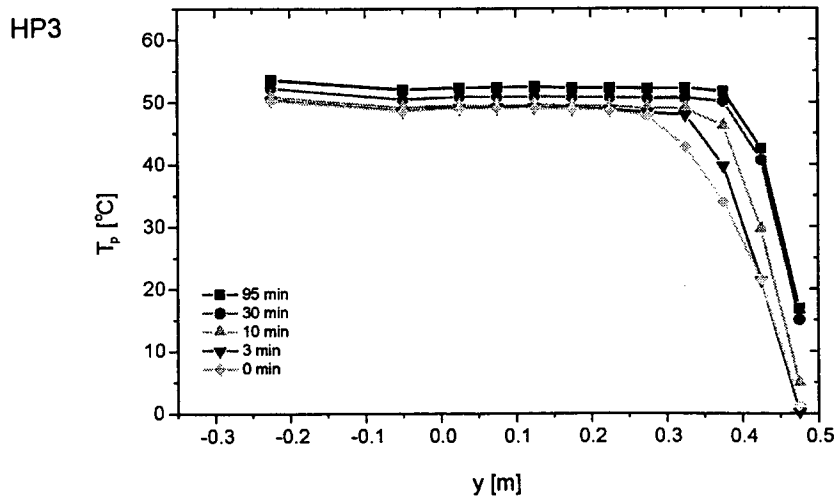
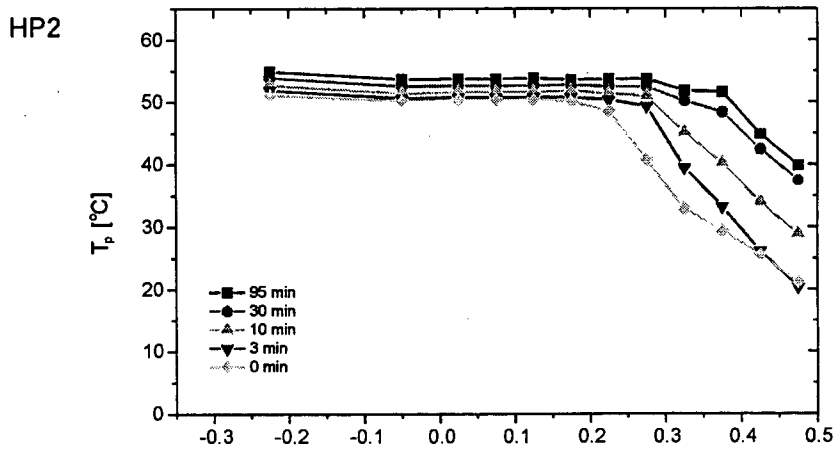
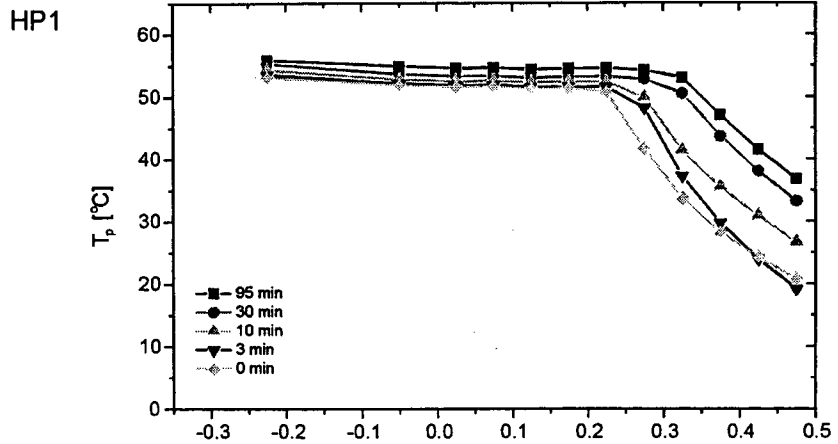
HP3



HP1: continues at 40 W

HP2: 20 → 40 W

HP3: continues at 40 W



Test run D

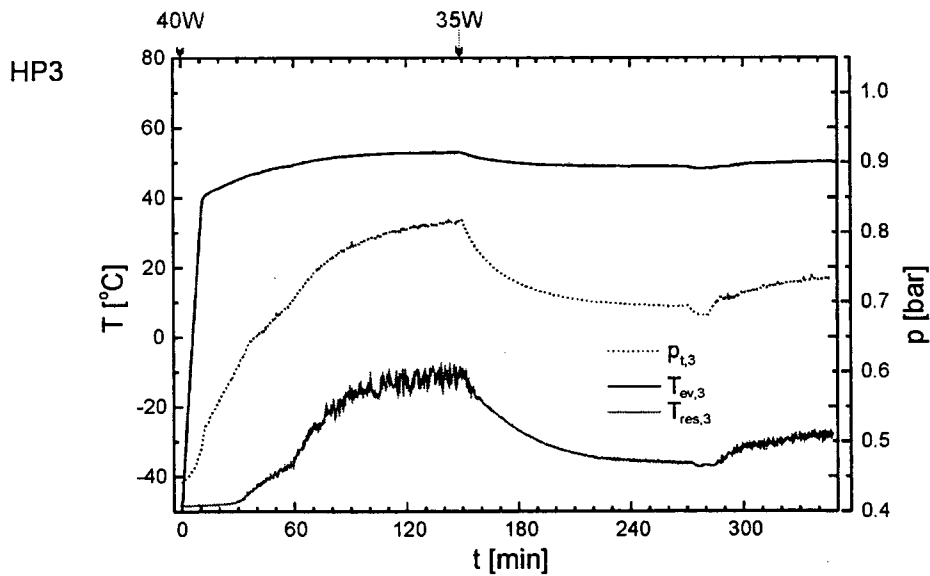
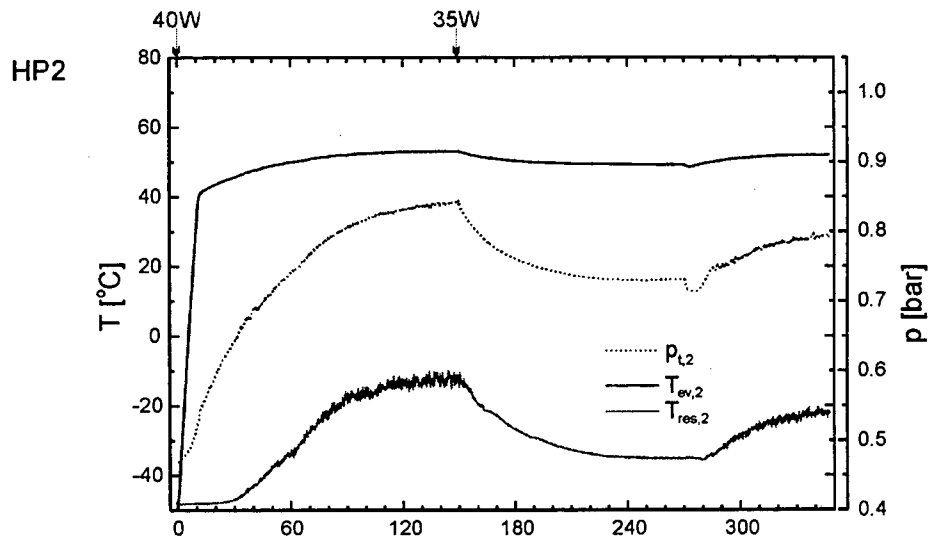
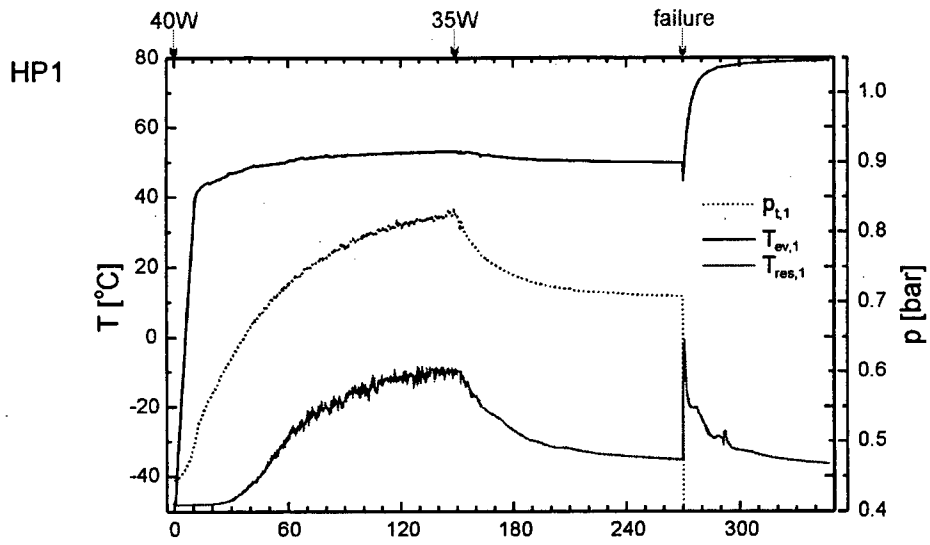
19/03/99

entire radiator, reservoirs sheathed with kapton tape

argon masses: 200 mg, 212 mg, 200 mg

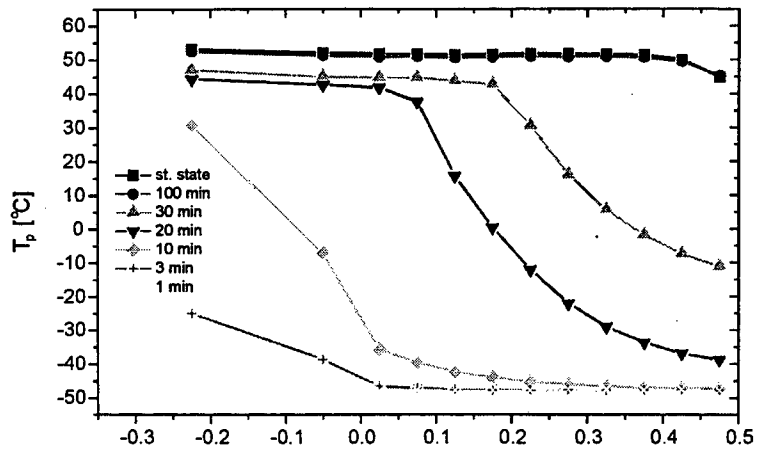
 T_{∞} : -50 °C

Time [min]	Power [W]	
0	40 (all HP's)	
149	35 (all HP's)	
270	35 (all HP's)	HP1 fails
347	0 (all HP's)	switch-off

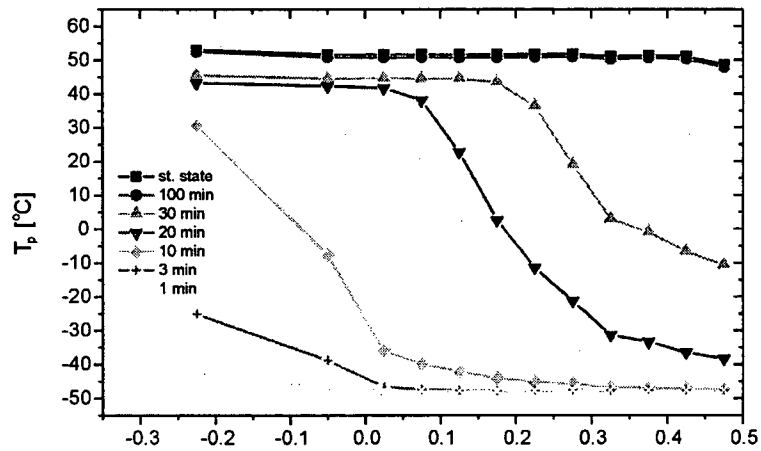


all HP's: 0 → 40 W

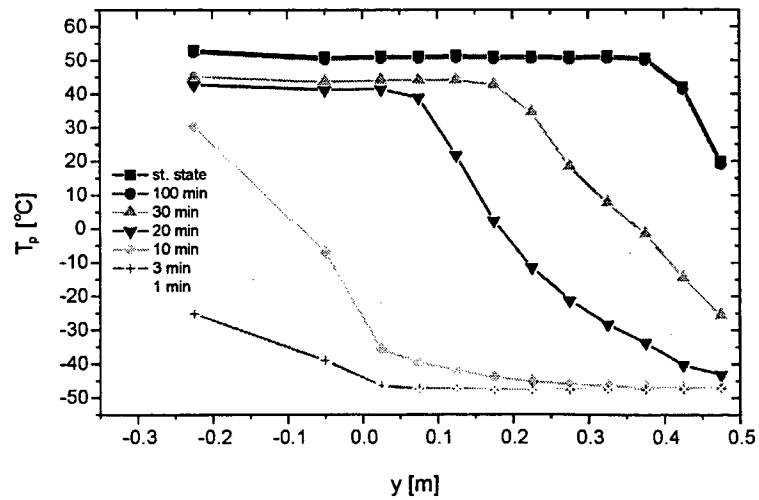
HP1



HP2

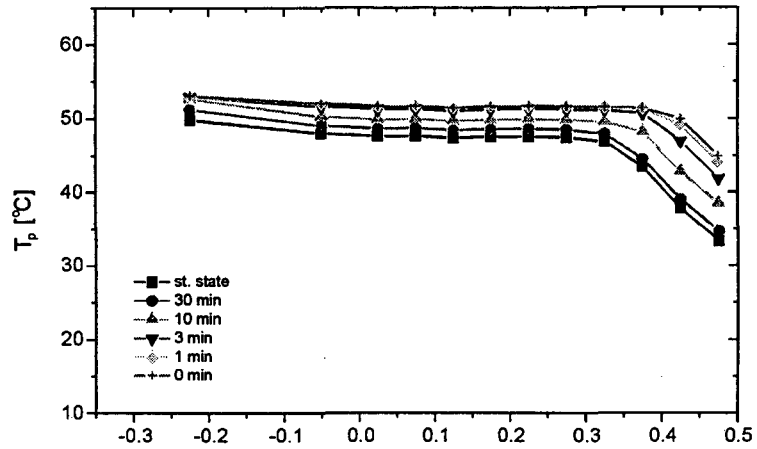


HP3

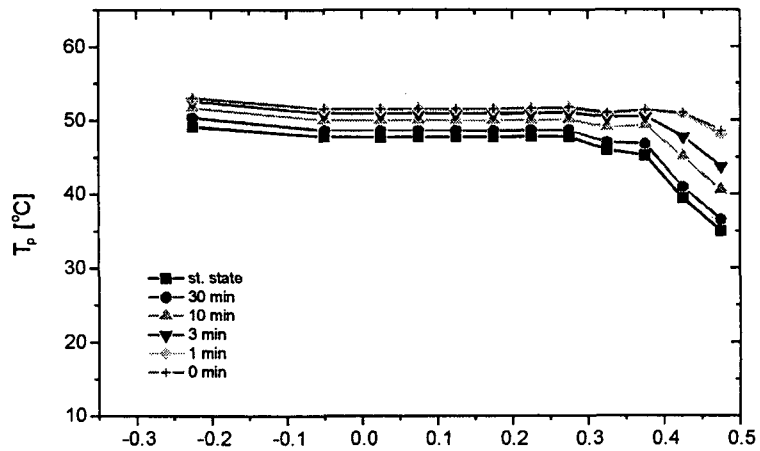


all HP's: 40 → 35 W

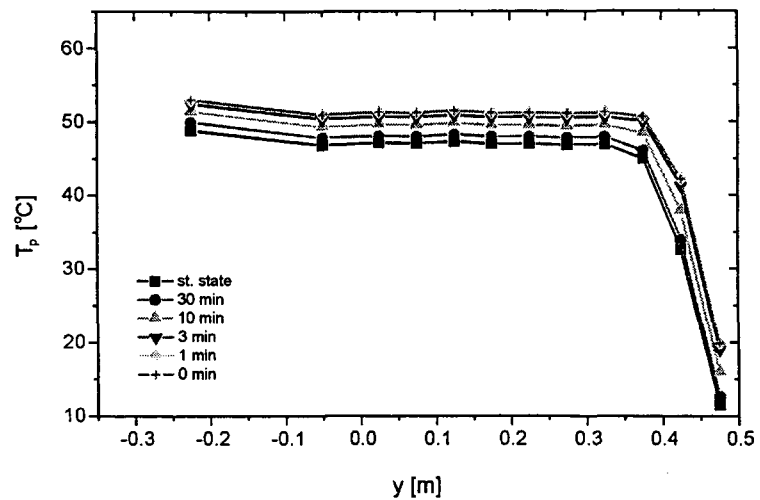
HP1



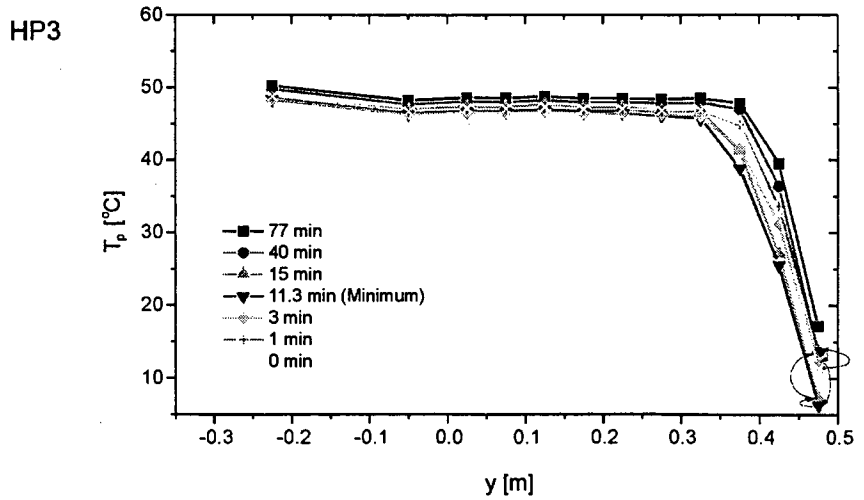
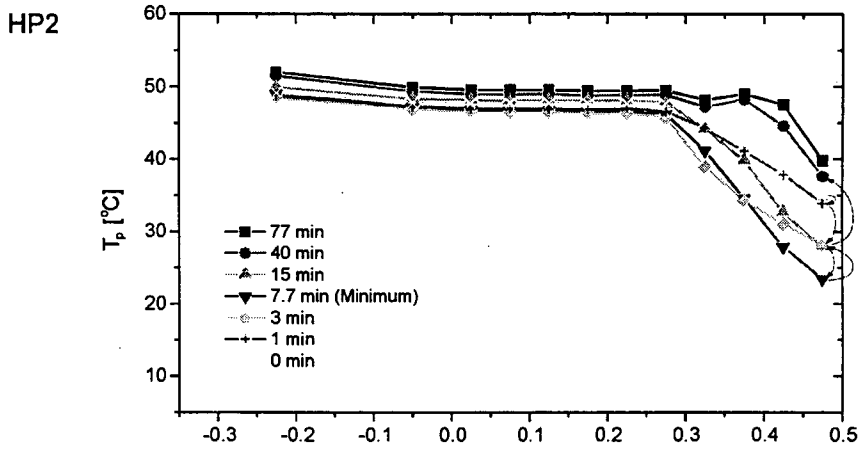
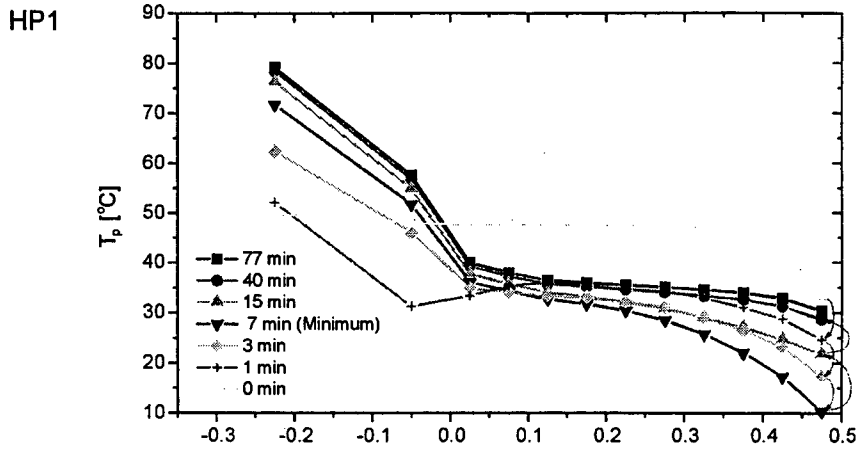
HP2



HP3



HP1 fails
(all HP's continue at 35 W)



Test run E

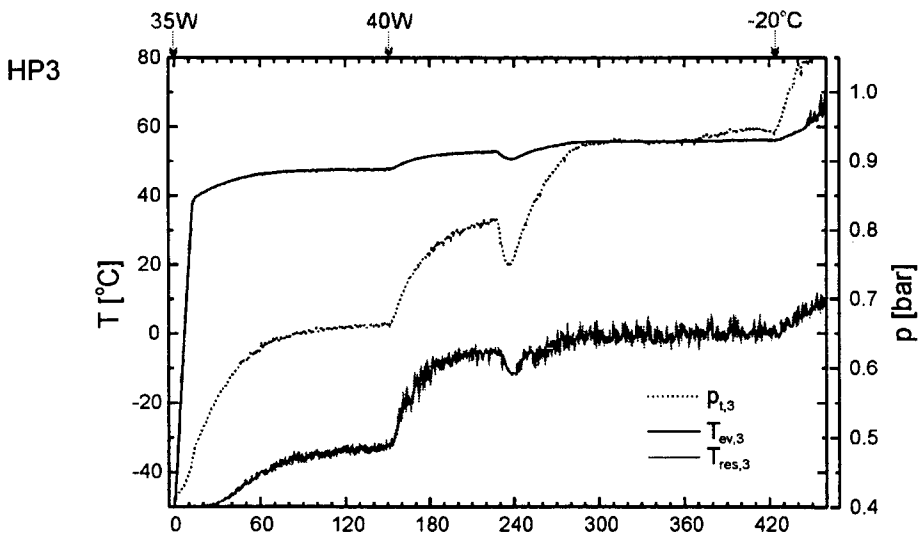
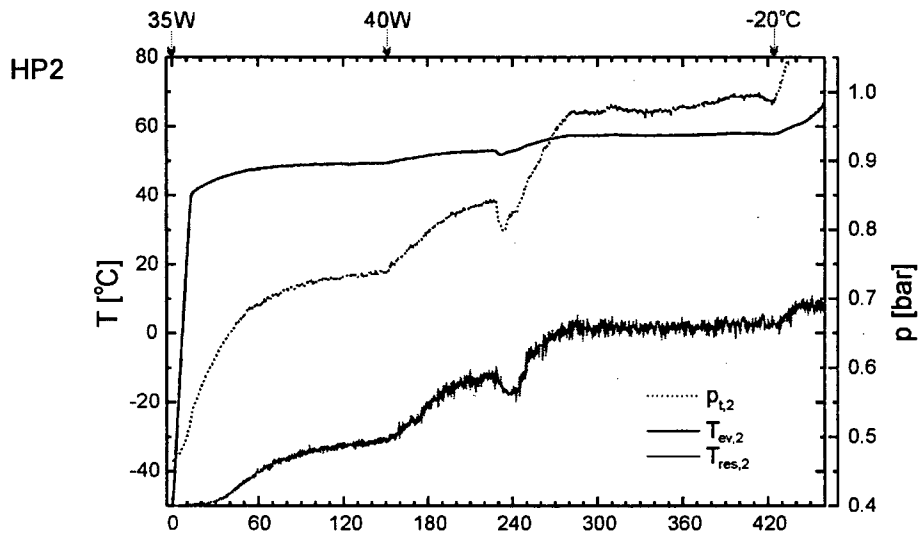
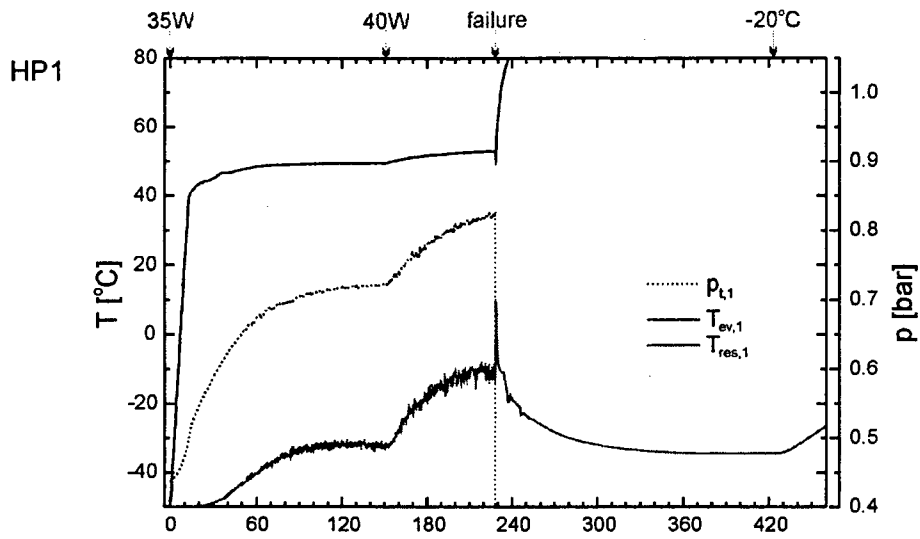
20/03/99

entire radiator, reservoirs sheathed with kapton tape

argon masses: 198 mg, 210 mg, 198 mg

 T_{∞} : -50 °C (-20 °C)

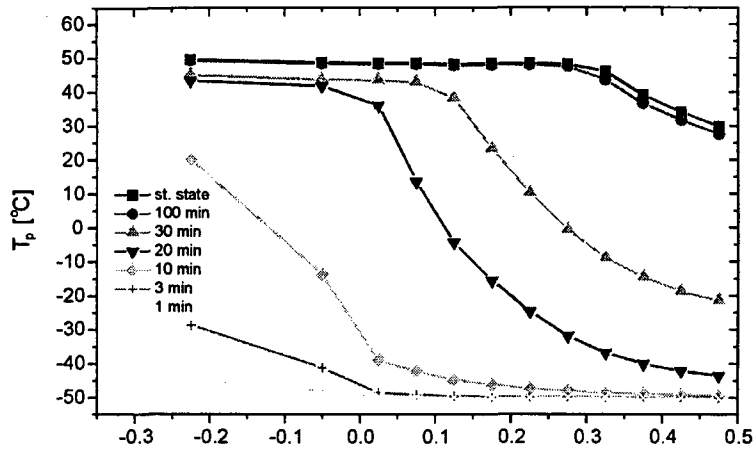
Time [min]	Power [W]	T_{∞} [°C]	
0	35 (all HP's)	-50	
151	40 (all HP's)	-50	
228	40 (all HP's)	-50	HP1 fails
423	40 (all HP's)	-20	
460	0 (all HP's)		switch-off



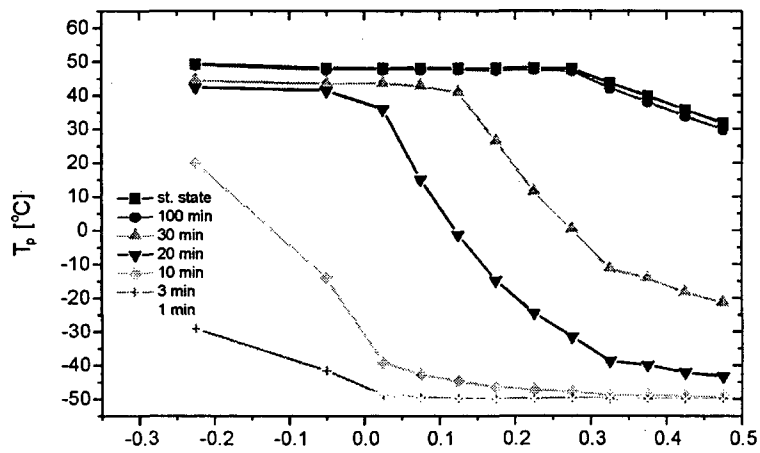
t [min]

all HP's: 0 → 35 W

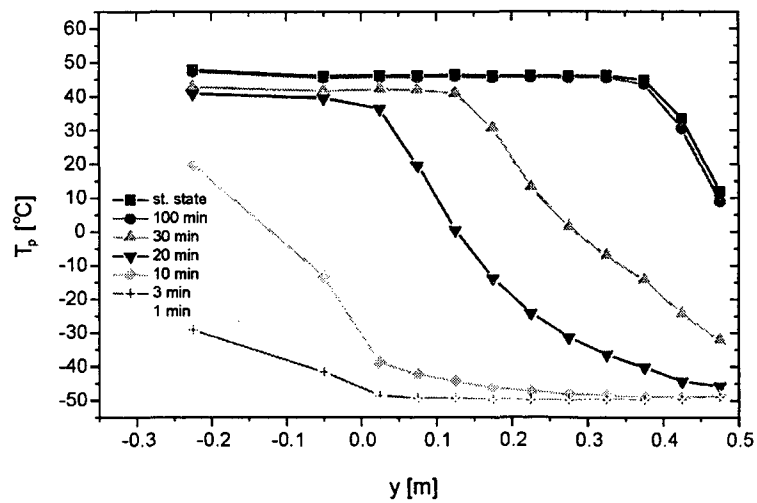
HP1



HP2

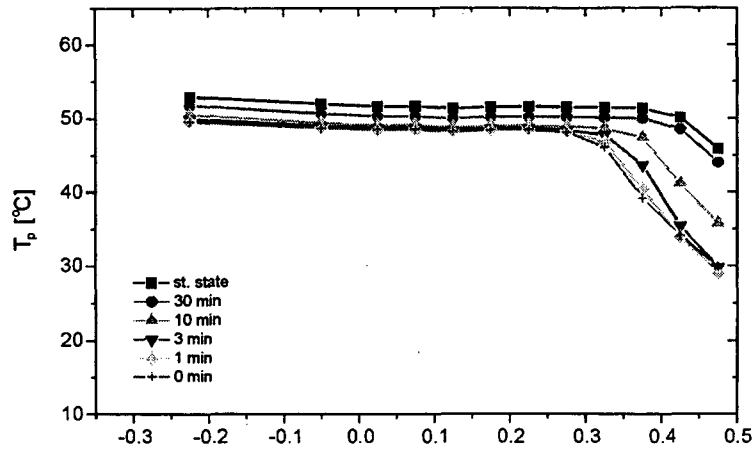


HP3

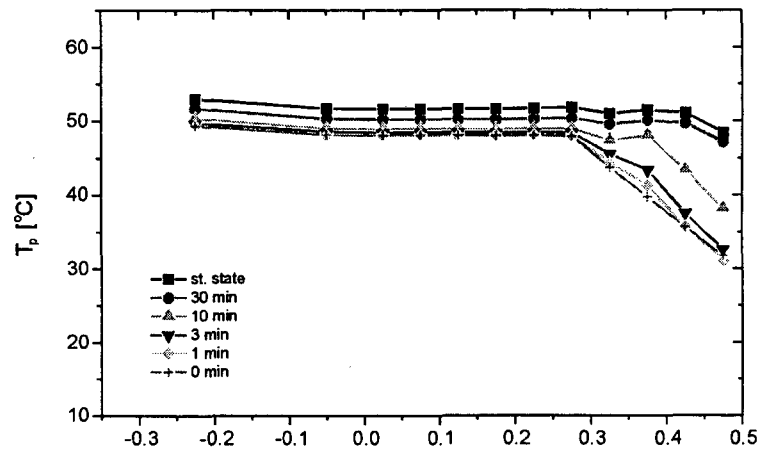


all HP's: 35 → 40 W

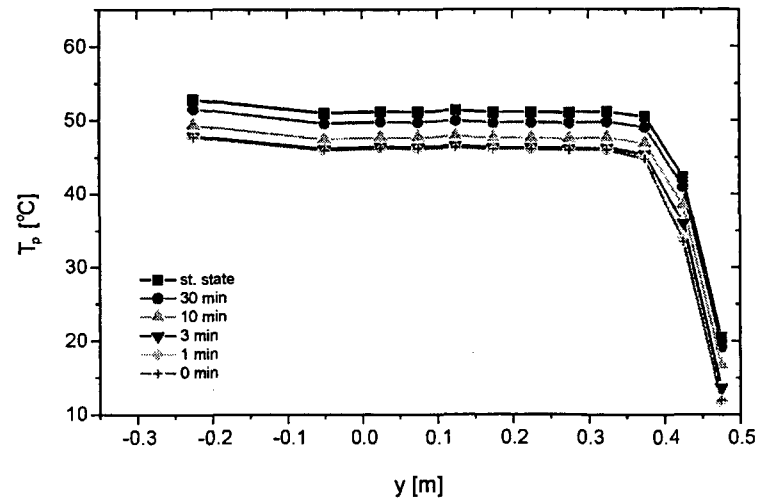
HP1



HP2

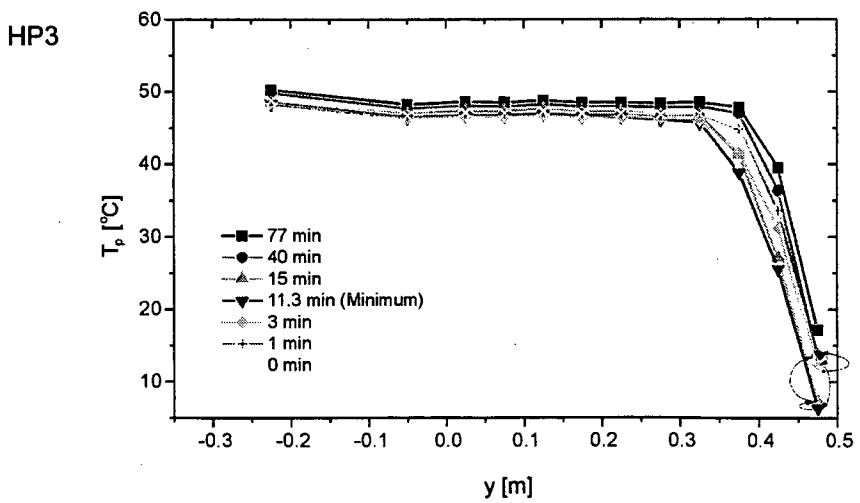
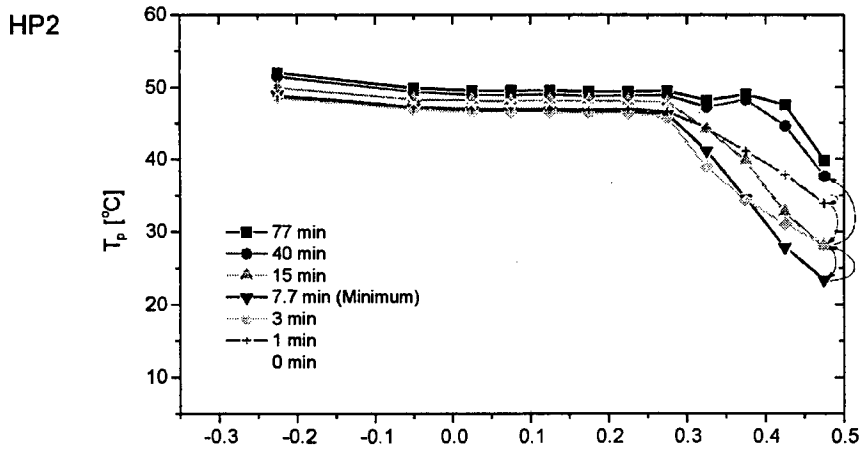
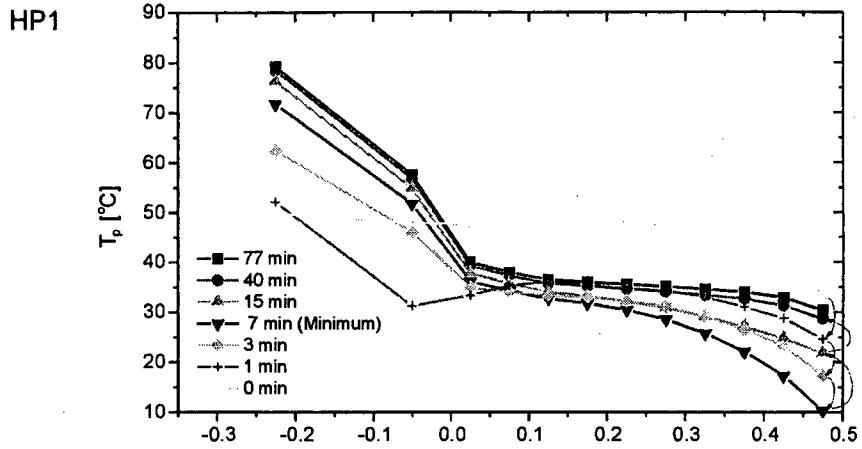


HP3

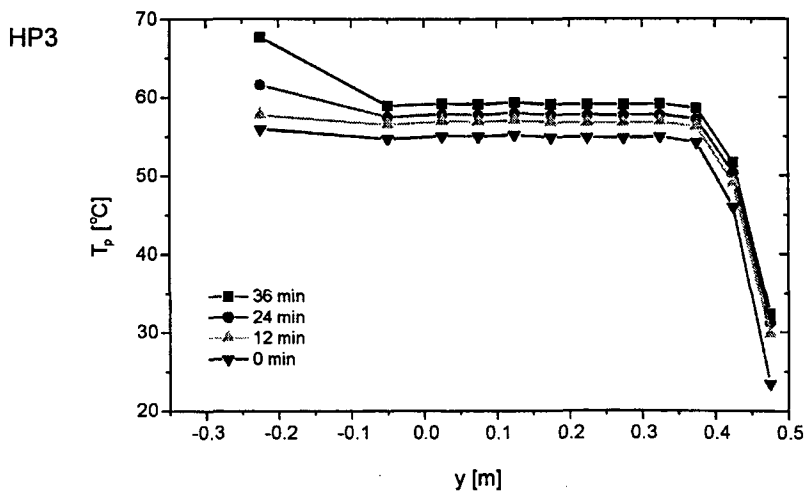
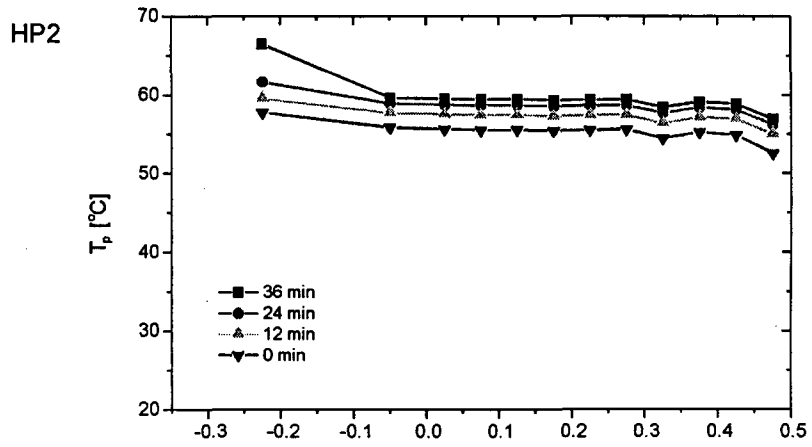


HP1 fails

(all HP's continue at 40 W)



sink temperature rise: -50 → -20 °C



Test run F

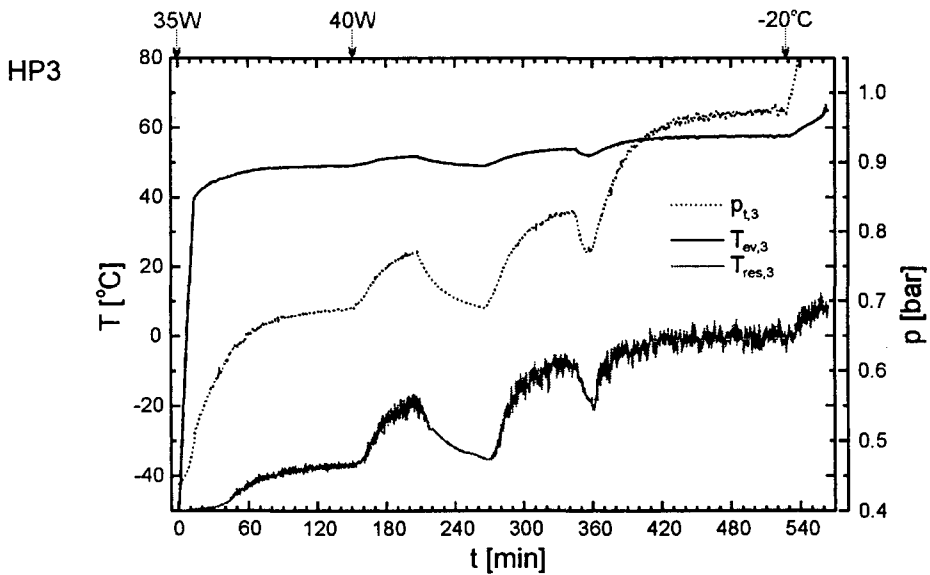
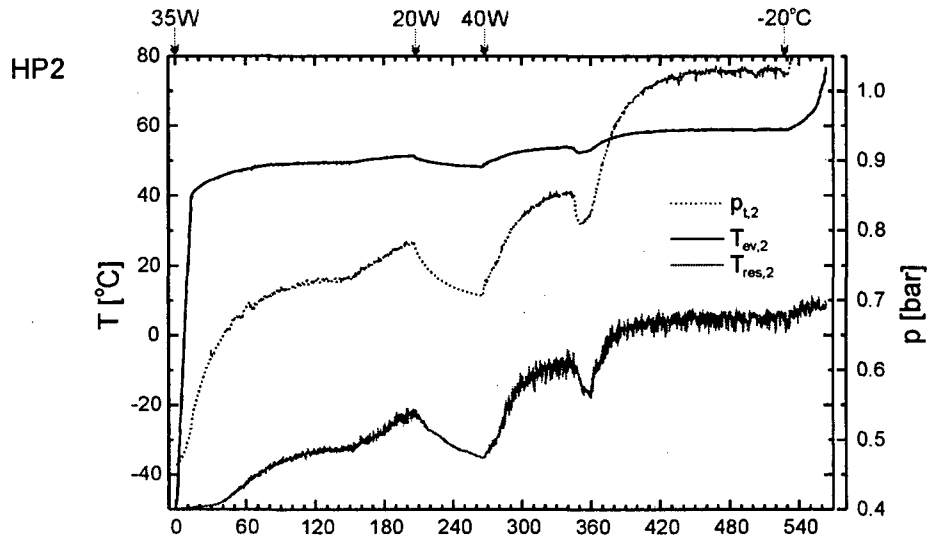
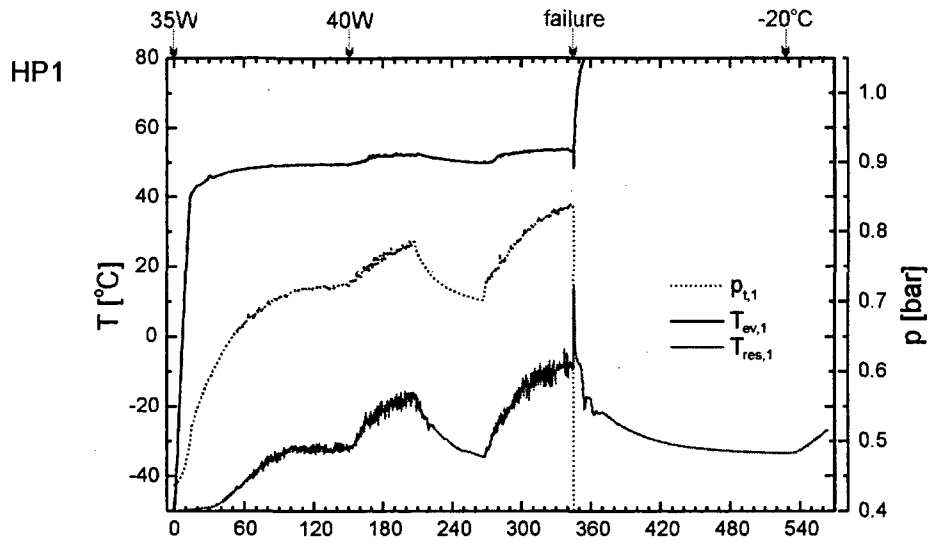
23/03/99

slitted radiator, reservoirs sheathed with kapton tape

argon masses: 197 mg, 210 mg, 198 mg

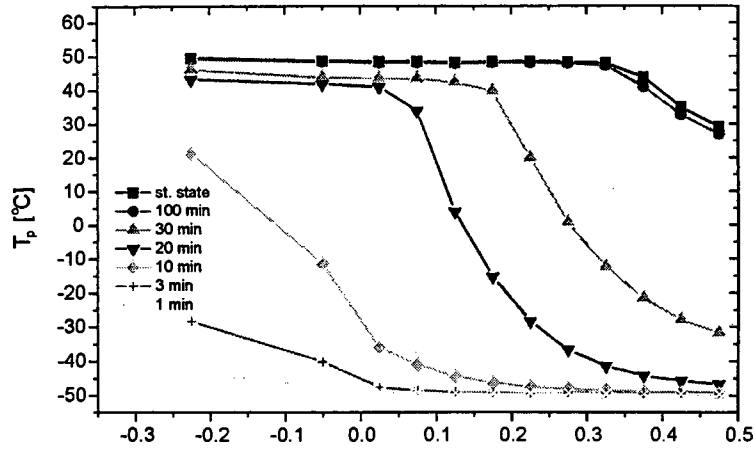
 T_{∞} : -50 °C (-20 °C)

Time [min]	Power [W]	T_{∞} [°C]	
0	35 (all HP's)	-50	
151	40/35/40	-50	
208	40/20/40	-50	
268	40 (all HP's)	-50	
345	40 (all HP's)	-50	HP1 fails
528	40 (all HP's)	-20	
564	0 (all HP's)		switch-off

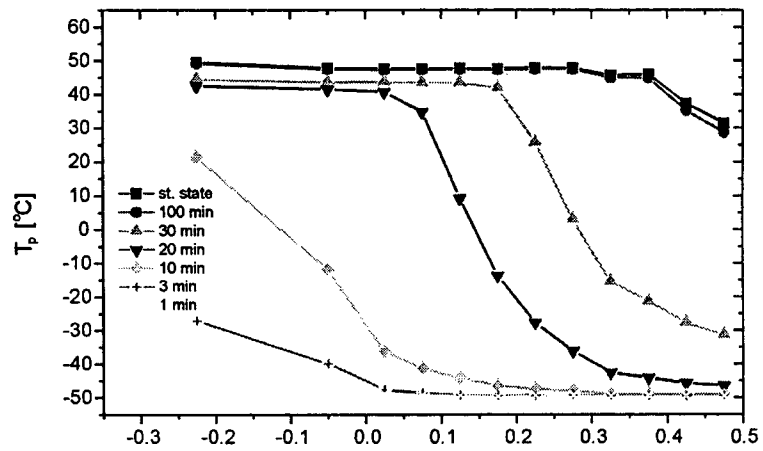


all HP's: 0 → 35 W

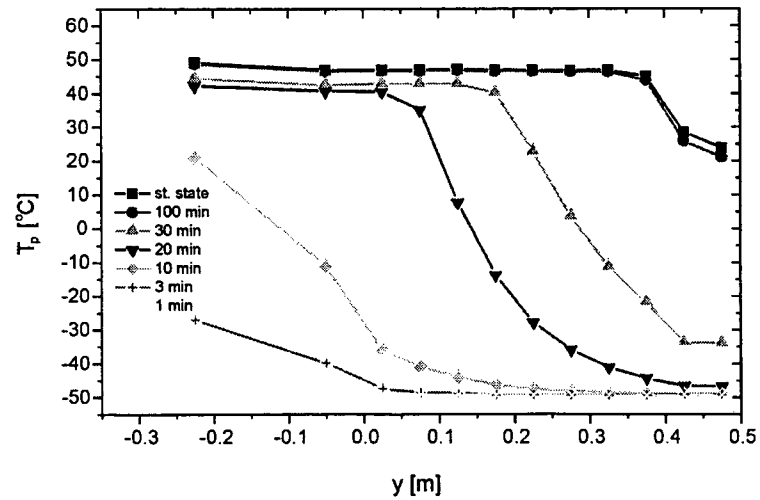
HP1



HP2



HP3

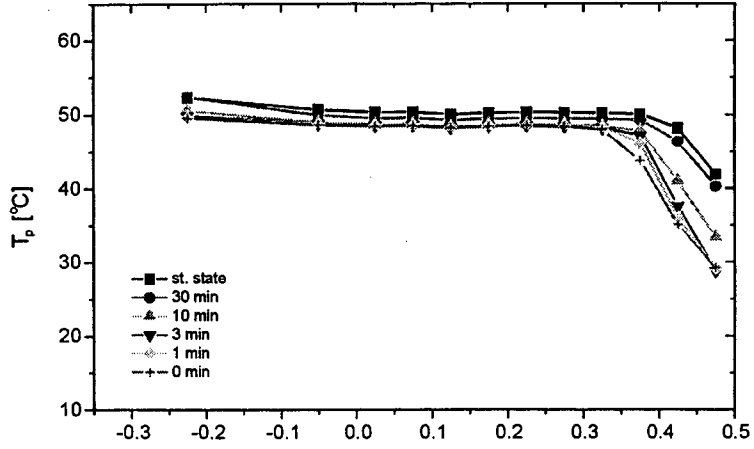


HP1: 35 → 40 W

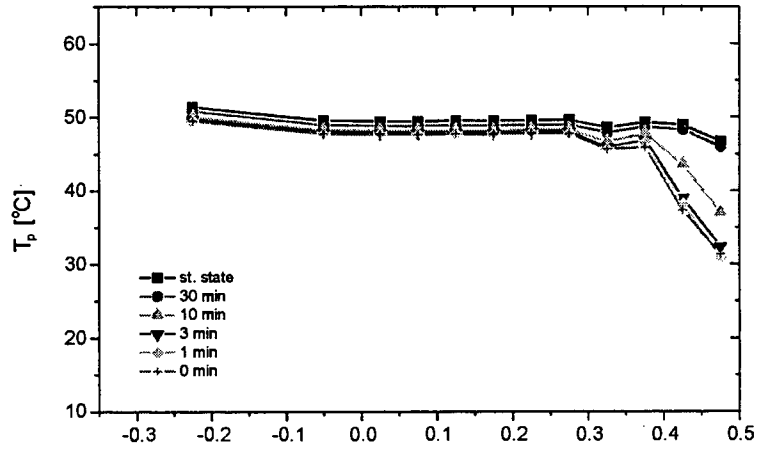
HP2: continues at 35 W

HP1: 35 → 40 W

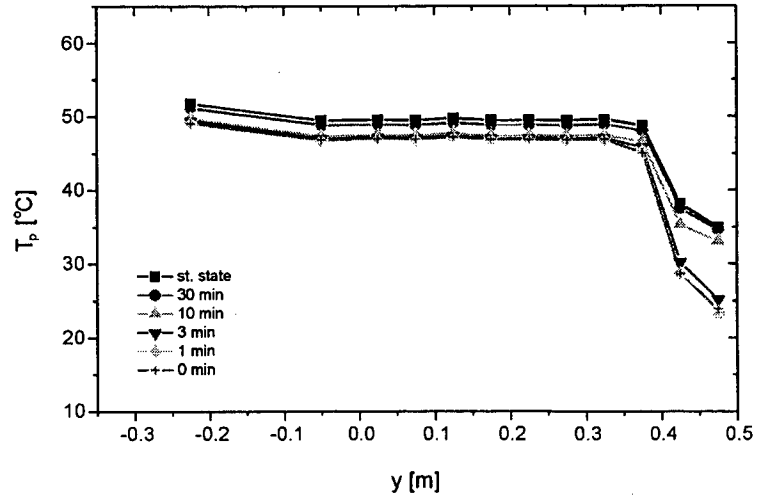
HP1



HP2



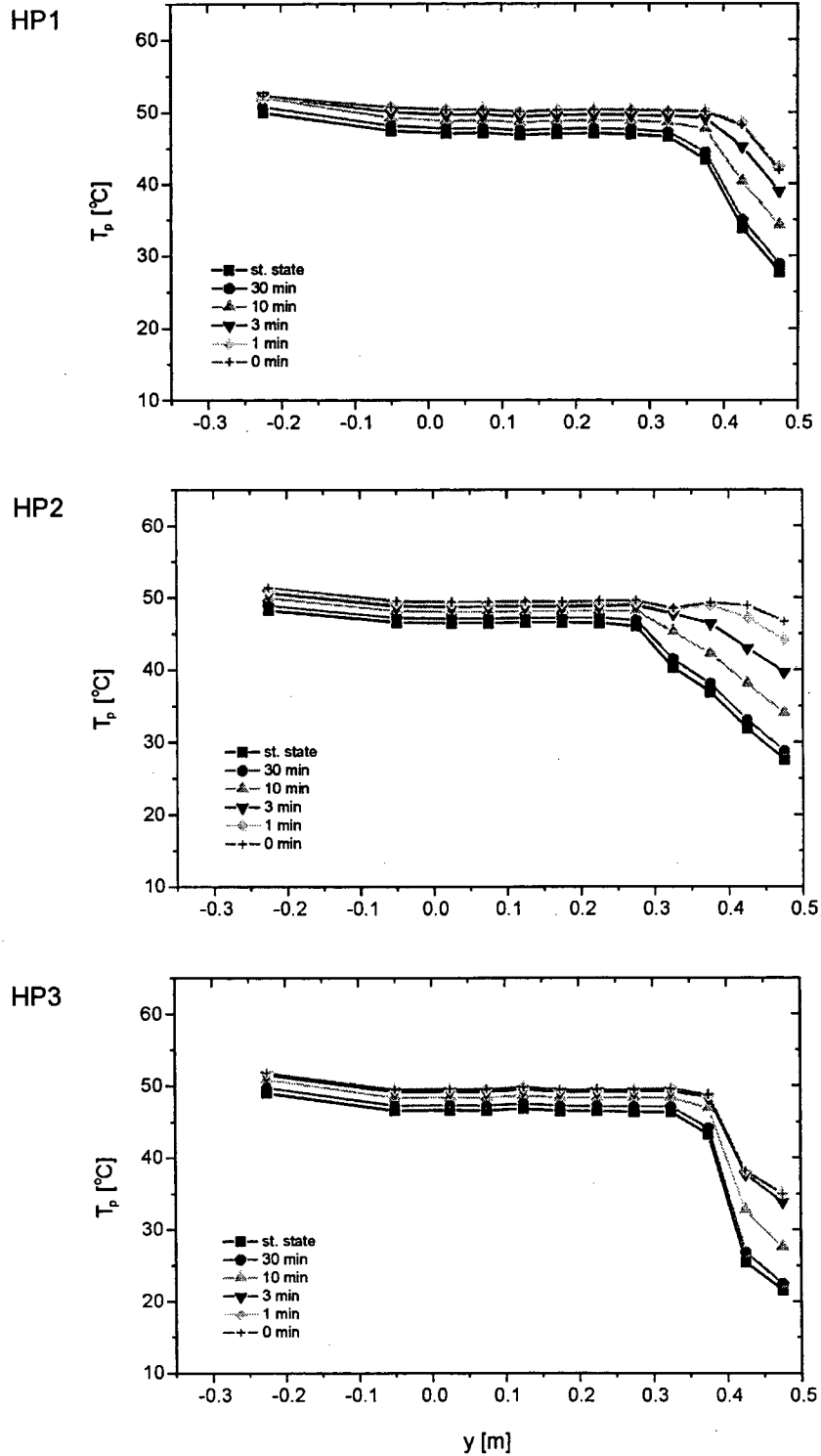
HP3



HP1: continues at 40 W

HP2: 35 → 20 W

HP1: continues at 40 W

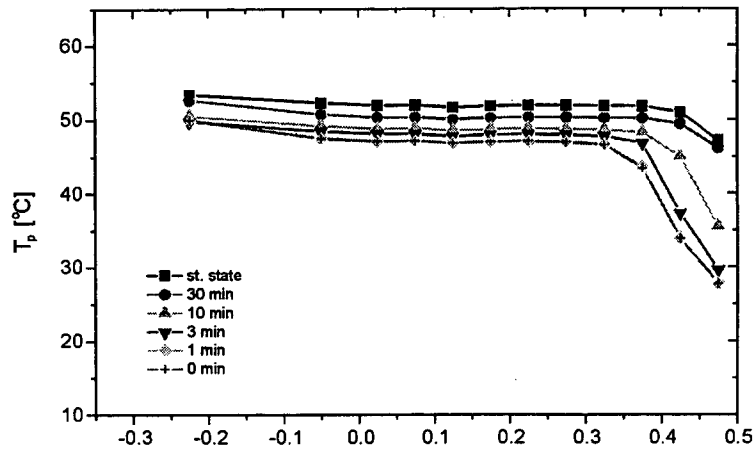


HP1: continues at 40 W

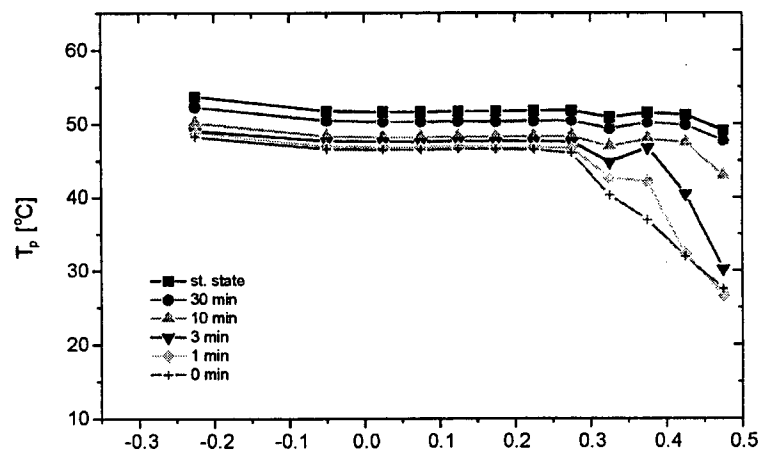
HP2: 20 → 40 W

HP1: continues at 40 W

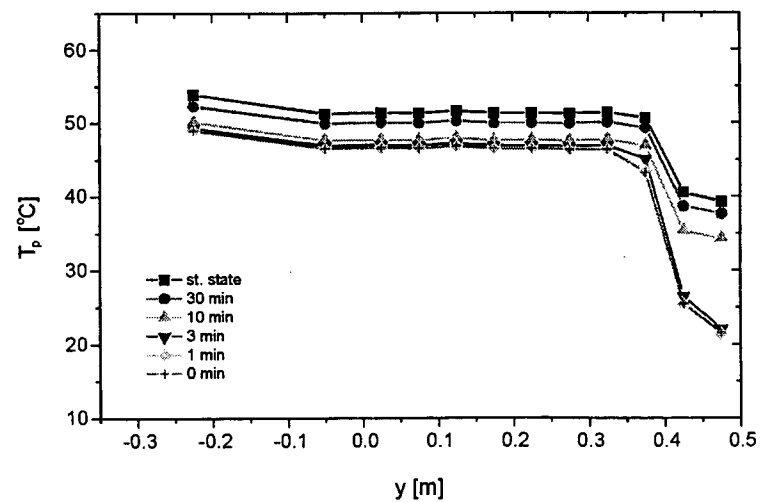
HP1



HP2

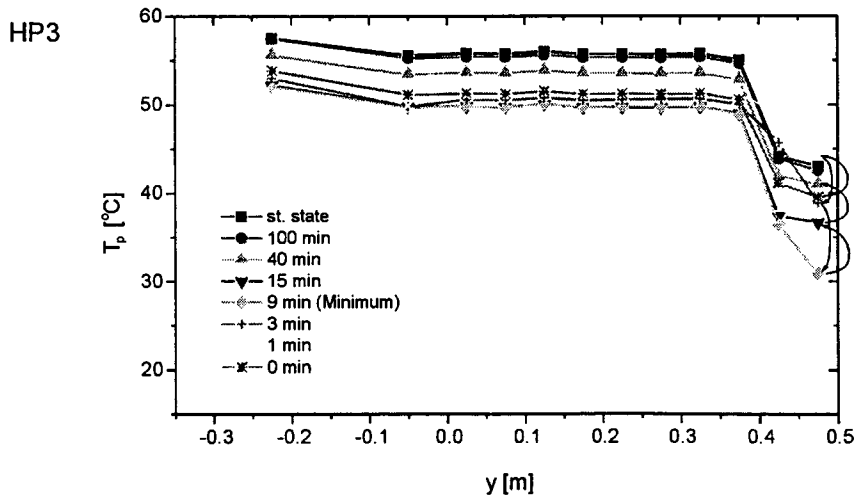
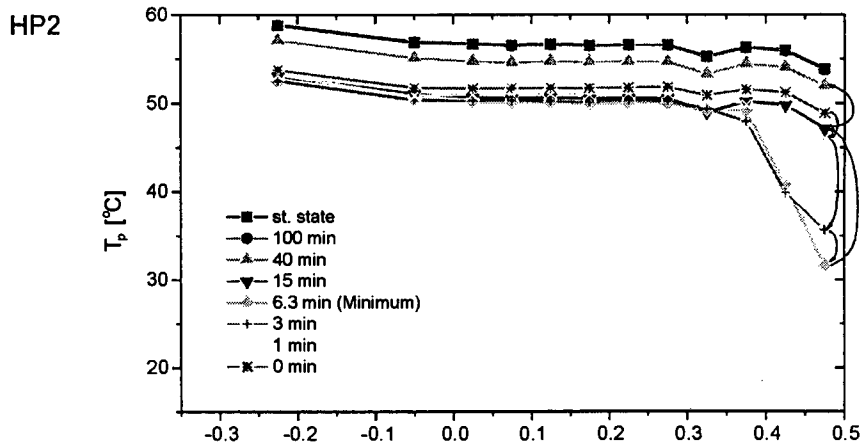
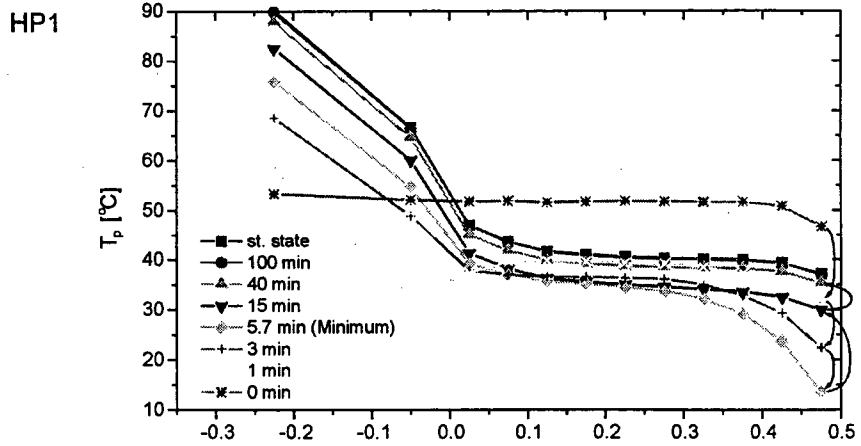


HP3

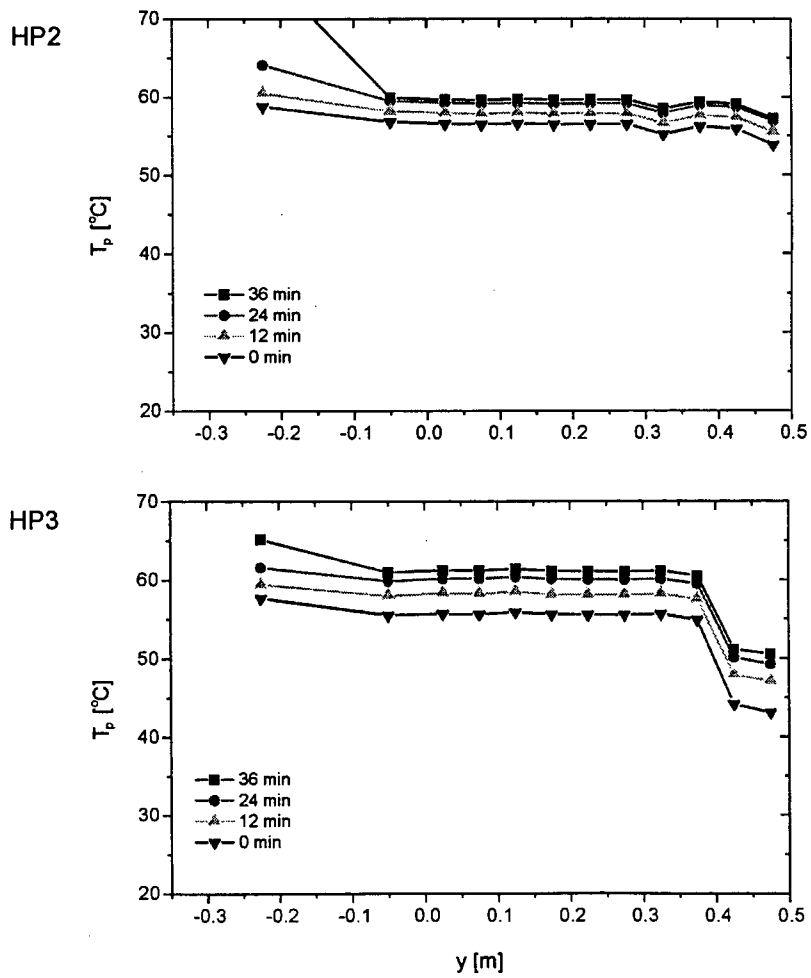


HP1 fails

(all HP's continue at 40 W)



sink temperature rise: $-50 \rightarrow -20 \text{ }^{\circ}\text{C}$



A4. SINGLE GLHP TEST DATA PLOTS (RUNS 0 – 3)

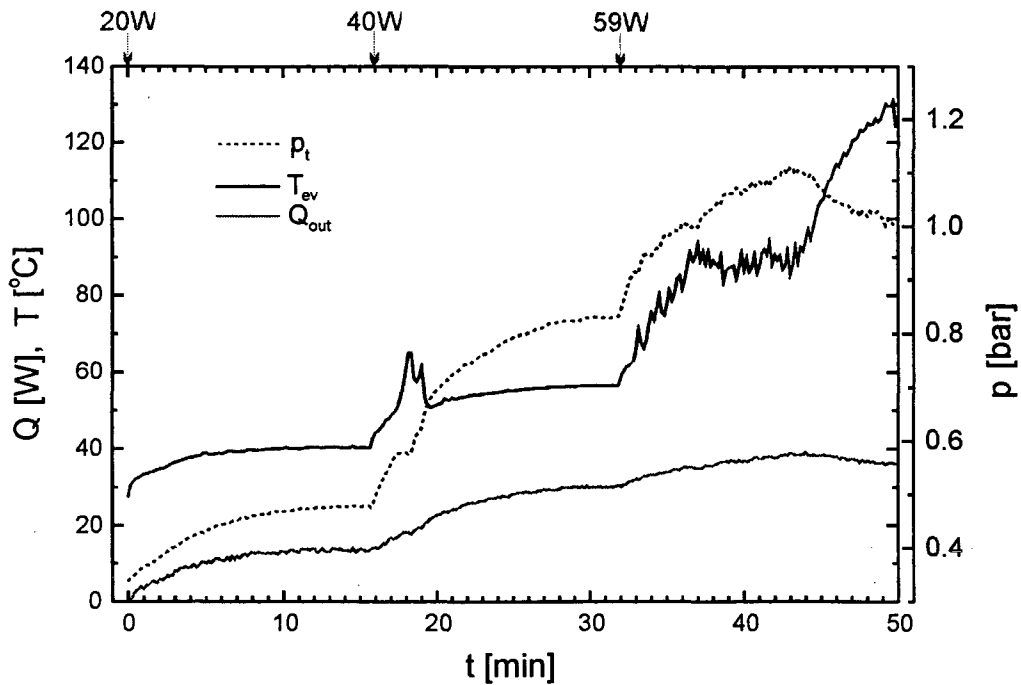
Test run 0

6/03/99

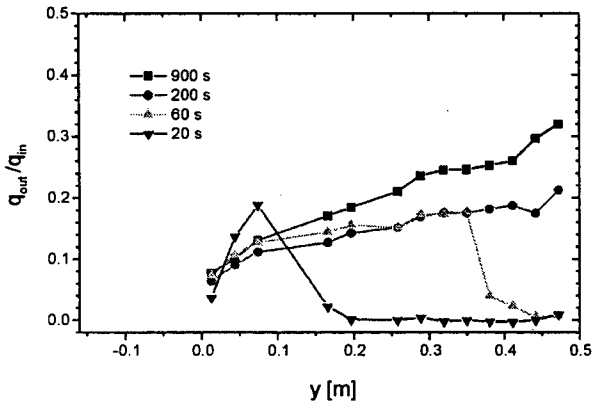
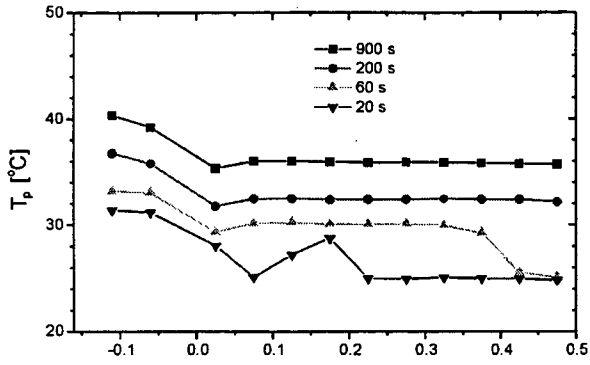
no argon charge

reservoir maintained at 50 °C

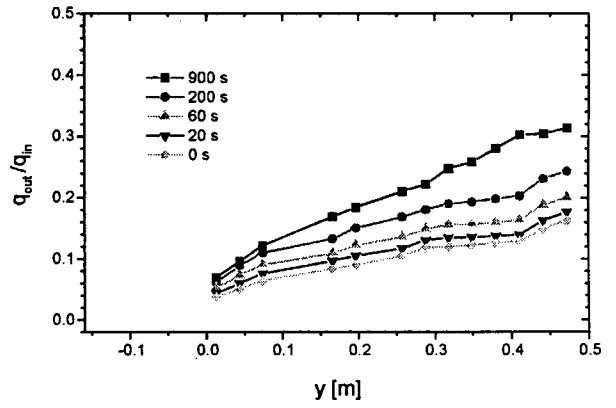
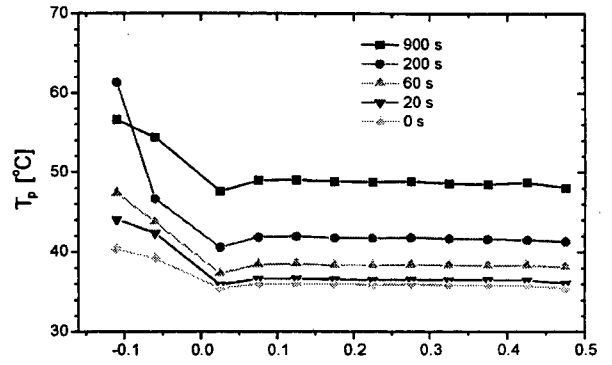
Time [min]	Power [W]	
0	20	
16	40	
32	59	
50	0	switch-off



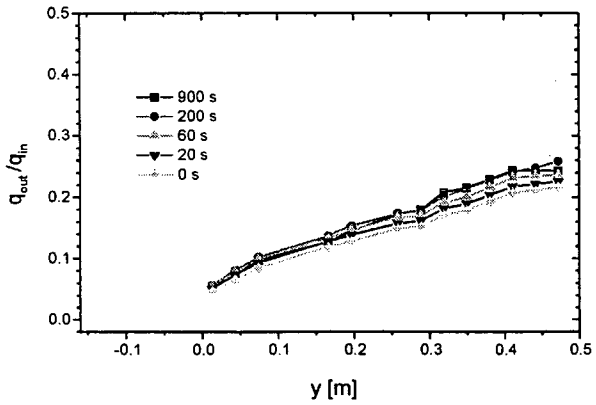
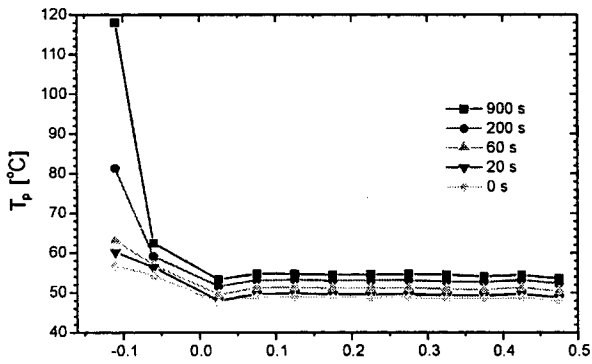
0 → 20 W



20 → 40 W



40 → 59 W



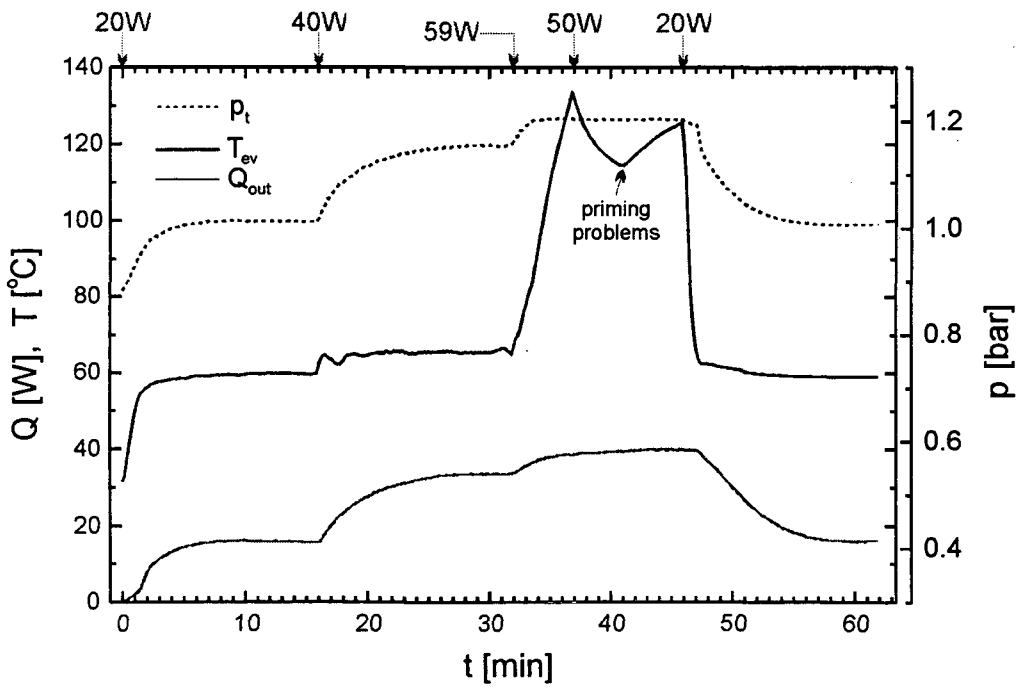
Test run 1

7/03/99

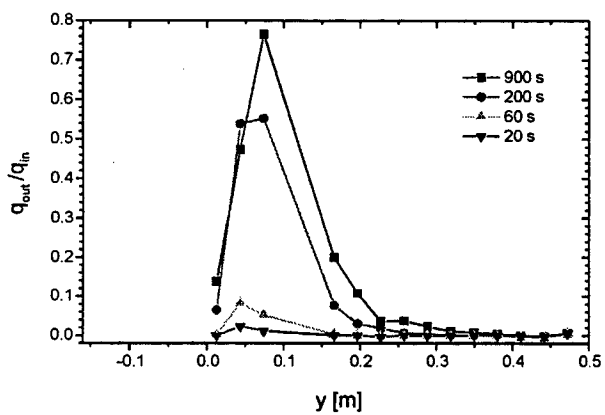
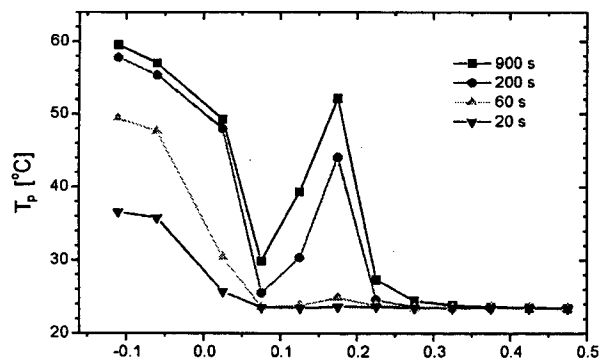
argon mass: 144 mg

 T_{∞} : 23.3 °C

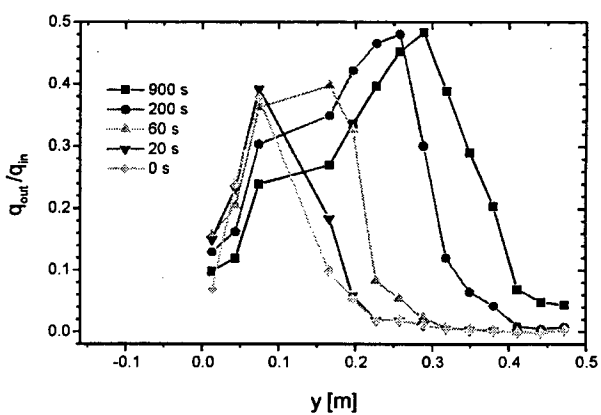
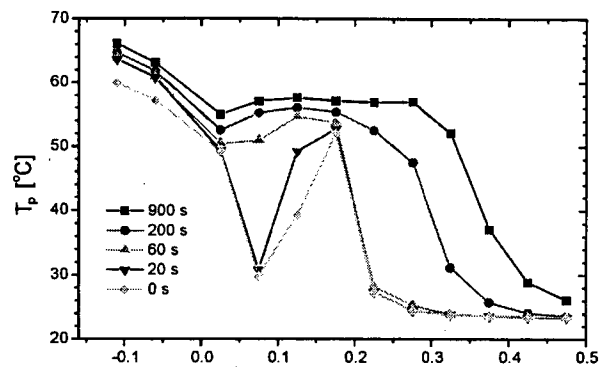
Time [min]	Power [W]	
0	20	
16	40	
32	59	
37	50	
46	20	
50	0	switch-off



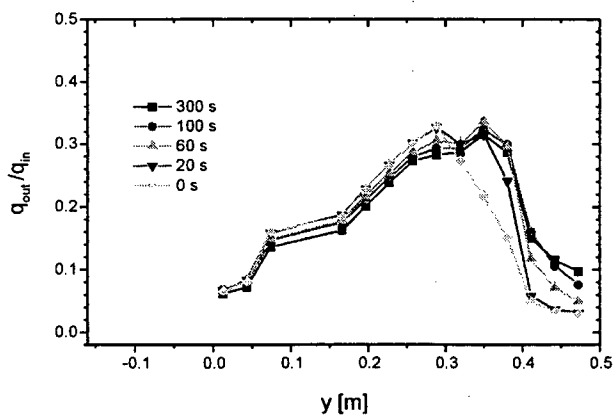
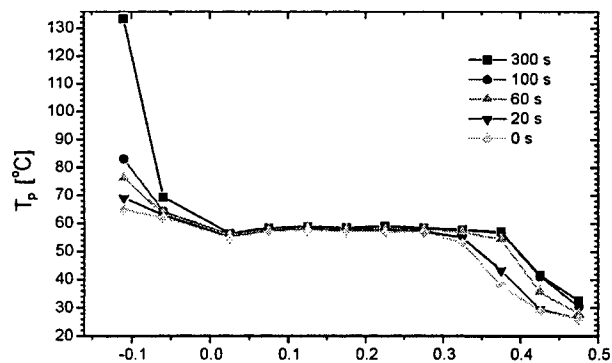
0 → 20 W



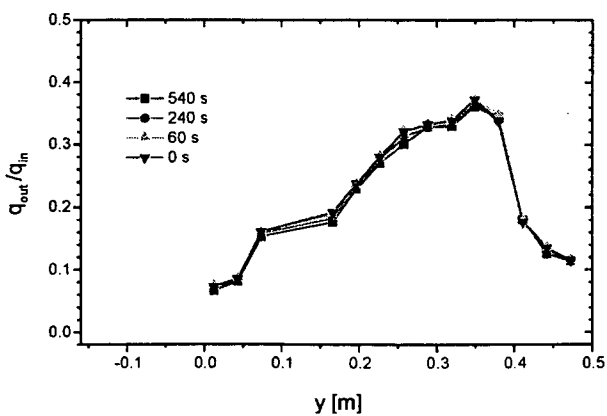
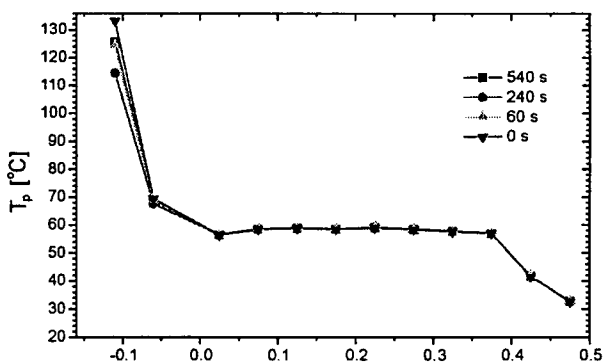
20 → 40 W



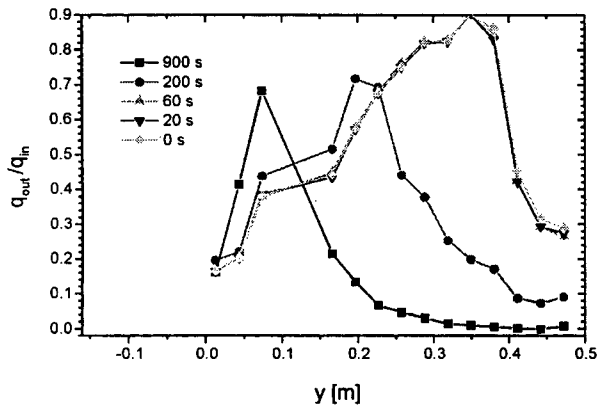
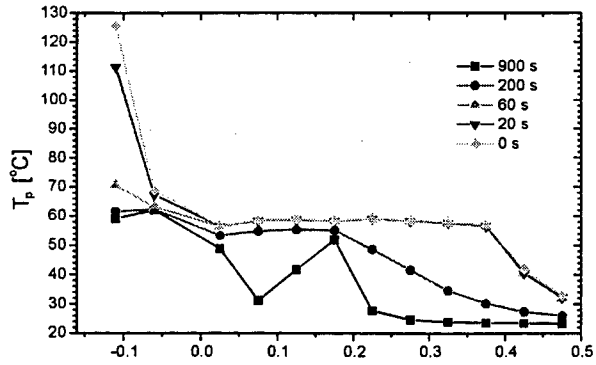
40 → 59 W



59 → 50 W



50 → 20 W

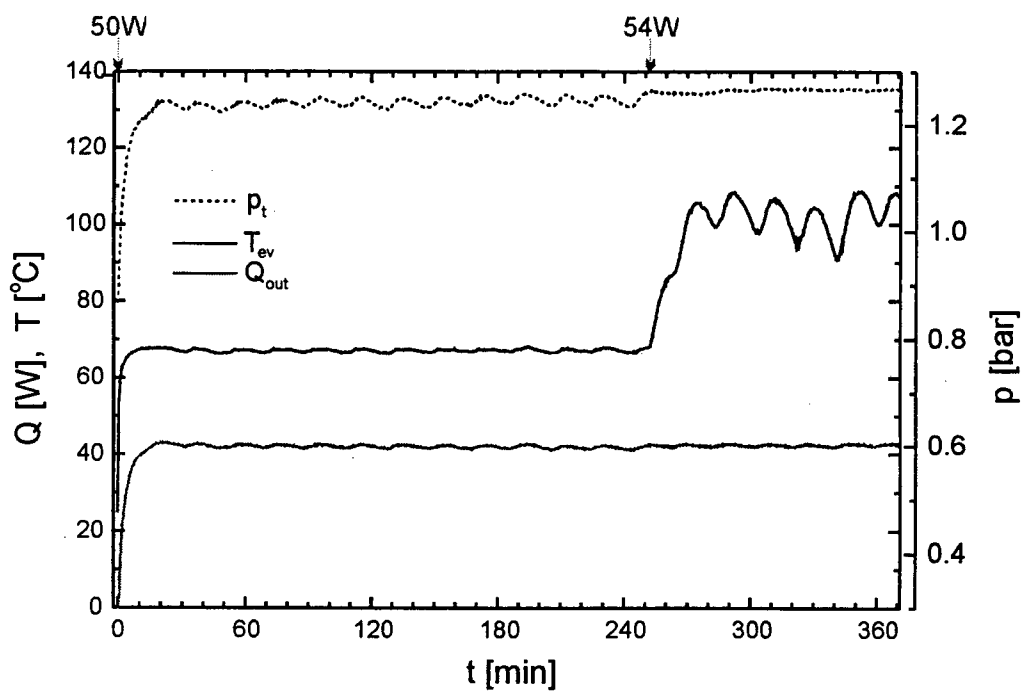
Test run 2

14/03/99

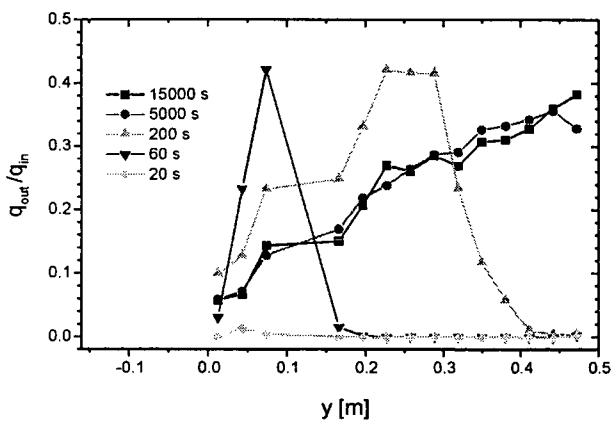
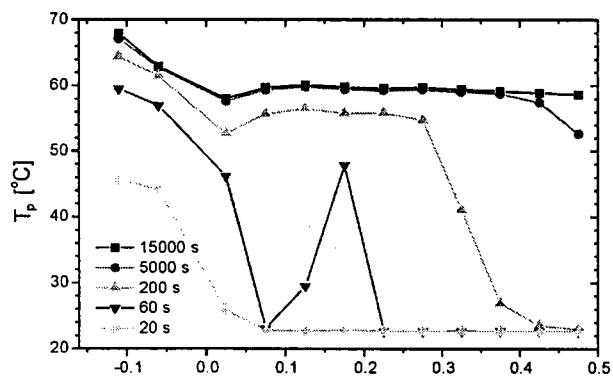
argon mass: 144 mg

 T_{∞} : 23.4 °C

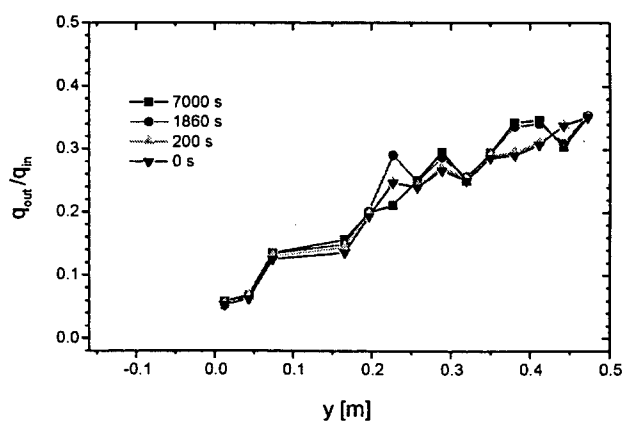
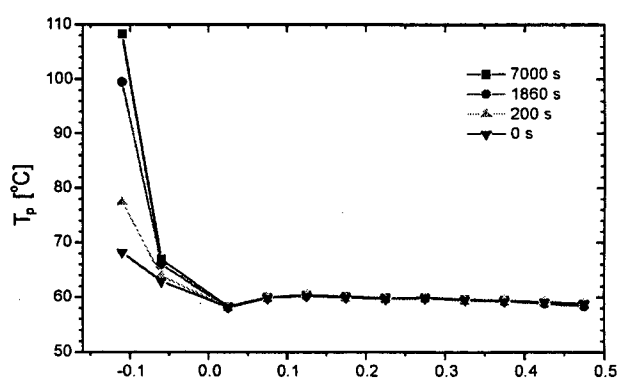
Time [min]	Power [W]	
0	50	
252	54	
371	0	switch-off



0 → 50 W



50 → 54 W



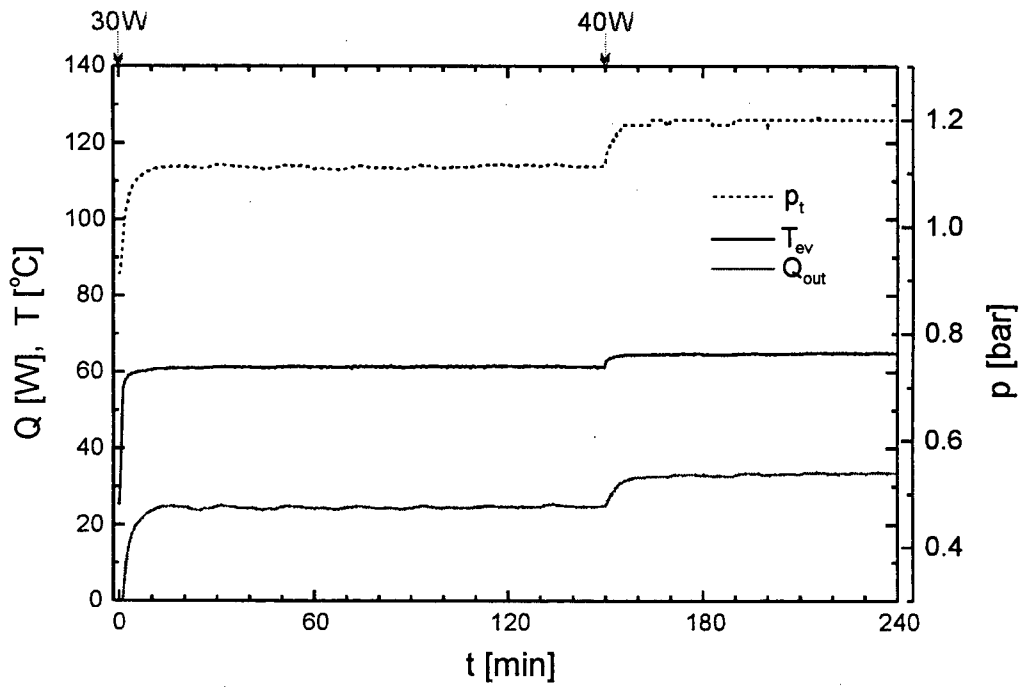
Test run 3

21/03/99

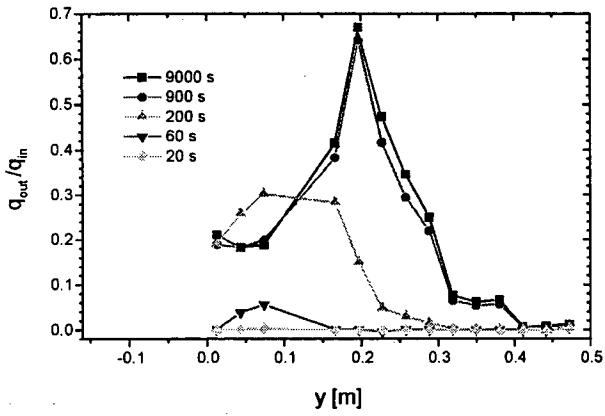
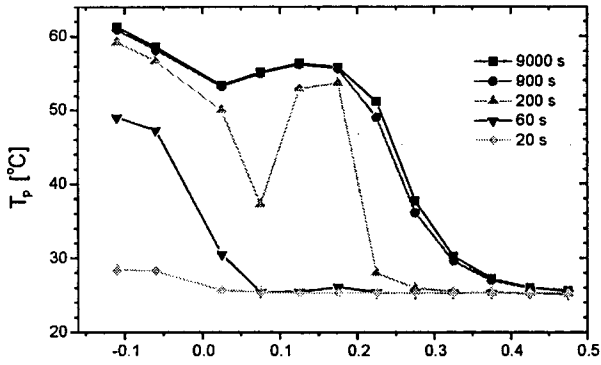
argon mass: 144 mg

 T_{∞} : 25.2 °C

Time [min]	Power [W]	
0	30	
150	40	
240	0	switch-off



0 → 30 W



30 → 40 W

